LIGHTWEIGHT IN-PLANE ACTUATED DEFORMABLE MIRRORS
FOR SPACE TELESCOPES

DISSERTATION

Michael J. Shepherd, Lieutenant Colonel, USAF

AFIT/DS/ENY/06-03

DEPARTMENT OF THE AIR FORCE
AIR UNIVERSITY

AIR FORCE INSTITUTE OF TECHNOLOGY

Wright-Patterson Air Force Base, Ohio

Lightweight In-Plane Actuated Deformable Mirrors for Space Telescopes

DISSERTATION

Presented to the Faculty

Department of Aeronautical and Astronautical Engineering

Graduate School of Engineering and Management

Air Force Institute of Technology

Air University

Air Education and Training Command

In Partial Fulfillment of the Requirements for the

Degree of Doctor of Philosophy

Michael J. Shepherd, BS, MS

Lieutenant Colonel, USAF

September 2006

AFIT/DS/ENY/06-03

Lightweight In-Plane Actuated Deformable Mirrors for Space Telescopes

Michael J. Shepherd, BS, MS
Lieutenant Colonel, USAF

Approved:

Date

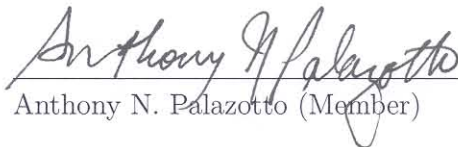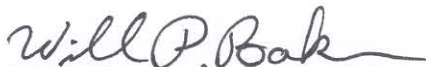_____   _____
Richard G. Cobb (Chairman)   29 Aug 06

_____   _____
Glen P. Perram (Dean's Representative)   31 Aug 06

_____   _____
Anthony N. Palazotto (Member)   29 Aug 06
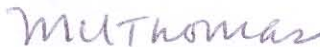
_____   _____
William P. Baker (Member)   29 Aug 06

Accepted:

_____   _____
M. U. Thomas   6 Sep 06
Dean, Graduate School of Engineering and Management   Date

AFIT/DS/ENY/06-03

Abstract

This research focused on lightweight, in-plane actuated, deformable mirrors, with the ultimate goal of developing a 20-meter or larger diameter light gathering aperture for space telescopes. Membrane optics is the study of these structures which may be stowed compactly and unfurled in orbit. Applications of the technology could potentially revolutionize deep space exploration and earth surveillance. This effort comprised four research areas in the field of membrane optics for quasi-static applications: modelling, analytical solutions, surface control strategy, and scaling.

The underlying differential equations for a unimorph plate-membrane were developed. Unimorph actuation refers to a piezoelectric actuator offset from the planar neutral axis that imparts a bending moment on the structure. The assumptions for quasi-static piezoelectric theory, the piezoelectric-thermal analogy, and plate-membrane elastic behavior were reviewed.

Initially, experimental results were compared to theory using a 0.127 meter diameter deformable mirror testbed. The mirror was modelled using finite elements with MSC.Nastran software, where a boundary tension field was determined using laser vibrometer data. A non-linear solution technique was used to incorporate the membrane stiffening from the applied tension. Statically obtained actuator influence functions were compared to experimentally achieved data, and then a least squares approach was used as the basis for creating a quasi-static control algorithm. Experimental simultaneous tracking of Zernike tip, tilt, and defocus modes was successfully demonstrated.

The analytical solutions to plate-membrane and beam-string ordinary differential equation representing the deformable mirror equations were developed. A simplified approach to modelling the axisymmetric cases was also presented. Significantly, it was shown both analytically and through numerical analysis that static actuation

for a mirror with a discrete electrode pattern and a high tension-to-stiffness ratio was simply a localized piston displacement in the region of the actuator.

Next, a novel static control strategy, the *Modal Transformation Method*, was developed for membrane mirrors. The method was implemented in finite element simulation, and shows the capability of the in-plane actuated mirror to form Zernike surfaces within an interior, or *clear aperture*, region using a number of statically-actuated structural modes.

Lastly, the scaling problem for membrane optics was addressed. Linear modelling was shown to correctly explain the behavior of small-scale laboratory models, but full non-linear models were required to account for all the dominant terms which govern full-scale large aperture membrane telescopes. In the test cases analyzed, non-linear deformations of a full-scale mirror were orders of magnitude less than suggested by linear theory. The results suggest non-linear effects must be considered in feasibility studies for future large aperture membrane telescopes.

This document thus charts a rigorous course towards the goal of realizing large-scale in-plane actuated space telescopes. From fundamental equations, assumptions, and solutions; to control algorithms for small-scale deformable mirrors; and through analysis designed to ease the transition to larger scale applications, this contemporary discourse addresses a collection of fundamental challenges in the emerging field of membrane optics.

Acknowledgements

This work truly is a testimony to exceptional caliber of the professors at AFIT, and to the character of the colleagues who helped me in this endeavor. To thank each one would require a separate volume; however, I humbly offer my deepest gratitude.

I would like thank Dr. David Walker, who provided me with the opportunity to attend AFIT. I am grateful to Captains Eric Trad and Gina Peterson, two master's students who poured heart and soul into this project, and taught me far more then they might ever realize. I would also like to recognize the financial sponsorship provided by the Air Force Office of Scientific Research under Lt Col Sharon Heise.

My committee members, Dr. Anthony Palazotto and Dr. William Baker, were both enthusiastic supporters and dedicated, patient tutors. In those rare moments when slight headway was made, they were the first to offer gracious praise while simultaneously recognizing further boundaries to be explored. I am deeply indebted to these two very fine scholars and gentlemen. I am also very appreciative of the efforts of Dr. Glen Perram, who acting as our Dean's representative, made comments which significantly improved the clarity of the dissertation.

My research chairman, Dr. Richard Cobb, had a profound impact on me both academically and professionally. I greatly benefitted from his tutelage, and while I aspire to model myself after him, I cannot imagine I will ever match his curiosity, intellect, humor and creative spark, all of which make him such an exceptional mentor.

I would like to thank my beautiful bride who shared every day as my closest confidant and ally, and was truly the one person who made this all possible. I am also grateful for my children, each of whom bring joy to my life. I love them each and all.

Finally, I dedicate this work to my parents, who provided me the impetus to always reach higher, and believed in me from the start...

Michael J. Shepherd

Table of Contents

List of Figures

xii

xiv

List of Tables

List of Abbreviations

Lightweight In-Plane Actuated Deformable Mirrors for Space Telescopes

I. Introduction

1.1 Introduction

The Air Force Office of Scientific Research (AFOSR), the sponsor agency of this research effort, is extremely interested in the application of smart material technology to lightweight space-borne large-scale optical systems.

Increasing mirror aperture size will provide enormous benefits to the intelligence community. For instance, using space-based surveillance, a single 30-meter membrane mirror in a 5000-km equatorial orbit would obtain the same atmospheric-limited 10-cm accuracy as current low earth orbit satellites, but could provide *global* (sub-polar) coverage [9]! The motivation is clear–very large (20-meter and greater diameters) rigid mirror structures are prohibitively large for all current and proposed launch technologies. To overcome this severe packaging limitation, various flexible mirror configurations involving active membrane elements, such as inflated lenticulars, dual cylindrical parabolic dishes, and formation flights of flat membrane mirrors, have been proposed to fulfill this critical niche [24, 25, 149]. A conceptual design of a large-scale optical system is shown in Figure 1.1. Investigation of optical membrane structures, a field of research here coined *membrane optics*, is the primary focus of this research effort.

1.2 Research Goal

The research proposed in this document will develop static modelling procedures for a space-based optical system reliant upon in-plane piezoelectric actuators to induce surface deformations to micron-level precision. The technologies proposed may be used either to create a deformable mirror for an adaptive optics system, or to increase

1
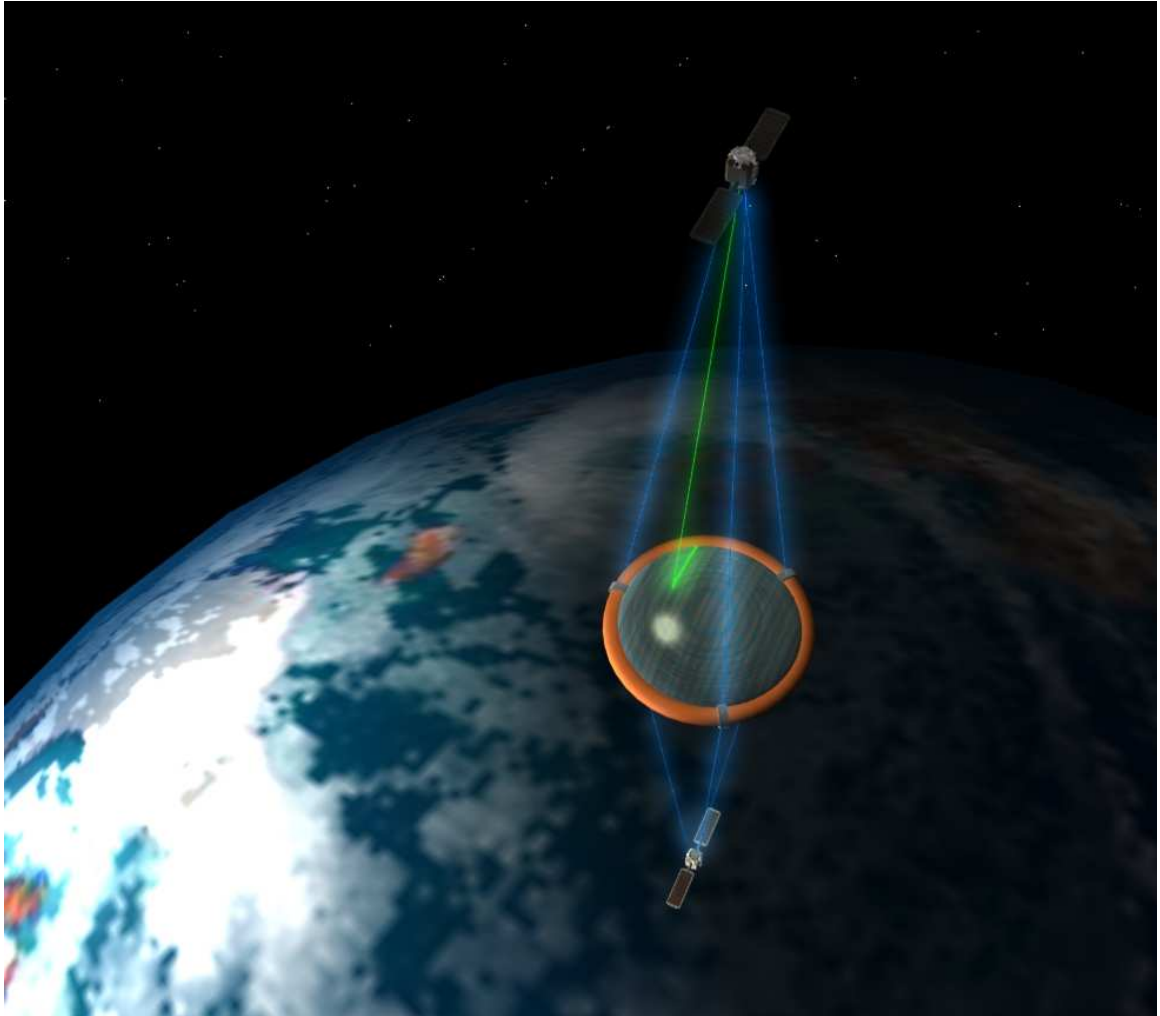
(a) In this artist's rendition of an earth-facing space telescope, an electron beam scans the piezoelectric actuating layer on the non-reflective side of a membrane optic to precisely form the mirror's surface. The primary mirror is a membrane element 20-meters in diameter. It is suspended in a torroidal ring of rigidizable material. A second satellite is placed at the focal length of several hundred meters, and houses the secondary mirror surface and sensors. This document investigates the surface shaping of the membrane optic–the satellite dynamics and remote actuation mechanisms are other areas of on-going research.

Figure 1.1:   Large space-based optics *AFIT*.

the surface stability by providing disturbance rejection to an otherwise non-active mirror. Furthermore, the research seeks to bridge the gap between the terminology of the optics community and the underlying structural behavior presented by the physics of the flexible, deformable mirror structure. Thus, the objective of this research project is to produce a model of the in-plane actuated mirror system suitable for quasi-static structural control to optical commands. The scope of the research was guided by the following research statement.

- *Investigate and develop a method for low-order static modelling of in-plane actuated, tensioned, lightweight, fixed-rigid boundary, circular apertures for control of large space-based optics.*

1.3 Mission Impact

The research detailed herein advances the state-of-the-art for membrane optics. Successful contributions will increase likelihood of fielding a large-scale membrane mirror to support Department of Defense surveillance activities. Significant gains offered to the scientific community include

- Demonstrated first experimental closed-loop control of an in-plane actuated structure on an optical scale;

- Developed axisymmetric plate-membrane solutions resulting in near finite-element quality results in closed form;

- Developed the *Modal Transformation Method*, a directive strategy for Zernike control on a membrane mirror, and demonstrated through simulation that when used on an in-plane actuated membrane mirror, near error-free low-order Zernike surfaces may be constructed;

- Performed scaling analysis for membrane optics which shows the path to large-scale optics lies in non-linear analysis and highlights the key areas unique to membrane mirrors and unimorph actuation.

1.4 Document Organization

This document is organized into eight chapters.

- Chapter I introduces the research area and provides the thesis statement.

- Chapter II provides the contextual background of the research area, and provides an outline of current research in the field of membrane optics.

- Chapter III outlines the development of piezoelectric theory, presents the piezoelectric-thermal analogy, and develops the governing equation for an in-plane actuated circular plate-membrane.

- Chapter IV presents the non-linear finite element modelling and experimental closed-loop quasi-static control efforts performed on a 0.127m diameter test article, the AFIT deformable mirror testbed.

- Chapter V analyzes the linear piecewise continuous axisymmetric ordinary differential equation for an in-plane actuated beam-string and plate-membrane. An analytical solution method is presented, as well as an approximation method, and the results are compared to the non-linear finite element model of Chapter IV.

- Chapter VI formulates the Modal Transformation Method. For circular apertures, the Zernike basis set is used to describe the optical path disturbances for control, but is incompatible with the fixed edge condition of the deformable mirror. The Modal Transformation Method uses an algebraic combination of Bessel-based statically actuated vibration mode shapes to perform static surface control.

- Chapter VII discusses the problem of scale as it relates to membrane optics. In much of the research to date, small-scale models are used to demonstrate technologies. It is demonstrated through finite element simulation that the scale of the model directly influences the shape and magnitude of surface deformation.

Specifically, non-linear effects not readily observed in small-scale models may be present in large-scale applications.

- Chapter VIII summarizes the salient points of this work, and presents a myriad of possibilities as candidates for future research.

In addition to these chapters, supporting appendices fill in the technical details associated with the experimental and analytical modelling, such as the operating parameters of the optical measurement system and the source code for the finite element computer models.

1.5 Summary

This chapter outlined the dissertation objective of producing a model for the in-plane actuated mirror system suitable for structural control as it relates to space-borne telescopes. The next chapter will provide a survey of the current literature on the subject.

II. A Survey of Membrane Optics

Chapter objectives:

- *Provide description and key terms for membrane optics*
- *Present a survey of current literature*

2.1 Introduction

Fielding a space telescope with a primary light gathering aperture composed of lightweight, flexible material is a subject of intensive study over the last decade. The primary geometry explored in this dissertation is the flat circular piezoelectric in-plane actuated deformable mirror, of which extensive research has only been conducted at the Air Force Institute of Technology. To understand the problem, and the corresponding choice of the configuration for this investigation, a more general survey of the field of space telescopes must be examined.

Thus, we embark on a study of the research in the field of large aperture, lightweight space telescopes and the supporting technologies to date, the study which comprises the field of *Membrane Optics*. This chapter is divided into sections focusing on both essential background material and highlights of state-of-the-art reported research which serves as the contextual backdrop. The sections are:

- Optics for space telescopes,
- Deformable mirror technology,
- Smart actuators,
- System design considerations for space telescopes.

The first section is an overview of optical issues that arise when discussing a space telescope that may not be familiar to the practicing mechanical or aerospace engineer. The next section on deformable mirrors discusses the three primary activation strategies for flat deformable mirrors with respect to modelling and control. This section shows the distinct advantages in-plane actuation offers for large aperture space borne telescopes. Next, a discussion of smart actuators, or those materials that undergo a strain in response to a certain stimuli such as voltage, outlines the materials under investigation with regard to space applications. It is here we find polyvinylidene fluoride (PVDF) is a likely candidate for space telescopes. Lastly, a section on system design considerations details on-going efforts undertaken towards the major issues facing the testing and fielding of a space telescope.

2.2 Optics for Space Telescopes

2.2.1 Definitions.   As the intended audience for this dissertation is one versed in structural mechanics, but not necessarily in optics, some elementary definitions are presented below. The definitions may be found in texts such as those by Born and Wolf [28] or Hecht [63] except where otherwise noted.

- *Areal density.* For lightweight optics, the areal density is the mass of the mirror divided by the area of the mirror.

- *Clear aperture.* The light gathering area of an optical system. The term may also be used to indicate the diameter of a circular clear aperture region. In general, the larger the aperture, the brighter the image.

- *Focal length.* For spherical mirrors, the focal length is one-half the radius. For concave parabolic mirrors, it is the distance from focus closest to the mirror's surface to the mirror's center. In general, the longer the focal length, the greater the magnification.

- *Fried parameter, r_0* The minimum distance where a wavefront may be assumed to be planar in the presence of atmospheric turbulence [63, p. 229]

- *Ground projected instantaneous field of view.* The ground projected instantaneous field of view (GIFOV) is the "geometric projection of a single detector width, w, onto the earth's surface [122]." In its simplest form, it may be represented by the equation where f is focal length and H is altitude:

$$\text{GIFOV} = \frac{wH}{f} \qquad (2.1)$$

- *Focal ratio/f-number.* The ratio of the focal length, f, to the diameter of the clear aperture region, D.

$$f/\# \equiv \frac{f}{D} \qquad (2.2)$$

- *Influence Functions.* As popularized by Menikoff, use his very general definition: "The influence functions describe the shape to which the mirror will deform when forces are applied to the actuators [89]."

- *Optical quality.* A generic term referring to the tolerance of a surface or wavefront of visible wavelengths. For the purpose of this document, optical quality is used to refer to micron-order or less displacements or tolerances.

- *Paraboloidal.* A 3-dimensional mirror shape of a rotated parabola about the central axis designed to focus light rays from an infinite source at the focus, or focal length. Note that a parabola of focal length f is defined as:

$$z(r) = \pm\sqrt{4fr}. \qquad (2.3)$$

where r is the radial coordinate and $z(r)$ describes the surface. Other mirror types such as ellipsoidal and hyperboloidal may also be employed in space telescopes.

- *Paraxial region.* The interior of a spherical mirror where the shape approaches that of paraboloidal mirror.

8

- *Relative aperture.* The inverse of the f-number.

- *Quasi-static.* For the purpose of this document, quasi-static is used to indicate a frequency of interest below the fundamental structural resonant frequency. The sole exception to this occurs in Section 3.2, where different assumptions are applied in the development of piezoelectric theory.

- *Zernike polynomials.* Historically, the distortions of a wavefront through a circular aperture are described by the Zernike polynomial basis set as popularized by Noll in his paper "Zernike Polynomials and Atmospheric Turbulence" [97]. The Zernike polynomials are a complete set of polynomials orthogonal over a unit circle. The coefficients of Zernike polynomials are used to describe the abberations in a wavefront, usually due to atmospheric disturbances, but may also be used to describe any set of data (such as surface deflections) within a circular aperture. Some low-order Zernike polynomials are provided in Table 2.1, with the normalization constant used to achieve an orthonormal basis set. Note that definition of the angle θ in comparison to the Cartesian coordinates may change the orientation of the X- and Y-tilts. Zernike polynomials will be examined in greater detail in Chapter VI.

Table 2.1:   Zernike polynomials.

Traditional Index	Normalization	Function	Name
1	1	1	Piston
2	2	$r\sin(\theta)$	Y-Tilt
3	2	$r\cos(\theta)$	X-Tilt
4	$\sqrt{6}$	$r^2\sin(2\theta)$	45 Astigmatism
5	$\sqrt{3}$	$2r^2 - 1$	Focus
6	$\sqrt{6}$	$r^2\cos(2\theta)$	0 Astigmatism

2.2.2 Adaptive Optics System.   The major components of an earth-based adaptive optics system are presented in Figure 2.1 such as presented by Hecht [63]. The light from a distant object, such as a star, is distorted by the atmosphere, and then collected by a large concave primary mirror. The light rays are focused, and then

9

sent through active optics. A fast-steering mirror is used to correct for disturbances in tip and tilt, and then the image is further refined to correct higher order aberrations with a deformable mirror. The image is then split using a beam splitter. A wavefront sensor is used to determine the error signal for future correction commands to the active optics, while imaging sensors gather the final image for interpretation.
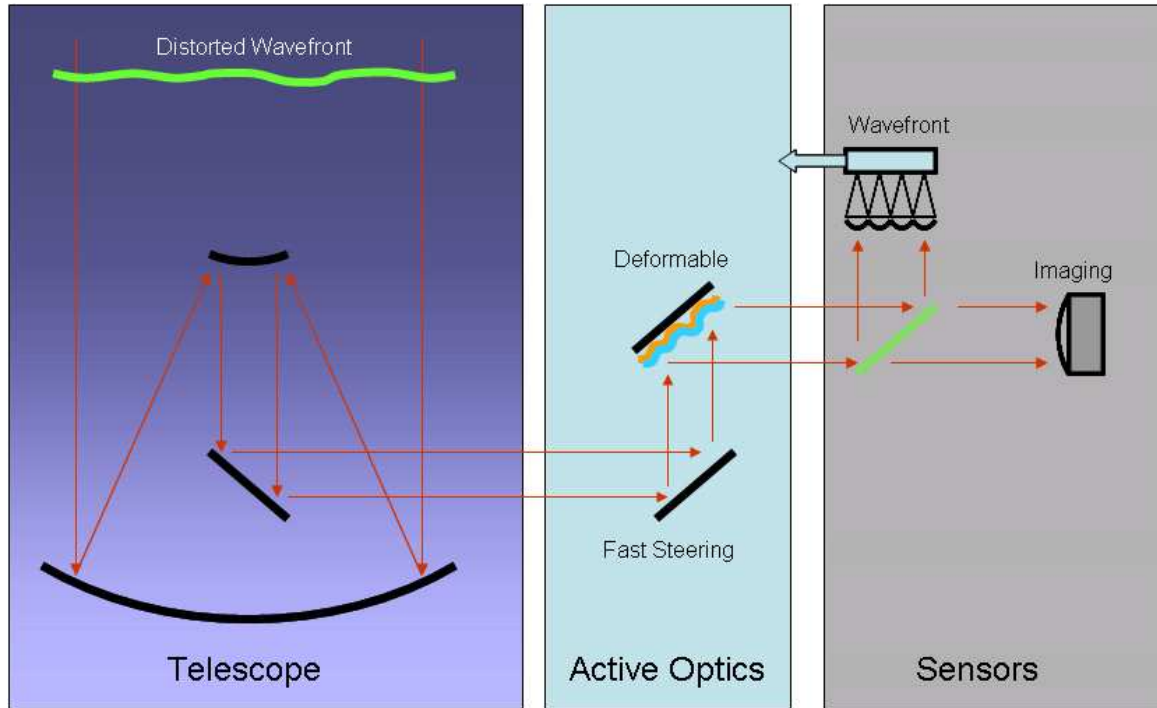
Figure 2.1:   Earth-based adaptive optics system.

A space-based telescope used for earth surveillance would presumably need the same components if resolution were increased to where real-time atmospheric corrections were required. A rudimentary calculation demonstrates this point. The diffraction limited resolution s of a notional space-surveillance satellite with a primary mirror of diameter $D = 2.0m$, at an orbit of $H = 500km$, for visible light with a max wavelength of $\lambda = 660nm$ would be [63, p. 224]:

$$s = 1.22\frac{\lambda}{D}H = 1.22\frac{660nm}{2.0m}500km = 0.20m. \tag{2.4}$$

The scene is diffraction limited to a resolution of approximately 20 cm. This compares to a Fried parameter which is of similar magnitude [63, p. 229], and thus in very general terms is at the limit of resolution before adaptive optics are required. If the mirror radius is increased without a corresponding change in altitude, adaptive optics would be required for best performance for real-time imagery.

2.3   Deformable Mirrors

Deformable mirrors are used in adaptive optics systems to correct for atmospheric aberrations, as described in the preceding section. For membrane optics in space telescopes, deformable mirrors may be used in large scale structures to correct for distortions in the mirror's surface due to deployment or disturbances. Thus, the study of deformable mirrors herein is not for the traditional application as presented in Section 2.2.2, but instead to understand the mechanics required to create a space-deployed primary mirror, which would very likely require active fine surface control to maintain optical precision.

Deformable mirrors may be classified according to their actuation mechanism: conventional, boundary, volume changing, and in-plane actuated. Table 2.2 details a chronology of the modelling for flat deformable mirrors, together with construction type and solution techniques.

From Table 2.2, pay particular attention to the circular in-plane actuated plate-membrane mirror. This type of mirror has received attention from researchers at AFIT, but the general academic community has provided little other insight. This is a curious omission, as a space based membrane optic with in-plane actuation must have both plate-like and membrane-like behaviors.

What is of particular interest is if the primary light gathering aperture of a space telescope was able to respond to high-spatial bandwidth surface shaping commands, it is conceivable that it could combine the light gathering and active optics functions into a single device, simplifying a space-based system. This potentially could offer

Table 2.2: Modelling chronology for deformable mirrors.

Author(s)	Date	Mirror type	Domain & model	Influence function [89]	Remarks
Adelman [4]	1977	In-plane (unimorph)	Circular plate (clamped central support)	Analytic	Introduced the term *unimorph*.
Pearson and Hansen [106]	1977	Conventional	Circular membrane	Experimental curve fit	Compared performance to segmented mirror.
Steinhaus and Lipson [133]	1979	In-plane (unimorph)	Rectangular Plate	Experimental and analytical	Plate glass mirror with PZT actuator regions.
Albertinetti [7]	1979	Conventional	Circular plate	Experimental	
Halevi [60]	1983	In-plane (unimorph)	Rectangular plate	Fourier series	Static cases replicated earlier experimental work of Stenhaus and Lipson.
Claflin and Bareket [32]	1986	Conventional (electrostatic)	Circular membrane	Least squares fit to analytical solution	Introduced the concept of optically active (later, clear aperture) region for Zernike polynomial fits for circular domains.
Menikoff [89]	1991	Conventional	Circular plate	Fourier series	Actuators were coupled through a backing structure, which was effective at removing pinning error.
Hiddleston, Lyman, and Schafer [64]	1991	Conventional	Rectangular plate	Curve fit to finite element data using bi-cubic spline	Less susceptible to pinning error than traditional curve fit.
Wang and Hadaegh [147]	1996	Conventional (electrostatic)	Circular membrane	Contraction mapping	Accounted for non-linear throw of actuator.
Redmond et al [114]	1999	In-plane (bimorph)	Beam and rectangular plate	Analytic	Optical tolerances not achieved.
Wagner, Agnes, and Magee [144]	2000	In-plane (unimorph)	Circular plate-membrane	Experimental	Demonstration of micron level deflections.
Agnes and Wagner [6]	2001	In-plane (unimorph)	Circular plate-membrane with spring support	Asymptotic for actuated region only	Solution method used beam boundary conditions.
Errico et al [43]	2002	Conventional (electrostatic)	Circular membrane	Analytic	
Lee, Uhm, Lee, and Youn [76]	2003	Conventional	Plate	Localized deflections based on beam theory	Influence functions were independent of the domain of the mirror.
Rogers [117]	2003	In-plane (bimorph)	Axisymmetric circular plate-membrane	Asymptotic finite element	
Flint and Denoyer [45]	2003	In-plane	Circular membrane	Numerical least squares fit	Actuators modelled as line loads and as in-plane forces.
Bush et al (Intellite) [29]	2004	Conventional (electrostatic)	Circular membrane	Slope control based on finite element least squares curve fit together with analytical solution	Results compared to experimental data.
Todovinin, Thomas, and Vdovin [136]	2004	Conventional (electrostatic)	Circular membrane	Discrete analytical solution.	Noted difficulty in obtaining offset bias for large aperture applications necessary for electrostatic control.
Sumali et al [134]	2005	In-plane	Rectangular plate with pinned corners	Analytic	Compared to experimental data with area of least agreement at boundary

significant improvements in overall system performance, and provides impetus to this research.

2.3.1 *Conventional.* For the purpose of this document, conventional deformable mirrors are those structures typically discussed by the optics community. Conventional refers to an actuation scheme where actuators act directly on the non-reflecting side of a mirror with a deformable face, and require a backing structure to which actuators are attached. Conventional deformable mirrors are the type of deformable mirror pictured in the texts by Goodman [54] and Hecht [63]. A graphic showing a conventional deformable mirror is presented in Figure 2.2.
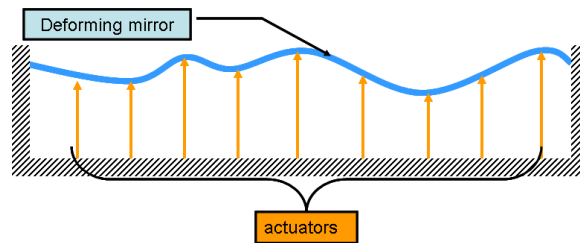
Figure 2.2:   Side view of conventional deformable mirror.

Menikoff, in defining the term *influence function*, was attempting to characterize a conventional deformable mirror's response to point load actuators applied to the backing surface of a plate-like glass mirror as seen in Figure 2.3 [89]. Menikoff modelled the mirror as a deformable plate without any tension and with actuators connected as linear springs. The resulting differential equations are solved using a Fourier series approach.

By coupling the impact of one actuator to another through the deformable mirror, Menikoff alleviated a common problem with linear solutions to a deformable mirror problem, referred to as pinning error. *Pinning error* occurs when a summation of linear models is used and linear supposition does not apply [140]. If all actuators are actuated equally, a simple summation of linear solutions shows a surface of bumps, but in reality a flat surface between actuators should be observed.
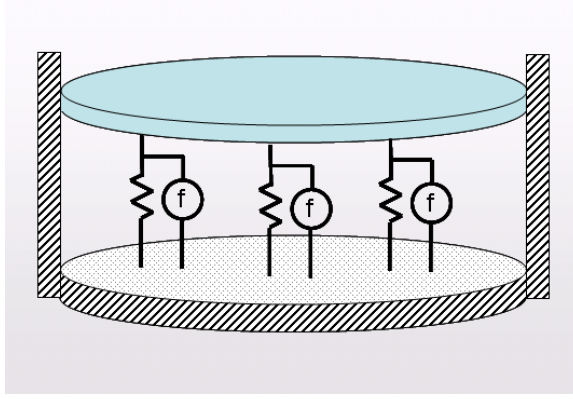
Figure 2.3:   Menikoff conventional mirror modelling scheme

Electrostatic mirrors fall under the category of conventional deformable mirrors, and were proposed for use in a space telescope by Angel [9]; Gorinevsky, Hyde, and Cabuz [55]; Stamper et al [130]; and Errico et al [43]. An electrostatic mirror uses the attraction between electrodes to exert a pressure on the surface.

Of interest is the 50-mm 79-acutator electrostatic membrane deformable mirror constructed and investigated in the paper by Tokovinin et al [136]. Only the interior 35-mm "pupil" region was actuated–the remainder of the membrane was unused, a "transition zone to the fixed boundary." The researchers used a discrete solution of Poisson's equation, $\nabla^2 w = f$, and iteratively solved for influence functions. The researchers also concluded that for large membranes the distance between electrodes and the membrane mirror would necessarily be large, increasing required control voltages thus making large scale membranes difficult to control.

Tokovinin's conclusions, together with the electrostatic mirror's characteristics of non-linear actuation forces (inversely proportional to the distance between electrodes), bias requirements (the force between electrodes is attractive only), and reliance upon a stiff (and presumably heavy) backing structure, lead us to seek an alternate approach for lightweight space telescope applications.

As another aside, it may be seen that researchers on electrostatic membranes struggled with representing Zernike mode shapes with membrane deformable mir-

14

rors, due to incompatible boundary conditions. This issue is addressed directly in Chapter VI.

2.3.2 Boundary. Boundary control relies upon actuators along the mirror boundary to provide shear and moment inputs at the edge. In 1982, Malin et al [83] demonstrated the concept by performing closed-loop computer control of a hexagonal shaped mirror. In 1983, the concept was extended to a circular deformable mirror in a journal article authored by members of the Air Force Weapons Laboratory in Kirtland, NM [96]. The researchers noted several areas of concern with cross coupling of boundary control actuators, diminishing the ability to perform surface control. The concerns included: low tolerance to miss-match in actuator performance, susceptibility to small deviations of actuator alignment, and the requirement for the mirror to be perfectly isotropic.

Boundary manipulation of a curved shell was modelled in finite elements by Marker and Jenkins [85] and by Bishop [26]. Solter, Horta, and Panetta [129] experimentally characterized boundary actuators acting on thin-film flat membranes. Lindler and Flint [78,79] and Hall, Lindler, and Flint [61] experimentally used boundary actuators to improve the surface precision of doubly curved shells. The results show that boundary control may be used to initially achieve a global parabolic shape from a near-parabolic curved shell domain, and dynamically excite vibration mode shapes, but also serve to show that finer static actuation of the surface beyond the parabolic shape was not possible. This limits boundary control's applicability for thermal disturbance rejection and fine surface control required of an active optical element.

2.3.3 Volume Changing. Imagine a two-dimensional surface that could change its thickness locally in the direction normal to the surface. Ideal static shape control would be possible. That is the concept under investigation as reported by Ruggiero, Jacobs, and Babb [120]. They report the use of micro-electro-mechanical (MEM) devices that use electrostatic actuation to actively reduce the individual ac-

tuator thickness in the out-of-plane direction. These devices will have void areas through which the electrode actuators will sweep, changing the element thickness, without an attendant change of mass. Layers of these MEMs devices are hypothesized to create surface deformations of up to 5 millimeters with areal densities on the order of 1.75 kg/m^2. This technology is in its infancy, and surface resolutions are not reported. The method would require a significant grid of electrodes to be effective, and will require further development before the technology may be applied to a full scale problem. A single volume changing MEMs element is presented in Figure 2.4.
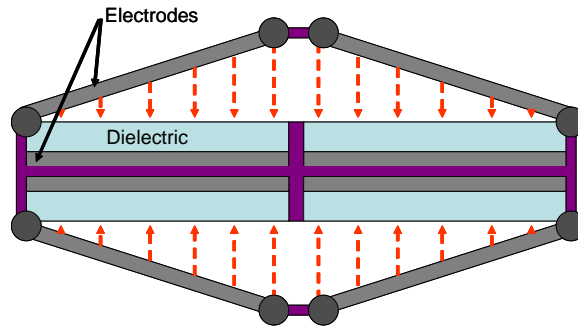
Figure 2.4:   MEMs volume changing element using electrostatic actuation.

2.3.4 In-plane Actuated.   In-plane actuated deformable mirrors rely on piezoelectric (or other types of electro- or magnetostrictive actuators) regions to strain offset from and parallel to the structure's neutral axis, thus imparting a surface curvature. The term in-plane actuation was chosen in lieu of the term bimorph corrector mirrors used by Tyson [140] to describe this class of deformable mirrors, due to the fact that the term bimorph is overly precise. The class may be further subdivided into three types based on the actuation mechanism, as shown in Figure 2.5 and described below.

- *Unimorph* The unimorph deformable mirror utilize piezoelectric actuators bonded to the mirror backing plate. Each piezoelectric actuator expands or contracts, and based upon its difference from the composite structure's neutral axis, induces a surface curvature. The regions of actuation corresponding to the elec-

16
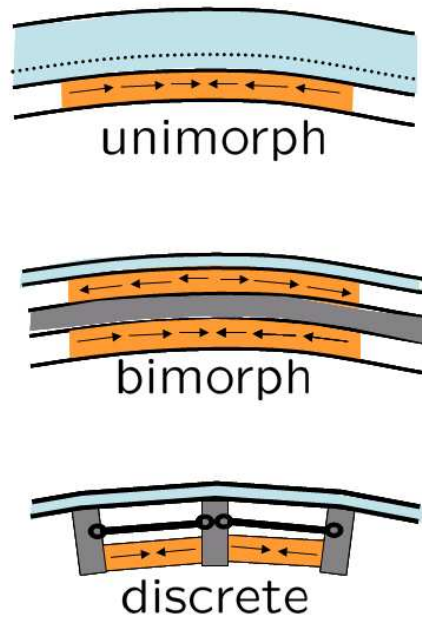
Figure 2.5:   In-plane actuated deformable mirrors

trode pattern on the faces of the piezoelectric layer. The term *unimorph* was suggested for this type of actuator configuration by Adelman in 1977 [4].

- *Bimorph* Similar to the unimorph, the bimorph utilizes piezoelectric actuators, but in pairs at each actuator location. The piezo-pair act in opposite directions to produce a local curvature. As the mirror coating is reduced, the system approaches a symmetric structure, which is easier to model. However, the manufacturing complexity is increased by having to apply opposite voltages on each piezo component of the piezo-pair. Some caution must be used when searching the early literature as the term *bimorph* was used in 1979 by Itek corporation to describe a class of mirrors that utilized piezo-beam cantilevers acting on pushrods connected to the mirror in a conventional actuator configuration [7].

- *Discrete* The discrete in-plane actuator utilizes fixed blocks affixed to the backing side of the continuous mirror. A piezo-actuator pushes laterally on the blocks, which pivot on a central axis. The surface therefore deforms in segments. This type of in-plane actuated mirror is generally best suited to micro-electrical-

17

mechanical systems such as those proposed by Yang [153]. A derivative of this approach that used longerons and ribs to transmit the forces to a deformable mirror plate was developed by Philen and Wang [108, 109]. Anderson, Lindler and Flint [8] proposed a hybrid piezoelectric-hydraulic actuator. The actuator could potentially miniaturized for use as a discrete in-plane actuator.

The great advantage of in-plane actuation is the weight savings due to the lack of requirement for a backing structure, increased stroke versus conventional mirrors, and the potential to reduce or eliminate the need for substantial boundary supports.

AFIT researchers Rogers and Agnes developed a comprehensive series of articles espousing the method of integral multiple scales approach to solve the piezoelectric-actuated beam-string problem, culminating with the modelling of an axisymmetric optical bimorph deformable mirror [6, 115–118]. The methods used greatly simplified finite element modelling where typical beam shape functions were replaced with asymptotic shape functions which approximated the non-linear analytical behavior of a piezoelectrically actuated beam. Isoparametric elements were not developed, and the model as presented was not applicable for unimorph construction nor non-axisymmetric deformable mirrors, limiting the method's applicability.

2.4 Smart Actuators

A *smart*, or shape changing, strain inducing, actuator embedded within the physical structure is required for any type of in-plane actuation. Piezoelectric materials have long been the material of choice, but alternatives such as thermal, dielectric elastomers, and ionic electroactive polymer actuators will be discussed below with an eye towards space-borne applications in an optical sensing system.

2.4.1 Thermal Actuation.
Thermal actuation of a structure for optical applications has not been well investigated. Control could theoretically be applied with a heat load using any material with a coefficient of thermal expansion. The slow time constants, the rate difference of heating and cooling, and difficulty in maintaining

a temperature field all appear to limit this as an actuation method for high bandwidth, high precision optical applications.

Shape memory alloys most commonly rely on a change in temperature to activate. Das et al [37] correctly point out that a shape memory alloy is an alloy material that may be deformed at a low temperature, and upon heating returns to its original state. Pollard and Jenkins [110] investigated this actuation method to deploy a membrane mirror. The binary (2-phase) nature of this material makes it impractical to use for fine surface control, plus shape memory alloys suffer the same temperature control liability as does thermal actuation. Although under investigation for use in MEMs devices [65], its usage for post-deployment surface control of space-borne telescopes appears limited.

2.4.2 Dielectric Elastomers. Dielectric elastomer actuators are perhaps the least complex of the strain-inducing actuators whose characteristics were summarized by Madden [81] and are briefly repeated here. Two metallic plates, which are positively attracted to each other in the presence of an electric field are used to sandwich a layer of a dielectric polymer such as silicone, as in Figure 2.6.

(a) Dielectric elastomer construction.

(b) Dielectric elastomer under an applied voltage.
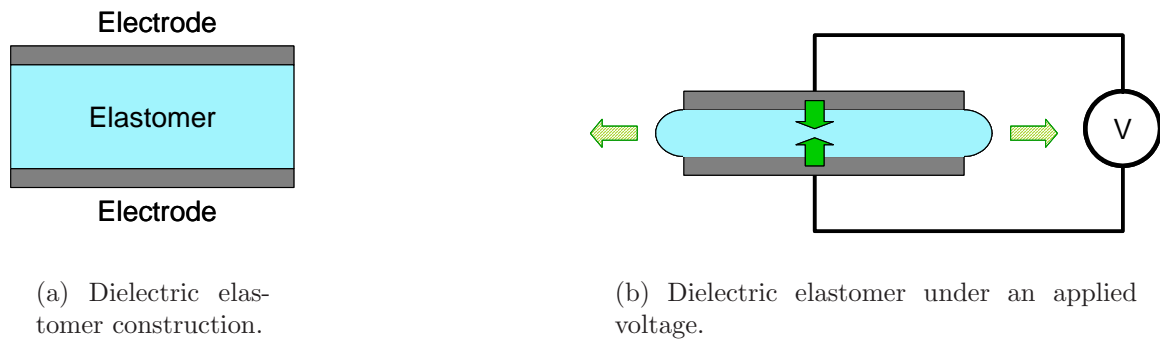
Figure 2.6:   Dielectric elastomer.

When a voltage is applied, the plates compress the dielectric with a pressure proportional to the relative permittivity and free space permittivity and the square of the quantity of voltage divided by the spacing of the electrodes. Assuming the layer is incompressible, the dielectric polymer material displaces in the axial directions.

Simply stated, this relationship means when the dielectric polymer is squeezed in one direction, it must expand in the other two.

Although elegantly simple in concept, the main drawback of dielectric elastomer actuators are the high voltages required for thick polymer layers. However, it is proposed that using 100 nanometer layers will reduce required voltages to the neighborhood of 10 volts. Another drawback is the reliance on incompressible materials for actuation, which, for now are currently limited in the temperature operating range they can withstand. For instance, a silicone-based dielectric elastomer actuator is limited from -100°C to 250°C [81]. Thermal control will be required for space applications. The use of dielectric elastomer actuators for optical and aerospace applications have been proposed by Apollonov et al [14], Costen, Su, and Harrison [34], and Ruggiero, Jacobs and Babb [120].

2.4.3 Ionic Electroactive Polymers. Ionic Electroactive Polymers (EAP), or "artificial muscles", may offer a host of new capabilities for future efforts in quasi-static shape control of deformable mirrors. Ionic EAP, such as Carbon Nanotubes, Conductive Polymers (CP), and Ionic Polymer Metallic Composites (IPMC) produce a strain by a redistribution of ions from oppositely charged electrodes transported via a conducting electrolyte [81]. When placed under a voltage potential, cations in a polymer matrix immediately swell clusters on the side nearest the negative electrode (cathode), and shrink on the side nearest the positive electrode (anode). However, over time, the pressure gradient in the structure replaces the lost volume of cation with a similar amount of liquid, until equilibrium is achieved. A diagram depicting actuation and eventual relaxation of the IPMC is shown in Figure 2.7.

Advantages for aerospace applications were summarized by Bar-Cohen et al [19–21, 124] and include the ability to produce large strain/bending displacements at low voltage levels . Demonstrated rates of 50 percent strain were shown by Tung et al [139], versus normal piezoelectric (see Section 2.4.4) rates of less than one percent. However, all at present require a liquid electrolyte to operate, and although ideal for naval
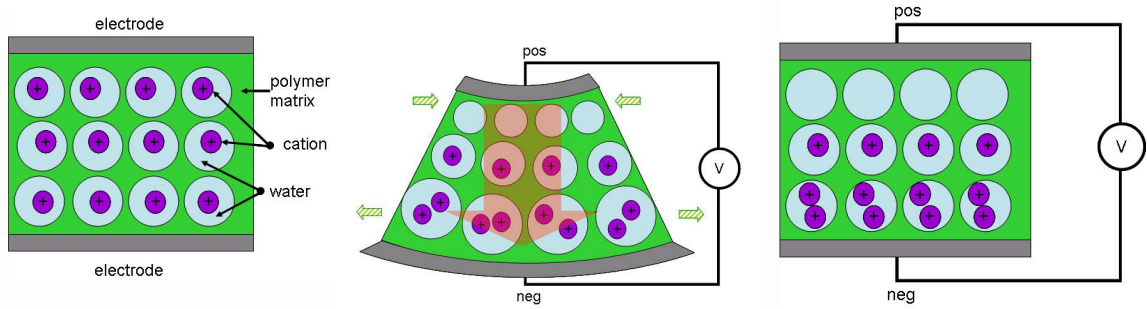
(a) The IMPC is composed of a polymer matrix sandwiched between electrodes. The polymer allows the free transport of cations to embedded clusters within the structure.

(b) Under an initial applied voltage, the cations quickly migrate through the matrix to clusters near the cathode region. A pressure gradient, depicted by the red arrow, develops due to the swelling and contraction of the clusters. Bimormph type of actuation results, depicted by the green arrows.

(c) After the initial expansion phase, the IMPC fatigues as the liquid is pumped from the swollen clusters to the shrunken clusters by the pressure gradient until equilibrium is achieved.

Figure 2.7:   Ionic Polymer Metallic Composite theory of operation.

locomotive applications [103], this limitation must be overcome for space applications, as a liquid electrolyte requires thermal control and is massive. Furthermore, individual drawbacks include high current requirements for CP, poor efficiencies for Carbon Nanotubes, and inability to maintain a steady-state strain for Ionic Polymer Metallic Composites [81, 139]. Recent analytical and experimental static and dynamic modelling of EAP activated structures have been undertaken by Otake et al [98–100] and Kaneda et al [70].

2.4.4 Piezoelectric .   While dielectric elastomer and ionic polymer metallic composites show future promise for use in smart structures, piezoelectric actuators offer the best near-term solution. Piezoelectric gets its name from *Piezein*, which is Greek for squeeze. Piezoelectric actuators "squeeze" when an electric field is applied [71]. The squeezing actually comes from a volume change of the piezo, which differentiates these actuators from dielectric elastomers. Classical modelling of piezoelectric materials may be found in the texts by Tiersten [135] and Mindlin [90], with

modern nomenclature given by the IEEE standard on piezoelectricty [1]. A distinct advantage of piezoelectric material is the ability to hold a constant strain under an applied current. Figure 2.8 illustrates the volume change of a piezoelectric actuator under electric potential.
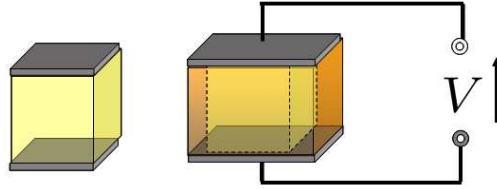
Figure 2.8:   Piezoelectric actuator before and after applied voltage.

Piezoelectric materials may be ceramic- or polymer-based, along with naturally occurring quartz and other crystals. Ceramic-based piezoelectric material generally is directional, due to a process called poling, where the piezoelectric properties are strengthened by applying an electric field at high temperatures, leaving a residual polarization [71]. The most widely investigated piezoelectric material is the ceramic lead zirconate titanate (PZT). The investigation of PZT as an in-plane actuator was conducted by Steel, Harrison, and Harper, including the directional effects of poling, hysteresis, and strain [131]. Steinhaus and Lipson created a PZT forced deformable plate mirror [133]. Further investigations, including detailed hysteretic data, is available in the report by Haertling et al [59]. In general, however, PZT is too stiff for membrane optics applications, whereas piezoelectric polymers offer a much more suitable compliance.

The most common piezoelectric polymer in membrane optics applications is polyvinylidene fluoride (PVDF). The use of PVDF as an actuator for a deformable mirror has been experimentally investigated by researchers at AFIT [80, 107, 127, 128, 137, 143, 144] and Sandia [134]. Polymer-based piezoelectric actuators generally require much greater voltages than ceramic-based actuators [21]. However, efforts by Sessler and Berraissoul [123] and Huang et al [67] to increase the strain rates available

from PVDF through excitation by electrons during the poling process, and work by Dargaville et al [36] to space qualify PVDF, increase the interest in the actuation method.

A significant enabling technology for the use of piezoelectric actuators on the in-plane actuated deformable mirrors of Section 2.3.4 is the electron gun remote actuation, as demonstrated by researchers at the University of Kentucky [57, 58, 82, 95] and investigated numerically by Bao et al [18]. By using an electron beam to charge the electrode field of the piezoelectric actuators, wiring to the individual electrodes is eliminated. In a space application, one could have a single beam generator to control the system that is not attached to the mirror structure itself except for the ground electrode, simplifying and isolating the mirror structure and control system.

Unfortunately, the strain response has shown to be non-linear as the speed and predictability of the strain differs depending on positive or negative control voltage. For positive voltage, the results are linear with small time constants. In contrast, negative voltage deflections are characterized by greatly increased time constants, and reduced precision due to un-characterized non-linear behavior [57, 58].

The most recent published experimental results for electron gun piezoelectric actuation were from Choi et al at the NASA Langley Research Center and Norfolk State University who demonstrated piezoelectric static actuation of a unimorph membrane with voltages up to 230V using 18 Watt X-band microwave drivers positioned 1.8 meters from the membrane [31] in 2004.

Although beyond the scope of this work, it is noted that piezoelctric materials such as PZT and PVDF may also be used as sensors. Piezoelectric actuators are pyroelectric, that is, they give off a charge when heated. Experimental investigation of this behavior may be found in the work by Dias [39]. Also, piezoelectric materials may be used as strain rate sensors, as investigated analytically and experimentally by Lee and O'Sullivan [75] and Lee, Chiang, and O'Sullivan [73].

23

2.4.5 Photostrictive. Photostrictive actuators convert high energy light, such as laser light, into mechanical strain energy, and are analogous to piezoelectric actuators. Shih and Tzou [126] and Shih, Smith, and Tzou [125] investigated the modelling of smart structures with this type of actuation. The compound exhibiting the photostrictive behavior was PLZT, composed of lead, lanthanum, zirconium and titanium. Like ceramic based piezoelectric actuators, it is most likely too stiff for membrane applications. The primary advantage of such an actuator would be the non-contacting nature of the control input (light) without the need for individual electrodes as is the case for piezoelectric material. Another advantage is that existing modelling techniques for piezoelectric actuators is directly analogous for this actuation method.

2.5   System Design Considerations for Large Space Telescopes

Design of a large aperture space telescope has unique challenges beyond the already substantial task associated with launching and maintaining a surveillance satellite. Some specific research areas such as scaling, optical surface measurement, dynamic testing, mirror construction, as well as a host of other fields well outside of the scope this research effort are identified in the following sections.

2.5.1   Scaling of Laboratory Testing to Actual Flight Vehicles. There is limited research specifically identifying the scaling issues of small-scale deformable mirror laboratory testing to large scale in-plane actuated space-borne optical systems. The issue of scaling for membrane optics is discussed in Chapter VII.

2.5.2   Static Measurement of Optical Surfaces. Actual experimental testing of large scale optical membrane mirrors is limited–in fact no membrane optical surface in the 20-meter class has been constructed or tested to date. Some methods which may be employed in the future are summarized in this section.

Photogrammetry is used for measurement of a surface by tracking a series of projected coordinates, or "dots" on a surface with camera equipment and processing of the visual images. Videogrammetry is the same method applied a series of frames of images to gather dynamic data. The method has been used extensively by NASA researchers in their work on Gossamer structures [40,41], and the method is described in detail by Pappa et al [102]. As noted by Papa et al, photogrammetry relies on an opaque surface so that the images of the surface are captured, and usually the white dots are affixed to transparent or reflective surfaces. However, by using special manufacturing techniques to embed a laser fluorescent dye in the test article, new methods using laser illumination may overcome this restriction. Surface measurements are on the order of 1-millimeter accuracy, well-above optical quality.

Ronchigrams, or images from Ronchi tests, are used to identify the aberrations of a spherical lens. An overview of the test methodology was provided by Mansuripur [84]. Briefly summarized, it involves shining coherent, monochromatic light from a test source through a grating (the "Ronchi ruling"), and then viewing the resulting image for defects. This is a widely accepted test method to visually observe low order errors in a lens' profile.

Interferometry uses the destructive and constructive features of light to determine a change in optical path, which can be equated to a change in displacement of a reflective surface, such as a deformable mirror. The Michelson Interferometer, as described by Hecht [63], uses a beam splitter to divide a laser light source, one of which is directed to a test mirror, the second of which is reflected off of a reference mirror. The images are then recombined at a sensor, and then added constructively so that a change in beam path results in a lower intensity at the sensor. Nanometer level surface metrology is possible, however, for distortions in the surface greater than one wavelength of light (usually 635 nanometers), the sensor suffers from ambiguity, and is therefore not appropriate for measuring large surface displacements without another input (such as an accurate model of the surface). For a current example, the method was used by Bush et al [29] to measure electrostatic mirror deflection.

Shack-Hartmann wavefront sensing is a common method for determining the surface deformation of a deformable mirror, the theory of which may be found in the text by Roggeman [119] among other sources. Generally stated, the Shack-Hartmann method determines the local slope across a mirror's surface, to which a 2-dimensional surface is fitted. A light source is used to illuminate the surface, and then the incoming reflected wavefront is directed through a sub-aperture grid onto a charge-coupled device (CCD). The change in incident angle through the sub-aperture lenslets result in a change in position of highest intensity light on the array corresponding to a change in the surface slope. The resolution performance of the Shack-Hartmann wavefront sensor is governed by the fineness of the CCD array. Also, the more closely spaced the sub-aperture lenslets, the lower the maximum measurable slope, as an ambiguity between adjoining sensors develops. Shack-Hartmann sensing is used for the experimental testing herein.

2.5.3 Dynamic Testing of Large-scale Membranes. Researchers at NASA Langley have conducted dynamic analysis of many lightweight structures. The inflatable/rigidizable hexapod with tensioned reflective membrane was subjected to a battery of tests to compare experimental data to the finite element model of the hexapod/membrane structure [5, 25]. The 673-node MSC.Nastran model utilized CQUAD4 elements for the membrane, and CBEAM, CTRIA3, and rigid elements for the frame. Non-linear solution techniques were used, and compared to a state-space model generated by an Eigenstructure Realization Algorithm (ERA). Air damping was found to be small, as the structure was lightly damped, and further testing revealed frame modes as well as membrane modes were present in the composite structure.

Preliminary work in support of the NASA Gossamar Spacecraft Initiative experiments was conducted on a 40-in. square, thin polyamide Kapton membrane with tethered corner boundary conditions [49, 50]. Unlike the optical membrane, this solar sail membrane was lightly tensioned. Testing with shaker and impact hammer excitation showed that variation in membrane tension and non-linear responses made

characterization of modes difficult. Furthermore, the primary mode of the structure was difficult to precisely excite; a condition the researchers attributed to ambient noise from air circulation around the test article.

A larger scale test from the same program was NASA's evaluation of the 10-m Solar Sail [49]. The testing is some of the only dynamic testing of a large scale membrane in near vacuum conditions, and took place at the highly specialized Plum Brook facility. Vacuum chamber testing was determined to be necessary since air damping effects on a large scale membrane were significant: "air within two millimeter of either side of the sail surface is alone equal in mass to a 3-micron sail film." Unfortunately, testing was hampered by laser radar scanner difficulties with the surface reflection and low-level air currents in the near-vacuum atmosphere which excited the primary mode of the structure. Photogrammetry methods for data analysis were not used due to the data acquisition systems' inability to operate in a non-pressurized environment. Therefore, the testing was inconclusive, and led to the recommendation for future testing to be conducted in 2005. Figure 2.9 is a photograph of the solar sail inside the vacuum chamber at the Plum Brook facility.

From the research reported to date, it appears that smaller scale testing will continue to be an important aspect of membrane space telescope development in the future due to the difficulties with limited test sites and lack of proven large scale measurement equipment. Small-scale testing at the Air Force Institute Technology was pioneered by Wagner [144] and Sobers [128]. The test set up used by these early researchers, including the measures taken to reject environmental disturbances while performing optical level measurements, will be reviewed as part of the experimental testing presented in Section 4.2.2.

2.5.4   Primary Mirror Construction.   In 1980, Vaughan [142] published the algorithm to pressurize a flat membrane into a parabolic shape. In 1986, Holmes et al [66] documented the development of the first large scale membrane mirror, where the German company, Schlaich and Partner, created a 17-meter parabolic solar collector. The

Figure 2.9:   Solar sail at Plum Brook facility *courtesy NASA.*

shaping was from a pressure force of a vacuum applied to the non-reflective side. The mirror was far from lightweight, as the optical coating consisted of glass tiles bonded to the surface.

This inflated lenticular concept dominated the research efforts of the 1990's and into this decade, with works by Steele et al [132], Bishop [26], Wilkes [150,151], Rogers and Agnes [116] and Bao [18] all using this as the baseline configuration. The concept suffers in space-borne applications for one main reason: in space, vacuum cannot be applied to a structure to induce the parabolic curvature. Instead, a membrane lenticular is inflated, and must have an clear canopy over the light gathering region. This canopy must be completely transparent (not physically realizable) or partially negate the benefits of increased aperture size. This canopy and the reflector must also contain the pressurizing gas without leaking, and thus should be impervious to space debris, as just a small leak could conceivably require tons of gas to maintain inflation, negating any lightweight advantages of the membrane mirror. Thus, an

inflated lenticular of a lightweight large aperture is of limited utility for a space-based telescope.

Manufacturing a mirror with intrinsic stresses to hold the mirror shape upon deployment is another type of mirror construction. Modelling the response of membrane structures with an embedded strain field was the focus of the publication by Ash et al [15]. Glaese et al [53] and Mevicon corporation [44, 47] have researched and manufactured a series of doubly curved membrane shell mirrors. The meter class mirrors are of near optical quality, and may be rolled flat. Pictures of the mirrors are presented in Figure 2.10.

Figure 2.10: Mevicon form stiffened shell lightweight mirrors ©*Mevicon Inc., used with permission.*

The tensioned membrane and thin shell mirror is the final concept investigated. Proposed first by Bekey [24], it proposes using thin shell with piezoelectric elements to shape the surface into a desired parabolic shape. Later, Wilkes et al [152] would propose using a tensioned membrane with a plunger in the center to create the necessary curvature. The Bekey concept is further discussed Chapter VII.

Combining elements of both the tensioned membrane and the intrinsic stress mirror is the NASA L2 proposal [3]. In the NASA L2 proposal, shape memory alloy is used to create the initial parabolic shape (the intrinsic stress) and with piezoelectric actuators reacting on the tensioned surface.

2.5.5 Other System Considerations. Research to develop a fully-functional space telescope with a membrane primary aperture beyond the scope of the work

presented above will be required in areas such as deployment, materials, wrinkling, formation station keeping, and orbital mechanics.

Deployment of a membrane mirror may be broken into two areas: unfurling from a stowed configuration and the actuating mechanism. Simply rolling a pre-curved mirror flat and letting in unfurl due to an embedded tension field is the method proposed by Flint [47]. A proposed membrane folding technique was suggested by Furuya and Inoue [48] for membrane solar sails, although it is not clear if a reflective material could withstand the plastic yields folding would cause. Shape memory alloys are candidates for pulling the membrane mirror into its deployed shape, and have been separately examined by Hill et al [65] and Pollard and Jenkins [110], and Duvvuru and Jenkins [42]. The thermal control problem that ensues remains unresolved.

Materials research in fields of perfecting optical quality polymer membranes is on-going. Kapton has been experimentally evaluated for use in space membranes by Heald, Potvin and Jiang [62] and for the James Webb Space Telescope heat shield by Waldie and Gildman [145], especially in regard to thermal stability and change in flatness due to temperature. SRS Technology produced CP-1 polyamide has been reported by Patrick and Moore [105] and Patrick et al [104] to have excellent optical properties in tensioned membrane applications.

Wrinkling will surely be an issue for any membrane structure, presumably due to the profoundly negative impacts it would have on an optical presentation. Wrinkling effects on the optical problem are not well-investigated at present, although Blandino, Johnston, and Dharamsi [27] and Blandino et al [27] have investigated the effects of wrinkling specifically in regard to the gossamer membrane problem.

Station keeping and orbital mechanics problem of a large earth facing space telescope have not been directly investigated in the open literature. The formation station keeping problem for the NASA L2 membrane mirror experiment was outlined by Açikmeşe et al [3]. Tragessor and Tuncay [138] presented an earth-facing teth-

ered satellite constellation that could possibly be extended to the long focal length membrane mirror problem.

2.6   Summary

This chapter provided the contextual background for research in the field of membrane optics. A summary of current research and literature encompassing space telescope optics, deformable mirror technology, different smart actuation mechanisms, and space system test and design considerations was presented. From this survey, the piezoelectric in-plane actuated deformable mirror is found to have several potential advantages for the use in membrane optics systems. The advantages include weight savings due to no requirement for a backing structure, increased stroke, and lack of a requirement for boundary supports. To further the advancement in our understanding of this type of mirror, let us begin the next chapter with a discussion of established modelling techniques. Chapter III outlines the equations chosen to describe the structural behavior of the in-plane actuated deformable mirror.

III. Modelling of Smart Structures

> *Chapter objectives:*
>
> - *Present piezoelectric theory and assumptions*
> - *Develop the piezoelectric-thermal analogy*
> - *Introduce the model for in-plane actuated structures*

3.1   Introduction

To enable a study of the in-plane actuated deformable mirror, a review of the mechanics which govern the actuation and structural responses must be undertaken. The purpose of this chapter is to develop an analytical framework for analysis, and to provide a comprehensive list of the assumptions and constraints under which the framework is valid.

The nature of the actuating mechanism, the piezoelectric actuator, is the subject of Section 3.2. An analogy between piezoelectric-induced and thermal strain is reviewed in Section 3.3 for inclusion in analytical modelling or finite element models. The derivation of a circular composite plate-membrane with in-plane piezoelectric actuation forms Section 3.4 based on the work of Nayfeh and Pai [94]. The derivation provides the governing equations for the work contained herein.

3.2   Linear Theory of Piezoelectricity

Throughout this document, the linear theory of piezoelectricity is used in all of the models presented. This is common in the literature, as the IEEE Standard of Piezoelectricity [1] gives the constitutive piezoelectric relationships as linear functions. To understand the assumptions that go into the linear theory, a short review of the foundational work on which the standard is based is in order.

The linear theory of piezoelectricity from the IEEE Standard on Piezoelectricity [1] was based on the derivations presented in Tiersten's 1969 text titled *Linear Piezoelectric Plate Vibrations* [135]. By the author's own account, this "monograph" was based upon a series of classes taught by the author from 1965 to 1966 to the Piezoelectric Crystal Device Department of Bell Telephone Laboratories to expound the theory of piezoelectric crystals as developed by Professor Mindlin of Columbia University [90, pp. 281-290]. During the period of the lectures, the "monolithic crystal filter" was discovered independently by researchers in the U.S. and Tokyo, and consequently was introduced into the lecture material forming the nucleus of the book. Now, some 40 years later, the original derivations form the backbone of the standard, but bear re-examination to see the underlying assumptions of piezoelectric[1] linear theory. This section is taken in its entirety from the two volumes cited unless specifically stated, otherwise with only clarifying remarks provided by this author, and with no claim or pretense of originality.

Four equations set the scene for the derivation, and are the result of multiple linearizing assumptions.

3.2.1 Stress Equation of Motion. The force equations of motion, assuming the stress vector varies in a continuous fashion over a unit volume, is given in tensor notation as as the three equations represented by:

$$\tau_{ij,i} + f_j = \rho \ddot{u}_j. \tag{3.1}$$

The stress tensor is symmetric, that is $\tau_{ij} = \tau_{ji}$ and the state of stress can be given in six versus nine values. For this problem, the external force is assumed to be $f_j = 0$. To refresh our familiarity with tensor notation, one can expand Equation 3.1 for $j = 1$ under the zero external force assumption to be:

---

[1]Piezoelectric, or equivalently *biased electrostriction*, as presented in the early literature.

$$\frac{\partial \tau_{11}}{\partial x_1} + \frac{\partial \tau_{21}}{\partial x_2} + \frac{\partial \tau_{31}}{\partial x_3} + 0 = \rho \ddot{u}_1. \tag{3.2}$$

The linear derivation of the components of stress are the classical equations of elastic displacement in a Lagrangian coordinate system, that is, for the deformed body, one cannot distinguish between pre- and post- deformation values of stress [121].

3.2.2 Quasi-Static Electric Field. To arrive at a linear theory for piezoelectric behavior, the assumptions behind a quasi-static[2] electric field must be introduced. Piezoelectric actuators yield a force in the presence of an electric field. The second equation for linear piezoelectric field relates the electric field directly to the scalar electric potential, as shown below.

Piezoelectric actuators are considered polarizable but non-magnetizable such that magnetic field intensity is then the same as the magnetic flux vector. This simplifying assumptions allows the use of units in the familiar classical mechanics terms of mass (M), length (L), and time (T).[3]

For piezoelectric systems which are polarizable (but not magnetizable), the magnetic field intensity is assumed to equal the magnetic flux vector. Thus, Maxwell's equations may be written as:

---

[2]Later, in Chapter IV, the term quasi-static shall be used to describe motion of the piezoelectric mirror below its fundamental mechanical vibration mode frequency. For these low frequency signals, the quasi-static assumptions of this chapter will also apply.

[3]The complete derivation of Maxwell's equations makes use of electromagnetic theory where the one constant, c, the velocity of light in a vacuum is the fundamental constant. For a thorough description of units and dimensions in electromagnetic theory, the reader is directed to the text *Classical Electricity and Magnetism* by Panofsky and Phillips [101].

$$e_{ijk}H_{k,j} = \frac{1}{c}\frac{\partial D_i}{\partial t} \tag{3.3}$$

$$H_k = e_{klm}A_{m,l} \tag{3.4}$$

$$E_i = -\phi_{,i} - \frac{1}{c}\frac{\partial A_i}{\partial t} \tag{3.5}$$

$$D_i = E_i + 4\pi P_i \tag{3.6}$$

$$D_{i,i} = 0. \tag{3.7}$$

Table 3.1:   Maxwell's equations symbology for piezoelectricity.

$\mathbf{A}^*$	vector electric potential
$\mathbf{D}$	electric displacement vector
$\mathbf{E}$	electric field intensity
$\mathbf{H}$	magnetic field intensity
$\mathbf{P}$	polarization
c	material wave speed
e_{ijk}	alternating symbol
ϕ	scalar electric potential

* Bold indicates vector quantity (example $\mathbf{q}$) with components $< q_1, q_2, q_3 >$.

Electromagnetic waves are assumed to uncouple from the elastic waves in the piezoelectric material through the assumption

$$\left|\frac{1}{c}\frac{\partial A_i}{\partial t}\right| \ll |\phi_{,i}|. \tag{3.8}$$

In words, this means the time rate of change of the applied electric field normalized by the wave speed constant is much less than the rate of change of the associated scalar electric potential in the chosen direction. Following from this assumption, one may neglect the contribution of $\frac{1}{c}\frac{\partial A_i}{\partial t}$ and Equation 3.5 is approximated by

$$E_i = -\phi_{,i} \tag{3.9}$$

which relates the electric field directly to the scalar electric potential.

3.2.3 Strain Displacement Relationship. For a vector displacement field where $\mathbf{u}^* - \mathbf{u} = d\mathbf{u}$ represents the difference in displacement after deformation. Given the assumption of an infinitesimal fiber[4], the displacement field $\mathbf{u}$ may be expanded termwise in a Taylor series as such that the displacement of a coordinate on one end of the infinitesimal fiber to the other may be represented as

$$u_i^* = u_i + \frac{\partial u_i}{\partial x_j} dx_j + \text{higher order terms.} \tag{3.10}$$

For an infinitesimal fiber, the linearizing assumption is that higher order terms are negligible. Thus write the relative displacement as

$$du_i = \frac{\partial u_i}{\partial x_j} dx_j. \tag{3.11}$$

Since $\frac{\partial u_i}{\partial x_j}$ is a second rank (dyadic) tensor in a Lagrangian coordinate system, it may be decomposed into symmetric and antisymmetric terms:

$$S_{ij} = \frac{1}{2}(u_{i,j} + u_{j,i}) \tag{3.12}$$

and

$$\omega_{ij} = \frac{1}{2}(u_{j,i} - u_{i,j}). \tag{3.13}$$

The sum of Equations 3.12 and 3.13 yields:

$$u_{i,j} = S_{ij} + \omega_{ji}. \tag{3.14}$$

---

[4]An *infinitesimal fiber* may be thought of as a fiber so small, its deformation may be described solely by changes in length and rotation.

Therefore, the relative displacement is the taken from the derivative of Equation 3.14

$$du_i = S_{ij}dx_j + w_{ji}dx_j. \tag{3.15}$$

If one makes a linearizing assumption of no rigid body rotation then one can set $w_{ji} = 0$ which in effect says that the relative displacement between two infinitesimally close coordinates is therefore

$$du_i = S_{ij}dx_j. \tag{3.16}$$

3.2.4   First Law of Thermodynamics for Piezoelectricity.   By conservation of energy, one may write the following relationship for a piezoelectric body with a surface area, (S), and volume, (V). First make the assumption that the piezoelectric energy equation is isothermal. The rate of increase of kinetic and internal energy is set equal to the rate of work performed by the surface tractions minus the flux of electric energy outward from the surface. The conservation of energy equation is presented using the symbology in Table 3.2:[5]

$$\frac{\partial}{\partial t}\int_V \frac{1}{2}\rho\dot{u}_j\dot{u}_j + \mathrm{U}dV = \int_S t_j\dot{u}_j - n_j\phi\dot{D}_jdS. \tag{3.18}$$

Begin by applying the divergence theorem (Gauss' Equation) to the right hand side terms. Recall the divergence theorem as

$$\int_S \mathbf{F} \cdot \mathbf{n} \; dS = \int_V \nabla \cdot \mathbf{F}dV. \tag{3.19}$$

---

[5]The equation for the electric displacement vector was given in Equation 3.6 in Gaussian units. In M-L-T units, the equation is

$$\mathbf{D} = \varepsilon\mathbf{E} + \mathbf{P} \tag{3.17}$$

where ε is the material permittivity (ε_0 represents the permittivity of free space, $8.8542 \times 10^{-12}C^2N^{-1}m^{-2}$.)

Table 3.2:   Conservation of energy symbology.

n	unit *outward* normal
t	traction (stress vector)
u	displacement field
τ_{ij}	stress tensor
U	internal energy function
ρ	mass density
V	volume
S	surface

Thus, recognize the equivalent volume integrals, utilizing the relationship $t_j = n_j\tau_{ij}$ where n_i represents the components of the normal vector, and recalling τ_{ij} is symmetric (note: $t_j = \tau_{ij}n_j = \tau_{ji}n_j = \tau_{ij}n_j = n_j\tau_{ij}$):

$$\int_S n_j\tau_{ij}\dot{u}_j dS = \int_V (\tau_{ij}\dot{u}_j)_{,i}\, dV \tag{3.20}$$

$$\int_S -n_j\phi\dot{D}_j dS = \int_V -\frac{\partial}{\partial x_j}(\phi\dot{D}_j)dV$$

$$= \int_V -(\phi\dot{D}_j)_{,j}\, dV \tag{3.21}$$

Rewriting Equation 3.18 with the terms above yields

$$\frac{\partial}{\partial t}\int_V \frac{1}{2}\rho\dot{u}_j\dot{u}_j + \mathrm{U}dV = \int_V (\tau_{ij}u_j)_{,i} -(\phi\dot{D}_j)_{,j}\, dV. \tag{3.22}$$

Since the linearizing assumption that we cannot distinguish between pre- and post-deformation position has already been made, one may further assume that density and volume remain constant with respect time, thus allowing the time derivative to be brought inside the integrand. Then, because the integration volume is arbitrary, the terms inside the integrand must be equal for the integrals to be equal, and one is left with the equation

$$\rho(\dot{u}_j\ddot{u}_j + \ddot{u}_j\dot{u}_j) + \dot{\mathrm{U}} = (\tau_{ij}\dot{u}_j)_{,i} -(\phi\dot{D}_j)_{,j}. \tag{3.23}$$

Taking advantage of τ_{ij} symmetry, one may write

$$\rho \dot{u}_j \ddot{u}_j + \dot{\mathrm{U}} = \tau_{ij} \dot{u}_{j,i} + \tau_{ij,i}\, \dot{u}_j - \phi \dot{D}_{j,j} - \phi_{,j}\, \dot{D}_j. \tag{3.24}$$

From the earlier sections, make use of Equation 3.1, the stress equation of motion, setting the external forces to zero such that

$$\tau_{ij,i} = \rho \ddot{u}_j \tag{3.25}$$

and using the charge equation of electrostatics, Equation 3.7, further simplifying Equation 3.24 to

$$\dot{\mathrm{U}} = \tau_{ij} \dot{u}_j - \phi_{,j}\, \dot{D}_j. \tag{3.26}$$

Now, taking advantage of the strain displacement symmetry[6] (where $\omega_{ij} = 0$ in Equation 3.14, effectively eliminating rigid body rotation of the infinitesimal element) and stress tensor symmetry and substituting for the electric field potential in Equation 3.9, and further simplifying the expression. The result is what Tiersten called *the first law of thermodynamics for piezoelectricity*. The first law of thermodynamics for piezoelectricity relates the time rate of change of internal energy in terms of mechanical and electric functions:

$$\dot{\mathrm{U}} = \tau_{ij} \dot{S}_{ij} + E_i \dot{D}_i. \tag{3.27}$$

In other words, the time rate of change mechanical energy of the system $\tau_{ij} \dot{S}_{ij}$ and the electric field multiplied by the time rate of change of the applied electric displacement field, or flux, combine to form the total energy change for a piezoelectric material. This is the second important equation for analyzing piezoelectric material.

---

[6]The strain tensor is thus S_{ij}. Readers may be more familiar with the symmetric tensor in the notation ϵ_{ij}. This notation is avoided since E, ε and e are used in this section.

3.2.5 Piezoelectric Constitutive Equations. In this section, the final two important equations for the linear theory of piezoelectricity, the *piezoelectric constitutive equations*, are derived. In order to formulate the equations, a method is used by Tiersten where he defines electric enthalpy in an analogous manner to the definition of enthalpy in heat transfer[7].

Begin by defining the electric enthalpy[8], H, as the scalar expression

$$H \equiv U - E_i D_i. \tag{3.28}$$

If one takes the time derivative $dH/dt = \dot{H}$ this results in

$$\dot{H} = \dot{U} - E_i \dot{D}_i - \dot{E}_i D_i. \tag{3.29}$$

Substituting into Equation 3.27 results in the electric enthalpy rate of change equation

$$\dot{H} = \tau_{ij} \dot{S}_{ij} - D_i \dot{E}_i. \tag{3.30}$$

One can see that H is simply a function of the strain tensor and electric field, and may be written as $H(S_{ij}, E_i)$. Thus, one may alternately write Equation 3.30 as

$$\dot{H} = \frac{\partial H(S_{ij}, E_i)}{\partial S_{ij}} \dot{S}_{ij} + \frac{\partial H(S_{ij}, E_i)}{\partial E_i} \dot{E}_i. \tag{3.31}$$

Substituting this result into Equation 3.30, the following relationship is obtained

$$(\tau_{ij} - \frac{\partial H}{\partial S_{ij}}) \dot{S}_{ij} - (D_i + \frac{\partial H}{\partial E_i}) \dot{E}_i = 0. \tag{3.32}$$

---

[7]Enthalpy in heat transfer is simply $E = U + PV$, where E is enthalpy, U is total energy, and PV represents pressure times volume.

[8]The same derivation is provided in Reddy's text *Mechanics of Laminated Composite Plates: Theory and Analysis* [113]. In the text he provides an alternate name for enthalpy, the *electric Gibbs free-energy function.*

Since Equation 3.32 must hold true for any arbitrary $\dot{S}_{ij}$ and $\dot{E}_i$, then

$$\tau_{ij} = \frac{\partial H}{\partial S_{ij}} \tag{3.33}$$

$$D_i = -\frac{\partial H}{\partial E_i}. \tag{3.34}$$

Tiersten then constructed the quadratic form of H, further restricting the development of the equations to linear theory only. The quadratic form chosen was

$$H = \frac{1}{2}c^E_{ijkl}S_{ij}S_{kl} - e_{ijk}E_iS_{jk} - \frac{1}{2}\varepsilon^S_{ij}E_iE_j \tag{3.35}$$

where there are 21 elastic stiffness constants c^E_{ijkl} such that $c^E_{ijkl} = c^E_{ijlk} = c^E_{jikl} = c^E_{klij}$, there exist 18 piezoelectric coupling coefficients e_{ijk} satisfying the relationship $e_{ijk} = e_{ikj}$, and 6 dielectric constants ε^S_{ij} with symmetry such that $\varepsilon^S_{ij} = \varepsilon^S_{ji}$. The following result is the piezoelectric constitutive equation[9]:

$$\tau_{ij} = c^E_{ijkl}S_{kl} - e_{kij}E_k \tag{3.36}$$

$$D_i = e_{ikl}S_{kl} - \varepsilon^S_{ik}E_k. \tag{3.37}$$

Equations 3.36 and 3.37 therefore serve to show that a stress in a piezoelectric medium is a function of mechanical strain and applied electric field. In the next section, alternate expressions of the two equations are provided introducing variables commonly provided by piezoelectric manufacturers.

3.2.6 Material Symmetry and Alternate Expressions of the Piezoelectric Constitutive Equation. Equations 3.36 and 3.37 may be expressed in matrix form[10] [35]

---

[9]In the IEEE Standard on Piezoelectricity [1], the letter T is substituted for τ.

[10]At this time, a small point of confusion when dealing with the piezoelectric nomenclature from an elastician's background is addressed. Hooke's law may be more familiar in the traditional form $\epsilon = E\sigma$. Rewriting Equation 3.36 using this notation results in the stress-strain relation

$$\{\tau\} = \left[c^E\right]\{S\} - \left[e\right]^T\{E\} \tag{3.39}$$

$$\{D\} = \left[e\right]\{S\} + \left[\varepsilon\right]\{E\} \tag{3.40}$$

where the stress vector convention is

$$\{\tau\} = \begin{Bmatrix} \sigma_{11} \\ \sigma_{22} \\ \sigma_{33} \\ \sigma_{23} \\ \sigma_{13} \\ \sigma_{12} \end{Bmatrix}. \tag{3.41}$$

Tiersten recognized that polarized ferroelectric ceramics, what is now given the general term of *piezoelectric actuator*, possess "symmetry of a hexagonal crystal". The transversely isotropic stiffness matrix has the form

$$c^E = \begin{bmatrix} c_{1111} & c_{1122} & c_{1133} & 0 & 0 & 0 \\ c_{1122} & c_{2222} & c_{1133} & 0 & 0 & 0 \\ c_{1133} & c_{1133} & c_{3333} & 0 & 0 & 0 \\ 0 & 0 & 0 & c_{1313} & 0 & 0 \\ 0 & 0 & 0 & 0 & c_{1313} & 0 \\ 0 & 0 & 0 & 0 & 0 & \frac{1}{2}(c_{1111} - c_{1122}) \end{bmatrix} \tag{3.42}$$

$$\{\sigma\} = \left[E\right]^{-1}\{\epsilon\} - \left[e\right]^T\{E\} \tag{3.38}$$

which is equivalent to Equation 3.39.

which is written in a more compact notation in Tiersten's text as

$$
c^E = \begin{bmatrix}
c_{11} & c_{12} & c_{13} & 0 & 0 & 0 \\
c_{12} & c_{22} & c_{13} & 0 & 0 & 0 \\
c_{13} & c_{13} & c_{33} & 0 & 0 & 0 \\
0 & 0 & 0 & c_{44} & 0 & 0 \\
0 & 0 & 0 & 0 & c_{44} & 0 \\
0 & 0 & 0 & 0 & 0 & c_{66}
\end{bmatrix}
\tag{3.43}
$$

where $c_{66} = \frac{1}{2}(c_{11} - c_{12})$. Furthermore, the *piezoelectric coupling coefficient matrix* and *dielectric coefficient matrix* reduce to the following

$$
\begin{bmatrix} e \end{bmatrix} = \begin{bmatrix}
0 & 0 & 0 & 0 & e_{15} & 0 \\
0 & 0 & 0 & e_{15} & 0 & 0 \\
e_{31} & e_{32} & e_{33} & 0 & 0 & 0
\end{bmatrix}
\tag{3.44}
$$

and

$$
\begin{bmatrix} \varepsilon \end{bmatrix} = \begin{bmatrix}
\varepsilon_{11} & 0 & \\
0 & \varepsilon_{11} & 0 \\
0 & 0 & \varepsilon_{33}
\end{bmatrix}.
\tag{3.45}
$$

For the actuation problem, one is most interested in the the constitutive relationship of Equation 3.36. However, the piezoelectric coupling coefficient matrix $\begin{bmatrix} e \end{bmatrix}$ is not generally provided in manufacturer data. In its place, the *piezoelectric coupling matrix* $[d]$ is provided such that it satisfies

$$
\begin{bmatrix} e \end{bmatrix}^T = \begin{bmatrix} c^E \end{bmatrix} \begin{bmatrix} d \end{bmatrix}^T
\tag{3.46}
$$

or equivalently

$$\left[e\right] = \left[d\right]\left[c^E\right]^T = \begin{bmatrix} 0 & 0 & 0 & 0 & d_{15} & 0 \\ 0 & 0 & 0 & d_{15} & 0 & 0 \\ d_{31} & d_{32} & d_{33} & 0 & 0 & 0 \end{bmatrix}\left[c^E\right]^T. \qquad (3.47)$$

Furthermore, most manufacturers neglect reporting the cross terms d_{15}. With those terms neglected, a direct analogy to thermal elements may be made. This is the linear piezoelectric constitutive relationship that will be used throughout the remainder of this document.

3.3 Piezoelectric to Thermal Analogy for Finite Elements

The use of finite elements to model piezoelectric-actuated structures is hardly surprising given the similarity between thermal-elastic and piezoelectric-elastic relationships. Using the piezoelectric-thermal analogy to overcome the limitation in MSC/NASTRAN of not including piezoelectric elements was reported in the AIAA Journal in 1997 [16]. Cote and researchers from Université de Sherbrooke, Canada outlined the identical method updated with more recent MSC/NASTRAN nomenclature [35]. This section presents a synopsis of their methodology.

Hooke's law with thermal strain effects (but without piezoelectric effects) may be found in any fundamental elasticity textbook as

$$\left\{\tau\right\} = \left[c^E\right]\left(\left\{S\right\} - \left\{\alpha\right\}\Delta T\right) \qquad (3.48)$$

where α_i are the thermal expansion coefficients and $\Delta T = T - T_0$ represents the change in temperature from an initial temperature. Rewriting Equation 3.39 with the substitution for the piezoelectric coupling coefficient matrix in Equation 3.46 results in

$$\left\{\tau\right\} = \left[c^E\right]\left(\left\{S\right\} - \left[d\right]^T\left\{E\right\}\right) \qquad (3.49)$$

44

where it may readily be seen that a direct analogy may be drawn between piezoelectric and thermal strains through the relationship

$$\left[d\right]^T \left\{E\right\} = \left\{\alpha\right\} \Delta T. \tag{3.50}$$

Due to the sparsity of the piezoelectric coupling matrix, d, only five equations remain. The electric field vector may be written in terms of the applied voltage V_i and actuator thickness h_p, that is

$$\frac{1}{h_p} \left\{V\right\} = \left\{E\right\}. \tag{3.51}$$

If the simplifying assumption is made that only the out-of-plane voltage is considered (i.e., the voltage across the electrodes, V_3) and in-plane voltages are considered negligible and ignored ($V_1 = V_2 = 0$), Equation 3.50 reduces to the result of Cote's derivation of the piezoelectric-thermal analogy

$$\frac{d_{31}}{h_p} V_3 = \alpha_1 \Delta T \tag{3.52}$$

$$\frac{d_{32}}{h_p} V_3 = \alpha_2 \Delta T \tag{3.53}$$

$$\frac{d_{33}}{h_p} V_3 = \alpha_3 \Delta T. \tag{3.54}$$

For implementation into finite element programs such as MSC/NASTRAN, set the reference temperature to zero (no initial electric field or corresponding piezoelectric-strain). The applied voltage V_3 may then be applied as a corresponding temperature

T with

$$\begin{Bmatrix} \alpha_1 \\ \alpha_2 \\ \alpha_3 \\ \alpha_4 \\ \alpha_5 \\ \alpha_6 \end{Bmatrix} = \frac{1}{h_p} \begin{Bmatrix} d_{31} \\ d_{32} \\ d_{33} \\ 0 \\ 0 \\ 0 \end{Bmatrix}. \tag{3.55}$$

Alternately, the effect of actuator thickness could be shifted to a scale on the applied voltage by dividing V_3 by h_p.

Cote notes two limitations of the piezoelectric-thermal analogy. One is the relationship of the applied voltage and actuator thickness, especially when in-plane effects are ignored. Second, these equations are useful for actuators, but not as sensor equations, as applying a strain does not provide a corresponding change in temperature in the thermal relationship. The most obvious limitation of the piezoelectric-thermal analogy is the limited inability to introduce both thermal loads and piezoelectric forcing. Although thermal loads could be scaled to act through the piezoelectric coefficients, heat transfer problems and those problems where non-linear thermal expansion coefficients do not match the piezoelectric coefficients may not be addressed through this analogy. This limitation is addressed in the development of a piezoelectric-elastic-thermal model developed by Tzou [141]. Although a restrictive limitation, for the experimental work presented later in this document, thermal effects are negligible.

3.4   Model of Circular Plate-Membrane with Embedded Piezoelectric Elements

To conduct modelling of a circular deformable mirror, it is essential to have a basic understanding of plate theory as it applies to the circular plate problem. This section begins with a development of the equations for a linear plate. Then, the modelling for a non-linear in-plane actuated plate-membrane through the use of the von Kármán strain field is presented in an abbreviated form, as the development follows

46

the methods for a linear plate. By making a series of simplifying assumptions, one governing equation is arrived upon, which is then further simplified for use throughout this document. The purpose of this section therefore seeks to present a methodical approach for arriving at the governing equations for the membrane optics in this document, while cataloging a list of assumptions made along the way.

The equations for a circular plate may easily be derived in cylindrical coordinates. Although available in a number of text books, the method by Nayfeh and Pai sets a basic foundation which may be readily expanded to include non-linear terms, composite layers, and piezoelectric-thermal actuation terms. The method that follows is entirely based upon their text *Linear and Non-Linear Structural Mechanics* [94, ch. 7, pp. 371-468], with clarifying notes and equations added as necessary.

3.4.1 Linear Plate Theory. Consider a circular plate over the domain $0 \leq r \leq R$ and $0 \leq \theta \leq \theta_0$. The undeformed position vector ($\mathbf{P}$ of an arbitrary point on the plate is given by the three parameter family r, θ, z as shown in Figure 3.1 and given here as:
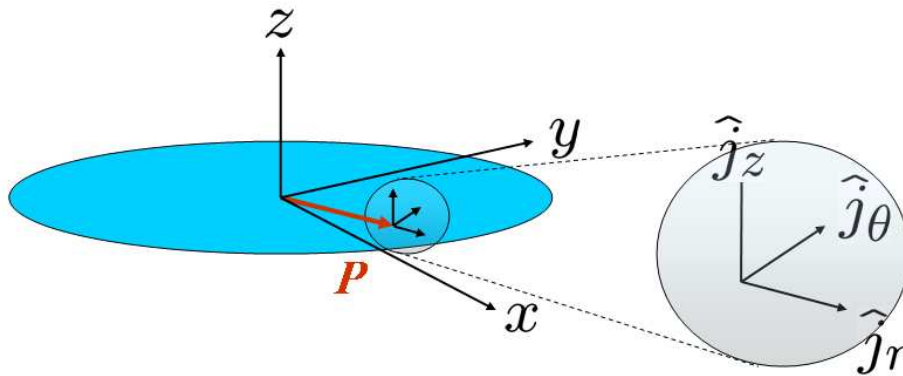
Figure 3.1:   Cylindrical coordinate system

$$\mathbf{P} = r \cos \theta \hat{i}_x + r \sin \theta \hat{i}_y. \tag{3.56}$$

Obtain the tangent and normal vectors to the surface:

47

$$\hat{j}_r = \frac{\partial \mathbf{P}}{\partial r} = \cos\theta \hat{\imath}_x + \sin\theta \hat{\imath}_y \tag{3.57}$$

$$\hat{j}_\theta = \frac{1}{r}\frac{\partial \mathbf{P}}{\partial \theta} = -\sin\theta \hat{\imath}_x + \cos\theta \hat{\imath}_y \tag{3.58}$$

$$\hat{j}_z = \hat{j}_r \times \hat{j}_\theta = \hat{\imath}_z \tag{3.59}$$

Thus the base vectors of the x, y, z coordinate system are related to the base vectors of the cylindrical coordinate system r, θ, z by the familiar transformation:

$$\begin{Bmatrix} \hat{j}_r \\ \hat{j}_\theta \\ \hat{j}_z \end{Bmatrix} = \begin{bmatrix} \cos\theta & \sin\theta & 0 \\ -\sin\theta & \cos\theta & 0 \\ 0 & 0 & 1 \end{bmatrix} \begin{Bmatrix} \hat{\imath}_x \\ \hat{\imath}_y \\ \hat{\imath}_z \end{Bmatrix} \tag{3.60}$$

Further noting the unit vectors maintain the relationship along the curvilinear axes

$$\frac{\partial \hat{j}_r}{\partial y} = \frac{1}{r}\hat{j}_\theta \tag{3.61}$$

$$\frac{\partial \hat{j}_\theta}{\partial y} = -\frac{1}{r}\hat{j}_r. \tag{3.62}$$

Nayfeh and Pai [94, pg. 357] then define the initial curvature matrices $\mathbf{K}_r^0$ and $\mathbf{K}_\theta^0$ such that:

$$\mathbf{K}_r^0 = \begin{bmatrix} \hat{j}_{r,x} \cdot \hat{j}_r & \hat{j}_{r,x} \cdot \hat{j}_\theta & \hat{j}_{r,x} \cdot \hat{j}_z \\ \hat{j}_{\theta,x} \cdot \hat{j}_r & \hat{j}_{\theta,x} \cdot \hat{j}_\theta & \hat{j}_{\theta,x} \cdot \hat{j}_z \\ \hat{j}_{z,x} \cdot \hat{j}_r & \hat{j}_{z,x} \cdot \hat{j}_\theta & \hat{j}_{z,x} \cdot \hat{j}_z \end{bmatrix} \tag{3.63}$$

$$\mathbf{K}_\theta^0 = \begin{bmatrix} \hat{j}_{r,y} \cdot \hat{j}_r & \hat{j}_{r,y} \cdot \hat{j}_\theta & \hat{j}_{r,y} \cdot \hat{j}_z \\ \hat{j}_{\theta,y} \cdot \hat{j}_r & \hat{j}_{\theta,y} \cdot \hat{j}_\theta & \hat{j}_{\theta,y} \cdot \hat{j}_z \\ \hat{j}_{z,y} \cdot \hat{j}_r & \hat{j}_{z,y} \cdot \hat{j}_\theta & \hat{j}_{z,y} \cdot \hat{j}_z \end{bmatrix} \tag{3.64}$$

where the comma signifies differentiation.

Thus $\mathbf{K}_r^0 = \mathbf{0}$ and

$$\mathbf{K}_\theta^0 = \begin{bmatrix} 0 & \frac{1}{r} & 0 \\ -\frac{1}{r} & 0 & 0 \\ 0 & 0 & 0 \end{bmatrix}, \tag{3.65}$$

With a coordinate system defined, write a displacement vector in cylindrical coordinates from Kirchhoff theory. The theory assumes plane sections remain plane so there is no warping, and plane sections further remain perpendicular to the neutral axis such there is no transverse shear. Therefore, the displacement vector $\mathbf{u}$ as pictured in Figure 3.2 has the form:

$$\begin{aligned} \mathbf{u} &= u_1\hat{\jmath}_r + u_2\hat{\jmath}_\theta + u_3\hat{\jmath}_z \tag{3.66} \\ &= (u - zw_r)\hat{\jmath}_r + (v - \frac{z}{r}w_\theta)\hat{\jmath}_\theta + (w)\hat{\jmath}_z. \tag{3.67} \end{aligned}$$

Note that a simplified notation where the subscript of a scalar amount indicates a derivative. This is consistent with Nayfeh and Pai's notation [94, ch. 7] and also the work of Rogers [117]. The components of linear strain are defined by the relationships:[11]

---

[11]It may be more familiar to see the linear strain-displacement relationship in the form

$$\epsilon_{rr} = \frac{\partial u_1}{\partial r}, \qquad\qquad \epsilon_{\theta\theta} = \frac{u_1}{r} + \frac{1}{r}\frac{\partial u_2}{\partial \theta}, \qquad\qquad \epsilon_{zz} = \frac{\partial u_3}{\partial z}$$

$$\gamma_{r\theta} = \frac{1}{r}\frac{\partial u_1}{\partial \theta} + \frac{\partial u_2}{\partial r} - \frac{u_2}{r}, \qquad \gamma_{rz} = \frac{\partial u_1}{\partial z} + \frac{\partial u_3}{\partial r}, \qquad \gamma_{\theta z} = \frac{\partial u_2}{\partial z} + \frac{1}{r}\frac{\partial u_3}{\partial \theta}.$$

However, these relationships are equivalent to the work presented. To see this, perform Nayfeh's method in the text. Begin by calculating the following to calculate $\epsilon_{r\theta}$:

$$\frac{\partial \mathbf{u}}{\partial r} = \frac{\partial u_1}{\partial r}\hat{\jmath}_r + \frac{\partial u_2}{\partial r}\hat{\jmath}_\theta$$

$$\frac{1}{r}\frac{\partial \mathbf{u}}{\partial \theta} = (\frac{1}{r}\frac{\partial u_1}{\partial \theta} - \frac{u_2}{r})\hat{\jmath}_r + (\frac{u_1}{r} + \frac{\partial u_2}{\partial r})\hat{\jmath}_\theta.$$
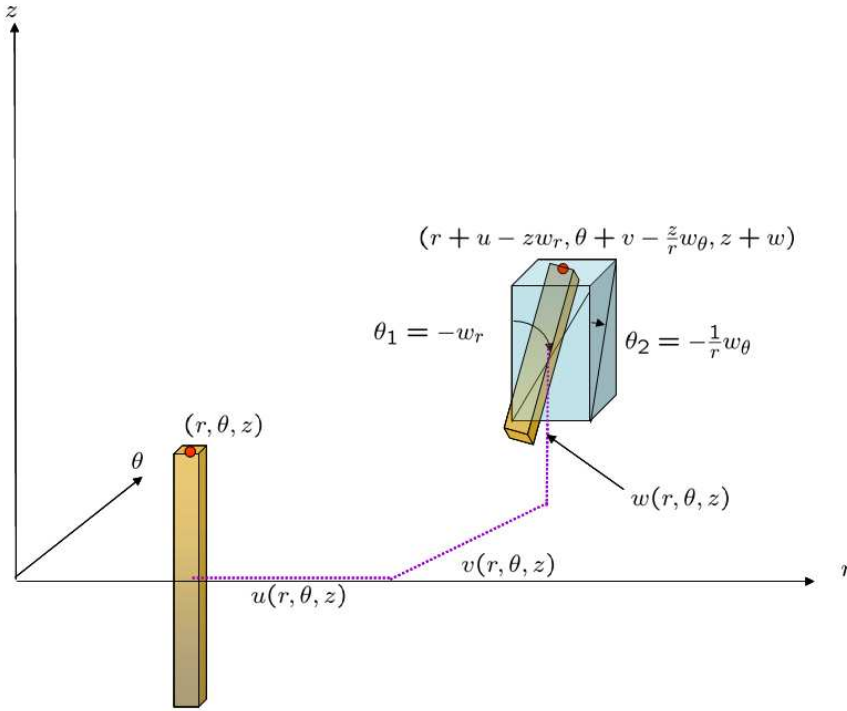
Figure 3.2:   Cylindrical coordinate system depicting Kirchhoff displacements.

$$\epsilon_{rr} = \frac{\partial \mathbf{u}}{\partial r} \cdot \hat{j}_r$$

$$\epsilon_{\theta\theta} = \frac{1}{r}\frac{\partial \mathbf{u}}{\partial \theta} \cdot \hat{j}_\theta$$

$$\epsilon_{zz} = \frac{\partial \mathbf{u}}{\partial z} \cdot \hat{j}_z$$

$$\epsilon_{r\theta} = \frac{\partial \mathbf{u}}{\partial r} \cdot \hat{j}_\theta + \frac{1}{r}\frac{\partial \mathbf{u}}{\partial \theta} \cdot \hat{j}_r$$

$$\epsilon_{rz} = \frac{\partial \mathbf{u}}{\partial r} \cdot \hat{j}_z + \frac{\partial \mathbf{u}}{\partial z} \cdot \hat{j}_r$$

$$\epsilon_{z\theta} = \frac{\partial \mathbf{u}}{\partial z} \cdot \hat{j}_\theta + \frac{1}{r}\frac{\partial \mathbf{u}}{\partial \theta} \cdot \hat{j}_z \qquad (3.68)$$

Next, write the equation for $\epsilon_{r\theta}$

$$\epsilon_{r\theta} = \frac{\partial \mathbf{u}}{\partial r} \cdot \hat{j}_\theta + \frac{1}{r}\frac{\partial \mathbf{u}}{\partial \theta} \cdot \hat{j}_r = (\frac{1}{r}\frac{\partial u_1}{\partial \theta} + \frac{\partial u_2}{\partial r} - \frac{u_2}{r}).$$

Again, from Nayfeh and Pai's terminology, they have substituted ϵ for what is classically given the variable γ for shear strain. The normal components are exactly equivalent.

It may be quickly shown that $\epsilon_{zz} = \epsilon_{rz} = \epsilon_{z\theta} = 0$. However, the spatial derivatives of the unit vectors must be taken using the chain rule, and the in-plane strains make use of the curvature matrices such that:

$$\epsilon_{rr} = (\frac{\partial u_1}{\partial r}\hat{\jmath}_r + \mathbf{u}\mathbf{K}_r^0) \cdot \hat{\jmath}_r$$
$$\epsilon_{\theta\theta} = (\frac{1}{r}\frac{\partial u_2}{\partial r}\hat{\jmath}_\theta + \mathbf{u}\mathbf{K}_\theta^0) \cdot \hat{\jmath}_\theta$$
$$\epsilon_{r\theta} = (\frac{\partial u_2}{\partial r}\hat{\jmath}_\theta + \mathbf{u}\mathbf{K}_r^0) \cdot \hat{\jmath}_\theta + (\frac{1}{r}\frac{\partial u_1}{\partial r}\hat{\jmath}_r + \mathbf{u}\mathbf{K}_\theta^0) \cdot \hat{\jmath}_r \qquad (3.69)$$

One may use the relationships noted in Equation 3.62. Specifically, note the derivative of the displacement vector with respect to the θ variable is

$$\frac{\partial \mathbf{u}}{\partial \theta} = (u_\theta - zw_{r\theta} - v + \frac{z}{r}w_\theta)\hat{\jmath}_r + (v_\theta - \frac{z}{r}w_{\theta\theta} + u - zw_r)\hat{\jmath}_\theta + \frac{1}{r}w_\theta\hat{\jmath}_z \qquad (3.70)$$

Therefore, the strains of Equation 3.69 are:

$$\begin{Bmatrix} \epsilon_{rr} \\ \epsilon_{\theta\theta} \\ \epsilon_{r\theta} \end{Bmatrix} = \begin{Bmatrix} u_r - zw_{rr} \\ \frac{1}{r}(v_\theta + u - \frac{z}{r}w_{\theta\theta} - zw_r) \\ v_r + \frac{1}{r}(u_\theta - v - 2zw_{r\theta} + \frac{2z}{r}w_\theta) \end{Bmatrix} \qquad (3.71)$$

An energy approach based on Hamilton's principle is used to obtain equations of motion. Hamilton's principle without body forces is given by the variational formulation

$$\int_0^t (\delta T - \delta V + \delta W_{nc})dt \qquad (3.72)$$

where W_{nc} is the problem-specific non-conservative work. Nayfeh and Pai provide the following definitions for the variations of kinetic energy δT and potential energy δV:

$$\delta T = -\int_z \int_S \rho \ddot{\mathbf{u}} \cdot \delta \mathbf{u} \ \ rdrd\theta dz \tag{3.73}$$

$$\delta V = \int_z \int_S \boldsymbol{\sigma} \cdot \delta \boldsymbol{\epsilon} \ \ rdrd\theta dz \tag{3.74}$$

It is straightforward to compute the values for $\ddot{\mathbf{u}}$ and $\delta \mathbf{u}$. Once computed, substitute into Equation 3.73. To simplify the bookkeeping, Nayfeh and Pai define the area-normalized moments of inertia terms

$$I_0 \equiv \int_z \rho dz, \qquad I_1 \equiv \int_z z\rho dz, \qquad I_2 \equiv \int_z z^2 \rho dz. \tag{3.75}$$

The kinetic energy equation is therefore:

$$\delta T = -\int_S \left[(I_0 \ddot{u} - I_1 \ddot{w}_r)\delta u + (I_0 \ddot{v} - \frac{1}{r}I_1 \ddot{w}_\theta)\delta v + I_0 \ddot{w}\delta w + \cdots \right.$$
$$\left. (I_2 \ddot{w}_r - I_1 \ddot{u})\delta w_r + \frac{1}{r}(\frac{1}{r}I_2 \ddot{w}_\theta - I_1 \ddot{v})\delta w_\theta \right] \ rdrd\theta. \tag{3.76}$$

Exchanging the order of differentiation and variation yields:

$$\delta T = -\int_S \left[(I_0 \ddot{u} - I_1 \ddot{w}_r)\delta u + (I_0 \ddot{v} - \frac{1}{r}I_1 \ddot{w}_\theta)\delta v + I_0 \ddot{w}\delta w + \cdots \right.$$
$$\left. (I_2 \ddot{w}_r - I_1 \ddot{u})\frac{\partial}{\partial r}\delta w + \frac{1}{r}(\frac{1}{r}I_2 \ddot{w}_\theta - I_1 \ddot{v})\frac{\partial}{\partial \theta}\delta w \right] \ rdrd\theta. \tag{3.77}$$

Integrate by parts to eliminate the partial operators $\frac{\partial}{\partial r}$ and $\frac{\partial}{\partial \theta}$. For instance, to integrate the $\frac{\partial}{\partial r}$ terms by parts, let $u = r(I_2 \ddot{w}_r - I_1 \ddot{u})$ and let $dv = \frac{\partial}{\partial r}\delta w dr$. Thus integration by parts yields:

$$\delta T = -\int_S \left[(I_0\ddot{u} - I_1\ddot{w}_r)\delta u + (I_0\ddot{v} - \frac{1}{r}I_1\ddot{w}_\theta)\delta v + \cdots \right.$$
$$\left. \left\{ I_0\ddot{w} - \frac{1}{r}\frac{\partial}{\partial r}(I_2 r\ddot{w}_r - I_1 r\ddot{u}) - \frac{1}{r}\frac{\partial}{\partial \theta}\left(\frac{1}{r}I_2\ddot{w}_\theta - I_1\ddot{v}\right) \right\}\delta w \right] r dr d\theta - \cdots$$
$$\int_\theta \left[r(I_2\ddot{w}_r - I_1\ddot{u}) \right]_{r=0}^{r=R}\delta w d\theta - \int_r \left[\frac{1}{r}I_2\ddot{w}_\theta - I_1\ddot{v} \right]_{\theta=0}^{\theta=\theta_0}\delta w dr \quad . \tag{3.78}$$

Now that the terms for kinetic energy in Hamilton's equation have been defined, the potential energy terms are addressed. It is necessary to define some bookkeeping notation so the equations remain manageable. Utilizing the planar stress assumption that the principal stress normal to the surface is much smaller than the in-plane stresses, one may write $\sigma_{zz} = 0$ and define the constitutive relationship:

$$\begin{Bmatrix} \sigma_{rr} \\ \sigma_{\theta\theta} \\ \sigma_{r\theta} \end{Bmatrix} = c^E \begin{Bmatrix} \epsilon_{rr} \\ \epsilon_{\theta\theta} \\ \epsilon_{r\theta} \end{Bmatrix}$$

$$= \begin{bmatrix} c_{11} & c_{12} & c_{16} \\ c_{21} & c_{22} & c_{26} \\ c_{61} & c_{62} & c_{66} \end{bmatrix} \left(\begin{Bmatrix} u_r \\ \frac{1}{r}(v_\theta + u) \\ \frac{1}{r}(u_\theta + rv_r - v) \end{Bmatrix} - z \begin{Bmatrix} w_{rr} \\ \frac{1}{r^2}(w_{\theta\theta} + rw_r) \\ \frac{1}{r^2}(2rw_{r\theta} - 2w_\theta) \end{Bmatrix} \right), \tag{3.79}$$

where for transversely isotropic layers with Young's modulus E and Poisson's ratio ν the constitutive stiffness matrix is [121][12]

---

[12]When computing the constitutive relationship for planar stress, an incompressible material with a Poisson's value of $\nu \to 0.5$ is easily accounted for. This is not the case if plane strain assumptions are made. For plane strain where $\epsilon_{zz} = 0$,

$$\begin{bmatrix} c_{11} & c_{12} & c_{16} \\ c_{21} & c_{22} & c_{26} \\ c_{61} & c_{62} & c_{66} \end{bmatrix} = \frac{E}{(1+\nu)(1-2\nu)} \begin{bmatrix} 1-\nu & \nu & 0 \\ \nu & 1-\nu & 0 \\ 0 & 0 & (1-2\nu) \end{bmatrix}. \tag{3.80}$$

Thus it is seen that stiffness entries become infinite effectively preventing displacement, or "locking" the equations. This is not the case for plane stress.

$$\begin{bmatrix} c_{11} & c_{12} & c_{16} \\ c_{21} & c_{22} & c_{26} \\ c_{61} & c_{62} & c_{66} \end{bmatrix} = \frac{E}{1 - \nu^2} \begin{bmatrix} 1 & \nu & 0 \\ \nu & 1 & 0 \\ 0 & 0 & \frac{1}{2}(1 - \nu) \end{bmatrix}. \tag{3.81}$$

Define the in-plane extension force intensities, N_1 and N_2, and the in-plane shear intensity, N_6, as well as moment intensities on edge of plate element, M_1, M_2 and M_6 as:

$$\begin{Bmatrix} N_1 \\ N_2 \\ N_6 \end{Bmatrix} \equiv \int_z \begin{Bmatrix} \sigma_{rr} \\ \sigma_{\theta\theta} \\ \sigma_{r\theta} \end{Bmatrix} dz, \qquad \begin{Bmatrix} M_1 \\ M_2 \\ M_6 \end{Bmatrix} \equiv \int_z z \begin{Bmatrix} \sigma_{rr} \\ \sigma_{\theta\theta} \\ \sigma_{r\theta} \end{Bmatrix} dz \tag{3.82}$$

One may note that there are no terms for transverse shear intensity, such as would be required with a Mindlin formulation. The terms could easily be added, as Nayfeh and Pai do in another section of their text. Now combine Equations 3.82 and 3.79 to yield

$$\begin{Bmatrix} N_1 \\ N_2 \\ N_6 \\ M_1 \\ M_2 \\ M_6 \end{Bmatrix} = \begin{bmatrix} A_{ij} & B_{ij} \\ B_{ij} & D_{ij} \end{bmatrix} \begin{Bmatrix} u_r \\ \frac{1}{r}(v_\theta + u) \\ \frac{1}{r}(u_\theta + rv_r - v) \\ -w_{rr} \\ \frac{-1}{r^2}(w_{\theta\theta} + rw_r) \\ \frac{-1}{r^2}(2rw_{r\theta} - 2w_\theta) \end{Bmatrix} \text{ for } i, j = 1, 2, 6. \tag{3.83}$$

If the plate is a laminated structure, such as a piezoelectric actuator layer and a substrate layer which comprise the AFIT deformable mirror introduced in Section 2.3, it would be helpful to expand Equation 3.83 to incorporate this characteristic. In general, Nayfeh and Pai provide for N laminae, where the kth laminae is located

between the two planes $z = z_k$ and $z = z_{k+1}$ and the total thickness is t, resulting in the following expressions:

$$A_{ij} = \sum_{k=1}^{N} \int_{z_k}^{z_{k+1}} c^{E(k)} dz \text{ for } i, j = 1,2,6, \tag{3.84}$$

$$B_{ij} = \sum_{k=1}^{N} \int_{z_k}^{z_{k+1}} c^{E(k)} z dz \text{ for } i, j = 1,2,6, \tag{3.85}$$

$$D_{ij} = \sum_{k=1}^{N} \int_{z_k}^{z_{k+1}} c^{E(k)} z^2 dz \text{ for } i, j = 1,2,6. \tag{3.86}$$

similar expression could be written for the inertia terms in equation 3.75.

Now one is ready to write the potential energy term by applying Equation 3.74. It is at this point that Nayfeh and Pai introduce the transverse shear intensities, Q_1 and Q_2.

$$\delta V = \int_S \left\{ N_1 \delta u_r + \frac{1}{r} N_6 \delta u_\theta + \frac{1}{r} N_2 \delta v_\theta + N_6 \delta v_r \cdots \right.$$
$$- M_1 \delta w_{rr} - \frac{1}{r^2} M_2 \delta w_{\theta\theta} - \frac{1}{r} M_6 \delta w_{r\theta} - \frac{1}{r} M_6 \delta w_{\theta r} \cdots$$
$$+ \frac{1}{r} N_2 \delta u - \frac{1}{r} N_6 \delta v - \frac{1}{r} M_2 \delta w_r + \frac{2}{r^2} M_6 \delta w_\theta \cdots$$
$$\left. Q_1 \delta w_r + \frac{1}{r} Q_2 \delta w_\theta - Q_1 \delta w_r - \frac{1}{r} Q_2 \delta w_\theta \right\} r \, dr \, d\theta \qquad (3.87)$$

$$= \int_S \left\{ \left[\frac{\partial}{\partial r}(r N_1) + \frac{\partial}{\partial \theta} N_6 - N_2 \right] \delta u \cdots \right.$$
$$+ \left[\frac{\partial}{\partial \theta} N_2 + \frac{\partial}{\partial r}(r N_6) + N_6 \right] \delta v \cdots$$
$$\left[\frac{\partial}{\partial \theta}(r Q_1) + \frac{\partial Q_2}{\partial \theta} \right] - \left[\frac{\partial}{\partial r}(r M_1) + \frac{\partial}{\partial \theta} M_6 - r!_1 - M_2 \right] \delta w_r \cdots$$
$$\left. - \frac{1}{r} \left[\frac{\partial}{\partial \theta} M_2 + \frac{\partial}{\partial r}(r M_6) + 2 M_6 \right] \right\} dr \, d\theta \cdots$$
$$+ \int_\theta \left[N_1 \delta u + N_6 \delta v + \left(Q_1 + \frac{1}{r} \frac{\partial}{\partial \theta} M_6 \right) \delta w - M_1 \delta w_r \right]_{r=0}^{r=R} r \, d\theta \cdots$$
$$+ \int_r \left[N_6 \delta u + N_2 \delta v + \left(Q_2 + \frac{\partial}{\partial r} M_6 \right) \delta w - \frac{1}{r} M_2 \delta w_\theta \right]_{\theta=0}^{\theta=\theta_0} dr \cdots$$
$$- 2 M_6 \delta w \Big|_{(r,\theta)=(R,0),(0,\theta_0)}^{(r,\theta)=(0,0),(R,\theta_0)} . \qquad (3.88)$$

Now substituting the kinetic and potential equations into Hamilton's equation, Equation 3.72, setting the coefficient of the variational terms equal to zero yields the following system of equations [94, pp. 409-410]. It is at this stage that Nayfeh and Pai choose to introduce linear viscous damping coefficients, μ_i, to the velocity terms [94, pg 391]. Although not rigorously developed the terms are consistent with the introduction of damping in linear systems and are included here. Equivalent damping ratio terms as presented by De Silva are shown in Table 3.3.

$$\frac{\partial}{\partial r}N_1 + \frac{1}{r}\frac{\partial}{\partial \theta}N_6 + \frac{1}{r}(N_1 - N_2) = I_0\ddot{u} - I_1\ddot{w}_r + \mu_1\dot{u} \qquad (3.89)$$

$$\frac{\partial}{\partial r}N_6 + \frac{1}{r}\frac{\partial}{\partial \theta}N_2 + \frac{2}{r}N_6 = I_0\ddot{v} - \frac{1}{r}I_1\ddot{w}_\theta + \mu_2\dot{v} \qquad (3.90)$$

$$\frac{\partial Q_1}{\partial r} + \frac{1}{r}\frac{\partial Q_2}{\partial \theta} + \frac{Q_1}{r} = I_0\ddot{w} + \mu_3\dot{w} \qquad (3.91)$$

$$-\frac{\partial}{\partial r}M_6 - \frac{1}{r}\frac{\partial}{\partial \theta}M_2 - \frac{2}{r}M_6 + Q_2 = \frac{1}{r}I_2\ddot{w}_\theta - I_1\ddot{v} \qquad (3.92)$$

$$\frac{\partial}{\partial r}M_1 + \frac{1}{r}\frac{\partial M_6}{\partial \theta} + \frac{1}{r}(M_1 - M_2) - Q_1 = -I_2\ddot{w}_r + I_1\ddot{u}. \qquad (3.93)$$

Table 3.3:   Equivalent damping-ratio expressions for common types of damping where ω is frequency and x is dependent variable [38].

type	force per unit mass
viscous	$\mu\dot{x}$
hysteretic	$\frac{\mu}{\omega}\dot{x}$
structural	$\mu|x|sgn(\dot{x})$
structural Coulomb	$\mu\, sgn(\dot{x})$

To solve for the motion of the plate, apply the boundary conditions as shown if Table 3.4.1. The boundary conditions are obtained by, in Meirovitch's words, "invoking the arbitrariness of the virtual displacements in a judicious manner." [88][13] In order to do that, Hamilton's equation must be examined. Either the virtual displacement or its coefficient in the boundary terms must vanish. For example, in Equation 3.88, the first term in the line integral evaluated at $r = 0, R$ is $N_1\delta u$. Therefore, either N_1 or u must vanish when evaluated at $r = 0, R$. The remainder of the table is easily constructed.

For an isotropic plate of thickness h, modulus E, and Poisson's ratio ν, $B_{ij} = 0$ and $A_{ij} = \frac{-12}{h^2}DD_{ij}$ where D is the flexural rigidity of the plate defined as

---

[13]For a thorough explanation in terms of arbitrary admissible functions and the principle of least action, the reader is referred to *Calculus of Variations* by Gelfand and Fomin [51], or equivalent.

Table 3.4:   Boundary conditions for circular plate with Kirchhoff hypothesis.

position	value 1	value 2
$r = 0, R$	$\delta u = 0$	N_1
$r = 0, R$	$\delta v = 0$	N_6
$r = 0, R$	$\delta w = 0$	$Q_1 + \frac{1}{r}\frac{\partial}{\partial \theta}M_6$
$r = 0, R$	$\delta w_r = 0$	M_1
$\theta = 0, \theta_0$	$\delta u = 0$	N_6
$\theta = 0, \theta_0$	$\delta v = 0$	N_2
$\theta = 0, \theta_0$	$\delta w = 0$	$Q_2 + \frac{\partial}{\partial r}M_6$
$\theta = 0, \theta_0$	$\delta w_\theta = 0$	M_2
$(r, \theta) = (0, 0)$	$\delta w = 0$	M_6
$(r, \theta) = (R, 0)$	$\delta w = 0$	M_6
$(r, \theta) = (0, \theta_0)$	$\delta w = 0$	M_6
$(r, \theta) = (R, \theta_0)$	$\delta w = 0$	M_6

$$D \equiv \frac{Eh^3}{12(1 - \nu^2)}. \tag{3.94}$$

In this case, $I_1 = 0$ (integration of an odd function over a symmetric interval) and the system of equations of motion reduce to the single equation for $w = w(r, \theta)$:

$$D\nabla^4 w + \rho h \ddot{w} - I_2 \ddot{w} + \mu_3 \dot{w} = 0 \tag{3.95}$$

3.4.2   Mode Shapes.   To analyze Equation 3.95, define $\kappa \equiv \rho h - I_2$, and assume the separable solution by letting $w(r, \theta, t) = e^{(-\alpha + i\beta)t}W(r, \theta)$

$$e^{(-\alpha+i\beta)t}\left[D\nabla^4 W(r, \theta) + \kappa(\alpha^2 - 2i\alpha\beta - \beta^2)W(r, \theta) + \mu_3(-\alpha + i\beta)W(r, \theta)\right] = 0. \tag{3.96}$$

Solving for the mode shapes is accomplished by letting $\alpha = \frac{\mu_3}{2\kappa}$. Then the mode shape portion of Equation 3.96 becomes

$$D\nabla^4 W(r, \theta) - \kappa\left(\frac{\mu_3^2}{4\kappa^2} - \beta^2\right)W(r, \theta) = 0. \tag{3.97}$$

Mode shapes are obtained for a given boundary condition for a chosen β. Furthermore, the strength of the damping term directly is observed to affect the frequency of the mode shape. Finally, for the thin plate assumption, the quantity κ must be positive (see Equation 3.75).

For the cases where the inertia and damping terms are relatively small and thus neglected, Equation 3.95 becomes

$$D\nabla^4 w + \rho h \ddot{w} = 0 \tag{3.98}$$

as presented in elementary texts such as the one by Meirovitch [88].

3.4.3 In-plane Actuated Plate-membrane. To make the above equations useful for our study of in-plane actuated deformable mirrors, the in-plane forces must be introduced. In the previous derivation, the in-plane relationships are uncoupled from the out-of-plane displacements equations, due to the strain field chosen. By using a non-linear strain field, coupling that occurs will allow us to introduce both tension fields (membrane characteristics) as well as use unimorph and bimorph piezoelectric actuators.

To do so, Nayfeh and Pai use the von Kármán strains by adding the components $\frac{1}{2}w_r^2$ to the ϵ_{rr} term, $\frac{w_\theta^2}{2r^2}$ to the $\epsilon_{\theta\theta}$ term, and $\frac{w_r w_\theta}{r}$ to the $\epsilon_{r\theta}$ term. Thus, Equation 3.71 becomes:

$$\epsilon_{rr} = e_1 - zw_{rr}$$
$$\epsilon_{\theta\theta} = e_2 - z\left(\frac{w_{\theta\theta}}{r^2} + \frac{w_r}{r}\right)$$
$$\epsilon_{r\theta} = \gamma_6 - 2z\left(\frac{w_{r\theta}}{r} - \frac{w_\theta}{r^2}\right)$$
$$\epsilon_{zz} = \epsilon_{rz} = \epsilon_{\theta z} = 0 \tag{3.99}$$

where

$$e_1 = u_r + \frac{1}{2}w_r^2$$

$$e_2 = \frac{v_\theta}{r} + \frac{u}{r} + \frac{w_\theta^2}{2r^2}$$

$$\gamma_6 = \frac{u_\theta}{r} - \frac{v}{r} + v_r + \frac{w_r w_\theta}{r}. \tag{3.100}$$

The piezoelectric forcing is introduced as well, but must be carefully treated. In the Nayfeh and Pai text, it is assumed in the derivations that the material coordinate system for the forcing elements could be formed in the (r, θ) polar coordinate system. More than likely, the piezoelectric forcing elements will align in the $x - y$ Cartesian coordinate system, and thus are introduced as such.

The equations for in-plane piezoelectric forcing elements with the piezoelectric-thermal analogy for transversely isotropic material properties of Young's modulus of E_p and Poisson's ratio of ν_p and piezoelectric coefficients d_{31} and d_{32} aligned in the $x-$ and $y-$direction (and hence must be transformed for use in this coordinate cylindrical system). The terms are:

$$N_1^P = \frac{E_p}{1 - \nu_p} \int_Z \left(\cos^2 \theta d_{31} + \sin^2 \theta d_{32} \right) \frac{V_3}{h_p} dz \tag{3.101}$$

$$N_2^P = \frac{E_p}{1 - \nu_p} \int_Z \left(\sin^2 \theta d_{31} + \cos^2 \theta d_{32} \right) \frac{V_3}{h_p} dz \tag{3.102}$$

$$N_6^P = \frac{E_p}{1 - \nu_p} \int_Z \left(\cos \theta \sin \theta d_{31} - \cos \theta \sin \theta d_{32} \right) \frac{V_3}{h_p} dz. \tag{3.103}$$

V_3 is the applied voltage in the perpendicular ($z-$direction) and h_p is the thickness of the actuator, consistent with the Section 3.3. One may also write the moment terms for the piezoelectric actuators:

60

$$M_1^P = \frac{E_p}{1 - \nu_p} \int_Z \left(\cos^2 \theta d_{31} + \sin^2 \theta d_{32} \right) \frac{V_3}{h_p} z \, dz \qquad (3.104)$$

$$M_2^P = \frac{E_p}{1 - \nu_p} \int_Z \left(\sin^2 \theta d_{31} + \cos^2 \theta d_{32} \right) \frac{V_3}{h_p} z \, dz \qquad (3.105)$$

$$M_6^P = \frac{E_p}{1 - \nu_p} \int_Z \left(\cos \theta \sin \theta d_{31} - \cos \theta \sin \theta d_{32} \right) \frac{V_3}{h_p} z \, dz. \qquad (3.106)$$

To introduce membrane forcing is relatively simple. Begin by adding the pre-strains to Equation 3.83. Assuming the pre-strain acts on the neutral axis, membrane tension can be added by adding the constant N^0 to the N_1 and N_2 terms.

The resulting system of equations then compares to the derivation by Nayfeh and Pai [94, pg. 415]:

$$
\begin{Bmatrix} N_1 \\ N_2 \\ N_6 \\ M_1 \\ M_2 \\ M_6 \end{Bmatrix}
=
\begin{bmatrix} [A_{ij}] & [B_{ij}] \\ -[B_{ij}] & -[D_{ij}] \end{bmatrix}
\begin{Bmatrix} e_1 \\ e_2 \\ \gamma_6 \\ \frac{\partial^2}{\partial r^2} w \\ \left(\frac{1}{r} \frac{\partial}{\partial r} + \frac{1}{r^2} \frac{\partial^2}{\partial \theta^2} \right) w \\ 2 \left(\frac{1}{r} \frac{\partial^2}{\partial r \partial \theta} + \frac{1}{r^2} \frac{\partial}{\partial \theta} \right) w \end{Bmatrix}
+ I_{6 \times 6}
\begin{Bmatrix} -N_1^P + N^0 \\ -N_2^P + N^0 \\ -N_6^P \\ -M_1^P \\ -M_2^P \\ -M_6^P \end{Bmatrix} . \qquad (3.107)
$$

3.4.4 Neutral Axis Calculations. To write the equations at this point for unimorph actuation would still leave us with a series of coupled, non-linear equations, due to the non-symmetric ply lay up and the corresponding matrix coefficients in the A_{ij}, B_{ij}, and D_{ij}.

In order to address these coupling terms, the neutral axis of the composite, unimorph structure must be found. First, observe Figure 3.3, where h_s is the thickness of the substrate, h_p is the thickness of the piezoelectric actuator, and d_{NA} is the unknown distance between the bottom surface of the composite and the neutral axis.

Calculate the neutral axis by summing the in-plane stress over the thickness and setting equal to zero ($\sum M_{cw+}$):
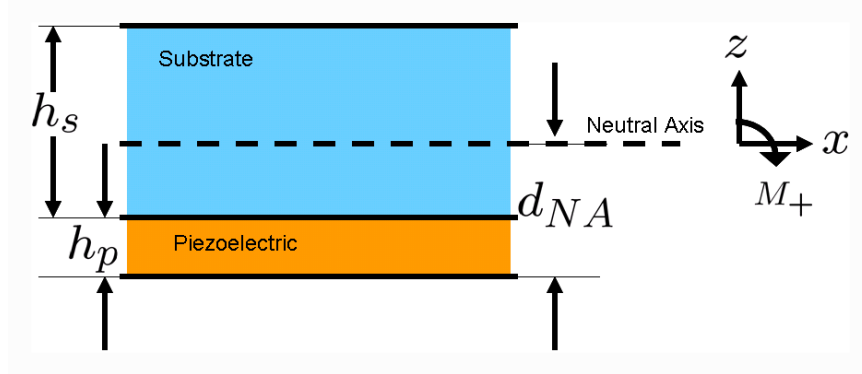
Figure 3.3: Neutral axis depiction.

$$\int_{-d_{NA}}^{-d_{NA}+h_p} \frac{E_p}{1+\nu_p} z dz + \int_{-d_{NA}+h_p}^{h_p+h_s-d_{NA}} \frac{E_s}{1+\nu_s} z dz = 0. \tag{3.108}$$

Define the parameter, γ, as

$$\gamma \equiv \frac{1+\nu_p}{1+\nu_s}. \tag{3.109}$$

Next, multiply Equation 3.108 by the quantity $(1+\nu_p)$ to yield

$$\int_{-d_{NA}}^{-d_{NA}+h_p} E_p z dz + \int_{-d_{NA}+h_p}^{h_p+h_s-d_{NA}} \gamma E_s z dz = 0. \tag{3.110}$$

Integrate and multiply by 2 to leave the expression:

$$E_p\left\{\left((h_p - d_{NA})^2 - (d_{NA})^2\right)\right\} + \gamma E_s\left(h_p + h_s - d_{NA}\right)^2 - E_s\left(h_p - d_{NA}\right)^2 = 0. \tag{3.111}$$

With some algebra, one may solve for d_{NA} as

$$d_{NA} = \frac{1}{2}\frac{E_p h_p{}^2 + \gamma E_s(2h_p h_s + h_s{}^2)}{E_p h_p + \gamma E_s h_s} \tag{3.112}$$

A quick check of the work is made by checking the case where $E_p = E_s \equiv E$ and $\gamma = 1$, such as for a homogenous plate. In this case, letting $h_p = h_s \equiv h$ results in $d_{NA} = h$, or exactly half the thickness of the plate, as expected.

Next, make the following observations. In many cases in the literature, the assumption $h_p \ll h_s$ is made (such is the case in the text by Preumont [112, pg. 48]). Then, Equation 3.112 reduces to

$$d_{NA} = \frac{1}{2}h_s. \tag{3.113}$$

However, restraint must be exercised when implementing this assumption. With this result it is implicitly assumed that the order of the Young's modulus for the piezoelectric material is the same or smaller than the order of the substrate modulus. For PZT actuators on an aluminum beam, this may be valid, but for the construction of deformable mirrors, this may not always be the case, and will be addressed in the subsequent section.

To minimize areal density (for unimorph construction), the mirror should be constructed so that in no case is $d_{NA} < h_p$. When $d_{NA} > h_p$, actuating moment is being added at the expense of areal density. In general (assuming similar material densities), construct the mirror such that $h_p = d_{NA}$. From Equation 3.112, one may solve this case to determine desired thickness of the substrate layer for a given piezoelectric material thickness,

$$h_s = h_p \sqrt{\frac{E_p}{\gamma E_s}}. \tag{3.114}$$

Now one is ready to examine the governing equations for a structure with a non-symmetric ply lay-up, specifically the case for unimorph actuation.

3.4.5 Matrix Coefficients for Force and Moment Equations. Having defined the terms that locate system's neutral axis, our desire at this point is to write the

matrices A_{ij}, B_{ij}, and D_{ij} for the unimorph system as modelled by Equation 3.83. Specifically, it is desired to set the conditions necessary to look at the uncoupled behavior when the terms of B_{ij} are equal to zero such that one may write a single governing equation of the form earlier presented as Equation 3.95.

Begin by first analyzing Equation 3.85 for B_{ij}. Writing B_{11} with the neutral axis terms previously defined, one has

$$
\begin{aligned}
B_{11} &= \int_{-d_{NA}}^{-d_{NA}+h_p} \frac{E_p}{1-\nu_p^2} z\,dz + \int_{-d_{NA}+h_p}^{h_s+h_p-d_{NA}} \frac{E_s}{1-\nu_s^2} z\,dz \\
&= \frac{1}{2}\frac{E_p}{1-\nu_p^2}\left\{\left((h_p-d_{NA})^2-(d_{NA})^2\right)\right\} + \frac{1}{2}\frac{E_s}{1-\nu_s^2}\left(h_p+h_s-d_{NA}\right)^2 - \ldots \\
&\quad \frac{1}{2}\frac{E_s}{1-\nu_s^2}\left(h_p-d_{NA}\right)^2.
\end{aligned}
\tag{3.115}
$$

It is desired this term to equal zero to uncouple the series of equations. If the mirror is constructed such that $d_{NA} = h_p$, Equation 3.115 reduces to:

$$
B_{11} = -\frac{1}{2}\frac{E_p}{1-\nu_p^2}{h_p}^2 + \frac{1}{2}\frac{E_s}{1-\nu_s^2}{h_s}^2.
\tag{3.116}
$$

Next, introduce γ from Equation 3.109, in order to write

$$
B_{11} = -\frac{1}{2}\frac{E_p}{1-\nu_p{}^2}{h_p}^2 + \frac{1}{2}\frac{\gamma E_s}{(1-\nu_p)(1-\nu_s)}{h_s}^2.
\tag{3.117}
$$

Applying the results specifying the relationship between thickness and modulus for unimorph construction of materials of the same density as set fourth in Equation 3.114 yields

$$
B_{11} = \frac{1}{2}\frac{E_p {h_p}^2}{1-\nu_p^2}\left(-1+\frac{1-\nu_p}{1-\nu_s}\right)
\tag{3.118}
$$

$$
= \frac{1}{2}\frac{E_p {h_p}^2}{1-\nu_p^2}\left(\eta-1\right).
\tag{3.119}
$$

where η is the non-dimensional parameter here defined as

$$\eta \equiv \left(\frac{1 - \nu_p}{1 - \nu_s}\right). \qquad (3.120)$$

Next, compute compute B_{12} under the same conditions as applied to the previous computation for B_{11} to obtain

$$B_{12} = \frac{1}{2}\frac{E_p {h_p}^2}{1 - \nu_p^2}\left(-\nu_p + \nu_s\eta\right). \qquad (3.121)$$

To put this term in a more easily analyzed form, add and subtract the quantity ν_p to the right hand side of the equation.

$$B_{12} = \frac{1}{2}\frac{E_p {h_p}^2}{1 - \nu_p^2}\left(-\nu_p + \nu_p\eta - \nu_p\eta + \nu_s\eta\right), \qquad (3.122)$$

$$= \frac{1}{2}\frac{E_p {h_p}^2}{1 - \nu_p^2}\left(\nu_p(\eta - 1) + (\nu_s - \nu_p)\eta\right). \qquad (3.123)$$

Next, define δ, which will be a small non-dimensional parameter used to decouple the leading order equations:

$$\delta \equiv \nu_s - \nu_p. \qquad (3.124)$$

For ease of notation, define two matrices E_{ij} and $\tilde{E}_i j$:

$$[E_{ij}] \equiv \begin{bmatrix} 1 & \nu & 0 \\ \nu & 1 & 0 \\ 0 & 0 & \frac{1-\nu}{2} \end{bmatrix} \qquad (3.125)$$

$$[\tilde{E}_{ij}] \equiv \begin{bmatrix} 0 & 1 & 0 \\ 1 & 0 & 0 \\ 0 & 0 & -\frac{1}{2} \end{bmatrix}. \qquad (3.126)$$

65

Then apply the same methodology to write the other terms of B_{ij} resulting in the equation:

$$[B_{ij}] = \frac{1}{2} \frac{E_p h_p^2}{1 - \nu_p^2} \left\{ (\eta - 1)[E_{ij}] + \delta\eta[\tilde{E}_{ij}] \right\} \tag{3.127}$$

One final bit of simplification shows that δ multiplies the entire equation as

$$[B_{ij}] = \delta \frac{1}{2} \frac{E_p h_p^2}{1 - \nu_p^2} \left\{ \frac{1}{1 - \nu_s}[E_{ij}] + \eta[\tilde{E}_{ij}] \right\}. \tag{3.128}$$

Using the same procedure, one may write the terms for A_{ij} and D_{ij}. The terms are:

$$[A_{ij}] = \frac{E_p h_p}{1 - \nu_p^2} \left\{ (1 + \frac{h_p}{h_s}\eta)[E_{ij}] + \delta\frac{h_p}{h_s}\eta[\tilde{E}_{ij}] \right\} \tag{3.129}$$

$$[D_{ij}] = \frac{1}{3} \frac{E_p h_p^3}{1 - \nu_p^2} \left\{ (1 + \frac{h_s}{h_p}\eta)[E_{ij}] + \delta\frac{h_s}{h_p}\eta[\tilde{E}_{ij}] \right\}. \tag{3.130}$$

Pause to look at the equations as written. Observe that δ determines the strength of the cross-coupling terms of B_{ij}. If one assumes the difference between the material constants ν_p and ν_s is small, a leading order equation may be written:

$$[A_{ij}] = A^E[E_{ij}], \tag{3.131}$$

$$[B_{ij}] = [0]_{3\times 3}, \tag{3.132}$$

$$[D_{ij}] = -D^E[E_{ij}]. \tag{3.133}$$

where

$$A^E \equiv \frac{E_p h_p}{1 - \nu_p^2}(1 + \frac{h_p}{h_s}\eta), \qquad (3.134)$$

$$D^E \equiv \frac{1}{3}\frac{E_p h_p^3}{1 - \nu_p^2}(1 + \frac{h_s}{h_p}\eta).. \qquad (3.135)$$

Thus, to put our modelling in a tractable form, one may choose only to model to leading order. Later, in Chapter IV, the AFIT deformable mirror testbed where the substrate Poisson's ratio is $\nu_s = 0.497$, and the piezoelectric Poisson's ratio is $\nu_p = 0.3$ is introduced. This results in one of the largest δ terms constructed of current materials. Future constructs would generally have both Poisson's ratios in the neighborhood of $\nu = 0.25$ to 0.30. It is also noted that the Young's modulus of both layers should be similar, as it affects the ratio of h_s to h_p as per Equation 3.114, and could serve to offset the small term δ. For the AFIT deformable mirror, $\frac{h_p}{h_s} \approx 0.01$. Thus, the A_{ij} and B_{ij} terms are equally valid, but the D_{ij} term would contain error when truncated.

3.4.6 Governing Equations. With the coupling terms assumed small, write the leading order behavior of the system as a single equation for the static case. The dynamic case is ignored as beyond the scope of this research, but the inertia term corresponding to the non-symmetric lay up would have to be treated as well if the dynamic case was important.

The equation was derived using exactly the same procedures as in Section 3.4.1, with the added terms as defined in Sections 3.4.3 through 3.4.5.

The resulting differential equation is:

$$D^E \nabla^4 w = \cdots$$

$$\left\{ N_1 \frac{\partial^2}{\partial r^2} + N_2 \left(\frac{1}{r} \frac{\partial}{\partial r} + \frac{1}{r^2} \frac{\partial^2}{\partial \theta^2} \right) + 2N_6 \left(\frac{1}{r} \frac{\partial^2}{\partial r \partial \theta} - \frac{1}{r^2} \frac{\partial}{\partial \theta} \right) \right\} w \cdots$$

$$- \left\{ \frac{\partial^2}{\partial r^2} + \frac{2}{r} \frac{\partial}{\partial r} \right\} M_1^P - \left\{ \frac{1}{r^2} \frac{\partial^2}{\partial \theta^2} - \frac{1}{r} \frac{\partial}{\partial r} \right\} M_2^P \cdots$$

$$- \left\{ \frac{2}{r} \frac{\partial^2}{\partial r \partial \theta} + \frac{2}{r^2} \frac{\partial}{\partial \theta} \right\} M_6^P, \tag{3.136}$$

Boundary conditions from Table 3.4.1 are amended to include those in Table 3.4.6

Table 3.5: Revised boundary conditions for non-linear plate.

position	value 1	value 2
$r = 0, R$	$\delta w = 0$	$Q_1 + \frac{1}{r} \frac{\partial}{\partial \theta} M_6 + N_1 \frac{\partial w}{\partial r} + \frac{N_6}{r} \frac{\partial w}{\partial \theta}$
$\theta = 0, \theta_0$	$\delta w = 0$	$Q_2 + \frac{\partial}{\partial r} M_6 + N_2 \frac{\partial w}{\partial \theta} + N_6 \frac{\partial w}{\partial r}$

Again, it is emphasized that this governing equation is for unimorph construction. To do so, write the axial tension piezoelectric terms and the moment terms below for this case from Equation 3.106 using the definitions in Section 3.4.4[14]

---

[14]Before proceeding further, it is noted that the piezoelectric terms are cumbersome because of our chosen coordinate system. If one had chosen a Cartesian coordinate system, the operator on the piezoelectric terms would be of a much more compact form. In a Cartesian frame, the piezoelectric force in the x-direction is:

$$M_1^{P(x)} = \frac{E_p}{1 - \nu_p} \int_Z \left(d_{31} + d_{32} \right) \frac{V_3}{h_p} z \, dz. \tag{3.137}$$

The y-direction is the same except the terms d_{31} and d_{32} are exchanged. Then, the operator on the piezoelectric terms on the right-hand side of Equation 3.136 becomes $-\frac{\partial^2}{\partial x^2} M_1^{P(x)} - \frac{\partial^2}{\partial x^2} M_2^{P(y)}$.

$$N_1^P = V_3 \frac{E_p}{1 - \nu_p} \left(\cos^2 \theta d_{31} + \sin^2 \theta d_{32} \right), \tag{3.138}$$

$$N_2^P = V_3 \frac{E_p}{1 - \nu_p} \left(\sin^2 \theta d_{31} + \cos^2 \theta d_{32} \right), \tag{3.139}$$

$$N_6^P = V_3 \frac{E_p}{1 - \nu_p} \left(\cos \theta \sin \theta d_{31} - \cos \theta \sin \theta d_{32} \right), \tag{3.140}$$

$$M_1^P = -\frac{1}{2} V_3 \frac{E_p}{1 - \nu_p} \left(\cos^2 \theta d_{31} + \sin^2 \theta d_{32} \right) h_p, \tag{3.141}$$

$$M_2^P = -\frac{1}{2} V_3 \frac{E_p}{1 - \nu_p} \left(\sin^2 \theta d_{31} + \cos^2 \theta d_{32} \right) h_p, \tag{3.142}$$

$$M_6^P = -\frac{1}{2} V_3 \frac{E_p}{1 - \nu_p} \left(\cos \theta \sin \theta d_{31} - \cos \theta \sin \theta d_{32} \right) h_p. \tag{3.143}$$

It may be beneficial to write Equation 3.136 in a form where one can see the in-plane elastic, piezoelectric, and membrane pretension effects. To do so, define the in-plane axial force terms

$$\left\{ \begin{array}{c} N_1^e \\ N_2^e \\ N_6^e \end{array} \right\} \equiv A^E [E_{ij}] \left\{ \begin{array}{c} e_1 \\ e_2 \\ \gamma_6 \end{array} \right\} \tag{3.144}$$

Thus defined, the axial force from Equation 3.107 and the A^E from Equation 3.135 has the form:

$$\left\{ \begin{array}{c} N_1 \\ N_2 \\ N_6 \end{array} \right\} = \left\{ \begin{array}{c} N_1^e - N_1^P + N^0 \\ N_1^e - N_1^P + N^0 \\ N_6^e - N_6^P \end{array} \right\} \tag{3.145}$$

Then, rewrite Equation 3.136 by making the above substitutions yielding:

$$D^E \nabla^4 w - N^0 \nabla^2 w = \cdots$$

$$\left\{ (N_1^e - N_1^P)\frac{\partial^2}{\partial r^2} + (N_2^e - N_2^P)\left(\frac{1}{r}\frac{\partial}{\partial r} + \frac{1}{r^2}\frac{\partial^2}{\partial \theta^2}\right) \cdots \right.$$

$$\left. + 2(N_6^e - N_6^P)\left(\frac{1}{r}\frac{\partial^2}{\partial r \partial \theta} - \frac{1}{r^2}\frac{\partial}{\partial \theta}\right) \right\} w \cdots$$

$$-\left\{ \frac{\partial^2}{\partial r^2} + \frac{2}{r}\frac{\partial}{\partial r} \right\} M_1^P - \left\{ \frac{1}{r^2}\frac{\partial^2}{\partial \theta^2} - \frac{1}{r}\frac{\partial}{\partial r} \right\} M_2^P \cdots$$

$$-\left\{ \frac{2}{r}\frac{\partial^2}{\partial r \partial \theta} + \frac{2}{r^2}\frac{\partial}{\partial \theta} \right\} M_6^P. \qquad (3.146)$$

The voltage function $V_3(r,\theta)$ deserves emphasis here. The equations are developed such that the voltage could be any arbitrary function applied over the interior of structure. However, in many cases, one may think of the voltage as occurring between an electrode on the top and bottom surface. For these discrete applications, each electrode will have its own associated voltage function. The area that the electrode covers may be defined as area S_i. In this case, the voltage for the ith actuator will be some magnitude V_i times an indicator function $H_i(r,\theta)$ is simply the indicator function defined as:

$$H_i(r,\theta) = \begin{cases} 1, (r,\theta) \in S_i \text{ (and hence an active piezoelectric area)}, \\ 0, (r,\theta) \notin S_i. \end{cases} \qquad (3.147)$$

Now further simplifications are introduced to arrive at the equations used later in this document. Analytical analysis of the governing equation is performed in Chapters V, VI, and VII.

In Chapter V, the in-plane terms for N^ϵ and N^P are ignored, such that a piecewise linear equation results. Further simplifications include analyzing the axisymmetric case such that θ dependence vanishes and $d_{31} = d_{32}$. Furthermore, only a single electrode is considered. Therefore, $M_1^P = M_2^P \equiv MH$ where H is again the indicator

function from Equation 3.147 and M is the magnitude from Equations 3.141 and 3.143. Equation 3.146 reduces to:

$$D^E \nabla^4 w - N^0 \nabla^2 w = -M \nabla^2 H, \tag{3.148}$$

where in this case the Laplacian operator is $\nabla^2 = \frac{\partial^2}{\partial r^2} + \frac{1}{r} \frac{\partial}{\partial r}$.

In Chapter VI, an even simpler form of the equation is used, where the in-plane actuated structure is seen to act essentially as a "bed of nails" in response to an applied voltage. If the plate term D^E is very small, and $d_{31} = d_{32}$, and again the in-plane effects are ignored, arriving at the following equation for J discrete actuators:

$$-N^0 \nabla^2 w(r, \theta) = M_i \nabla^2 \sum_{i=1}^{J} H_i(r, \theta), \tag{3.149}$$

where

$$M_i = \frac{1}{2} \frac{E_p d_{31}}{1 - \nu_p} h_p V_i. \tag{3.150}$$

Finally, in Chapter VII the axisymmetric non-linear equation is analyzed. Since the equation assumes an isotropic material (that is, the Young's modulus and Poisson's of both the substrate and the piezoelectric material are the same), $D^E = D$.

$$D\nabla^4 w(r) - N^O \nabla^2 w(r) + N^P \nabla^2 w(r) \dots$$
$$- N_1^\epsilon \left(\frac{\partial w(r)}{\partial r}\right)^2 \frac{\partial^2}{\partial r^2} w(r) - N_2^\epsilon \left(\frac{\partial w(r)}{\partial r}\right)^2 \frac{1}{r} \frac{\partial}{\partial r} w(r) \dots$$
$$= \nabla^2 M_P. \tag{3.151}$$

One final point is to be emphasized. In many of the works in the literature, the structural stiffening of the piezoelectric layer is neglected. The magnitude of the forcing has the form $M = \frac{1}{2}E_p d_{31} h_s V$. Thus noted, the linear model may be compared directly to those in the works by Lee et al [72–75], Bailey and Hubbard [17], and Preumont's text [112, pp. 48-51].

3.5 *Summary of Modelling Techniques*

This chapter introduced the basics of modelling a smart structure. A rigorous re-examination of the linear theory of piezoelectric theory makes clear the fundamental assumptions in linear piezoelectric theory. The piezoelectric-thermal analogy was detailed, and will form the basis for finite element and continuous models seen later in Chapters IV and V. Finally, the analytical model for an in-plane actuated plate-membrane were developed in the polar coordinate system.

The assumptions and observations made in this chapter are summarized here. The assumptions for quasi-static linear piezoelectric theory were:

- Piezoelectric material may be polarized, but not magnetizable in direction. Thus the magnetic flux and magnetic field intensity are interchangeable fields.

- Electromagnetic forcing is uncoupled from elastic waves.

- Strain-displacement relationships are for an infinitesimal fiber, with symmetry (zero rotation).

- Density and volume remain constant, and the piezoelectric reactions are isothermal.

- Electric enthalpy is assumed to be quadratic, restricting the relationships to linear terms.

The assumptions for the piezoelectric-thermal analogy were:

- The effects of the in-plane electric field were ignored.

- Piezoelectric sensing is not addressed.

- Thermal and piezoelectric forces should not be simultaneously applied, except in the case of purely linear expansion coefficients. The heat transfer problem may not be addressed.

The assumptions for the developing a plate membrane model were:

- Unimorph construction was assumed.

- Dynamic cases were ignored.

- Density of membrane substrate and piezoelectric are equal for the purpose of determining best layer thickness.

- Difference in Poisson ratio differences between the substrate and actuator were assumed small and coupling terms are ignored..

- Membrane tension was assumed to act only on the composite structure neutral axis, and was assumed constant (no active boundary control).

- Piezoelectric forces were assumed to be applied only on the interior of the structure, and not at the boundary.

With the modelling efforts complete, a study of in-plane actuated deformable mirrors may begin. In the next chapter, analytical solutions to the equations developed in this chapter are presented. Later, we will return to examine the effects of scaling on the differential equations in Chapter VII.

IV. Finite Element Modelling and Experimental Closed-Loop Control

> *Chapter objectives:*
>
> - *Introduce the MSC.Nastran finite element model*
> - *Develop quasi-static control algorithm*
> - *Report experimental closed-loop Zernike tracking results*

4.1 Introduction

To demonstrate initial feasibility of the in-plane actuated deformable mirror, a 0.127 meter diameter test article was constructed, modelled using the finite element method, and successfully controlled.

The research presented in this chapter compares experimental data with non-linear finite element modelling using MSC.Nastran software, and implements control algorithms developed from the results of the finite element modelling. By developing a finite element model that is validated with experimental data, a truth source was created upon which future modelling and control efforts may be tested without having to conduct laboratory trials. It is presumed this will be a necessary approach for the large membrane mirror space applications.

As a demonstration of the capability of the finite element modelling in this chapter, a controller was built that relied upon influence functions derived solely from the finite element modelling. The controller used a least squares approach to create an influence function matrix in an integral controller.

Optical precision shaping of the test article mirror surface, expressed in terms of a Zernike coefficient basis set as obtained from a Shack-Hartmann wavefront sensor,

was demonstrated in a series of quasi-static closed-loop control tests. Micron-scale control inputs to the defocus Zernike coefficient were tracked with an average absolute accuracy of 0.16 microns. For a multiple output system, the control system tracked the tip, tilt, and defocus modes with absolute average errors of 0.14, 0.09, and 0.18 microns, respectively, indicating that increasing the dimension of the control system did not significantly degrade its performance.

Significantly, this is the first demonstration of experimental closed-loop control for this class of deformable mirror.

4.2 Experimental Test Setup

A flat, circular, unimorph, in-plane actuated tensioned membrane mirror with piezoelectric actuators was constructed for the experimental testing. The material properties were characterized by direct measurement, manufacturer data, and the use of a laser vibrometer for frequency analysis. Surface deflections were measured using a Wavescope Shack-Hartmann wavefront sensor, converted from an output data stream of 42 Zernike coefficients. The control signal was generated in Matlab/Simulink and implemented using dSPACE to command seven power amplifiers. A flow chart depicting the experimental test setup is shown in Figure 4.1. A more detailed description of the test setup follows.

4.2.1 Test Article. The manufacture of a flat, circular, unimorph in-plane actuated tensioned membrane mirror was covered in detail by Sobers, Agnes and Mollenhauer [128]. In summary, the mirror is a composite structure of a 1.5 millimeter Room Temperature Vulcanizing (RTV) Silicone substrate, with a near-optical quality (optical quality for this document is defined as deflections or scales of one wavelength of light, usually on the order of 633 nm) coating of gold approximately five microns thick on the reflective side and a 52-micron polyvinylidene fluoride (PVDF) actuating layer on the other. The boundary of the membrane mirror was clamped in tension in a 0.127 meter diameter circular aluminum ring. Although every effort was made
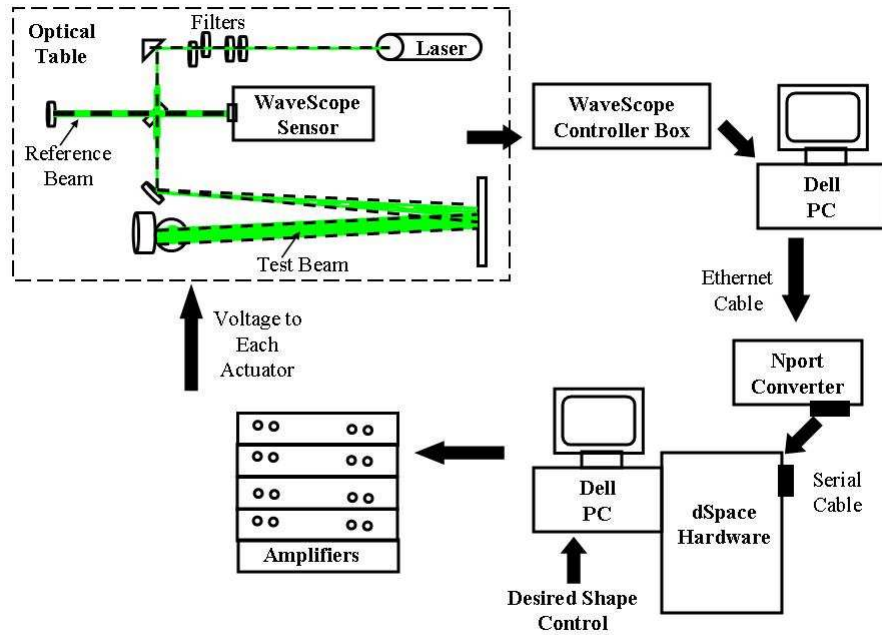
Figure 4.1:   Experimental test setup.

to uniformly tension the mirror, frequency response data would later indicate a non-uniform tension field existed (see Section 4.3.2).

A widely separated electrode pattern was etched in the bottom surface electrode to form six radial actuators and one center axisymmetric circular actuator as shown in Figure 4.2. The PVDF material was non-orthotropic in nature as the strength of the piezoelectric coefficient in the y-direction was over seven times the strength of the coefficient in the x-direction. The PVDF actuators were capable of being energized singly or in combination with static and dynamic potentials up to plus and minus 600 volts.

Rather than bonding leads directly to the deformable mirror, thin electrodes ran to the boundary where the leads were attached. The small (and later neglected for modelling purposes) electrode regions ran axially outwards from each actuator. Another design consideration was that all electrodes had to be manufactured (etched) by hand, and resulting tolerances were not as tightly controlled as might be expected

76
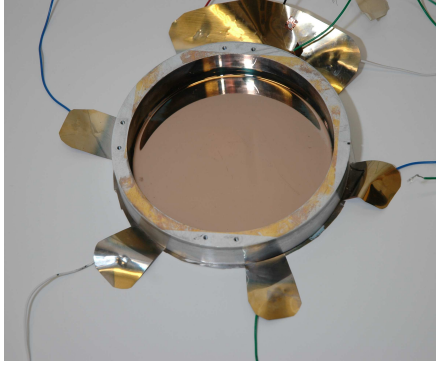
(a) Reflective mirror surface.
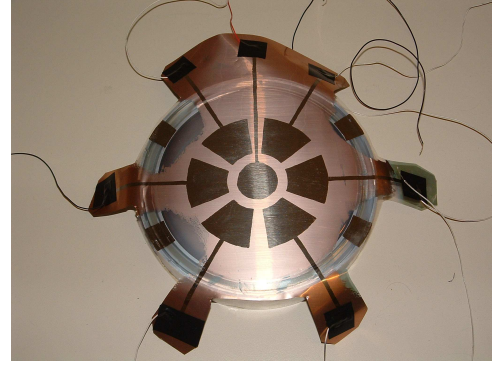
(b) Piezoelectric electrode pattern on the non-reflective (back) side of the deformable mirror.

Figure 4.2:   AFIT 0.127 meter diameter deformable mirror.

with computer-aided construction techniques. The design dimensions of the actuators are presented in Table 4.1. The material properties are explicitly stated in Tables 4.2 and 4.3. The values are from manufacturer data, with the exception of the Poisson's value for silicone, which was experimentally obtained by Lutz [80], and the thickness of the silicone layer, which was derived by Trad [?] from the pre- and post- silicone coating weight measurements of the structure and then dividing by the material density.

Table 4.1:   Deformable mirror dimensions.

Radius (mirror)	0.0635 m
Radius (center actuator)	0.0127 m
Inner radius (actuators 2-7)	0.0190 m
Outer radius (actuators 2-7)	0.0444 m
Arc length (actuators 2-7)	50 degrees

4.2.2   Mirror Surface Measurement.   A flowchart depicting the experimental setup was presented in Figure 4.1. The optical table was designed to reduce external vibrations and was presented in the earlier work by Sobers et al [128], as a lightweight membrane is highly susceptible to any environmental disturbances. The table floats on four air-isolation legs, and has a plexiglass cover to attenuate airborne disturbances

Table 4.2:   GE silicone RTV615 material properties.

Parameter	Value [12]	Units
thickness	0.0015	m
Young's modulus	1.013	$10^6 N/m^2$
Poisson's ratio[*]	0.497	
density	1020	kg/m^3
shrinkage	0.2%	
useful temperature range	-60 to 204	$°C$

[*] The value for Poisson's ratio was experimentally
determined.

Table 4.3:   PVDF film properties.

Parameter	Value [10]	Units
thickness	52	micron, $10^{-6}m$
d_{31}	3	$10^{-12}\frac{m/m}{V/m}$ or $\frac{C/m^2}{N/m^2}$
d_{32}	23	$10^{-12}\frac{m/m}{V/m}$ or $\frac{C/m^2}{N/m^2}$
Young's modulus	2-4	$10^9 N/m^2$
density	1780	kg/m^3
useful temperature range	-40 to 100	$°C$

such as acoustic noise and air currents. A 20-mWatt helium-neon laser ($\lambda = 633$ nm)
was used to illuminate the deformable mirror test article and reference mirror via a
beam splitter. The mirror was tested while in a horizontal position on the optics table
to allow the membrane surface to articulate freely constrained only by the clamped
frame boundary condition (see Figure 4.3). Light entering the WaveScope passes
through a monolithic lenslet module (MLM) that focuses the light onto an RS-170v
monochrome Shack-Hartmann wavefront sensor. The fidelity of the data collected
using the WaveScope depends on the size and number of the lenslets in the MLM.
The data may only be acquired over a limited region of the surface of the mirror
due to equipment limitations, an approximate 0.076 meter diameter region. For the
purposes of this work, this observable region is called the mirror's *clear aperture.*

The WaveScope sensor sends surface data to a video frame grabber in a per-
sonal computer. When performing calibration, laser returns are reflected off of the de-
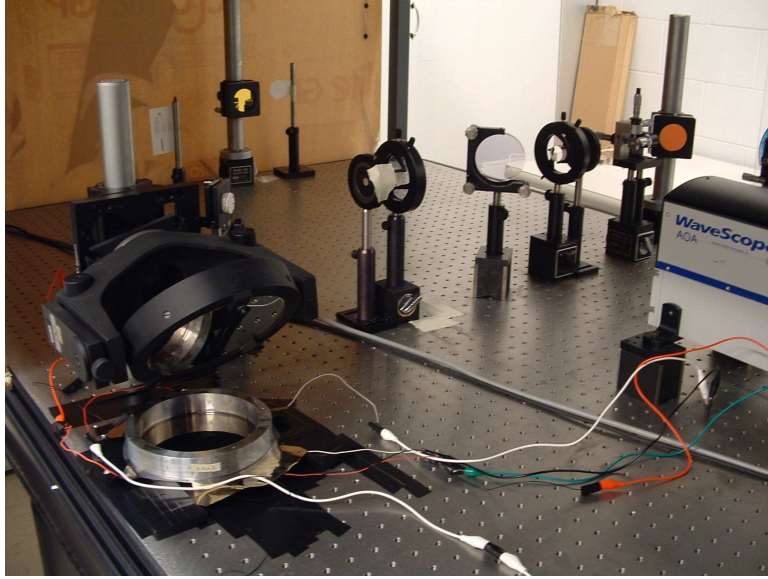
Figure 4.3:   Mirror (bottom left) with Shack-Hartmann sensor.

formable mirror test article and reference mirror into the WaveScope sensor. Regions of the lenslet array which do not receive bright enough returns to provide accurate measurements (presumably due to construction of the mirror surface) are automatically discarded from the collected data. A minimum valid rate of 70% was achieved for all tests. Images from the Shack-Hartmann sensor are shown in Figure 4.4.

The wavefront path difference of these valid data points are fitted with a WaveScope proprietary algorithm. The algorithm calculates, displays, and exports up to 42 Zernike coefficients of the illuminated surface. The Zernike polynomials efficiently describe classical abberations for a circular aperture of unit radius, the linear combination of which represent the surface deflection.

Recall from Chapter II, the Zernike functions are an orthogonal basis set over a circular aperture of normalized radius. Use of the Zernike basis set for optical applications was popularized by Noll [97], and a description of the terms are available in any introductory optics text book as well as an expanded description in Chapter VI. The Zernike polynomial basis set for Wavescope is presented in Appendix D.
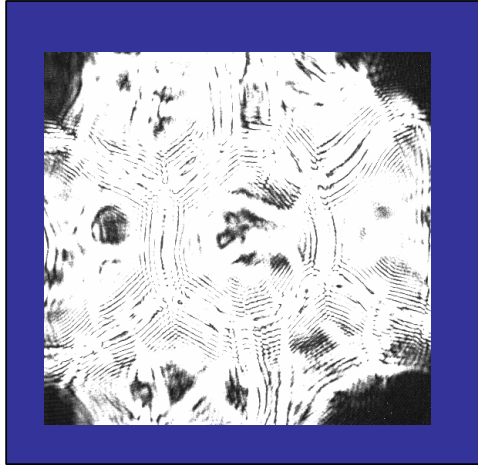
(a) Mirror surface clear aperture region at maximum laser illumination level.
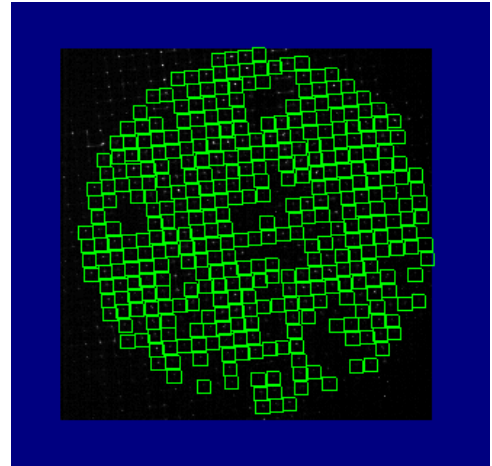
(b) Typical grid depicting 370/450 of available apertures used by Shack-Hartmann sensor.

Figure 4.4:   Mirror as viewed through Shack-Hartmann sensor.

Zernike coefficient values were updated at a maximum rate of 400 Hz, but due to data transfer and integration issues with the dSPACE controller, experimental results were limited to 2.5 Hz. Thus, some open-loop qualitative observations could be made at the higher frequency, but analysis such as a power spectral density or transfer functions could not be obtained for the combined WaveScope/dSPACE system.

4.2.3   Closed-Loop.   Zernike coefficients calculated by the Wavescope sensor were exported across an ethernet cable to a NPort ethernet-to-serial converter at the 2.5 Hz rate. The serial cable is connected to the dSPACE hardware interface board. The dSPACE and second PC receive and store the data, implement real-time control through a Simulink model and Control Desktop software, and output control voltages to a stack of Trek PZD 700 Dual Channel Amplifiers. The loop is completed as each of seven amplifiers powers its respective actuator to deform the test article mirror surface. The control algorithm is explained in Section 4.4, after first describing the development of the influence function matrix using the finite element model approach.

4.3 Non-linear MSC.Nastran Finite Element Model

The governing linear analytical equation for the out-of-plane displacement w of an isotropic plate-membrane with plate stiffness D^E and membrane tension N^0 undergoing piezoelectric actuation of uniform strength M^P over a region defined by an indicator function H of value one within the region, and zero outside of the region, as was defined in Chapter III.

$$D^E \nabla^4 w - N^0 \nabla^2 w = M^P \nabla^2 H, \tag{4.1}$$

where ∇^2 is the Laplacian operator, which in cylindrical coordinates is $\nabla^2 = \frac{\partial^2}{\partial r^2} + \frac{1}{r}\frac{\partial}{\partial r} + \frac{1}{r^2}\frac{\partial^2}{\partial \theta^2}$.

For the test mirror which is the subject of this investigation in this chapter, it was not clear if such a simplified system would be applicable. The underlying reason was that the tension field in the mirror (the membrane tension N_0) could not be assumed constant as in Equation 3.107. Furthermore, in Chapter III, it was shown that the governing equations were only applicable if the difference between the Poisson's ratio of the substrate and the piezoelectric material was small. For this case, the difference was $0.497 - 0.3 = 0.197$, for which the small assumption would appear invalid.

Instead, it was decided to create a non-linear finite element model in MSC.Nastran based on the piezoelectric-thermal analogy detailed in Chapter III. The finite element model would represent an analogous solution to the series of coupled non-linear equations as presented in Chapter III. The model was then compared to test data, and would serve as a useful truth source for the remainder of this document.

Using 100 radial divisions and 72 angular divisions comprising 7201 nodes, the model was built with 7128 CQUAD4 elements and 72 CRIA3 composite plate elements. The element properties were defined using a PCOMP card modelling the silicon substrate and PVDF layer. The PCOMP element derives equivalent internal

PSHELL and MAT2 cards to capture the membrane, bending, coupling, and transverse shear stiffness of the composite element [92]. A MAT1 card was used to enter the material properties from Section 4.2.
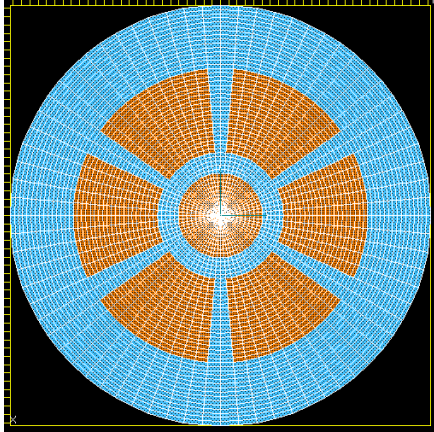
(a) Grid of CQUAD4 and CTRIA3 elements where orange areas indicate active piezoelectric region.
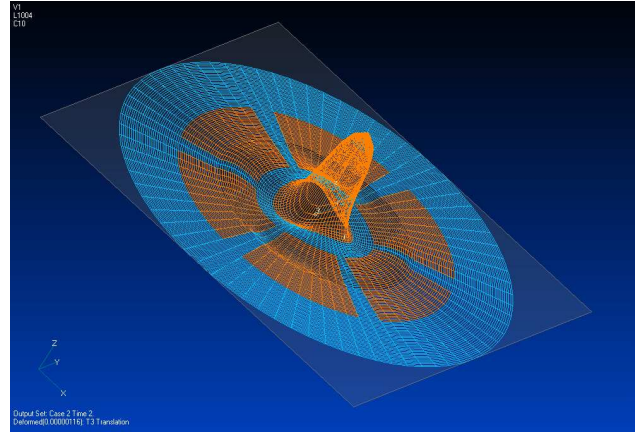
(b) Typical wireframe of static deflection under load. In this example, the center actuator is activated.

Figure 4.5:   MSC.Nastran model.

4.3.1   Piezoelectric-Thermal Analogy.   The piezoelectric-thermal analogy is implemented just as introduced in Chapter III, the active elements were given x- and y-coefficients for planar thermal expansion in their piezoelectric layer using the values from Table 4.3 and are colored orange in Figure 4.5. All other regions, plus the silicone substrate, were left thermally inert. Voltage was then applied as an equivalent temperature to the nodes of the corresponding actuators. In all cases, only a static voltage was applied.

4.3.2   Modelling Edge Tension.   When the deformable mirror was constructed, a suitable method of measuring and recording edge tension was not available. Although presumably the edge tension would be available for a commercially-manufactured mirror, due to the handmade nature of the test article, an alternate method to determine the pellicle tension field was required. It was decided to perform

82

a dynamic analysis of the test article, and then implement a tension field in the finite element model that would approximate the frequency and mode shapes for the first six recorded modes. A laser vibrometer was used to scan the surface of the mirror when excited by chirp signals produced by an air horn from 50-100 Hz and 100-250 Hz. It was determined that mode 2 was not observed in the data based upon an eigenvector analysis, the results of which are summarized in Figure 4.6; left image in each column is laser vibrometer mode shape data, right image is MSC.Nastran modal analysis solution. In the figure, the view of the mirror was of the reverse (non-reflective) side and was rotated 100 degrees (the reflective surface was incompatible for use with the laser vibrometer). The finite element model was of the same orientation.
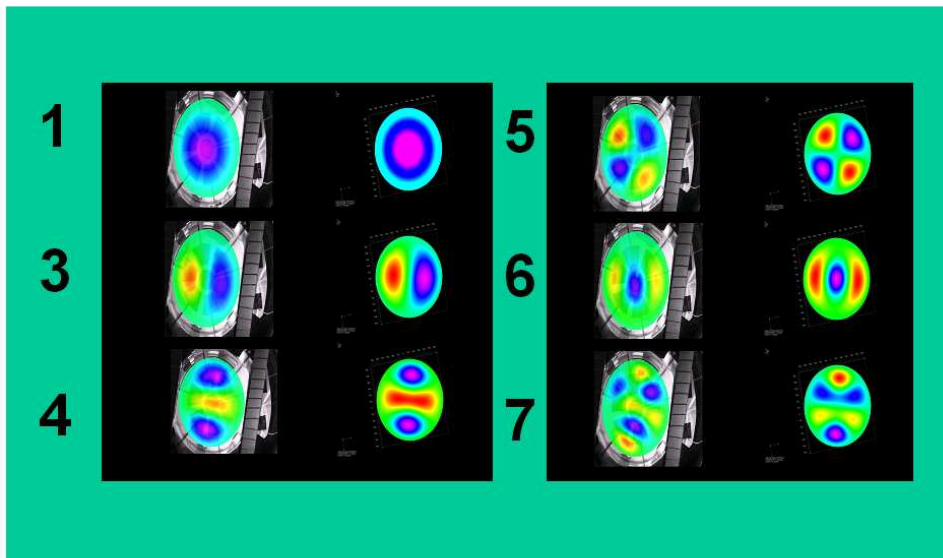
Figure 4.6:   Eigenvector comparison.

The natural frequency data and eigenvector data did not match the membrane theoretical solution for a circular boundary because of an apparent asymmetry in the tension field, despite best efforts to maintain symmetry when the mirror was constructed. Although a matching algorithm could likely prescribe a set of nodal forces to exactly match the first seven eigenvalue/eigenvector pairs, it was hypothesized that a perturbed elliptic tension field could provide satisfactory results without unneces-

83

sarily complicating the model. To implement the proposed membrane strain field, an edge tension, N, was implemented with a tangential force along the boundary governed by the equation:

$$N(R, \theta) = \varrho(1 + \varepsilon \cos^2 (\theta - \theta_0)). \tag{4.2}$$

To match the laser vibrometer modal data for the deformable mirror, the values of $\varrho = 170$ Newtons/meter, $\varepsilon = 0.7840$, and an orientation of $\theta_0 = 105^o$ were programmed in the model. The values were chosen using an empirical comparison. Using the modal analysis solution (SOL 103) the model eigenvalues and eigenvectors were compared to the experimental test data. The agreement achieved using the proposed strain field is shown in Figure 4.6 and Table 4.4, where the per cent error is simply:

$$\%_{\text{error}} = \frac{\omega_{\text{theory}} - \omega_{\text{experimental}}}{\omega_{\text{experimental}}} \times 100\%. \tag{4.3}$$

Table 4.4:   Modal frequency comparison.

Mode	Experimental	Membrane[*]	Error	MSC.Nastran	Error
1	76	$2.4048\kappa = 76$	0.0 %	76	0.0 %
2[†]	–	$3.8317\kappa = 121$	NA	116	NA
3	129	$3.8317\kappa = 121$	-6.2 %	129	0.0%
4	146	$5.1356\kappa = 162$	11.0 %	155	6.1 %
5	163	$5.1356\kappa = 162$	-0.6 %	165	1.2 %
6	188	$5.5201\kappa = 174$	-7.4 %	186	1.1 %
7	228	$6.3802\kappa = 202$	11.4%	198	13.2 %

[*] The frequencies for membrane theory were normalized to the first observed experimental modal frequency by the scale factor κ.
[†] The second modal frequency was not observed in the experimental test data.

4.3.3   MSC.Nastran Solution Strategy.   Linear solutions to the finite element model as presented cannot accurately represent the surface deflections of the physical structure. This is because the stiffening effect of the membrane tension from the boundary loading conditions is not present–the linear solution is the independent com-

bination of the linear stretching (resulting in constant surface deflections removed as a bias) and piezoelectric actuation of the non-tensioned plate (greatly exaggerated surface deflection due to the weak contribution of the plate's flexural rigidity). Therefore, a non-linear solution is required. In Chapter III, this was apparent as linear models uncoupled the in-plane forces from the out-of-plane displacements.

For a non-linear total Lagrangian finite element formulation, Green Strains are used. Although normally solved in an isoparametric space, one can write the Green Stains in a polar form [23, pg. 552]:

$$\epsilon_{rr} = \frac{\partial u}{\partial r} + \frac{1}{2}\left(\frac{\partial u}{\partial r}^2 + \frac{\partial v}{\partial r}^2 + \frac{\partial w}{\partial r}^2\right) \tag{4.4}$$

$$\epsilon_{\theta\theta} = \frac{1}{r}\frac{\partial v}{\partial \theta} + \frac{u}{r} + \frac{1}{2r^2}\left(\frac{\partial u}{\partial \theta}^2 + \frac{\partial v}{\partial \theta}^2 + \frac{\partial w}{\partial \theta}^2\right) \tag{4.5}$$

$$\epsilon_{r\theta} = \frac{1}{r}\frac{\partial u}{\partial \theta} + \frac{v}{r} + \frac{\partial v}{\partial r} + \frac{1}{r}\frac{\partial u}{\partial r}\frac{\partial}{\partial \theta} + \frac{1}{r}\frac{\partial v}{\partial r}\frac{\partial v}{\partial \theta} + \frac{1}{r}\frac{\partial w}{\partial r}\frac{\partial w}{\partial \theta}. \tag{4.6}$$

Typically, the bending terms under the Kirchhoff assumption are introduced, and the in-plane axial terms are neglected, resulting in the von Kármán strains used by Nayfeh and Pai and presented in this document as Equations 3.99 and Equations 3.100. Although the MSC.Nastran documentation for the CQUAD4 and CTRIA3 elements indicates only that membrane and bending are present [11, pp. 1143,1187], it is assumed the MSC.Nastran strain field is equivalent to the strain field used to derive the governing differential equations of Chapter III.

In finite elements, the problem is solved by introducing a tangent stiffness matrix, ^tK. For the forced finite element problem, with the matrix $\tilde{B}$ of shape functions, the tangential forces are $^t\boldsymbol{F} = \int_V \tilde{B}\tilde{S}dV$, where S represents the Second Piola-Kirchhoff stress matrix. Then, for an incremental displacement $^t\boldsymbol{u}$ corresponding to an incremental load:

$$\,^tK = \frac{\partial(^t\boldsymbol{F})}{\partial(^t\boldsymbol{u})}. \tag{4.7}$$

Taking the derivative, arrive at equations of the form:

$$\frac{\partial(^t\boldsymbol{F})}{\partial(^t\boldsymbol{u})} = \int_V B^T \frac{\partial\tilde{S}}{\partial\tilde{\epsilon}} \frac{\partial\tilde{\epsilon}}{\partial^t\boldsymbol{u}}dV + \int_V \frac{\partial B}{\partial^t\boldsymbol{u}}\tilde{S}dV \tag{4.8}$$

$$= \int_V B^T EBdV + \int_V \frac{\partial B}{\partial^t\boldsymbol{u}}\tilde{S}dV \tag{4.9}$$

$$= K_L + K_\sigma. \tag{4.10}$$

In the above equations, the matrix E is the material properties, and K_L is the linear stiffness matrix, while K_σ represents the non-linear stiffness matrix. For an updated Lagrangian approach, such as employed by MSC.Nastran [77, ch. 5], the strains are written in the updated coordinate system, and a Cauchy stress matrix is substituted, but the point of this discussion is the same.

To implement the non-linear solution in MSC.Nastran, the SOL 106 strategy was used and called the NLPARM card. The non-linear parameters were set for no less than 10 load increments with the default stiffness update method (AUTO). Within each load increment, a modified Newton-Raphson approach, the *BFGS* method, was used by MSC.Nastran to resolve a stiffness matrix "resembling" the tangential stiffness matrix as described above [77, ch. 3.5].

The BFGS method, named for Broyden-Fletcher-Goldfarb-Shannon, is an updated form of the modified Newton-Raphson, or *quasi-Newton*, approach. The following discussion of the stiffness updates is based on the explanation from the *MSC.Nastran Nonlinear Analysis Handbook* [77]. Defining the change in displacement as $\Delta u = \,^t\boldsymbol{u}^i - \,^t\boldsymbol{u}^{i-1}$ and $\Delta R = \,^t\boldsymbol{R}^i - \,^t\boldsymbol{R}^{i-1}$, where the change in load error is related to the change in forces by

$$\frac{\partial(^t\boldsymbol{F})}{\partial(^t\boldsymbol{u})} = -\frac{\partial(^t\boldsymbol{R})}{\partial(^t\boldsymbol{u})}. \tag{4.11}$$

Thus, $\Delta R = [K_{i+1}]\Delta u$, or $\Delta u = [K_{i+1}]^{-1}\Delta R$, where K^{-1} is the inverse Hessian matrix which must be determined. In the BFGS strategy, this inverse is found by the formula:

$$\begin{aligned}
[K_{i+1}]^{-1} =& [K_i]^{-1} + \Big(\frac{(1 + \{\Delta R\}^T[K_i]^{-1}\{\Delta R\})}{\{\Delta R\}^T\{\Delta u\}}\Big)\frac{\{\Delta u\}\{\Delta u\}^T}{\{\Delta u\}^T\{\Delta R\}} \cdots \\
& + \frac{\{\Delta u\}\{\Delta R\}^T[K_i]^{-1} + [K_i]^{-1}\{\Delta R\}\{\Delta u\}^T}{\{\Delta R\}^T\{\Delta u\}}
\end{aligned} \tag{4.12}$$

A line search parameter, α, is used to alter the step size while preventing the propagation of bad updates. The tolerances checked are based on numerical experiments. A simplified flow diagram is presented in Figure 4.7.
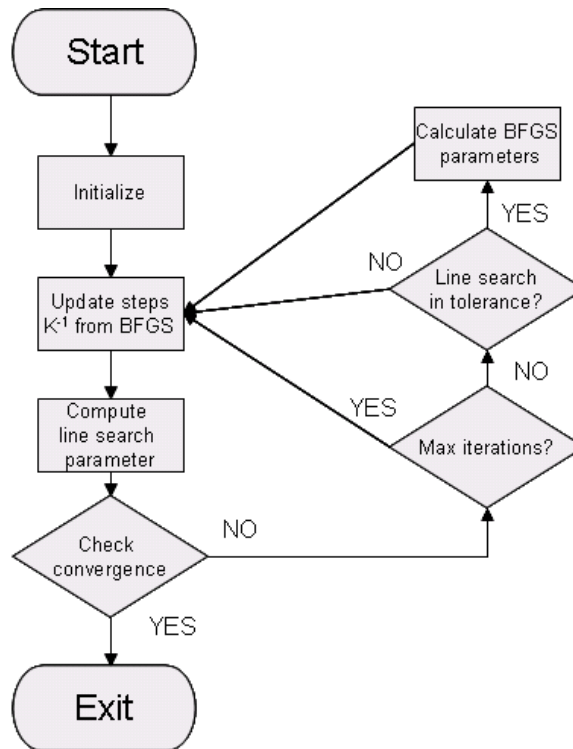
Figure 4.7:   MSC.Nastran Quasi-Newton flow chart.

Convergence was set to check load, work, and displacement default criteria, with a tolerance of no less than the default tolerance, which correspond to the "very high" accuracy designation [11, pg. 1709-1715]. In this manner, the membrane tension is allowed to stiffen the structure through the LGDISP parameter, which allowed geometric changes to the stiffness matrix. Difficulties in convergence due to singularities in the stiffness matrix for high membrane-to-bending stiffness structures [77] were overcome by using the parameter K6ROT set to 1.0E6. It should be noted that in general, the convergence criteria of load would be used for a stiffening structure (as presented), but all three tolerances were used and convergence was still achieved.

The edge tension was set using the FORCE card with a radial force along the boundary as determined by Equation 4.2. Next, a second subcase generates the piezoelectric load through the equivalent thermal loads set by TEMPERATURE(LOAD) and TEMPERATURE(INITIAL) cards, and sets the loads according to the actuator numbering scheme as shown in Figure 4.8. The bulk data file is available in abridged form in Appendix B.
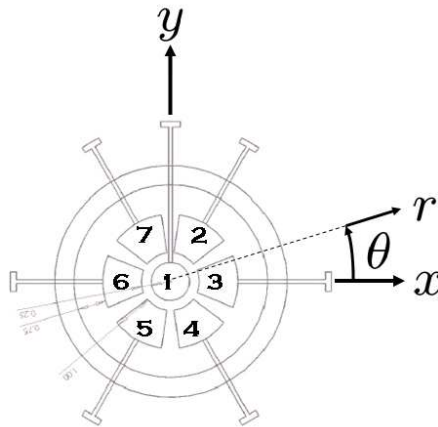
Figure 4.8:   Actuator numbering scheme.

With the non-linear finite element model so constructed, the next step was to compare experimental data with the model results.

4.3.4 Experimental versus Finite Element Static Deflections. Experimental data is compared to the static finite element solution in Figure 4.9. A 300 Volt load was individually applied to actuator 1, 2, and 3 as shown in the figure. The experimental surface was obtained from a linear combination of 42 Zernike basis functions that were averaged over approximately 80 consecutive measurements.

A baseline (0-volt) surface was subtracted from each plot to discount any initial surface and beam path irregularities. For the finite element solution, displacements in the vertical (z axis) direction were recorded, and then a surface was determined from the linear combination of the same 42 Zernike basis elements as fit to the data. The coefficients were determined using a projection with the error norm as described in Appendix A. This use of the same subset of basis functions enabled a direct comparison between the experimental and finite element data. This Zernike representation of the surface displacements is presented in Figure 4.9.

(a) Actuator 1 test data.   (b) Actuator 2 test data.   (c) Actuator 3 test data.

(d) Actuator 1 finite element model.   (e) Actuator 2 finite element model.   (f) Actuator 3 finite element model.
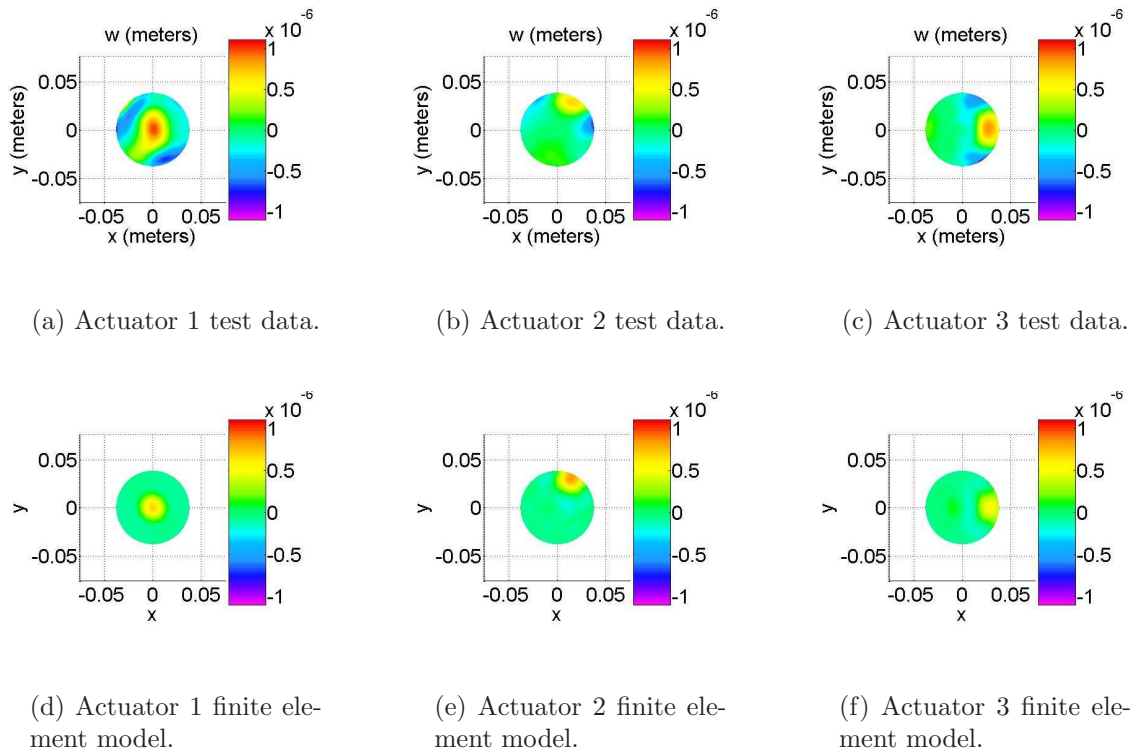
Figure 4.9:   Zernike representation of static deflections.

4.4 Quasi-static Surface Control

The controller created for this system was created imposing several constraints. First, the controller was built without any calibration data (that is, without any *a priori* knowledge of the WaveScope measurements). For some applications it may prove easier to control the system by applying demonstrated system identification techniques, however the objective of the work herein is to demonstrate existing finite element theory was sufficient for modelling and controlling this class of structure. Second, hardware and software constraints limited the data rate and number of available outputs available for control. However, given these constraints, demonstrated quasi-static surface control were achieved for this class of mirror with the controller as outlined in the following paragraphs.

To construct a controller for the system, conventional techniques were employed. The controller consisted of a static gain matrix, a proportional path, a bank of anti-windup integrators, and a smoothing filter. Rate transition filters were used to match the control input calculations with the measurement rate. An overview of the controller implementation is shown in Figure 4.10.

4.4.1   Static Gain Matrix.   A static gain matrix, K, was formed using static Zernike representations of surfaces formed by the MSC.Nastran finite element model. A linear static gain matrix was used for two reasons. One, the influence functions from the finite element were localized, and thus nearly independent. Second, the deflection versus voltage curve was nearly linear. The static deflection of the center node versus a voltage applied in 50-volt increments to the center actuator in the finite element model is shown in Figure 4.11. On the same figure, the linear relationship used for the static gain matrix is shown by a solid line.

The static shapes, represented by 42 Zernike coefficients, such as shown in Figure 4.9, were created in finite element simulation by applying 300 Volts to each of the actuators, and then normalizing to a one volt application. Each 42-element static response vector was placed in a matrix Y. Thus the static system was:
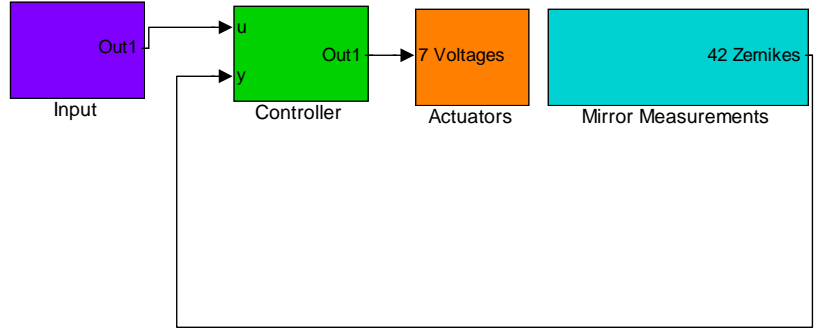
(a) System overview operating at 11 KHz.
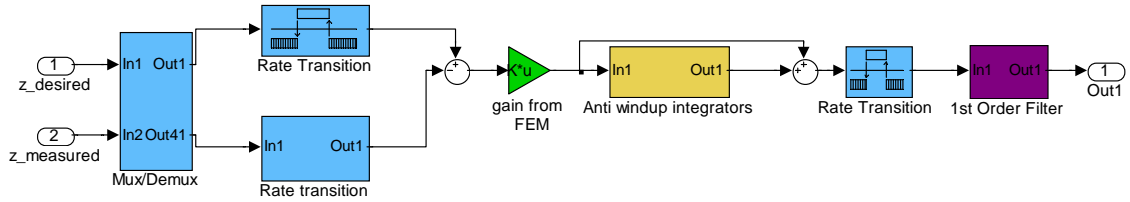
(b) Controller operating at 2.5 Hz (consistent with measurement rate) operating on error signal consisting of a static gain matrix, anti-windup integrators, and a proportional path. The control output is filtered to prevent "ringing" the mirror.

Figure 4.10:   Block diagram of system as implemented in Simulink software.

$$\Big[A\Big]_{42\times7}\Big[X\Big]_{7\times7} = \Big[Y\Big]_{42\times7}, \tag{4.13}$$

where

$$\Big[Y\Big]_{42\times7} = \Big[\big\{z_1\big\}_{42\times1} \quad \big\{z_2\big\}_{42\times1} \quad \cdots \quad \big\{z_7\big\}_{42\times1}\Big]_{42\times7}. \tag{4.14}$$

In the above equations, A was the unknown system and X was an identity 7×7 matrix corresponding to the one-volt application to each of the actuators. The vectors
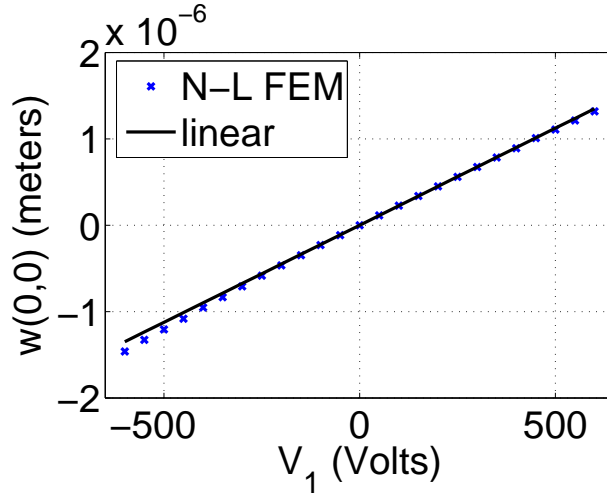
Figure 4.11:   Finite element model static deflection of center node versus voltage.

$z_1, z_2, \ldots, z_7$ represent the 42 Zernike coefficients for a one volt application to actuator 1, 2, through 7 respectively, as obtained from the Zernike fit to the forced response of the finite element model for each of the actuator cases. Again, it is emphasized that the response of the non-linear finite element model was assumed linear with respect to applied voltage–the non-linear aspect was only used to introduce the stiffening brought about by edge tension.

Trivially, $A = Y$. For the control problem where a desired surface z of up to 42 Zernike coefficients is desired, the problem to be solved is:

$$\left[A \right]_{42 \times 7} \left\{ v \right\}_{7 \times 1} = \left\{ z \right\}_{42 \times 1},\tag{4.15}$$

where v represents the control voltage inputs. Or simply require:

$$\left\{ v \right\} = \left[K \right] \left\{ z \right\},\tag{4.16}$$

where K is determined using

$$\left[K \right] \equiv \left[\left(\left[A \right]^T \left[A \right] \right)^{-1} \left[A \right]^T \right]_{7 \times 42}.\tag{4.17}$$

The solution represents the minimum 2-norm solution to Equation 4.13. For this system, where discontinuous actuators have non-overlapping surface displacement functions, the inverse will exist. However, increased actuator densities may require alternatives to Equation 4.17 in the cases where the surface displacement functions of the actuators intersect.

The gain matrix K acted on the error signal in the feedback path as shown in Figure 4.10, where the error signal is defined as:

$$\{z\} \equiv \{z_e\} = \{z_{desired}\} - \{z_{measured}\}. \tag{4.18}$$

It is emphasized that the gain matrix K was obtained entirely from finite element modelling, not experimentally derived data.

4.4.2 Proportional plus Integral Control. Once the appropriate gains were calculated by multiplication of the gain matrix with the error signal, the resulting voltages were sent through a proportional path for immediate response, plus stored with a bank of anti-windup integrators.

The anti-windup integrators had cutoffs set at plus and minus 600 volts corresponding to the saturation limits of the amplifiers (further input protection was in a saturation block just prior to the amplifiers). The goal of the anti-windup integrators was to reduce the lag from a build up of error if the desired signal exceeded the physical capacity of the system (that is, outside of the controllable space) and returned to within the operational limits. Without the anti-windup feature, built up error would effectively freeze the system, causing lags that could only be overcome with lengthy errors in the direction opposite the initial error.

4.4.3 Integration. The controller operated at 2.5 Hz, consistent with the measurement rate of the WaveScope sensor. The Simulink/dSPACE controller operated at a much higher frequency, and thus had to be stepped down in frequency

through rate transition blocks before entering the control and stepped up upon leaving the controller.

Open-loop testing, where higher frequency measurements could be qualitatively observed, showed considerable "ringing" of the mirror if 2.5 Hz step inputs were applied to the actuators. The ringing could not be observed at the slow measurement speed in the closed-loop testing. However, a first order filter with a 2.5 Hz cutoff frequency was installed after the rate transition block to the higher system frequency. This was used to smooth the control input to the amplifiers, and theoretically lessen the excitation of the mirror dynamics.

Due to processing limitations, only a limited number of the available outputs (that is, Zernike coefficients) could be used in the control system and recorded. Therefore, a subset of the available signals were stripped from the measurements in the Mux/Demux block of Figure 4.10 (b). For the testing presented in this document, the retained measurements were the Zernike coefficients for tip, tilt, and defocus (Wavescope Zernike coefficients Z_1, Z_2, Z_3).

4.5   Experimental Testing and Results

A series of quasi-static tracking tests were run to demonstrate the effectiveness of the in-plane actuated, tensioned deformable mirror under the control of a purely theoretically developed controller using standard finite element modelling and control practices.

Measurements were limited to tip, tilt, and defocus Zernike coefficients within the mirror's clear aperture due to the constraints listed in the previous section. Choosing these modes provided a suitable demonstration for the mirror's capabilities, but it is recognized by the research team that these are some of the less interesting modes for a deformable mirror. Typically, the tip and tilt modes of a deformable mirror are controlled by an independent control system acting on the rigid frame of the structure. Also, the focus error may be a function of the length of the beam path, and may

be corrected by adjusting the position of the mirror. For that reason, these modes are often ignored when characterizing the surface of a mirror in an optics system. However, these modes have the advantage of being intuitively recognizable due to their low order behavior, and were consequently chosen by the research team for this demonstration. In the testing that followed, as indicated earlier, an open-loop baseline signal (or bias) was subtracted from each Zernike coefficient prior to each closed-loop test (on the order of 1 to 10 microns for the tip, tilt, and defocus Zernike). However, given the nature of the test setup (where small thermal or other variation of the platform could slightly affect the beam path), it was not uncommon for a bias of approximately 0.3 to 0.4 microns to re-appear upon test completion in each of the tip, tilt, and defocus Zernike modes, and it is assumed that the control results presented also had to overcome these small biases as well.

The deformable mirror controller was run in two test configurations, indicated in Table 4.5. In the first configuration, the measurement of the defocus Zernike was the single output used to create an error signal. A sinusoidal command signal of 1.0 micron in amplitude at a 0.04 Hz frequency was input into the controller. The amplitude was statically obtainable by the mirror, and the frequency was well below both the dynamic modes of the mirror and the measurement update rate of 2.5 Hz. Then, the amplitude was increased to 2.0 microns, exceeding the mechanical limits of the mirror, to test the effectiveness of the anti-windup integrators.

Table 4.5: Test matrix.

Test	Commanded Zernike	Signal (meters)	Zernike polynomial
1a	Z_3, defocus	$1.0 \times 10^{-6} \sin{(2\pi 0.04t)}$	$\sqrt{3}(2r^2 - 1)$
1b	Z_3, defocus	$2.0 \times 10^{-6} \sin{(2\pi 0.04t)}$	$\sqrt{3}(2r^2 - 1)$
2	$\left\{ \begin{array}{c} Z_1,\ \text{tip} \\ Z_2,\ \text{tilt} \\ Z_3,\ \text{defocus} \end{array} \right\}$	$\left\{ \begin{array}{c} 0.6 \times 10^{-6} \sin{(2\pi 0.02t + \frac{\pi}{2})} \\ 0 \\ 1.0 \times 10^{-6} \sin{(2\pi 0.04t)} \end{array} \right\}$	$\left\{ \begin{array}{c} 2r\cos\theta \\ 2r\sin\theta \\ \sqrt{3}(2r^2 - 1) \end{array} \right\}$

In Test 2, three outputs of the mirror were tracked simultaneously. The chosen outputs were tip, tilt, and defocus. The tracking signal shown in Table 4.5 commanded

the tip Zernike at 0.02 Hz at 0.6 microns in amplitude and the focus Zernike at 0.04 Hz at 1.0 micron, while maintaining the tilt Zernike at 0 deflection.

The average absolute error for each test is presented in Table 4.6. The average absolute error was the absolute value of the command signal versus the measured coefficient taken pointwise at the sample rate, summed over the measurement period, and then divided by the total number of points. In Test 1b, the procedure was modified, such that when the command signal exceeded 1.0 micron (when the command was outside of the controllable space) the measurement was compared against a reference of 1.0 micron.

As a point of further clarification, the measurements in this section are of the Zernike coefficient, and are in meters. To obtain the total surface deflection, the measured Zernike coefficient must be multiplied by the non-dimensional Zernike polynomials in Table 4.5. The test results are now further discussed.

Table 4.6: Average absolute value of error signal.

Test	Zernike coefficient	Average error (meters)	Comments
1a	Z_3, defocus	0.16×10^{-6}	
1b	Z_3, defocus	0.31×10^{-6}	Note error for command outside of controllable space measured versus 1.0×10^{-6}
2	$\left\{ \begin{array}{c} Z_1,\ \text{tip} \\ Z_2,\ \text{tilt} \\ Z_3,\ \text{defocus} \end{array} \right\}$	$\left\{ \begin{array}{c} 0.14 \times 10^{-6} \\ 0.09 \times 10^{-6} \\ 0.18 \times 10^{-6} \end{array} \right\}$	

4.5.1 Single Zernike Measurement Tracking. The test results for the single measurement tracking are shown in Figure 4.12. The dashed line indicates the command input, the solid line is the closed-loop mirror response. For the first tracking test of the defocus Zernike, the signal is tracked with recognizable accuracy. However, the results show the existence of sharp, oscillatory behavior which may be attributed to two possible factors: One, system dynamics could be excited and aliased into the

measurements, or two, the measurement noise (amplified through the system gain) significantly affected the results. The behavior was present in all subsequent tests.
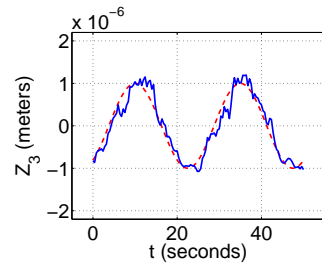
(a) Tracking defocus Zernike.
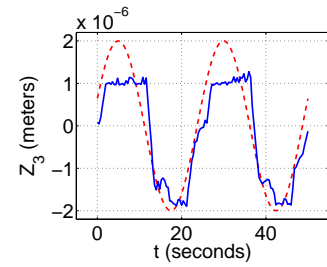
(b) Tracking defocus Zernike with amplitude in excess of controllable limit.

Figure 4.12: Experimental test 1 data.

Next, the amplitude of the commanded signal was increased to test the effectiveness of the anti-windup integrators. Clearly, the anti-windup integrators performed and did not allow a build of error to prevent signal tracking. However, the non-symmetric nature of response warrants a comment. The system responded with a maximum throw of plus one micron, yet a maximum negative deflection of 1.8 microns. This could be attributed to bias uncertainties in the beam path not removed prior to the closed-loop test, or attributed to material properties, and remains open for investigation. Another observation was the apparent lag in the response when deflections at the actuation limit were made. For this mirror construction, it is possible hysteretic effects may be present, attributable not only to the piezoelectric actuators but also due to the silicone substrate memory effects. System lags will need to be addressed for higher bandwidth applications.

4.5.2 Multiple Zernike Measurement Tracking. The results of the previous section demonstrated a single Zernike mode could be tracked, but no mention was made of the effect on the other optical modes. In the second test shown in Table 4.5, three Zernike modes were commanded and the tracking results are shown in Fig-

ure 4.13. Again, the dashed line indicates the command input, the solid line is the closed-loop mirror response.

(a) Tracking tilt Zernike.   (b) Tracking tip Zernike.   (c) Tracking defocus Zernike.
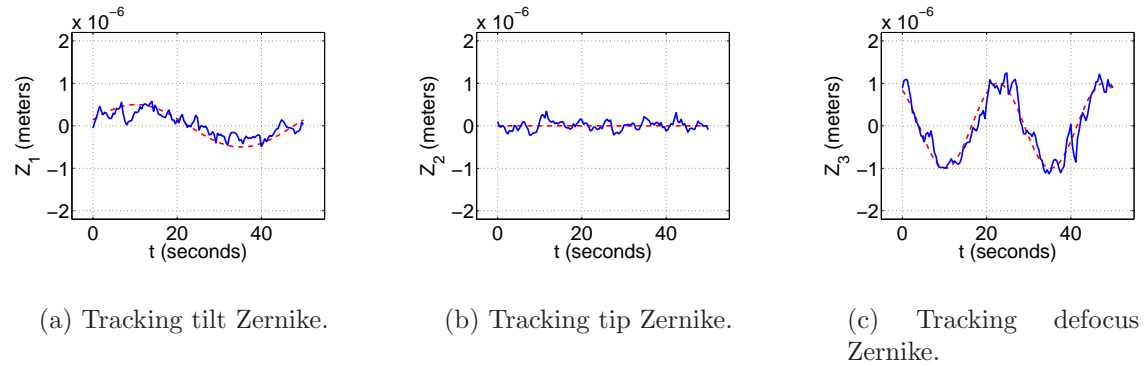
Figure 4.13:   Experimental test 2 data, recorded simultaneously.

Similar to the results presented in Section 4.5.1, the closed-loop system was able to maintain the three commanded signals with recognizable accuracy. Tracking of the tip and tilt Zernikes was far from error-free, but this difficulty can be partially attributed to the actuator layout (evidenced by the continuous center actuator). The far more important conclusion was that tracking tip and tilt did not appear to significantly detract from the tracking of the defocus Zernike.

Post-experiment analysis was conducted using the linear model derived from the finite element results (the $[A]$ matrix from Equation 4.15). Application of a pre-conditioning non-linear hysteresis model to the input voltages, and the addition of measurement noise to the Zernike outputs, were used in the simulation. The results were qualitatively similar to the experimental testing. Characterization of both the hysteresis and measurement is ongoing and will be reported separately. It is noted that system noise and non-linear effects such as hysteresis will govern the ultimate performance of the deformable mirror, especially higher frequency (non-quasi-static) applications.

4.6   Conclusions

The modelling and quasi-static closed-loop control of a 0.127 meter diameter, in-plane piezoelectric actuated deformable mirror was experimentally demonstrated. Modelling of the mirror was conducted using finite element modelling software. A static gain matrix was formed from the finite element results, and used as the basis for a quasi-static control system that employed proportional and integral control. Optical level, quasi-static control of this class of mirror was demonstrated by tracking both a single Zernike focus mode input, and by tracking multiple Zernike inputs tip, tilt, and defocus.

A prescriptive technique for modelling a tensioned deformable mirror with seven in-plane actuators actuators using available non-linear finite element modelling software was given. The method used dynamic data obtained with a laser vibrometer to characterize the tension in the membrane, and an equivalent edge loading was prescribed. For future applications, it is assumed this tensile edge loading would be recorded as part of the manufacturing process, and the dynamic testing would not be required. The geometric stiffness of the finite element model was updated using the edge loading and a non-linear solver.

The piezoelectric actuators were statically actuated, and the surface deflection of the deformable mirror was measured with a Shack-Hartmann wavefront sensor. The deflections were provided by a summation of 42 Zernike polynomials within the interior 60% of the mirror's radius, the *clear aperture*, as provided by the wavefront sensor software. For the experimental data, deflections were taken from a bias precondition due to the slight roughness of the mirror's surface. Deflections from baseline were on the scale of 1 micron, and agreed both in scale and general shape with the finite element model results.

A least squares fit of the finite element model deflection was used to form the central element of a multiple input/multiple output quasi-static control algorithm. The algorithm used the least squares static gain matrix to operate on an error sig-

99

nal of up to three Zernike coefficients at a rate well below the fundamental dynamic frequency of the mirror. Higher rates and number of data signals could not be supported with the experimental set up, but are not theoretically limited. Proportional and integral control were used. To preclude overwhelming the controller for errors beyond the achievable limits, anti-windup integrators and saturation limits were implemented. Additionally, the feedback signal was filtered on the input side to prevent exciting mirror dynamic modes (which could not be directly measured).

Both single Zernike tracking and multiple Zernike tracking were experimentally demonstrated. The Zernike modes chosen for the demonstration were tip, tilt and defocus. It was recognized these modes are generally not controlled by a deformable mirror, but the low spatial order of the modes made for a better demonstration given the mirror's relatively low number of actuators.

The defocus Zernike coefficient, Z_3, was commanded with a 1.0 micron in amplitude, 0.04 Hz in frequency. It was tracked with an average accuracy of 0.16 microns. When the amplitude of the command was doubled to a level beyond the actuation limits of the test article, the accuracy degraded to 0.31 microns, which was recognizable as a system lag following full scale deflection.

For the multiple Zernike tracking case, the defocus was again commanded at the 0.04 Hz rate and at an amplitude of 1.0 micron. Furthermore, the tilt mode, Z_1, was commanded with a 0.6 microns at half the rate (0.02 Hz) of the defocus signal, and the tip mode, Z_2, was commanded to zero deflection. The control system tracked the tip, tilt, and defocus modes with absolute average errors of 0.14, 0.09, and 0.18 microns respectively. When the error in tracking the defocus Zernike was compared to the single input, single output tracking case, the error increased by a slight 0.02 microns, indicating that increasing the dimension of the control system did not significantly degrade its performance.

The finite element models developed for this work were determined to adequately model the static structural response of the in-plane actuated mirror. The models

will be used for the remainder of this work as a structural truth source as further experimental demonstrations are not practical.

The success of this experimental demonstration highlights the promise of unimorph in-plane actuation for the control of deformable mirrors for the first time. In-plane actuation, with its intrinsic weight saving benefits of being self-contained without the need for a backing structure, combined with the system implementation advantages such as no bias requirement, ease of modelling, and demonstrated performance capability, make it a leading choice for incorporation into the future generation of membrane mirrors for space-borne telescope requiring precision shape control.

With a finite element model established as a truth source, we may turn our attention in the next chapter to focus on simpler analytical solution methods to the static actuation problem.

V. Analytical Influence Functions

Chapter objectives:

- *Develop analytical linear piecewise solution for in-plane actuated beam-string and plate-membrane*
- *Develop low-order approximate solution*

5.1   Introduction

In this chapter, we explore the behavior of the tensioned deformable mirror. This configuration typically exhibits both plate-like and membrane-like behavior. Proposed is a new approximation method for the solution to this class of mirror, where the normalized plate stiffness to tension ratio is small. The approximation function is based on the exact analytical solution to this class of problems. The approximation method allows the problem to be reduced to a simple pressure forced membrane equation, a geometry which may be more readily analyzed. A case study comparing the results of the approximation method to a high fidelity finite element model constructed in MSC.Nastran is provided.

5.2   The Search for a Low-Order Model

As previously stated, the choice of a deformable mirror stiffened by membrane tension and forced by piezoelectric in-plane bimorph or unimorph actuators may be a desirable configuration for membrane optics. Compared to a conventional mirror where discrete actuators are attached to a rigid backing structure and operate directly against the mirror's non-reflecting face, the in-plane actuated mirror may be lighter in weight, capable of remote actuation [82, 95], and potentially resolve higher spatial frequencies for a given number of actuators–all distinct advantages for space-borne

operations. However, much of the recent research regarding membrane mirrors has dealt with the modelling of electrostatically actuated mirrors, which are variations on the conventional scheme [29, 43, 91, 130].

Formulating a low-order, approximate, influence function would have distinct advantages for uncovering the analytical relationships and in reducing computational cost when compared to high-order, high-fidelity analytical and finite element model solutions. Thus a low-order method is sought both to increase the efficiency of model-based control algorithms, and to allow rapid parametric studies.

5.2.1 Background. Steinhaus and Lipson [133], and later Burke and Hubbard [68], recognized the usefulness of in-plane actuation for an optical structure, noting the inherent advantages of moment actuation and the theoretically achievable high spatial frequency. However, their analysis concentrated on the rigid (non-tensioned) deformable mirror. Analyzing a similar geometry, Lee et al [76] calculated influence functions for each actuator as an individual phenomena where each actuated area was mathematically treated as a separate domain with clamped boundary conditions, and fitted with an Euler-Bernoulli beam model with a correction factor. Martin et al [86, 87] modelled non-tensioned mirrors as well, but introduced the significant enabling technology of a non-contact electron gun to control the voltage applied to the piezoelectric actuators.

The in-plane actuated tensioned plate-membrane mirror proposed herein for space-borne applications has been rigorously modelled by Rogers and Agnes [118]. However, the methods proposed were limited to axisymmetric circular structures, mathematically complex, and lack some of the characteristics seen in the experimental and analytical work of Chapter IV. An important feature of the work was the recognition that the ratio of plate stiffness to membrane stiffness was a primary consideration for achievable shape control.

5.2.2 Governing Differential Equation. For this chapter, we limit our discussion to the one-dimensional beam-string and axisymmetric plate-membrane.

The beam-string (a clamped beam simultaneously under an axial load) is an important analytical tool, and is discussed in part because it helps to clarify procedures used in the study of the plate-membrane. Because of its analytical importance, it is emphasized here.

However, it is the circular plate-membrane that is our geometry of interest for in-plane actuated deformable mirror research. Analogous to the beam-string, the plate-membrane is a plate with a clamped boundary under uniform tension. In this chapter, the discussion is limited to a plate-membrane of circular axisymmetric construction, however the requirement will be relaxed for the forcing function as shown in Section 5.4.1, for cases where $d_{31} \neq d_{32}$.

The governing equation for the in-plane actuated structure as developed in Chapter III may be expressed as:

$$D\nabla^4 w - N\nabla^2 w = -M\nabla^2 H, \tag{5.1}$$

where the variables are defined in Tables 5.1 and 5.2. Note that an axisymmetric condition is assumed for the piezoelectric forcing, and the magnitude of the piezoelectric force M is separate from the function H which indicates the region of electrode coverage. Also note that a thermal analogy could be constructed by replacing $d_{31}V$ with $c^{(\alpha)}Tt_p$.

The indicator function, $H(\vec{x})$, for a surface electrode of area S is:

$$H(\vec{x}) = \begin{cases} 1, & \vec{x} \in \mathsf{S}, \\ 0, & \text{else.} \end{cases} \tag{5.2}$$

The dependent variable in place of $\vec{x}$ for the beam-string is x and the Laplacian operator is $\nabla^2 = \frac{\partial^2}{\partial x^2}$, while for the plate-membrane the dependent variable is r

104

and the Laplacian operator is $\nabla^2 = \frac{\partial^2}{\partial r^2} + \frac{1}{r}\frac{\partial}{\partial r} + \frac{1}{r^2}\frac{\partial^2}{\partial \theta^2}$ (under the assumption of axisymmetry, the θ dependence is removed, and $\nabla^2 = \frac{\partial^2}{\partial r^2} + \frac{1}{r}\frac{\partial}{\partial r}$).

Table 5.1:   Governing differential equation (Equation 5.1) explanation of terms.

Parameter	Beam-String	Units	Plate-Membrane	Units
D	EI	FL^2	$\frac{Eh^3}{12(1-\nu^2)}$	FL
N	P	F	N	FL^{-1}
M	$-\frac{Ed_{31}Vbt_s}{2}$	FL	$-\frac{Ed_{31}Vt_s}{2(1-\nu)}$	F

Table 5.2:   Nomenclature for governing differential equation.

Parameter	Description	Units
E	Young's Modulus	FL^{-2}
ν	Poisson's ratio	none
I	moment of inertia $\frac{bh^3}{12}$	L^4
h	total height	L
b	beam width	L
t_s	thickness of substrate	L
t_p	thickness of surface actuating layer	L
P	axial force	F
N	tension	FL^{-1}
$c^{(\alpha)}$	coefficient of thermal expansion	$(^o)^{-1}$
T	temperature (change)	$(^o)$
d_{31}	piezoelectric constant	LV^{-1}
V	applied voltage	V
R	(overall length or radius)	L

Equation 5.1 may have the dependent variable scaled by the length of the domain (length of beam or radius, R, thus define $\tilde{r} = \frac{r}{R}$), and dividing by the tension leaves us with:

$$\varepsilon^2 \nabla^4 w - \nabla^2 w = -\frac{M}{N}\nabla^2 H, \qquad (5.3)$$

where the normalized plate stiffness to tension ratio is $\varepsilon^2 = DN^{-1}R^{-2}$.

The indicator function may represent an active piezoelectric actuator covering a normalized interior region of $\tilde{r} \leq \alpha$. This function would have the form:

$$H(\tilde{r}) = \begin{cases} 1, & \tilde{r} \leq \alpha, \\ 0, & \text{otherwise.} \end{cases} \tag{5.4}$$

With the addition of the appropriate boundary conditions, the problem may now be solved. In the next section, the exact solution for this class of problem is presented.

5.3 Exact Analytic Linear Solutions when Forced by In-plane Actuators

5.3.1 *Beam String.* Given the deflection of a beam-string $w(x)$ governed by the equation:

$$\varepsilon^2 w^{iv}(x) - w''(x) = 0, \qquad\qquad 0 \leq x \leq 1 \tag{5.5}$$

with boundary conditions for a piezoelectric region between interior points α and β:

$$w(0) = w'(0) = w(1) = w'(1) = 0, \tag{5.6}$$

$$w(\alpha^-) = w(\alpha^+), \tag{5.7}$$

$$w'(\alpha^-) = w'(\alpha^+) \tag{5.8}$$

$$w(\beta^-) = w(\beta^+) \tag{5.9}$$

$$w'(\beta^-) = w'(\beta^+) \tag{5.10}$$

$$w''(\alpha^+) = w''(\beta^-) = \frac{-1}{2\varepsilon^2}\frac{M}{N} \qquad\qquad \alpha < \beta, \tag{5.11}$$

$$w''(\alpha^-) = w''(\beta^+) = \frac{1}{2\varepsilon^2}\frac{M}{N} \qquad\qquad \alpha < \beta, \tag{5.12}$$

where the prime superscript indicates the derivative with respect to x.

106

Pause for a moment to explain the inspiration behind the applied boundary conditions. Lee [72] derives the conditions where a piezoelectric forcing, introduced in Equation 5.1, may be transformed into a line load, comprised of line moments (such as in this case), and line forces. Note that the line moment applied to a structure is actually a bending couple at the center of which is an inflection point in the curvature of the structure [52, pg. 374]. Thus, the internal boundary conditions are nothing more than the opposite curvatures, which in the one-dimensional case are simply sign changes in the second derivative.

To provide some further insight, one may look at the equation for curvature, in its simplest form for an Euler-Bernoulli beam as

$$w''(x) = \frac{M(x)}{EI}. \tag{5.13}$$

The line moment is an instantaneous change in moment at a point α of magnitude M, creating a jump discontinuity. To create a set of internal boundary conditions, impose the condition that half of the strength of the moment is applied in opposite directions on either side of the internal boundary. This is represented as:

$$\frac{1}{2}M = EI \lim_{x \to \alpha^-} w''(x), \tag{5.14}$$

$$-\frac{1}{2}M = EI \lim_{x \to \alpha^+} w''(x). \tag{5.15}$$

Dividing both equations above by the tension N and recognizing $\varepsilon^2 = \frac{EI}{N}$ results in:

$$\frac{1}{2}\frac{M}{N} = \varepsilon^2 \lim_{x \to \alpha^-} w''(x), \tag{5.16}$$

$$-\frac{1}{2}\frac{M}{N} = \varepsilon^2 \lim_{x \to \alpha^+} w''(x). \tag{5.17}$$

Finally, to arrive at the boundary conditions in Equations 5.11 and 5.12 divide through by ε^2 to yield:

$$\frac{1}{2\varepsilon^2}\frac{M}{N} = \lim_{x \to \alpha^-} w''(x), \tag{5.18}$$

$$-\frac{1}{2\varepsilon^2}\frac{M}{N} = \lim_{x \to \alpha^+} w''(x). \tag{5.19}$$

With the boundary conditions now explained, it is time to turn one's attention to solving the problem. Begin by recognizing the exact solution to the differential equation, Equation 5.5, is:

$$w(x) = c_0 x + c_1 + c_2 e^{x/\varepsilon} + c_3 e^{-x/\varepsilon}. \tag{5.20}$$

A single linear solution will not exist, as there are 12 boundary conditions and the order of the equation is four. However, 4 of the conditions occur on internal boundaries. Thus, to solve the equation exactly, break the domain into three parts, which are called the left (L) $(x < \alpha)$, center (C) $(\alpha \le x \le \beta)$, and right (R) $(x > \beta)$. Begin by solving for the region, $w^{(C)}$ in the interior of the forced region, where $\alpha \le x \le \beta$, by making the substitution, $w^{(C)\,\prime\prime}(x) = v(x)$, to yield the homogenous differential equation for the curvature of the interior of the structure:

$$\varepsilon^2 v''(x) - v(x) = 0, \qquad\qquad \alpha \le x \le \beta \tag{5.21}$$

$$v(\alpha) = v(\beta) = -1. \tag{5.22}$$

This homogenous equation is solved by the combination of sinh functions:

$$v(x) = \frac{\sinh(\frac{x-\alpha}{\varepsilon}) - \sinh(\frac{x-\beta}{\varepsilon})}{\sinh(\frac{\alpha-\beta}{\varepsilon})}. \tag{5.23}$$

108

If one integrates the solution in Equation 5.23 twice, the general interior solution is offered:

$$w^{(C)}(x) = a_0 + a_1 x + \varepsilon^2 v(x). \tag{5.24}$$

Turning our attention to the area, $x < \alpha$, the solution to Equation 5.5 in this region is offered as $w^{(L)}(x)$:

$$w^{(L)}(x) = b_0 + b_1 x + b_2 \sinh \frac{x}{\varepsilon} + b_3 \cosh \frac{x}{\varepsilon}. \tag{5.25}$$

The boundary conditions for the left edge remain clamped, that is $w^{(L)}(0) = w^{(L)\prime}(0) = 0$.

Similarly, the solution proposed in the region $x > \beta$ as $w^{(R)}(x)$ is:

$$w^{(R)}(x) = c_0 + c_1(1 - x) + c_2 \sinh \frac{1 - x}{\varepsilon} + c_3 \cosh \frac{1 - x}{\varepsilon}, \tag{5.26}$$

again with clamped boundary conditions, $w^{(R)}(1) = w^{(R)\prime}(1) = 0$.

Imposing continuity of displacement and slope between the inner and outer solutions, and applying the given boundary conditions allows us to solve the system of 10 equations with 10 unknowns. For completeness, the boundary conditions are:

$$w^{(L)}(0) = w^{(L)\prime}(0) = 0, \tag{5.27}$$

$$w^{(R)}(1) = w^{(R)\prime}(1) = 0, \tag{5.28}$$

$$w^{(L)}(\alpha) = w^{(C)}(\alpha), \tag{5.29}$$

$$w^{(L)\prime}(\alpha) = w^{(C)\prime}(\alpha), \tag{5.30}$$

$$w^{(L)\prime\prime}(\alpha) = 1, \tag{5.31}$$

$$w^{(R)}(\beta) = w^{(C)}(\beta), \tag{5.32}$$

$$w^{(R)\prime}(\beta) = w^{(C)\prime}(\beta), \tag{5.33}$$

$$w^{(R)\prime\prime}(\beta) = 1. \tag{5.34}$$

The resulting system of equations is therefore:

$$b_0 + b_3 \qquad =0, \qquad (5.35)$$

$$b_1 + \frac{1}{\varepsilon}b_2 \qquad =0, \qquad (5.36)$$

$$c_0 + c_3 \qquad =0, \qquad (5.37)$$

$$-c_1 - \frac{1}{\varepsilon}c_2 \qquad =0, \qquad (5.38)$$

$$-a_0 - a_1\alpha + b_0 + b_1\alpha + b_2 \sinh\frac{\alpha}{\varepsilon} + b_3 \cosh\frac{\alpha}{\varepsilon} \qquad =-\varepsilon^2, \qquad (5.39)$$

$$-a_1 + b_1 + \frac{b_2}{\varepsilon} \cosh\frac{\alpha}{\varepsilon} + \frac{b_3}{\varepsilon} \sinh\frac{\alpha}{\varepsilon} \qquad =\varepsilon K_\alpha, \qquad (5.40)$$

$$b_2 \sinh\frac{\alpha}{\varepsilon} + b_3 \cosh\frac{\alpha}{\varepsilon} \qquad =\varepsilon^2, \qquad (5.41)$$

$$-a_0 - a_1\beta + c_0 + c_1(1-\beta) + c_2 \sinh\frac{1-\beta}{\varepsilon} + c_3 \cosh\frac{1-\beta}{\varepsilon} \qquad =-\varepsilon^2, \qquad (5.42)$$

$$-a_1 - c_1 - \frac{c_2}{\varepsilon} \cosh\frac{1-\beta}{\varepsilon} - \frac{c_3}{\varepsilon} \sinh\frac{1-\beta}{\varepsilon} \qquad =\varepsilon K_\beta, \qquad (5.43)$$

$$c_2 \sinh\frac{1-\beta}{\varepsilon} + c_3 \cosh\frac{1-\beta}{\varepsilon} \qquad =\varepsilon^2. \qquad (5.44)$$

where K_α and K_β are defined as:

$$K_\alpha \equiv \frac{1}{\sinh\frac{\alpha-\beta}{\varepsilon}} - \frac{1}{\tanh\frac{\alpha-\beta}{\varepsilon}} \qquad (5.45)$$

$$K_\beta \equiv \frac{-1}{\sinh\frac{\alpha-\beta}{\varepsilon}} + \frac{1}{\tanh\frac{\alpha-\beta}{\varepsilon}}. \qquad (5.46)$$

Further note $K_\alpha = -K_\beta$.

To solve algebraically, define the matrix M such that

$$M \equiv \begin{bmatrix}
0 & 0 & 1 & 0 & 0 & 1 & 0 & 0 & 0 & 0 \\
0 & 0 & 0 & 1 & \frac{1}{\varepsilon} & 0 & 0 & 0 & 0 & 0 \\
0 & 0 & 0 & 0 & 0 & 0 & 1 & 1 & 0 & 0 \\
0 & 0 & 0 & 0 & 0 & 0 & 0 & -1 & -\frac{1}{\varepsilon} & 0 \\
-1 & -\alpha & 1 & \alpha & s\alpha & c\alpha & 0 & 0 & 0 & 0 \\
0 & -1 & 0 & 1 & \frac{1}{\varepsilon}c\alpha & \frac{1}{\varepsilon}s\alpha & 0 & 0 & 0 & 0 \\
0 & 0 & 0 & 0 & s\alpha & c\alpha & 0 & 0 & 0 & 0 \\
-1 & -\beta & 0 & 0 & 0 & 0 & 1 & (1-\beta) & s\beta & c\beta \\
0 & -1 & 0 & 0 & 0 & 0 & 0 & -1 & -\frac{1}{\varepsilon}c\beta & -\frac{1}{\varepsilon}s\beta \\
0 & 0 & 0 & 0 & 0 & 0 & 0 & 0 & s\beta & c\beta
\end{bmatrix} \tag{5.47}$$

where

$$c\alpha = \cosh\frac{\alpha}{\varepsilon} \qquad\qquad s\alpha = \sinh\frac{\alpha}{\varepsilon}, \tag{5.48}$$

$$c\beta = \cosh\frac{1-\beta}{\varepsilon} \qquad\qquad s\beta = \sinh\frac{1-\beta}{\varepsilon}. \tag{5.49}$$

Next, define x and f as

$$x = \begin{Bmatrix} a_0 \\ a_1 \\ b_0 \\ b_1 \\ b_2 \\ b_3 \\ c_0 \\ c_1 \\ c_2 \\ c_3 \end{Bmatrix} \qquad f = \begin{Bmatrix} 0 \\ 0 \\ 0 \\ 0 \\ -\varepsilon^2 \\ \varepsilon K_\alpha \\ \varepsilon^2 \\ -\varepsilon^2 \\ \varepsilon K_\beta \\ \varepsilon^2 \end{Bmatrix} \qquad (5.50)$$

The system of equation is solved when $x = M^{-1}f$. It may be observed in Equation 5.49 that M becomes ill-conditioned as ε decreases. When solving the system algebraically, the solution is intractable in a purely symbolic form and provides little insight. However, when working with numerical values, a sample of the solutions obtained are presented in Figure 5.1.

5.3.2 Plate-membrane. A derivation of the axisymmetric (no angular terms) plate membrane may be set up in a similar manner. For this problem, assume a plate membrane of radius 1 with a piezoelectric actuator acting radially over a radius $\alpha < 1$.

Given:

$$\varepsilon^2 \nabla^4 w(r) - \nabla^2 w(r) = 0, \qquad\qquad 0 \le r \le 1 \qquad (5.51)$$

(a) $\varepsilon = 0.002, \alpha = 0.3, \beta = 0.7$

(b) $\varepsilon = 0.02, \alpha = 0.3, \beta = 0.7$

(c) $\varepsilon = 0.2, \alpha = 0.3, \beta = 0.7$

(d) $\varepsilon = 0.02, \alpha = 0.05, \beta = 0.5$
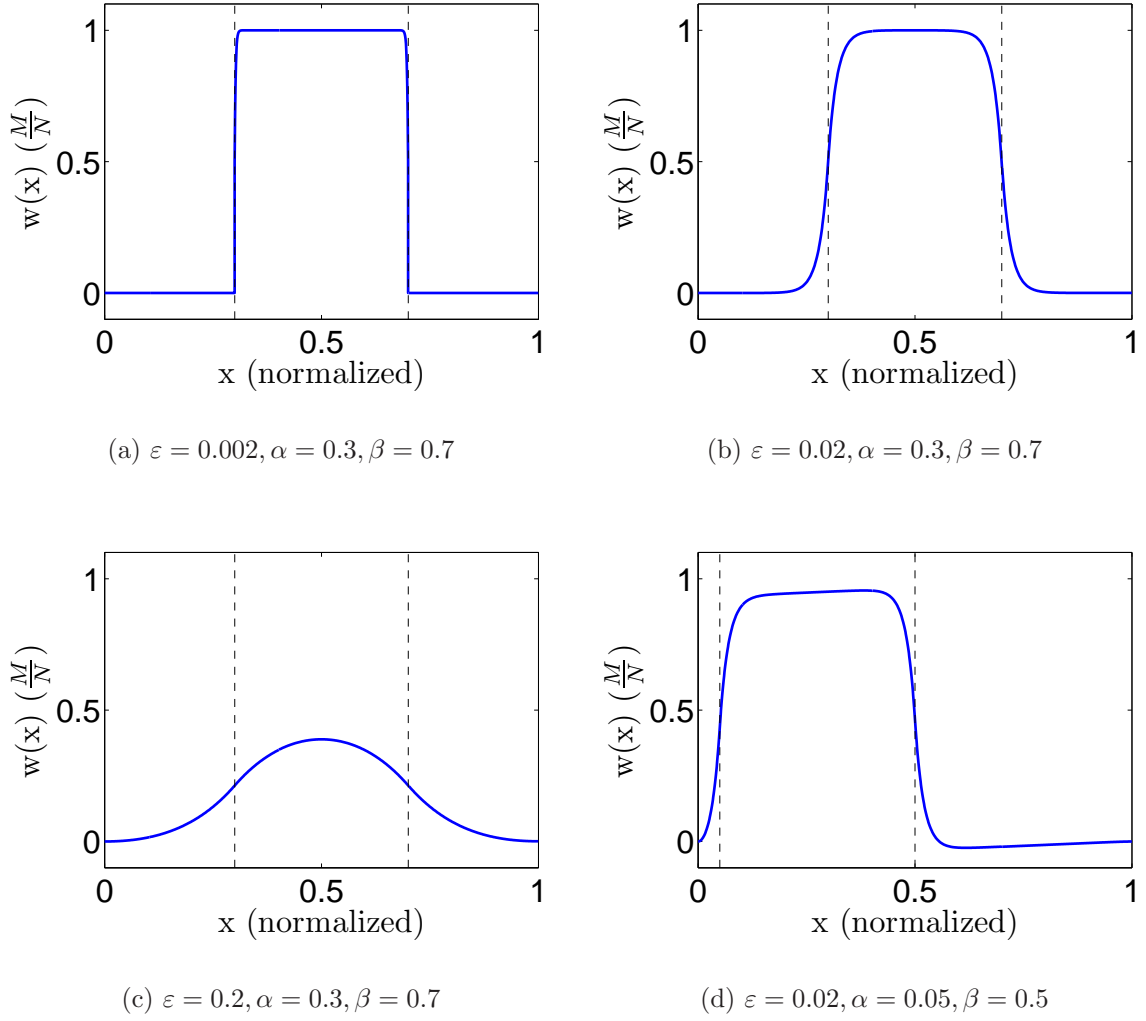
Figure 5.1:   Examples of beam-string solution for varying values of ε.

with boundary conditions for a piezoelectric region within a region of radius α:

$$w'(0) = 0 \text{ displacement is thus bounded,} \tag{5.52}$$

$$Q(0) = 0 \text{ shear force,} \tag{5.53}$$

$$w(1) = w'(1) = 0, \text{ clamped edge,} \tag{5.54}$$

$$\nabla^2 w(\alpha^+) = 1, w''(\alpha^-) = -1, \tag{5.55}$$

where the axisymmetric Laplacian operator is the familiar, $\nabla^2 = \frac{\partial^2}{\partial r^2} + \frac{1}{r}\frac{\partial}{\partial r}$.
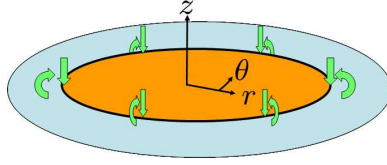
Figure 5.2:   Plate (or plate-membrane) forced by piezoelectric-actuator.

Again, the choice of boundary conditions is important. As the piezoelectric forcing to the plate problem $f(r)$ enters through the Laplacian operator acting on a indicator function, $H(r)$:

$$f(r) = M\nabla^2 H(r - \alpha) = M\big(\delta'(r - \alpha) + \frac{1}{r}\delta(r - \alpha)\big). \tag{5.56}$$

Thus, the forcing looks like a line moment (δ' term) and a line force (δ term), as indicated in Figure 5.2. Note that line forces and moments indicated by the green arrows in the figure are shown acting in the negative direction.

To represent the line moment, once again choose opposite curvatures at the boundary. However, the line force is another matter. At the internal boundary, the line force may be thought of as acting a slope condition[1]. Thus, on the interior of the piezoelectric actuated region one has both the contribution from the curvature term, and the corresponding term from the Laplacian of the line force. However, on the exterior of the region, the contribution of the line force is lost, and the term remaining is simply the line moment curvature of opposite sign. Also note the condition is already scaled to a unit curvature on the boundary, as done in Section 5.3.1.

The exact solution to the differential equation, Equation 5.51 is:

$$w(r) = c_0 + c_1 \log r + c_2 I_0(\frac{r}{\varepsilon}) + c_3 K_0(\frac{r}{\varepsilon}), \tag{5.57}$$

---

[1]If the unit dipole for the moment is integrated, it is a unit impulse–the line force. Integrating the curvature in a similar manner yields slope. Symbolically, represent this as $w'' \sim \delta'$. Then integration yields relationship $w' \sim \delta$.

114
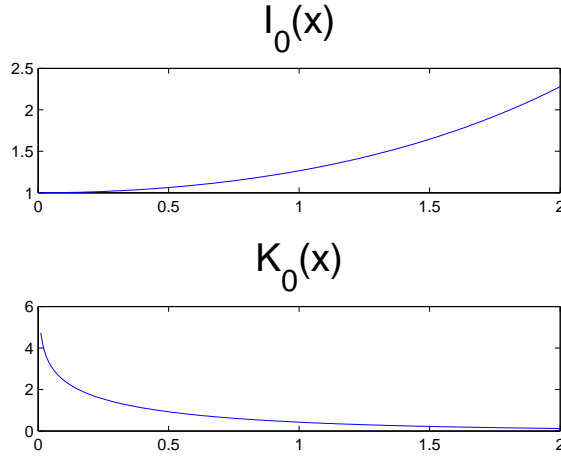
Figure 5.3:   Modified Bessel functions of the first and second kind.

but cannot account for all the boundary conditions. I_0 and K_0 are modified Bessel functions.

Again, Take a moment to refresh ourselves with some properties of the modified Bessel functions by viewing the graphs in Figure 5.3.[2]

Similar to the beam problem, a composite solution to account for the boundary conditions is sought. Again form piecewise solutions, one the inner (left) solution, and one the outer (right) solution. For the inner solution (interior to the piezoelectric actuated region) where $r < \alpha$, $w^{(L)}(r)$ is :

---

[2]Also note the properties for modified Bessel functions:

$$I_i' = I_{i-1} - \frac{i}{r}I_i \qquad\qquad = I_{i+1} + \frac{i}{r}I_i \qquad (5.58)$$

$$K_i' = -K_{i-1} - \frac{i}{r}I_i \qquad\qquad = -K_{i+1} + \frac{i}{r}I_i \qquad (5.59)$$

and

$$\lim_{x\to 0} I_0(x) = 1 \qquad\qquad \lim_{x\to\infty} I_0(x) = \infty,$$

$$\lim_{x\to 0} I_1(x) = 0 \qquad\qquad \lim_{x\to\infty} I_1(x) = \infty,$$

$$\lim_{x\to 0} K_0(x) = \infty \qquad\qquad \lim_{x\to\infty} K_0(x) = 0,$$

$$\lim_{x\to 0} K_1(x) = \infty \qquad\qquad \lim_{x\to\infty} K_1(x) = 0.$$

$$w^{(L)}(r) = b_0 + b_1 \log\left(\frac{r}{\varepsilon}\right) + b_2 I_0\left(\frac{r}{\varepsilon}\right) + b_3 K_0\left(\frac{r}{\varepsilon}\right). \tag{5.60}$$

Apply the boundary conditions at the center ("left") edge of the domain. Given the unbounded behavior of logarithmic and K_0 terms, take special care to account for the selection of these terms' coefficients. It is not correct to simply set these terms' coefficients equal to zero.

The asymptotic expansion for $K_0(x)$ as x approaches 0 may be expressed as a sum of singular and regular components:

$$\lim_{x \to 0} K_0(x) \sim K_0^{(S)} + K_0^{(R)}, \tag{5.61}$$

where

$$K_0^{(S)} = (-1)_0 \tilde{F}_1\left(; 1; \frac{x^2}{4}\right) \log\left(\frac{x}{2}\right) \tag{5.62}$$

$$K_0^{(R)} = \frac{1}{2} \sum_{k=0}^{\infty} \frac{2\psi(k+1) + 1}{k!^2} \left(\frac{x}{2}\right)^{2k}. \tag{5.63}$$

where $_0\tilde{F}_1$ is the *regularized hypergeometric function* and ψ is the *digamma function*.[3]

---

[3]The regularized hypergeometric function and digamma function are readily found in a reference manual such as the text edited by Abramowitz and Stegun [2], but many software packages, such as *Matlab* and *Mathematica* have built in functions to calculate these values. For the case presented with no first argument, the regularized hypergeometric function is termed the confluent hypergeometric limit function defined as

$$_0\tilde{F}_1(; a, x) = \lim_{q \to \infty} {}_0\tilde{F}_1(q; a, \frac{x}{q}).$$

For the values required in this section, the following is provided:

$$_0\tilde{F}_1\left(; 1; 0\right) = 1.0,$$
$$\psi(1.0) \approx -0.577216, \text{Euler-Mascheroni Constant [148]}$$
$$\psi(2.0) \approx 0.422784.$$

The leading order asymptotic behavior of the K_0 term is

$$K_0(x) \approx \left(-\log\left(\frac{x}{2}\right) + \frac{1}{2}\{2\psi(1) + 1\}\right) \tag{5.64}$$

$$\approx \left(-\log x + 0.115932\right) \tag{5.65}$$

Applying the boundary condition of zero slope at the center, we require the $K_0^{(S)}(r)$ term in Equation 5.61 to balance the logarithmic term as $r \to 0$, and thus choose $b_1 = b_3$. Rewriting Equation 5.61 with this substitution:

$$w^{(L)}(r) = b_0 + b_1 \log\left(\frac{r}{\varepsilon}\right) + b_2 I_0\left(\frac{r}{\varepsilon}\right) + b_1 K_0\left(\frac{r}{\varepsilon}\right). \tag{5.66}$$

The zero shear boundary condition at the center is our next source of information. The shear force, $Q(r)$ for an axisymmetric plate may be written as [94]:

$$Q(r) = \left(\frac{\partial}{\partial r} + \frac{1}{r}\right) M(r) \tag{5.67}$$

Also, the moment equation for an axisymmetric plate is given by:

$$M(r) = -\varepsilon^2 \left(\frac{\partial^2}{\partial^2 r} + \frac{\nu}{r}\frac{\partial}{\partial r}\right) w^{(L)}(r) \tag{5.68}$$

where ν is the non-dimensional Poisson's ratio.

Immediately recognize that if the shear is to vanish at the center ($r = 0$), the regular portion of the slope of the K_0 function must be annihilated by the slope of another regular function. Writing the two term expansions for K_0 and I_0 (again as $r \to 0$) the asymptotic behavior of the functions are:

$$K_0(r) \sim \psi(1.0) + \psi(2.0)\frac{r^2}{4} + O(r^4),$$

$$I_0(r) \sim 1 + \frac{r^2}{4} + O(r^4) \tag{5.69}$$

where $O(r^4)$ represents the fourth order error due to truncation of the series. Taking the first derivative eliminates the first term of each series above. Matching the next term in the expansions leads us to the conclusion:

$$b_2 = -\psi(2)b_1 \tag{5.70}$$

Our boundary conditions at the center have therefore allowed us to finally write Equation 5.60 as:

$$w^{(L)}(r) = b_0 + b_1[\log\left(\frac{r}{\varepsilon}\right) - \psi(2)I_0\left(\frac{r}{\varepsilon}\right) + K_0\left(\frac{r}{\varepsilon}\right)], \tag{5.71}$$

where the digamma function $\psi(2) \approx 0.422784$.

For the outer region $r > \alpha$ (exterior to the piezoelectric actuator) the solution in the following form is proposed:

$$w^{(R)}(r) = c_0 + c_1 \log r + c_2 I_0\left(\frac{r}{\varepsilon}\right) + c_3 K_0\left(\frac{r}{\varepsilon}\right), \tag{5.72}$$

with clamped edge conditions, $w^{(R)}(1) = w^{(R)\prime}(1) = 0$.

Again, imposing continuity of displacement and slope, solve the resulting system of equations. Thus equipped, write the algebraic system of equations. We have six equations with six unknowns $(b_0, b_1, c_0, c_1, c_2, c_3)$.

Clamped edge displacement equation:

$$c_0 + c_2 I_0\left(\frac{1}{\varepsilon}\right) + c_3 K_0\left(\frac{1}{\varepsilon}\right) = 0. \tag{5.73}$$

Clamped edge slope equation:

$$c_1 + c_2 \frac{1}{\varepsilon} I_1 \left(\frac{1}{\varepsilon}\right) - c_3 \frac{1}{\varepsilon} K_1 \left(\frac{1}{\varepsilon}\right) = 0. \tag{5.74}$$

Continuity of displacement at α:

$$b_0 + b_1 [\log \left(\frac{\alpha}{\varepsilon}\right) - \psi(2) I_0 \left(\frac{\alpha}{\varepsilon}\right) + K_0 \left(\frac{\alpha}{\varepsilon}\right)] + \ldots$$
$$- c_0 - c_1 \log \alpha - c_2 I_0 \left(\frac{\alpha}{\varepsilon}\right) - c_3 K_0 \left(\frac{\alpha}{\varepsilon}\right) = 0. \tag{5.75}$$

Continuity of slope at α:

$$b_1 [\frac{1}{\alpha} - \frac{\psi(2)}{\varepsilon} I_1 \left(\frac{\alpha}{\varepsilon}\right) - \frac{1}{\varepsilon} K_1 \left(\frac{\alpha}{\varepsilon}\right)] + \ldots$$
$$- c_1 \frac{1}{\alpha} - c_2 \frac{1}{\varepsilon} I_1 \left(\frac{\alpha}{\varepsilon}\right) + c_3 \frac{1}{\varepsilon} K_1 \left(\frac{\alpha}{\varepsilon}\right) = 0. \tag{5.76}$$

Internal boundary condition for inner solution at α:

$$\frac{b_1}{\varepsilon^2} [-\psi(2) I_0 \left(\frac{\alpha}{\varepsilon}\right) + K_0 \left(\frac{\alpha}{\varepsilon}\right)] = 1. \tag{5.77}$$

Internal boundary condition for outer solution at α:

$$c_1 \frac{-1}{\alpha^2} + c_2 \frac{1}{\varepsilon^2} [I_0 \left(\frac{\alpha}{\varepsilon}\right) - \frac{\varepsilon}{\alpha} I_1 \left(\frac{\alpha}{\varepsilon}\right)] + \ldots$$
$$c_3 \frac{1}{\varepsilon^2} [K_0 \left(\frac{\alpha}{\varepsilon}\right) + \frac{\varepsilon}{\alpha} K_1 \left(\frac{\alpha}{\varepsilon}\right)] = -1. \tag{5.78}$$

By applying the above boundary conditions, the problem may be again be solved as a system of linear equations. Again the system of equations is ill-conditioned for very small values of ε. Intuitively this is expected, for a system with insignificant plate stiffness would simply solve as the pure membrane linear solution, and would like just

like the input voltage function. Realistically, this also shows that plate thickness cannot vanish for a solution to exist. Furthermore, non-linear terms not present in our formulation would become important. These effect of these terms are investigated in Chapter VII.

An graph for the case $\varepsilon = 0.02$ is displayed in Figure 5.4. In the figure[4], the analytical solution of this section is compared to the approximate solution of Section 5.4.
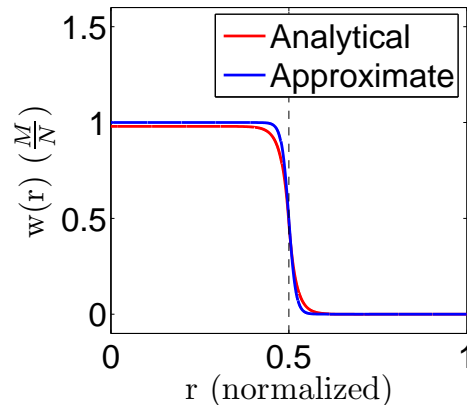
Figure 5.4:   Circular plate-membrane solution of displacement versus radius.

One may observe the solution yields an nearly constant response away from the location of the actuator edge at α, and a distinct boundary region in the location of α.

To get an axisymmetric ring solution for an actuator covering the area $\alpha \leq r \leq \beta$, the sum of a solution with radius β with the negative of a solution with radius α may be used to approximate the solution for cases where the boundary layers do not intersect to a appreciable amount. Otherwise, linear supposition does not hold and

---

[4]The value of $\varepsilon = 0.02$ is similar to a test configuration from the literature [118]. That is, for radius $R = 0.15m$, thickness $h = 150$ microns, $E = 4 \times 10^9 \frac{N}{m^2}$, $\nu = 0.3$ and $N = 143\frac{N}{M}$ when normalized to unit radius (see Chapter VII for more information on length scales) yields:

$$\varepsilon = \sqrt{\frac{D}{NR^2}} = \sqrt{\frac{4 \times 10^9 (152 \times 10^{-6})^3}{12(1 - 0.3^2)} \frac{1}{(143)(0.15)^2}} = 0.02$$

the solution may be re-derived in a similar fashion with another set of corresponding internal boundary conditions.

5.4 Approximate Solution Using Modified Pressure Distribution

Two important observations are made in regards to the solutions in the previous section.

One is the exact solutions to Equation 5.1 give little insight into the nature of the solution due to the highly complicated coefficients that arise when solving the requisite system of equations. An approximation method which uses more readily interpreted functions and solution strategies would be welcomed.

The second observation is that the linear solutions result in a deformed surface with very nearly step-like function behavior, together with relatively narrow boundary areas. Recognizing this step function behavior allows us to formulate an approximate behavior for actuators spaced at distances outside of the boundary region, but will force us to re-evaluate the optical performance of the tensioned in-plane actuated structures.

In developing the approximation, the discussion is limited to the domain of interest (for the circular mirror). For the approximation, an alternate method where the plate-like effects are modelled into the forcing function, reducing Equation 5.1 into a simple membrane acted on by pressure forces. For a sufficiently small value of normalized plate stiffness to tension ratio, $\varepsilon \ll 1$, one can replace the fourth-order differential operator with the simpler Laplacian operator, and transfer the corresponding plate effects to the continuous pressure forcing function defined here as:

$$\hat{H}(\tilde{r}) \equiv \frac{1}{2}\left\{1 - \tanh \frac{\tilde{r} - \alpha}{\varepsilon}\right\}. \tag{5.79}$$

Our approximate system is then:

$$-\nabla^2 \hat{w} = \frac{M}{N} \nabla^2 \hat{H} \tag{5.80}$$

The value for ε is again the same value from the non-dimensionalized differential equation, Equation 5.3. The tanh function is chosen because it has a boundary region of the same scale as the solutions in Section 5.3.2, and because when used in $\hat{H}$ above, Equation 5.3 approaches the behavior of Equation 5.80 as $\varepsilon \to 0$.

5.4.1 Green's Function.   One characteristic of piezoelectric material is that due to the method of construction, the expansion coefficient for one primary direction may be many times greater than the coefficient for the direction perpendicular to the primary direction. For this discussion, limit the non-isotropic behavior to the case where the expansion coefficients in the in-plane orthogonal (defined as the Cartesian x and y) directions are not equal. This is commonly annotated as $d_{31} \neq d_{32}$.

The forcing moment magnitude term for the axisymmetric membrane of Equation 5.1 may considered a rank one tensor:

$$M_i = \frac{E d_{3i} V t_s}{2(1 - \nu)} \qquad i = 1, 2. \tag{5.81}$$

with variables as defined in Table 5.2. Choosing a convenient value of V, this term may be represented in non-dimensionalized form as $\hat{M}_i$ such that for $\hat{M}_1 = \hat{M}_2 = N$ when isotropic, and $\frac{\hat{M}_2}{\delta} = \hat{M}_1 = N$ when non-isotropic, and $\hat{M}_1 > \hat{M}_2$.

To model this case, the moment forcing function is written in Cartesian coordinates (x and y) as suggested in Chapter III and further expanded upon in Appendix C. Equation 5.80 may now be written as:

$$-\nabla^2 w = \frac{\partial^2}{\partial x^2} \hat{H} + \delta \frac{\partial^2}{\partial y^2} \hat{H} \tag{5.82}$$

where delta is formally defined as

$$\delta \equiv \frac{d_{32}}{d_{31}} \tag{5.83}$$

Now, writing the operators $\frac{\partial^2}{\partial x^2}$ and $\frac{\partial^2}{\partial y^2}$ in polar coordinates (with no angular dependence in $\hat{H}$ all derivatives with respect to θ are eliminated):

$$\frac{\partial^2}{\partial x^2} = \cos^2 \theta \frac{\partial^2}{\partial r^2} + \frac{\sin^2 \theta}{r} \frac{\partial}{\partial r} \tag{5.84}$$

$$\frac{\partial^2}{\partial y^2} = \sin^2 \theta \frac{\partial^2}{\partial r^2} + \frac{\cos^2 \theta}{r} \frac{\partial}{\partial r}. \tag{5.85}$$

For the case of a fixed boundary on a circular domain, the Green's function for $\nabla^2 w = -\Phi$ is found in an engineering handbook: [111]

$$G(r, \theta, \xi, \eta) = \frac{1}{4\pi} \ln \frac{r^2 \xi^2 - 2R^2 r\xi \cos(\theta - \eta) + R^4}{R^2 (r^2 - 2r\xi \cos(\theta - \eta) + \xi^2)} \tag{5.86}$$

resulting in the statically deflected surface:

$$w(r, \theta) = \int_0^{2\pi} \int_0^R \Phi(\xi, \eta) G(r, \theta, \xi, \eta) \xi d\xi d\eta , \tag{5.87}$$

where ξ and η are arbitrary variables of integration.

5.5   Case Study: Approximate versus Finite Element Model

To demonstrate the method, the proposed approximate modelling technique is compared to a high-fidelity finite element model of a hypothetical in-plane actuated deformable mirror. The finite element model was chosen as a truth source over the solution in the Section 5.3.2 to provide a non-biased third party solution strategy, and was developed based on the model first presented in Chapter IV. A further advantage is that the finite element model incorporates non-linear effects.

5.5.1   Mirror Characteristics.   The notional mirror utilizes a two-ply laminate of similar physical characteristics, with the only difference being that one layer is piezoelectrically inert. The other layer is active and has a corresponding coefficient

of piezoelectric expansion. The mirror is constrained by a rigid, clamped, circular boundary. Only a portion of the active layer is used, simulating a centered circular electrode with a radius 0.083 meters, covering the inner $5/9^{ths}$ of the overall radius. The normalized plate stiffness to tension ration results in a value of $\varepsilon = 0.02$, and the remaining material properties and dimensions are presented in Table 5.3. A drawing (not to scale) of the structure is shown in Figure 5.5.

(a) Top view.　　　　　　　　　　　　　(b) Bottom view.
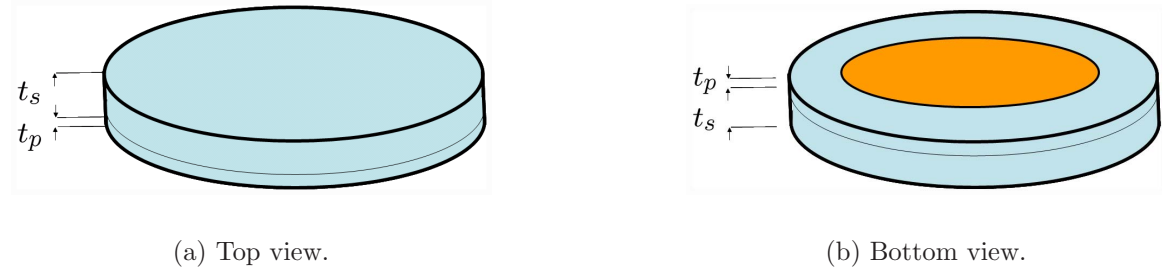
Figure 5.5:　Construction showing inert (blue) and active (orange) regions.

Table 5.3:　Notional mirror physical properties.

Property	Value	Units
E	4.0×10^9	N/m^2
ν	0.3	
d_{31}	-2.3×10^{-11}	m/V
d_{32} (isotropic)	-2.3×10^{-11}	m/V
d_{32} (non-isotropic)	-0.3×10^{-11}	m/V
V	192.4	V
N	1.262×10^2	N/m
t_s	100×10^{-6}	m
t_p	52×10^{-6}	m
α	0.083	m
R	0.15	m
M	1.262×10^{-3}	N
M/N	1.00×10^{-5}	m

5.5.2　Finite Element Model.　For a truth source, a non-linear finite element model was constructed using MSC.Nastran. The non-linear solution strategy was chosen for two reasons. The first was that tension added to the boundary of the plate model would only stiffen the structure if a non-linear solution was used. Second, any significant non-linear effects would show in the solution.

The piezoelectric actuation was modelled as an equivalent thermal load as previously detailed in Chapter IV. In summary, the domain of the mirror was meshed

using 100 radial divisions and 72 angular divisions comprising 7201 nodes, and the model was built with 7128 CQUAD4 elements and 72 CRIA3 composite plate elements. The PCOMP card was used to enter the element properties for the inert and active layers, and displacements were measured from the top surface (not neutral axis), as would be done with a physical system. An isotropic model with $d_{31} = d_{32}$ and a non-isotropic model with $d_{31} = \frac{d_{32}}{\delta}$ where $\delta \approx 0.13$ were created, with the d_{31} coefficient aligned with the x-axis.

5.5.3 Observations.   The observations in this section may be broken into two parts. In the first, the validity of the approximate modelling technique is discussed. In the second, the actuation method for an optical system itself is discussed in light of the demonstrated performance. The results are shown in Figure 5.6. Error was reported in percentage terms using the discrete Euclidean norm (see Appendix A). Plots a-c represent the isotropic piezoelectric forcing, and plots d-f represent non-isotropic forcing where the coefficient of expansion in the x-direction is approximately 7 times greater than the y-direction. The thin black line in all plots represents the radius of the interior active region.

The overall ability of the approximate function to accurately represent the solution to the problem as posed was satisfactory. The model achieved a high level of agreement in terms of surface error, with modelling of the boundary layer remaining the area of least agreement, as indicated in Figures 5.6 (c) and (f). The error (calculated using the discrete Euclidean method of Appendix A) in the isotropic configuration was 4.07×10^{-7} meters and for the non-isotropic configuration was 7.22×10^{-7} meters.

It is worthwhile to note that while most of the error is attributed to the approximation method of Section 5.4 not matching the exact linear solution of Section 5.3.2, the non-linear terms not modelled in the linear governing equation result in locally large strains at the boundary of the actuator, and are another source of error when comparing against the non-linear finite element model. Also, note that the finite el-

125

(a) Analytic isotropic approximation.

(b) Nonlinear isotropic finite element model.

(c) Absolute error comparison for isotropic models.

(d) Analytic non-isotropic approximation.

(e) Nonlinear non-isotropic finite element model.

(f) Absolute error comparison for non-isotropic models.
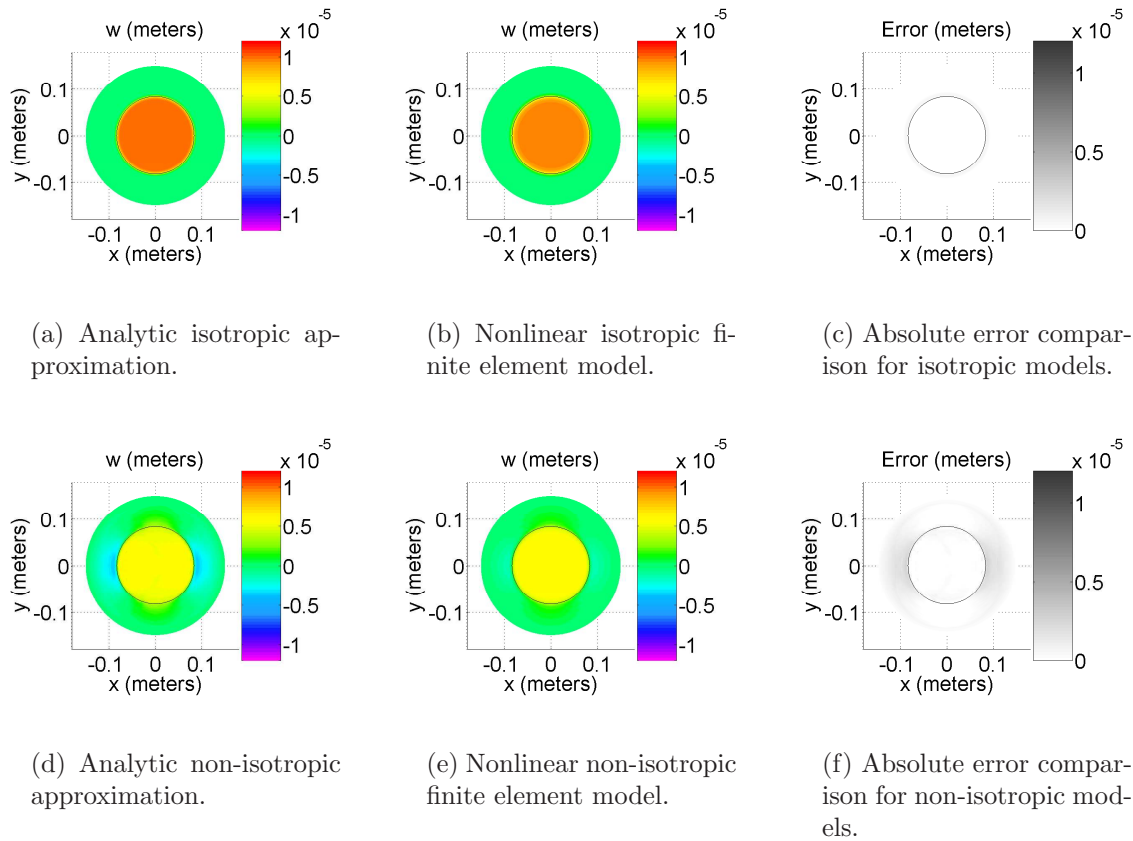
Figure 5.6:   Comparison of numerical and approximate solutions.

126

ement solution is highly dependent on mesh size at the border of the elements. In the narrow boundary layer, only a fraction of the total elements undergo appreciable deformation; a non-constant adaptive meshing program should yield an incrementally more accurate basis for comparison, but regardless, should not appreciably change the results as shown.

Despite the small error in the boundary layer, another important observation is made. For use in an optical system, this case study and the supporting solutions to the general differential equation call attention to the potential difficulty in using this actuation method for an optical system, as described below.

While this method may be able to predict actuated shapes with a small surface error for mirrors with widely spaced actuating regions (such as the electrode pattern in Figure 4.2), the resulting optical reflector would be challenging to use as an optical surface, due to the fact that the surface pattern would be a series of piston regions. In fact, for optical systems, one may be more interested in slope control of the surface to reflect an incident wave, than to tightly control the surface deformation regardless of its impact on the slope.

5.6   Conclusions

This chapter presented the exact analytical piecewise linear solution to the beam-string and plate-membrane problem characterized by a structure which is in-plane actuated, tensioned, and where the normalized stiffness to tension ratio is small. To obtain an analytical solution to this class of problem, the piezoelectric forcing was transformed from a forcing function to an internal boundary condition. The algebraic system of equations was found to be near-singular as stiffness to tension ratio vanished, further demonstrating the importance of the thickness term in the solution.

Then, a new approximation method for modelling influence functions was presented. A single case study was presented where a non-linear finite element model simulation was compared against the approximation method for an axisymmetric cir-

cular mirror with an interior actuator radius of 0.083 meters versus an overall radius of 0.15 meters.

The results were satisfactory. The maximum difference between the two solutions, while small, occurred in a boundary layer at the edge of actuated region, which was attributed to inherent error in the approximation function, non-linearities, and the chosen mesh of the finite element model.

A significant finding of this work was that if the proposed deformable mirror, with discrete, widely-spaced, actuators is used in an optical system, the results show difficulties remain in creating a surface which achieves not only a shape error tolerance, but a slope error tolerance as well, due to a solution constructed of primarily pistoning regions.

In the next chapter, a control methodology is introduced coined the Modal Transformation Method which allows for the implementation specific Zernike mode shapes upon a membrane mirror surface. Armed with the knowledge of the effect discontinuous actuators have on the membrane mirror surface deformation, an actuation grid for the second case study of the next chapter will be used that is finer than the boundary region due to the tension-to-plate stiffness parameter as seen in this chapter.

VI. The Modal Transformation Method

> *Chapter objectives:*
>
> - *Highlight incompatibility of Zernike mode with fixed edge membrane mirror*
> - *Develop matrix-based Modal Transformation Method*
> - *Present finite-element simulations demonstrating methodology*

6.1   Introduction

Active lightweight continuous mirrors, such as deformable membrane mirrors, provide the capability to form conjugate surfaces effective for removing atmospheric distortions of an incoming wavefront. For a circular aperture, the two-dimensional surface corrections are most often described by a truncated set of the Zernike polynomial basis functions. Simultaneously, there exists a requirement in active lightweight membrane mirrors to resist the effects of vibration disturbances which could build at resonance and adversely distort the membrane surface. The spatial content of this motion is typically described by a finite set of Bessel-function based vibration modes below a frequency of interest. To control the vibration modes, it is advantageous to actuate these same shapes for the purpose of attenuation. Perfect surface control would therefore have authority to command both Zernike and vibration mode shapes.

The *Modal Transformation Method* presented herein provide a simple algebraic transformation unique to this class of problem. A significant advantage these techniques is that it addresses the problem of the incompatible edge condition between the Zernike polynomial basis set and the fixed edge condition of the membrane mirror

by introducing a definitive term for the usable region of the membrane mirror, which as introduced in Chapter II is referred to as the *clear aperture.*

6.2 Background

Active quasi-static shape control of circular apertures to produce Zernike polynomial surfaces has been explored by several researchers. A complete review of the Zernike polynomials follows, but for now it suffices to say that Zernike polynomials will always have some displacement at their boundary, while the tensioned membrane structures envisioned in this application are characterized by a fixed, non-displacing, boundary.

Wang and Hadaegh [146] presented the problem of surface control for a circular deformable mirror in terms of the orthogonal basis set, and provide an example where as a circular membrane mirror is controlled by electrostatic actuators to form the axisymmetric Zernike shapes. However, the methods are limited to those shapes where the boundary condition may be imposed, but do provide a methodology for actuating a surface in modal coordinates.

Forming Zernike shapes on electrostatic membrane mirrors (mirrors that are forced by electrostatic attraction between electrode pairs on the mirror and a backing plate) has long relied on iterative techniques, fittings, and calibration curves. Claflin and Bareket [32] published the basic least squares fitting technique in 1986. Tokovinin, Thomas and Vdovin [136] presented the experimental results of a 50-mm 79 actuator electrostatic membrane mirror, where only the interior 35-mm "pupil" was actuated. The solution methodology of using numerical solutions to Poisson's equation (the governing equation for membrane structures) with an unused "transition zone" between the measured interior area and the fixed membrane boundary show the difficulty of using membrane mirrors to make Zernike shapes.

Flint and Denoyer showed the feasibility of using in-plane actuators mirrors to produce Zernike polynomial mode shapes, again on some interior region of a circular

membrane [45]. Their results showed the promise of the mirror type, but were tempered by difficulties in computing influence functions due to numerical instabilities. Another observation of Flint and Denoyer's was that the Zernike mode shapes were best observed when the interior 80-90 percent of the circular aperture was used for Zernike formation.

The purpose of this development is to cast the surface control problem to one in which desired surface shape, expressed in terms of Zernike polynomials, inside of a region defined as the *clear aperture*, can be achieved by the use of statically actuated vibration mode shapes (the Bessel-based functions that satisfy the fixed edge condition). The terminology "clear aperture" was used in a figure in a 1977 work by Pearson and Hansen [106] to describe an area on a deformable mirror where data was taken, and thus is similar to our purpose. A notional mirror is displayed in Figure 6.1 which shows a Zernike tilt surface deflection achieved inside of a clear aperture region, which highlights the incompatibility between the Zernike surface within the clear aperture, and the fixed boundary of the membrane mirror.
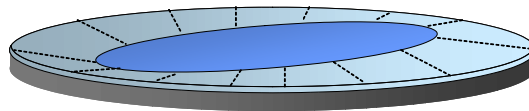
Figure 6.1:   Notional mirror with surface tilt achieved inside "clear aperture."

To achieve static surface control, an analytical formulation designated the *Modal Transformation Method* is developed. A brief outline of the technical development in the chapter is summarized here:

- Section 6.3 reviews the two commonly-used basis sets to describe a circular aperture. The Zernike polynomial basis set is favored by the optics community, while the Bessel-based vibration mode set is applied to physical solutions of the partial differential equation modelling a tensioned membrane. The fundamental premise of the modal transformation method is casting the problem of obtaining

Zernike polynomials using a linear combination of statically-actuated Bessel-function based vibration modes.

- Section 6.4 develops the transformation matrices for the radial behavior of the Zernike polynomials and approximated vibration modes in terms of an intermediary radial polynomial basis. The vibration modes must be approximated due to the infinite series representation of the Bessel functions, thus convergence and associated truncation error for a maximum radial polynomial degree is investigated.

- Section 6.5 outlines the modal transformation method. The method is inspired by the projection theorem and an existing analytical relationship between the Zernike polynomials and the Bessel functions. The transformation matrices of Section 6.4 are combined, and scaled to allow for increased accuracy inside of an interior, clear aperture region. Numeric issues with the transformation matrices are explored.

To show the significance of the methodology, the results are applied to a deformable membrane mirror modelled with finite elements in MSC.Nastran that utilizes piezoelectric in-plane actuation to create changes in surface curvature. Advantages in ease of numerical computation of actuator gains, combined with theoretical a priori knowledge of expected error are shown. Specifically, surface error is shown to be a function of design criterion such as mirror diameter, fineness of actuation grid, and diameter of the clear aperture region, and order of the Zernike mode achieved.

6.3   *Basis Sets for Circular Apertures*

Deformable membrane mirrors are employed to form conjugate surfaces to remove atmospheric distortions in an incoming wavefront. These conjugate surfaces are formed on the mirror surface through a combination of influence functions by energizing a particular actuator grid. For a flat circular aperture, the two-dimensional surface corrections are most often provided in the form of a scaled, truncated set of

the Zernike polynomial basis functions. Simultaneously, there exists a requirement in lightweight membrane mirrors to actively resist the dynamic effect which could build at resonance and adversely distort the membrane surface, modelled as a finite set of Bessel-function based vibration modes below a frequency of interest. Any influence functions formed on by membrane mirror would be comprised of this Bessel-function based vibration mode set. However, Zernike modes and vibration modes fundamentally differ in that a Zernike mode always has a vertical displacement at the edge, while the vibration mode does not displace vertically from the mirror frame. Pictorial representations for Zernike and vibration modes are provided in Tables 6.1 and 6.2 respectively.

Table 6.1:   Zernike mode shapes.

$n\backslash^{m^*}$	0	1	2	3	4
0	piston				
1		tilt			
2	defocus		astigmatism		
3		coma			
4	spherical				

[*] The radial degree, or degree of the radial polynomial, is n. The azimuthal frequency of the angular dependence is m .

Table 6.2: Vibration mode shapes with normalized natural frequency. ω_{mn}

$n \backslash m$	0	1	2	3	4
1	2.4048	3.8317	5.1356	6.3802	7.5883
2	5.5201	7.0156	8.4172	9.7610	11.0647
3	8.6537	10.1735	11.6198	13.0152	14.3725
4	11.7915	13.3237	14.7960	16.2235	17.6160

Inspired by the understanding of the pictorial representation of the two basis functions, this section begins with a discussion of the mathematical properties and notation associated with the Zernike polynomial, and a matrix representation of the Zernike polynomials is derived. The vibration modes are then reviewed for a circular membrane, and an analogous transformation matrix is created, with the primary difference being that the matrix was formed from an infinite series representation. Next, a direct Zernike to vibration mode transformation is created, both in integral form and then using radial coordinates. Definition of a clear aperture region–an interior region on a circular aperture where Zernike mode shapes will be formed–is then proposed and a series of examples follow.

6.3.1 Definition of the Zernike Polynomial. The optics community has used the modified set of Zernike polynomials, as first defined by Noll [97], to describe aberrations in an incoming wavefront. The Zernike polynomials, Z_i, are orthogonal over the interior of the domain of circular aperture of unit radius through the relationship

$$\int_0^{2\pi} \int_0^1 \frac{1}{\pi} Z_i Z_j r \, dr \, d\theta = \delta_{ij} \tag{6.1}$$

where δ_{ij} is the Kronecker delta. The polynomials, Z_i, are defined as:

$$\left.\begin{aligned} Z_{evenj} &= A_n^m R_n^m \cos m\theta, \\ Z_{oddj} &= A_n^m R_n^m \sin m\theta, \end{aligned}\right\} \qquad m \neq 0, \tag{6.2}$$

$$Z_j = A_n^m R_n^m \qquad , \qquad m = 0. \tag{6.3}$$

with A_n^m is the normalization constant and R_n^m is the radial polynomial for azimuthal frequency m and radial degree n. The radial polynomial, R_n^m is defined as

$$R_n^m(r) = \sum_{s=0}^{(n-m)/2} \frac{(-1)^s (n-s)!}{s!(m-s)!(n-m-s)!} r^{n-2s} \tag{6.4}$$

where the values of the azimuthal frequency, m, are less than or equal to the radial degree, n, $(m \leq n)$ and $n - m$ is even. The radial polynomials are presented in Table 6.3 [97].

The normalization constants, A_n^m, are defined to maintain the orthonormal relationship with respect to the weighted function in Equation 6.1:

$$A_n^m = \sqrt{2(n+1)}, \qquad m \neq 0, \tag{6.5}$$

$$A_n^m = \sqrt{(n+1)}, \qquad m = 0. \tag{6.6}$$

The normalization constants are the coefficients of the terms in Table 6.4. The Zernike polynomials may be alternately referred to as Zernike mode shapes, recognizing that for the purpose of this document the Zernike mode shapes represent desired surface deflections.

Table 6.3:   Radial polynomials R_n^m.

$n \backslash m$	0	1	2	3	4	5
0	1					
1		r				
2	$2r^2 - 1$		r^2			
3		$3r^3 - 2r$		r^3		
4	$6r^4 - 6r^2 + 1$		$4r^4 - 3r^2$		r^4	
5		$10r^5 - 12r^3 + 3r$		$5r^5 - 4r^3$		r^5
6	$20r^6 - 30r^4 + 12r^2 - 1$		$15r^6 - 20r^4 + 6r^2$		$6r^6 - 5r^4$	
7		$35r^7 - 60r^5 + 30r^3 - 4r$		$21r^7 - 30r^5 + 10r^3$		$7r^7 - 6r^5$
8	$70r^8 - 140r^6 + 90r^4 - 20r^2 + 1$		$56r^8 - 105r^6 + 60r^4 - 10r^2$		$28r^8 - 42r^6 + 15r^4$	
9		$126^9 - 280r^7 + 210r^5 - 60^3 + 5r$		$84r^9 - 168r^7 + 105r^5 - 20r^3$		$36r^9 - 56r^7 + 21r^5$

Table 6.4:   Zernike polynomials using Noll's ordering [97] where R_n^m are defined as in Table 6.3.

$n \backslash m$	0	1	2	3	4
0	$Z_1 = R_0^0$ Piston				
1		$Z_2 = 2R_1^1 \cos\theta$ $Z_3 = 2R_1^1 \sin\theta$ Tilt			
2	$Z_4 = \sqrt{3}R_2^0$ Defocus		$Z_5 = \sqrt{6}R_2^2 \sin 2\theta$ $Z_6 = \sqrt{6}R_2^2 \cos 2\theta$ Astigmatism		
3		$Z_7 = \sqrt{8}R_3^1 \sin\theta$ $Z_8 = \sqrt{8}R_3^1 \cos\theta$ Coma		$Z_9 = \sqrt{8}R_3^3 \sin 3\theta$ $Z_{10} = \sqrt{8}R_3^3 \cos 3\theta$	
4	$Z_{11} = \sqrt{5}R_4^0$ Spherical		$Z_{12} = \sqrt{10}R_4^2 \cos 2\theta$ $Z_{13} = \sqrt{10}R_4^2 \sin 2\theta$		$Z_{14} = \sqrt{10}R_4^4 \cos 4\theta$ $Z_{15} = \sqrt{10}R_4^4 \sin 4\theta$
5		$Z_{16} = \sqrt{12}R_5^1 \cos\theta$ $Z_{17} = \sqrt{12}R_5^1 \sin\theta$		$Z_{18} = \sqrt{12}R_5^3 \cos 3\theta$ $Z_{19} = \sqrt{12}R_5^3 \sin 3\theta$	

6.3.2   Definition of Vibration Modes.   While the Zernike mode shapes represent the commanded desired static shapes we wish the circular aperture to obtain, the dynamic motion of the circular membrane is governed by vibration mode shapes. The vibration mode shapes represent the eigenfunctions associated with the natural modes of the system. The vibration mode shapes of the uniform circular membrane of radius ($0 \leq r \leq R$), edge tension T, mass density per surface area ρ, and edge (boundary) condition $w(R, \theta, t) = 0$ may be found by solving the partial differential equation

$$T\nabla^2 w(r, \theta, t) - \rho \ddot{w}(r, \theta, t) = 0 \qquad (6.7)$$

136

through separation of variables where the separation constant $\lambda = \omega^2$ such that the spatial mode equation is

$$\nabla^2 W(r, \theta) + \beta^2 W(r, \theta) = 0, \qquad \beta = \frac{\rho \omega^2}{T}. \tag{6.8}$$

Using separation of variables technique to simplify the partial differential equation for the case of a pinned boundary $(W(R, \theta) = 0)$, the static mode shapes are obtained. The derivation may be found in a structural dynamics textbook, such as the text by Meirovitch [88]. The mode shapes are

$$W_n^m(r, \theta)_C = B_n^m J_m(\beta_{mn} r) \cos m\theta, \qquad \text{m, n} = 1, 2, \dots \tag{6.9}$$

$$W_n^m(r, \theta)_S = B_n^m J_m(\beta_{mn} r) \sin m\theta, \qquad \text{m, n} = 1, 2, \dots \tag{6.10}$$

$$W_n^0(r, \theta) = B_n^0 J_0(\beta_{0n} r), \qquad \text{n} = 1, 2, \dots \tag{6.11}$$

where

$$B_n^m = \frac{\sqrt{2}}{\sqrt{\pi \rho} R(J_{m+1}(\beta_{mn} R))}, \qquad \text{m} = 1, 2, \dots \tag{6.12}$$

$$B_n^m = \frac{1}{\sqrt{\pi \rho} R(J_1(\beta_{mn} R))}, \qquad \text{m} = 0. \tag{6.13}$$

The indices m and n represent the azimuthal frequency and radial frequency respectively. The radial frequency is actually the nth zero of the associated m^{th} order Bessel function, and may be thought of as the number of times the Bessel function crosses the radial axis between the center of the membrane and the boundary[1]. The vibration modes of the circular membrane are orthogonal through the relationship

$$\int_0^{2\pi} \int_0^R \rho W_n^m {}_I W_q^p {}_J r \, dr \, d\theta = \delta_{IJ} \delta_{mp} \delta_{nq}. \tag{6.14}$$

---

[1]The vibration mode shape always satisfies the boundary condition of zero displacement at the boundary through the condition $J_m(\beta_{mn} R) = 0$.

6.4 Matrix Representations of Modal Transformation

The purpose of this section is to formulate a matrix representation of the radial Zernike polynomial and vibration mode basis sets (note the azimuthal, or angular, behavior is identical for both basis sets). To do that, the radial behavior of each basis set is cast in terms of an intermediary polynomial basis. Since the Bessel function component of the vibration modes consists of an infinite series in the intermediary basis, the resulting modes are therefore an approximation to the vibration modes, subject to truncation error.

6.4.1 Zernike Transformation Matrix for a given Azimuthal Frequency.

Equation 6.3 terms $A_m^n R_m^n$ may be written in a summation form where the coefficients are as given in Table 6.3. For a given azimuthal frequency m, the summation will have the form[2]. where each row represents the maximum radial degree of the polynomial:

$$
\begin{aligned}
A_n^m R_n^m &= \sum_{k=0}^{N} (a_{2k}^{(m,n)}) r^{2k} r^m, \\
&= (a_0^{(m,n)} + a_2^{(m,n)} r^2 + \ldots + a_N^{(m,n)} r^{n-m}) r^m, \\
&= \begin{Bmatrix} a_0^{(m,n)} \\ a_2^{(m,n)} \\ \vdots \\ a_N^{(m,n)} \end{Bmatrix}^T \begin{Bmatrix} 1 \\ r^2 \\ \vdots \\ r^{2N} \end{Bmatrix} r^m.
\end{aligned} \tag{6.15}
$$

---

[2]It is emphasized that throughout this chapter in no case will a repeated subscript indicate summation

Furthermore, write a series of equations for a given azimuthal frequency m that encompass all radial degrees from m to a maximum degree of n such that

$$
\begin{Bmatrix} A_m^m R_m^m \\ A_m^{m+2} R_m^{m+2} \\ \vdots \\ A_m^{m+2N} R_m^{m+2N} \end{Bmatrix} = \begin{bmatrix} a_0^{(m,m)} & & & \\ a_0^{(m,m+2)} & a_2^{(m,m+2)} & & \\ & \vdots & \ddots & \\ a_0^{(m,m+2N)} & a_2^{(m,m+2N)} & & a_{2N}^{(m,m+2N)} \end{bmatrix} \begin{Bmatrix} 1 \\ r^2 \\ \vdots \\ r^{2N} \end{Bmatrix} r^m \qquad (6.16)
$$

The Zernike transformation matrix $\boldsymbol{A}_N^m$ may therefore be defined as the lower diagonal transformation matrix of size $N + 1 \times N + 1$ for an azimuthal frequency m with a maximum polynomial degree $2N + m$ from above. $\boldsymbol{A}_N^m$ is here defined as:

$$
\boldsymbol{A}_N^m \equiv \begin{bmatrix} a_0^{(m,m)} & & & \\ a_0^{(m,m+2)} & a_2^{(m,m+2)} & & \\ & \vdots & \ddots & \\ a_0^{(m,m+2N)} & a_2^{(m,m+2N)} & & a_{2N}^{(m,m+2N)} \end{bmatrix} .
$$

6.4.2   Vibration Mode Transformation Matrix for a given Azimuthal Frequency.
It is our desire to expand the vibration mode shapes from Section 6.3.2. To accomplish this, a vibration mode transformation matrix is created for a given azimuthal frequency, m.

To obtain our transformation matrix, begin by writing the series representation of the Bessel functions in terms of bookkeeping coefficients $\alpha_{2k}^{(m,n)}$:

139

$$J_m(\beta_{mn}r) = (\tfrac{1}{2}\beta_{mn}r)^m \sum_{k=0}^{\infty} \frac{(-1)^k(\tfrac{1}{2}\beta_{mn}r)^{2k}}{(k+m)!k!}, \tag{6.17}$$

$$= \sum_{k=0}^{\infty} \alpha_{2k}^{(m,n)} r^{2k+m}, \tag{6.18}$$

$$= \left(\alpha_0^{(m,n)} + \alpha_2^{(m,n)}r^2 + \ldots\right)r^m, \tag{6.19}$$

$$= \begin{bmatrix} \alpha_0^{(m,n)} & \alpha_2^{(m,n)} & \ldots \end{bmatrix} \begin{Bmatrix} 1 \\ r^2 \\ \vdots \end{Bmatrix} r^m. \tag{6.20}$$

Next, apply the vibration mode shape normalization coefficients from Equations 6.12 and 6.13 such that $b_{2k}^{(m,n)} = B_n^m \alpha_{2k}^{(m,n)}$, to arrive at

$$B_n^m J_m(\beta_{mn}r) = \sum_{k=0}^{\infty} (b_{2k}^{(m,n)}) r^{2k} r^m,$$

$$= \begin{bmatrix} b_0^{(m,n)} & b_2^{(m,n)} & \ldots \end{bmatrix} \begin{Bmatrix} 1 \\ r^2 \\ \vdots \end{Bmatrix} r^m. \tag{6.21}$$

Next, to write a transformation matrix analogous to Equation 6.17 for a given azimuthal frequency m, construct a series of equations from Equation 6.21 such that

$$\begin{Bmatrix} B_1^m J_m(\beta_{m1}r) \\ B_2^m J_m(\beta_{m2}r) \\ \vdots \end{Bmatrix} = \begin{bmatrix} b_0^{(m,1)} & b_2^{(m,1)} & \ldots \\ b_0^{(m,2)} & b_2^{(m,2)} & \ldots \\ & \vdots & \ddots \end{bmatrix} \begin{Bmatrix} 1 \\ r^2 \\ \vdots \end{Bmatrix} r^m. \tag{6.22}$$

Then construct a series of $N+1$ equations and truncate the approximations to a maximum radial polynomial degree of $2N + m$. The equations are

$$\left\{ \begin{array}{c} B_1^m J_m(\beta_{m1} r) \\ B_2^m J_m(\beta_{m2} r) \\ \vdots \\ B_{N+1}^m J_m(\beta_{m(2N)} r) \end{array} \right\} \approx \left[\begin{array}{cccc} b_0^{(m,1)} & b_2^{(m,1)} & \ldots & b_{2N}^{(m,1)} \\ b_0^{(m,2)} & b_2^{(m,2)} & \ldots & b_{2N}^{(m,2)} \\ & \vdots & & \ddots \\ b_0^{(m,N+1)} & b_2^{(m,N+1)} & \ldots & b_{2N}^{(m,N+1)} \end{array} \right] \left\{ \begin{array}{c} 1 \\ r^2 \\ \vdots \\ r^{2N} \end{array} \right\} r^m. \quad (6.23)$$

From Equation 6.23, define the $N + 1 \times N + 1$ vibration modal transformation matrix, $\boldsymbol{B}_N^m$ as

$$\boldsymbol{B}_N^m \equiv \left[\begin{array}{cccc} b_0^{(m,1)} & b_2^{(m,1)} & \ldots & b_{2N}^{(m,1)} \\ b_0^{(m,2)} & b_2^{(m,2)} & \ldots & b_{2N}^{(m,2)} \\ & \vdots & & \ddots \\ b_0^{(m,N+1)} & b_2^{(m,N+1)} & \ldots & b_{2N}^{(m,N+1)} \end{array} \right]. \quad (6.24)$$

The invertibility of the matrix $\boldsymbol{B}_N^m$ is discussed in Section 6.5.4. Furthermore, the Bessel terms in Equation 6.23 will only be correctly represented to the precision as discussed in the next section.

6.4.3 Convergence of the Bessel (Alternating) Series and Associated Truncation Error. The goal is to be able to transform information of the surface deformation from our Zernike subspace to vibration modal coordinates and vice-versa. To write the Zernike polynomials in terms of the modal coordinates, a finite expression of the Bessel functions in the intermediate coordinate system of radius and azimuthal angle is needed.

By definition the Bessel functions may be written as the series [154]

$$J_m(\beta_{mn} r) = (\frac{1}{2}\beta_{mn} r)^m \sum_{k=0}^{\infty} \frac{(-1)^k (\frac{1}{2}\beta_{mn} r)^{2k}}{(k+m)! k!}. \quad (6.25)$$

For the symmetric modes, m = 0, and Equation 6.25 may be reduced to

141

$$J_0(\beta_{0n}r) = \sum_{k=0}^{\infty} \frac{(-1)^k (\frac{1}{2}\beta_{0n}r)^{2k}}{k!^2}. \tag{6.26}$$

For instance, the first zero of $J_0(\beta R) = 0$ is $\beta_{01} = \frac{2.4048}{R}$ and the infinite summation where $\tilde{r} \equiv \frac{r}{R}$:

$$J_0(2.4048\tilde{r}) = 1 - 1.4458\tilde{r}^2 + 0.52258\tilde{r}^4 + O(\tilde{r}^6). \tag{6.27}$$

Returning to the general case of any non-negative integer m, to accomplish the desired transformation, the Bessel functions must be approximated by a truncated series. Note here that in the future sections the Zernike modes will be related to the Bessel-based vibration modes. Since the two basis sets have exactly the same azimuthal behavior, it is error in the radial terms that will contribute to overall error in the relationship.

To this end, the degree of truncation is estimated to ensure accuracy to within some approximation tolerance, ϵ.

Begin by defining

$$B_m^{\kappa}(\beta_{mn}r) \equiv \sum_{k=0}^{\kappa-1} \frac{(-1)^k (\frac{1}{2}\beta_{mn}r)^{2k+m}}{(k+m)!k!} \tag{6.28}$$

where again $\tilde{r} \equiv \frac{r}{R}$. From this point, drop the tilde, realizing that r is a normalized value. Note this is simply the first κ terms of the Bessel series.

Next, choose κ such that

$$\left| J_m(\beta_{mn}r) - B_m^{\kappa}(\beta_{mn}r) \right| < \epsilon. \tag{6.29}$$

Because the Bessel function is an alternating series the error in truncating the series is no worse than the first term neglected, that is

$$\left|J_m(\beta_{mn}r) - B_m^\kappa(\beta_{mn}r)\right| \leq \frac{\left(\frac{1}{2}\beta_{mn}r\right)^{2\kappa+m}}{(\kappa+m)!\kappa!}. \tag{6.30}$$

Further, because $m \geq 0$ recognize

$$\frac{\left(\frac{1}{2}\beta_{mn}r\right)^{2\kappa+m}}{(\kappa+m)!\kappa!} < \frac{\left(\frac{1}{2}\beta_{mn}r\right)^{2\kappa+m}}{(\kappa!)^2}. \tag{6.31}$$

For large values of κ, Stirling's formula may be used to simplify large values of the factorial expression $\kappa!$:

$$\kappa! \approx \kappa^\kappa e^{-\kappa}\sqrt{2\pi\kappa} \tag{6.32}$$

Applying Stirling's formula, the magnitude of the error becomes

$$\frac{e^{2\kappa}\left(\frac{1}{2}\beta_{mn}r\right)^{2\kappa+m}}{2\pi\kappa^{2\kappa+1}} < \epsilon. \tag{6.33}$$

Upon further simplification, our error bound formula is

$$\frac{\left(\frac{1}{2}\beta_{mn}r\right)^m}{2\pi\kappa}\left(\frac{e\beta_{mn}r}{2\kappa}\right)^{2\kappa} < \epsilon. \tag{6.34}$$

This truncation error represents an error bound on the radial portion of the truncated modes. In future constructs, when approximating Bessel functions, enough terms should be chosen so that this error is negligible.

6.5 Modal Transformation Method for Circular Apertures

In this section, a method is developed which allows Zernike surfaces to be projected on an interior region of a circular aperture by a linear combination of Bessel-based vibration mode shapes. In short, by comprising a desired optical surface in terms of physically realizable mode shapes, steady-state surface control should be readily achievable.

6.5.1 Projection of the Zernike Modes onto the Vibration Modes. The Zernike polynomials of Section 6.3.1 are related to the Bessel function of the first kind by the formula presented by Noll [97]:

$$R_n^m(r) = 2\pi(-1)^{(n-m)/2} \int_0^\infty J_{n+1}(2\pi\xi)J_m(2\pi\xi r)d\xi. \tag{6.35}$$

Therefore, it is expected and reasonable to express Zernike mode shapes in terms of vibration mode shapes. To do so, an approach based upon the orthogonal properties of the two basis sets and the projection theorem is detailed in the next section.

6.5.2 Existing Analytical Relationship. To define a Zernike mode in terms of a vibration mode, look at the case of the axisymmetric modes ($m = 0$) first. It is desired that

$$Z_i = \sum_{n=0}^{\infty} c_n^{(i)} W_n^0. \tag{6.36}$$

Therefore, one may write (assuming both mode shapes have been normalized to the same unit radius)

$$c_n^{(i)} = \frac{\int_0^{2\pi} \int_0^1 \frac{1}{\sqrt{\pi}} Z_i(r)W_n^0(r)rdrd\theta}{\int_0^{2\pi} \int_0^1 (W_n^0(r))^2rdrd\theta} \tag{6.37}$$

noting there is no dependence on θ such that the azimuthal integral term is replaced by the quantity 2π. The term $\frac{1}{\sqrt{\pi}}$ is required because Noll's scheme as presented in Equation 6.1 requires a linear weighting, which in our relationships is equally distributed among the Zernike modes. Further note the vibration modes are already normalized, thus Equation 6.37 reduces to

$$c_n^{(i)} = 2\pi \int_0^1 \frac{1}{\sqrt{\pi}} Z_i(r)W_n^0(r)rdr. \tag{6.38}$$

144

Substituting the results of mode shape Equations 6.11 and 6.13 with unit density (and $R = 1$) yields

$$c_n^{(i)} = \frac{2}{J_1(\beta_{0n})} \int_0^1 Z_i J_0(\beta_{0n} r) r dr. \tag{6.39}$$

The approximation of the piston Zernike mode using Equation 6.36 through Equation 6.39 arbitrarily truncated at 20 terms (statically-actuated axisymmetric vibration mode shapes) is presented in Figure 6.2.
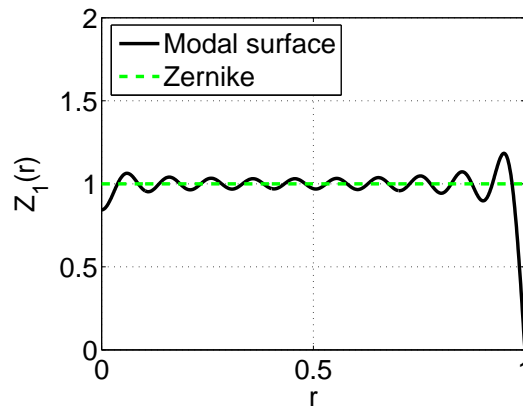
Figure 6.2:   Piston Zernike mode representation using projection theorem.

From this section, one may make the following observations. In Figure 6.2, even with a linear combination of 20 mode shapes, it is observed that nearly 20 per cent error occurs for a normalized radius of 0.9-1.0. Also, the representation is computationally intensive due to numeric integration. Thus, a simpler solution is sought where integration is avoided, and a bound on relative error may be forecast.

6.5.3 Zernike to Vibration Mode Matrix Transformation.   While Equation 6.36 allows the Zernike modes to be written in the form of integral equations, one may alternately apply the results of Sections 6.4.1 and 6.4.2 to write an approximate modal transformation. Begin by defining a vector of Zernike and vibration modes for a given frequency for radial degrees up to $2N$. For simplicity, define the axisymmetric case:

$$\boldsymbol{Z}_0 = \left\{\begin{array}{c} R_0^0 \\ \sqrt{3}R_2^0 \\ \vdots \\ \sqrt{2N+1}R_{2N}^0 \end{array}\right\} = \boldsymbol{A}_N^0 \left\{\begin{array}{c} 1 \\ r^2 \\ \vdots \\ r^{2N} \end{array}\right\}, \tag{6.40}$$

and

$$\boldsymbol{W}_0 = \left\{\begin{array}{c} W_1^0 \\ W_2^0 \\ \vdots \\ W_{N+1}^0 \end{array}\right\} = \boldsymbol{B}_N^0 \left\{\begin{array}{c} 1 \\ r^2 \\ \vdots \\ r^{2N} \end{array}\right\}. \tag{6.41}$$

Solve for radial vector, $\left\{1, r^2, \ldots, r^{2N}\right\}^T$ in Equation 6.41:

$$\left\{\begin{array}{c} 1 \\ r^2 \\ \vdots \\ r^{2N} \end{array}\right\} = (\boldsymbol{B}_N^0)^{-1}\boldsymbol{W}_0, \tag{6.42}$$

and then substitute into Equation 6.40 to yield the expression:

$$\boldsymbol{Z}_0 = \boldsymbol{A}_N^0(\boldsymbol{B}_N^0)^{-1}\boldsymbol{W}_0. \tag{6.43}$$

Through a similar manner write the non-axisymmetric equations:

$$\boldsymbol{Z}_{\boldsymbol{S}m} = \boldsymbol{A}_N^m(\boldsymbol{B}_N^m)^{-1}\boldsymbol{W}_{\boldsymbol{C}m}, \tag{6.44}$$

$$\boldsymbol{Z}_{\boldsymbol{C}m} = \boldsymbol{A}_N^m(\boldsymbol{B}_N^m)^{-1}\boldsymbol{W}_{\boldsymbol{S}m}, \tag{6.45}$$

where the modal vectors of length $N + 1$ are composed of modes of axisymmetric mode shapes ($\boldsymbol{Z_0}$, $\boldsymbol{W_0}$), modes with cosine angular dependence of frequency m ($\boldsymbol{Z_{Cm}}$, $\boldsymbol{W_{Cm}}$), and modes with sine angular dependence of frequency m ($\boldsymbol{Z_{Sm}}$, $\boldsymbol{W_{Sm}}$).

6.5.4   Near Singularity of the Modal Transformation Matrix.   The modal transformation matrix, $\boldsymbol{B}_N^m$, is most conveniently applied by defining it as a square matrix in Section 6.4.2, so that its inverse in Section 6.5.3 is unique. Non-square issues addressed with the pseudo-inverse are not included herein.

The size of $\boldsymbol{B}_N^m$ is determined by the number of (or highest degree) of vibration modes the designer will be able to actuate–those modes are essentially dependent on the fineness of the actuator grid. The value of N should be large enough so that actuated modes are represented with a small to negligible truncation error as derived in Equation 6.34. However, the resulting ($\boldsymbol{B}_N^m$) is ill-conditioned, and is not readily invertible for large values of N. A method for decomposing the matrix into a diagonal matrix $\tilde{\boldsymbol{N}}$ and remaining components $\tilde{\boldsymbol{B}}_N^m$ was applied to create lower condition number matrices for inversion.

Begin by defining:
$$\boldsymbol{B}_N^m \equiv \tilde{\boldsymbol{N}} \tilde{\boldsymbol{B}}_N^m \tag{6.46}$$

where the diagonal elements of $\tilde{\boldsymbol{N}}$ are defined as

$$\tilde{N}_{ii} = (B_N^m)_{ii} \tag{6.47}$$

.

The remaining off-diagonal elements of $\tilde{\boldsymbol{N}}$ are zero. Thus constructed, much of the ill-conditioned nature of $\boldsymbol{B}_N^m$ is shifted to $\tilde{\boldsymbol{N}}$, for which an analytical inverse readily exists.

As a simple example, for the case where $N = 2$ and $m = 0$, ρ and R are normalized to 1, and the factor $\frac{1}{\sqrt{\pi}}$ is removed, the matrices are:

$$\boldsymbol{B}_N^m = \begin{bmatrix} 1.0868 & -1.5712 & 0.5679 \\ -1.6581 & 12.6310 & -24.0552 \\ 2.0784 & -38.9115 & 182.1229 \end{bmatrix}, \tag{6.48}$$

$$\tilde{\boldsymbol{N}} = \begin{bmatrix} 1.0868 & 0 & 0 \\ 0 & 12.6310 & 0 \\ 0 & 0 & 182.1229 \end{bmatrix}, \tag{6.49}$$

$$\tilde{\boldsymbol{B}}_N^m = \begin{bmatrix} 1.0000 & -1.4458 & 0.5226 \\ -0.1313 & 1.0000 & -1.9045 \\ 0.0114 & -0.2137 & 1.0000 \end{bmatrix}. \tag{6.50}$$

In this example, the original condition number of $\boldsymbol{B}_N^m$ is reduced from 240.9 to 21.3 while the condition number of $\tilde{\boldsymbol{N}}$ is 167.5831, of little impact due to the ease of inverting $\tilde{\boldsymbol{N}}$ analytically, allowing $(\boldsymbol{B}_N^m)^{-1} = (\tilde{\boldsymbol{B}}_N^m)^{-1}(\tilde{\boldsymbol{N}})^{-1}$.

6.5.5 Defining a Clear Aperture Control Region. To this point, every effort made has focused on projecting a Zernike space onto a Bessel-based vibration mode space. A valiant effort, yet one that will prove frustrating due to the incompatibility of the boundary conditions for these competing basis sets. To avoid this inherent difficulty, it is proposed to formally define the clear aperture region as a subspace of the Bessel-based vibration mode space. Simply stated, the clear aperture region will be a circular region with some radius $a < R$, as was first introduced in Figure 6.1. Defining the scaled variable $\hat{r} = r/a$ for the Zernike polynomials in this subspace, and noting that on the clear aperture boundary $\hat{r} = 1$, one may relate the polynomial vector, $\left\{ 1, \hat{r}^2, \ldots, \hat{r}^{2N} \right\}$ to the radial vector $\left\{ 1, r^2, \ldots, r^{2N} \right\}$ with the diagonal matrix $\boldsymbol{S}_N^m$. The matrix $\boldsymbol{S}_N^m$ is

$$
\boldsymbol{S}_N^m = \frac{1}{a^m}
\begin{bmatrix}
1 & & & \\
 & \frac{1}{a^2} & & \\
 & & \ddots & \\
 & & & \frac{1}{a^{2N}}
\end{bmatrix}
\tag{6.51}
$$

such that

$$
\begin{Bmatrix} 1 \\ \hat{r}^2 \\ \dots \\ \hat{r}^{2N} \end{Bmatrix} \hat{r}^m = \begin{bmatrix} S \end{bmatrix} \begin{Bmatrix} 1 \\ r^2 \\ \dots \\ r^{2N} \end{Bmatrix} r^m .
\tag{6.52}
$$

Again, as in previous sections, the transformation matrix is for an azimuthal frequency m with a maximum polynomial degree $2N + m$. For Zernike shape control of the clear aperture region, the governing equations, Equations 6.43 - 6.45 scale to become

$$
\boldsymbol{Z}_0 = \boldsymbol{A}_N^0 \boldsymbol{S}_N^0 (\boldsymbol{B}_N^0)^{-1} \boldsymbol{W}_0 ,
\tag{6.53}
$$

$$
\boldsymbol{Z}_{\boldsymbol{S}m} = \boldsymbol{A}_N^m \boldsymbol{S}_N^m (\boldsymbol{B}_N^m)^{-1} \boldsymbol{W}_{\boldsymbol{C}m} ,
\tag{6.54}
$$

$$
\boldsymbol{Z}_{\boldsymbol{C}m} = \boldsymbol{A}_N^m \boldsymbol{S}_N^m (\boldsymbol{B}_N^m)^{-1} \boldsymbol{W}_{\boldsymbol{S}m} .
\tag{6.55}
$$

6.5.6 Application of Modal Transformation Method. With the underlying theory thus provided, a series of specific application of the modal transformation method for circular apertures is presented to show the applicable design criterion for deformable mirrors. Later, in Section 6.6, the method is applied in a series of finite element case studies.

To begin this discussion, the method is compared to the projection theorem used in Section 6.5.1. In Figure 6.3, the radial behavior of a surface composed of the first 20 axisymmetric statically-actuated vibration mode shapes is constructed

149

to approximate the axisymmetric Defocus Zernike mode, $Z_4 = \sqrt{3}(2r^2 - 1)$ over the entire surface (effectively, the clear aperture as previously presented is set to its maximum value of one). In Figure 6.3(a), the representation is constructed using coefficients from the projection theorem, and in Figure 6.3(b), the coefficients were generated using the modal transformation method for N = 20. The error between the desired Zernike surface and the vibration modal representation was calculated using the discretized weighted Euclidean norm (see Appendix A).

(a) Projection theorem.

(b) Modal transformation (N=20).
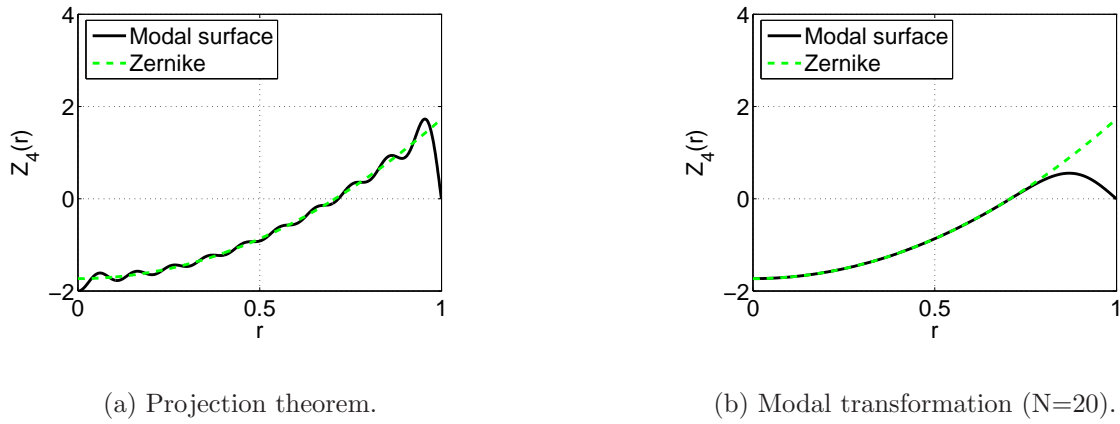
Figure 6.3:   Modal representations of the axisymmetric Defocus Zernike.

With the clear aperture thus set to one, the projection theorem results in the smaller error between the desired surface and its modal representation ($Error = 0.1753$ versus $Error = 0.3585$), and is the best achievable performance for the linear system. However, the shape of the modal surface in Figure 6.3(a) has evidence of distortion throughout its surface, while Figure 6.3(b) shows significant distortion only at the outer edge to meet the boundary condition.

Next, in Figure 6.4, the clear aperture is adjusted to values less than one, and the Defocus Zernike mode is constructed as before in Figure 6.3 using the first 20 axisymmetric vibration modes using the modal transformation for N = 20. In Figures 6.4(a)-(c), the radial behavior is plotted for clear apertures of 0.7, 0.8 and 0.9. It is quite apparent that for clear aperture of 0.7, the deviation between the desired Zernike shape and the modal surface is indistinguishable at the scale shown.

(a) Clear aperture = 0.7.   (b) Clear aperture = 0.8.   (c) Clear aperture = 0.9.
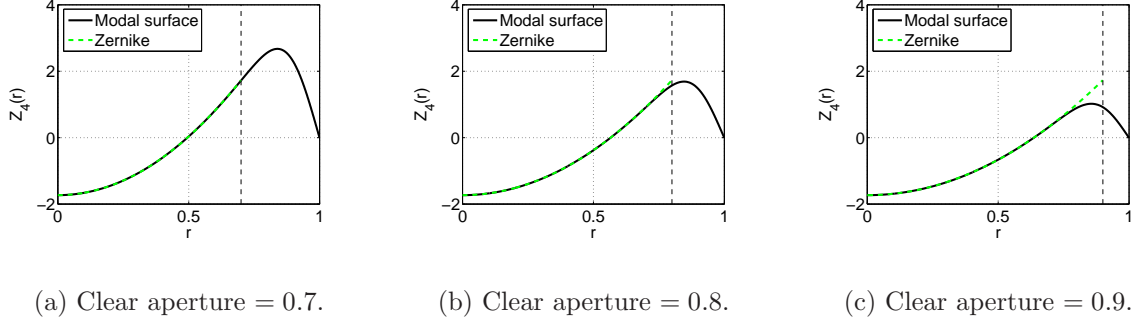
Figure 6.4:   Impact of Clear Aperture on representation of the Defocus Zernike.

With the clear aperture fixed at 0.7, another series of plots was constructed for Figure 6.5, again using the modal transformation method for $N = 20$. This series of plots show not only the intuitive improvement in accuracy by increasing the number of modes to actuate the surface, but also show the improvement is from the interior of the clear aperture to a maximum difference at the boundary of the clear aperture.

(a) $N = 3$.   (b) $N = 6$.   (c) $N = 10$.
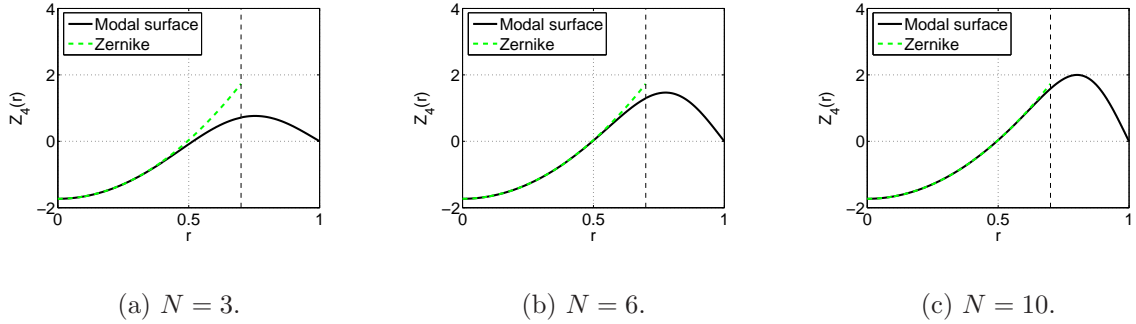
Figure 6.5:   Impact on representation of Defocus Zernike by varying N.

Figure 6.5.6 captures the information from both Figures 6.4 and 6.5 on a single graphic. The log of the surface error is shown to decrease with increasing the number of actuated modes and decreased clear aperture. For example, to get the level of error equal to 0.01, either set N = 1 and clear aperture to 0.09, or set N = 20 and clear aperture to 0.75.

For the structural engineer, these results may be transformed into design criterion for construction of a deformable mirror. Beginning with a desired optical surface error budget and a desired radius of the aperture region, the engineer may choose to

151
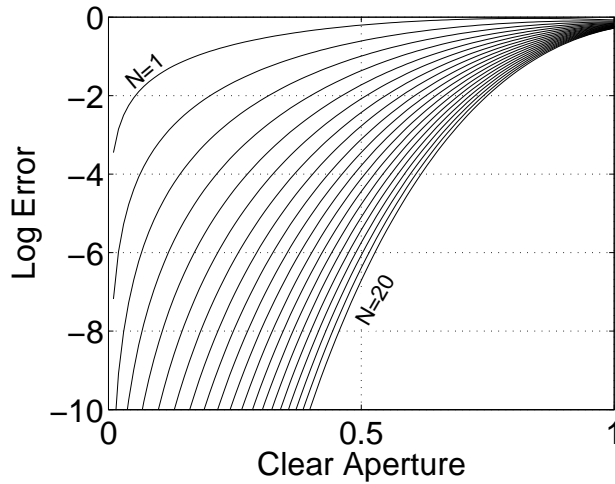
Figure 6.6:   Surface error of Defocus Zernike versus clear aperture with varying N.

actuate a greater number of vibration modes or reduce the clear aperture to achieve the desired performance. For the hardware implementation, actuating the number of modes (within the error budget) will be limited by the fineness of the available surface actuators and to a lesser extent the on-board computing capabilities and actuator energy requirements. With a fixed reflective area pre-defined, decreasing the clear aperture will effectively increase the radius of the overall structure, with whatever associated weight penalties that entails. However, it is aptly demonstrated that setting a clear aperture region to an arbitrary value, such as eighty percent, is neglecting the design optimization that could be performed by the engineer.

To demonstrate the effectiveness of the Modal Transformation Method, two case studies are presented.

6.6   Case Studies: Application of Modal Transformation Method

One of the primary goals of this research was to develop a control methodology for the in-plane actuated structure. To show ability of the Modal Transformation Method to perform this function, two case studies in static control are offered. In the first case study, a 61-actuator model based a the geometry of a deformable mirror under development at AFIT is constructed in MSC.Nastran. The Modal Transforma-

tion Method is used to form a Zernike mode surface, and the results are compared to a single iteration of a competing methodology using the projection of the desired surface deflection. In the second example, a hypothetical deformable mirror with a finely actuated electrode pattern is used to demonstrate the ability of the Modal Transformation Method, when used in an iterative scheme, to form low-order axisymmetric and non-symmetric modes.

6.6.1   61-actuator Finite Element Model.   A finite element model of the AFIT deformable mirror testbed was created in MSC.Nastran, based on the models of Chapter IV and shown in Figure 4.5. Briefly summarized, the model used the same dimensions of the experimental hardware, except instead of seven actuating regions, the surface was divided into 61 regions. The 3601 node model was comprised of 3384 CQUAD4 elements and 72 CRIA3 composite plate elements. The substrate and actuating layers were modelled, while the gold reflective layer and copper-nickel electrode layers were considered negligible. Piezoelectric forcing was introduced using the linear piezoelectric-thermal analogy [35] at the locations in Table 6.5. For the purposes of this example, the directionality of the piezoelectric dielectric constants was removed. Material properties are presented in Table 6.6. An example electrode pattern from a mirror under construction at AFIT is presented in Figure 6.7.
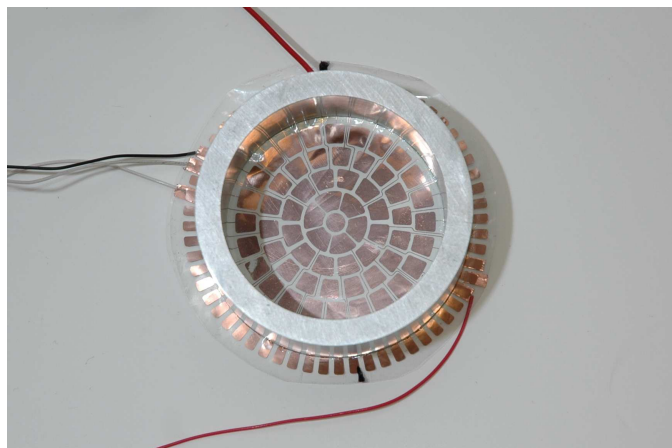
Figure 6.7:   Example electrode pattern.

Table 6.5:   Actuator locations for 61-actuator, 0.0624-m radius model.

inner radius (m)	outer radius (m)	azimuthal divisions	degrees per division
N/A	0.0071	1	360
0.0071	0.0212	6	60
0.0212	0.0353	12	30
0.0353	0.0494	18	20
0.0494	0.0622	24	15

Table 6.6:   Material properties.

Parameter	Silicone	PVDF	Units
Young's modulus	1.013	4000	$10^6 N/m^2$
Poisson's ratio	0.497	0.3	
d_{31}	N/A	23	$10^{-12} \frac{m/m}{V/m}$ or $\frac{C/m^2}{N/m^2}$
thickness	.0015	$52.0E{-}6$	m

A uniform edge tension was applied using an enforced displacement boundary condition in the radial direction. Then, using a non-linear static solution, the stiffness of the model was updated, and an equivalent thermal load was introduced to simulate voltage application at the various actuator locations.

The out-of-plane surface displacements were extracted for analysis. Zernike coefficients were calculated for the area inside of the clear aperture, which could then be used to formulate conclusions about the behavior of various control methodologies.

6.6.2   Static Control Methodology for Membrane Mirrors.   To provide a competing methodology for computing actuation voltages for static surface control of the Zernike polynomials and calculate the vibration mode shapes in this region, the deformable mirror was modelled as a fixed boundary membrane structure. The forcing functions were modelled consistent with existing smart structure theory, where the piezoelectric loads are simply line moments acting along the actuator boundary. With plate and non-linear in-plane tension effects neglected, the governing equation

154

(as developed in Chapter III, Equations 3.149 and 3.150) for the deformable mirror with J actuators is:

$$N^0 \nabla^2 w(r, \theta) = M_i \nabla^2 \sum_{i=1}^{J} F_i(r, \theta), \qquad (6.56)$$

where

$$M_i = \frac{1}{2} \frac{E}{1 - \nu} \frac{d_{31}}{h_p} V_i. \qquad (6.57)$$

In the above equation, N^0 is membrane tension, E is the piezoelectric modulus, ν_p is the Poisson's constant, d_{31} is the piezoelectric constant, h_p is the thickness of the piezoelectric layer, and V_i is the voltage across the electrodes.

This particular model was chosen because it represents the "bed-of-nails" solution to the problem–for the simplified model any voltage input should be represented by a corresponding deflection of the mirror's surface. If this model was completely accurate, it would show a simple projection would give us the required performance. However, one might suspect (and will demonstrated) this is not the case, as plate and non-linear terms will affect the response. Using the Modal Transformation Method, the impact of these neglected terms are lessened, and one finds this very simple modelling technique will yield extremely satisfactory results.

For the example, F_i is the area of electrode as shown in Figure 6.8. The ith region may be defined through heaviside functions with radial boundaries ξ_i^U and ξ_i^L and azimuthal boundaries ϕ_i^U and ϕ_i^L:

$$F_i(r, \theta) = \{H(r - \xi_i^L) - H(r - \xi_i^U)\} \cdot \{H(\theta - \phi_i^L) - H(\theta - \phi_i^U)\}. \qquad (6.58)$$

Again, it is quite obvious that solutions to the differential equation are simply a series of scaled step functions corresponding to the applied voltage on the actuated

155
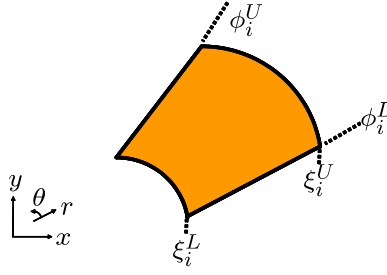
Figure 6.8: i^{th} actuator boundaries from Equation 6.58.

electrode. Later, the orthogonal nature of the solution will be used advantageously. For a unit voltage, these shapes are defined here as Ψ_i modes. To obtain a desired shape on the membrane surface, it is simply a matter of using the projection theorem to find the individual actuator gains.

For the direct projection method of control, the desired Zernike is constructed directly from the Ψ mode shapes. In the proposed modal transformation method, the Ψ mode shapes are actuated to replicate the membrane vibration mode shapes, and then the transformation constructs the desired Zernike surface on the clear aperture region using linear combinations of the approximated vibration mode shapes. Again, it is emphasized that the modal transformation method always satisfies the fixed edge boundary conditions, and further limits steep transitions if the Zernike modes are implemented on the interior clear aperture region.

6.6.3 Static Control Simulation and Results.   In the simulation example, voltages were applied to the MSC.Nastran non-linear finite element model. The desired shape was a simultaneous surface deflection corresponding to the axisymmetric Zernike defocus mode and the non-axisymmetric tilt mode associated with $cos(\theta)$. The clear aperture region was set to 0.78, inside the boundary of the last ring of actuators. A logic flow chart depicts these operations in Figure 6.9. In the direct projection method, the Zernike shapes are constructed in the clear aperture from a linear combination of the actuator (Ψ) modes. In this application of the modal transformation method, the vibration mode shapes are approximated using the projection

156

theorem to form linear combinations of actuator modes, and then those shapes are used in the modal transformation method algorithm using Equations 6.43 to 6.45. In the figure, indices i correspond to actuator mode, j to vibration mode, and k to desired Zernike surface. In this modal transformation method, the value of N was set to 20, and the number of actuated vibration modes at a given azimuthal frequency was limited to five. This limit corresponded to the number of actuation "rings", and thus the maximum number of zero crossings that was theoretically obtainable. The value of N ensured the truncation error of Equation 6.34 would be negligible.
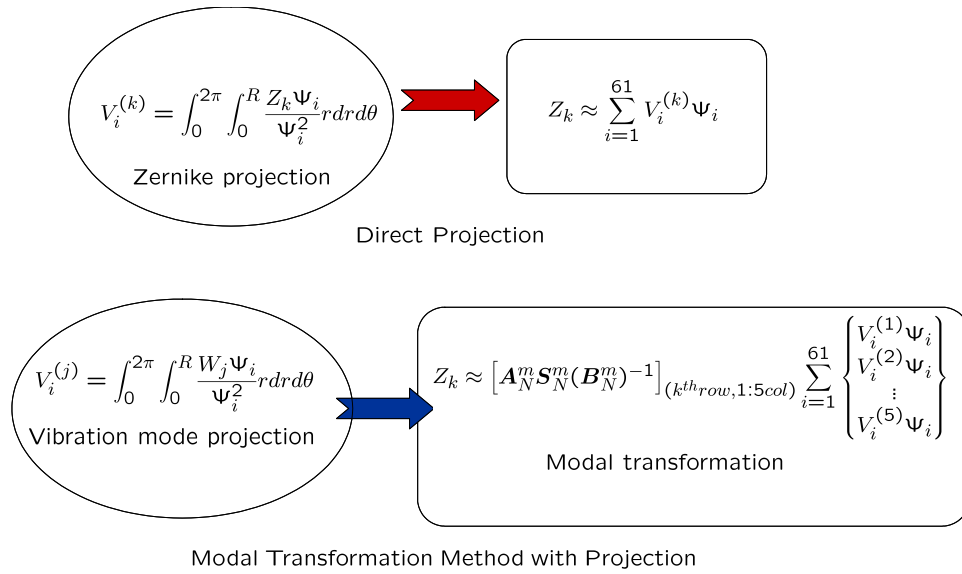
Figure 6.9:   Pseudocode for computing the voltages in Figure 6.10(a) and (d).

The voltage inputs $(V(x,y))$[3], finite element model simulation results $(w(x,y))$, and absolute error difference$(E(x,y))$ of the desired surface versus the simulated surface are provided for both the direct projection and modal transformation method for obtaining simultaneous defocus and tilt Zernike mode shapes across the clear aperture region in Figure 6.10. The clear aperture region is indicated by a black line at 0.78 of the surface radius.

---

[3]The Cartesian coordinates are used for the plotted surfaces. For translation to cylindrical coordinates (r, θ), $x = r\cos(\theta)$ and $y = r\sin(\theta)$.
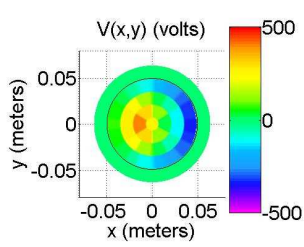
(a) Voltage distribution (in volts) on piezoelectric actuating grid for direct projection method.
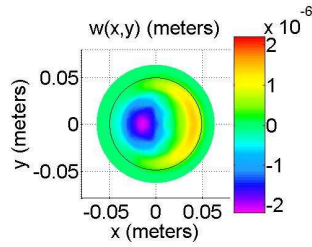
(b) FEM surface deflection for direct projection method.
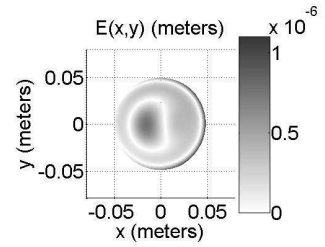
(c) Absolute error for direct projection method.
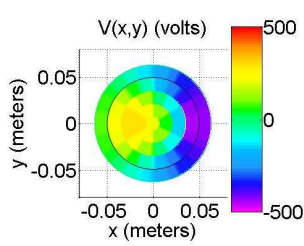
(d) Voltage distribution (in volts) for proposed modal transformation method.
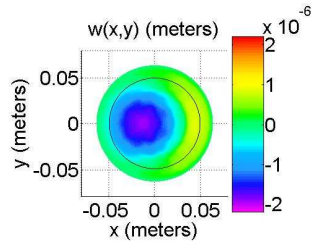
(e) FEM surface deflection for proposed modal transformation method.
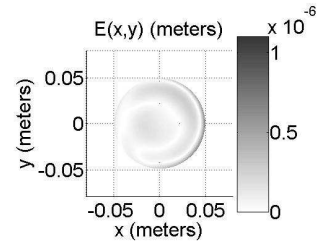
(f) Absolute error for proposed modal transformation method.

Figure 6.10:   Direct projection (top) versus Modal Transformation Method (bottom).

When calculating the voltage inputs for the 61 actuation regions in Figure 6.10(a) and (d), there was a slight scaling error between the competing methods, so the voltage was adjusted by a constant to achieve similar deflections. All other responses were linear for the micron level surface displacements in this simulation corresponding to input voltages between -600 to 600 Volts (the practical limit for PVDF material).

The surface deflection and error plots are compared in the remaining plots of Figure 6.10. To calculate surface error the desired defocus and tilt coefficients were subtracted from the generated surface inside of the clear aperture region. The piston mode was also neglected as it is of no consequence in optical systems as it is generally not measurable nor does it affect the mirror's optical performance.

While the absolute error plots in Figure 6.10 give some idea of the performance achievable using the modal transformation method, a break down of the surface terms by Zernike coefficients for axisymmetric Defocus mode (radial degree $n = 2$) and non-axisymmetric Tilt mode (radial degree $n = 1$) is presented in Figure 6.11(a) and (b). In both graphs, the desired (and achieved) Zernike coefficient was normalized for approximately 1×10^{-6} to one. The next three Zernike coefficients for next three higher radial order at the same azimuthal frequency were then normalized and plotted. The coefficients (and thus contribution to the error) for the sin terms and the higher azimuthal frequency terms (such as $\cos 2\theta, \cos 3\theta, etc$) were not significant and thus are not presented. Values of coefficients for other modes represent undesired surface deflection.

When comparing the modal transformation method with the direct projection method in Figure 6.11(a) and (b), the advantage of the modal transformation method is evident. The error, which shows as non-zero coefficients in the first and second higher order modes of both the symmetric and non-symmetric modes is lower for the modal transformation method. Only for the third highest radial order mode does the direct projection method enjoy a slight advantage, although the relative error at that high radial frequency in either case is low.

159
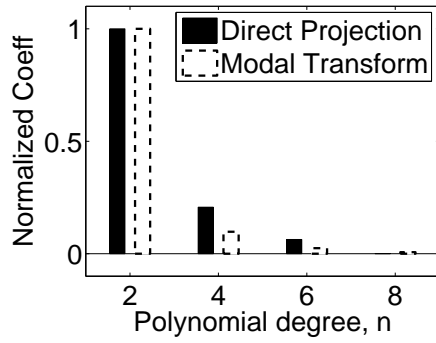
(a) Axisymmetric modes (m = 0).
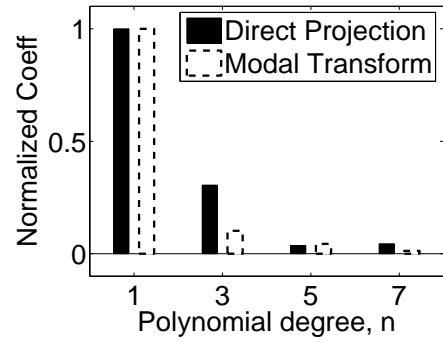
(b) Non-axisymmetric modes corresponding with $\cos\theta$ behavior (m = 1).

Figure 6.11:   Comparison of normalized Zernike mode coefficients.

The overall effect is that the modal transformation method may be used to generate Zernike data inside the defined clear aperture region with less error than a competing strategy. The other significant conclusion is that to apply the modal transformation method, actuated regions must occur outside of the clear aperture region, thus increasing the complexity of the system. In this example, 39 per cent more actuators were required when using the modal transformation method, which would require an attendant amount of power and system integration. However, it is the opinion of the researchers that the performance gain, and the resulting decrease in the overall diameter of a mirror structure, would far outweigh the increase in complexity. A systems level trade study is foreseen as a potential future effort.

6.6.4   Finely Actuated Finite Element Model.   A second finite element model was built to showcase the absolute advantages of the Modal Transformation Method when used in conjunction with a hypothetically achievable in-plane actuated deformable membrane mirror. For this model, the previous example was modified. The silicone layer was replaced by an inert substrate of equal thickness and material properties to the PVDF layer, resulting in a very thin (104 micron total thickness) mirror. The electrodes were replaced by a voltage distribution field at each finite

element grid point, and the number of grid points was increased to 9001. This would be representative of a finely actuated grid such as conceived to be manufactured with MEMS techniques or remotely actuated by electron gun.

A simple iterative technique was used to control the structure, where the desired Zernike mode error signal was summed and sent to the Modal Transformation Method to correct voltage fields as summation of the appropriate Bessel-based mode shapes. A schematic of the control diagram is presented in Figure 6.12.
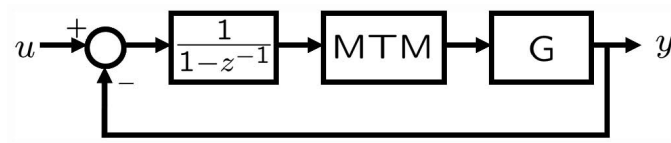
Figure 6.12:   Feedback algorithm.

For the simulations, the first four axisymmetric modes beginning with defocus and the first four non-symmetric modes with an azimuthal behavior of $m = 1$ $(\cos\theta)$ beginning with tilt were commanded. The results of this second series of simulations is presented in Figure 6.13.

(a) $m = 0, n = 2$.   (b) $m = 0, n = 4$.   (c) $m = 0, n = 6$.   (d) $m = 0, n = 8$.

(e) $m = 1, n = 1$.   (f) $m = 1, n = 3$.   (g) $m = 1, n = 5$.   (h) $m = 1, n = 7$.
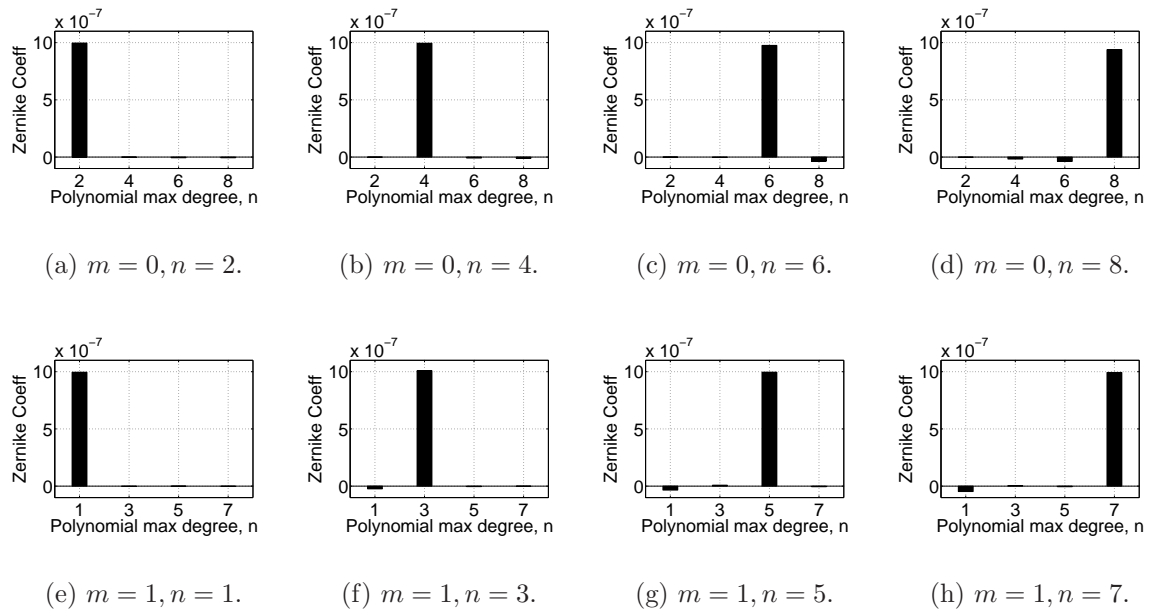
Figure 6.13:   Closed-loop simulation results.

161

From the data presented, it is clear that a low order Zernike surface was achieved with negligible error inside of a clear aperture region of an in-plane actuated mirror by using the Modal Transformation Method in conjunction with a finely spaced control grid.

6.7 Conclusions

In this chapter, the static shape control of a membrane mirror has been explored. Development of a methodology which prescribes the desired surface displacement of an interior, "clear aperture" region in terms of physically achievable mode shapes has been developed. In the development, surface error can be seen to be a function of the clear aperture radius relative to the mirror radius, and also as a function of the number and accuracy of achievable mode shapes, themselves a function of the fineness of the actuating grid.

In the examples presented, a non-linear finite element models simulation of deformable circular mirror with 61-piezoelectric unimorph actuators showed the advantages of the proposed modal transformation method to determine actuator gains to create a desired surface when compared to a direct projection method based solely on solving the governing membrane equation. A second simulation that given a continuous, finely meshed actuation grid of unimorph actuators, low-order Zernike modes may be formed within the clear aperture with virtually no error using the methods proposed.

Greater complexity in the system due to the increase in number of actuators and the subsequent increased power requirement appears to be the main tradeoff for the increased accuracy in quasi-static surface deflection performance when applying this control methodology. To better understand the overall system requirements, the scaling issue is discussed in the next chapter.

VII. Scaling Analysis for Membrane Optics

> *Chapter objectives:*
>
> - *Differentiate between scalable architecture and scaling*
> - *Develop a non-dimensional model for analysis*
> - *Investigate effects brought about by a change in scale*

7.1 Introduction

Space telescopes in current use are limited by payload limits in weight and most importantly diameter, the latter on the order of a couple of meters for a continuous surface reflector. To overcome this restriction, some space telescopes, such as the James Webb Space Telescope, are pushing the bounds of scalable architectures, where several smaller mirrors are used collectively to create one large aperture. As an alternative to using a scalable architecture, *membrane optics* research seeks an aperture which may be stowed compactly, and unfurled on orbit.

For the purpose of this chapter, *large-scale* generally refers a space-based membrane optic with a radius on the order of 10 meters. *Small-scale* refers to a scaled-down laboratory test article on the order of 10 centimeters in radius. In general, one may think of holding all parameters (including the thickness of the membrane optic) constant except for the radius when referring to these models.

Our discussion begins with an introduction to the problem of scale, where the method of a scalable architecture is contrasted with the problem of scaling a single structure from small-scale to large-scale. In Section 7.2, the governing differential equation for in-plane actuated mirrors is presented, and then transformed to a non-dimensional form. Different forms of the equation are analyzed in Section 7.3, includ-

ing the linear plate, the plate-membrane, and the full non-linear model. Section 7.4 presents a series of case studies conducted using an MSC.Nastran finite element model. To highlight the effects of scale, to illustrate plate versus membrane effects, and to show the impact of unimorph actuation. Finally, Section 7.5 wraps up the discussion with some conclusions and recommendations for researchers in the field.

7.1.1 *Scaling.* For most engineering problems of scale, developing a scalable architecture solution is a good first approach. A *scalable architechture* is defined here as one where additional performance is gained through the addition of like elements. For an excellent discussion of scalable architechtures as it applies to the solar sail problem (which is similar in many respects to the membrane optic problem, albeit with far less stringent shape control requirements), the reader is referred to the presentation by Greshik [56]. Figure 7.1 shows two examples of scalable architechtures.
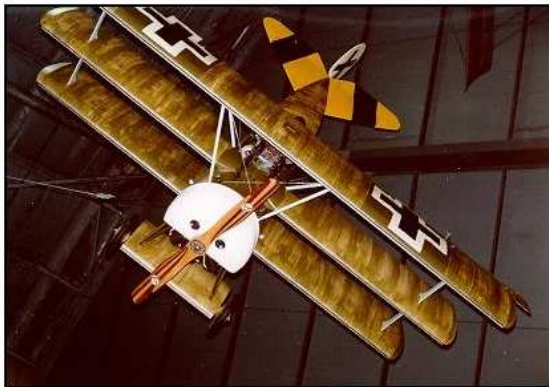
(a) WW1 era Fokker Dr.1 triplane *photo courtesy of the National Museum of the US Air Force.*
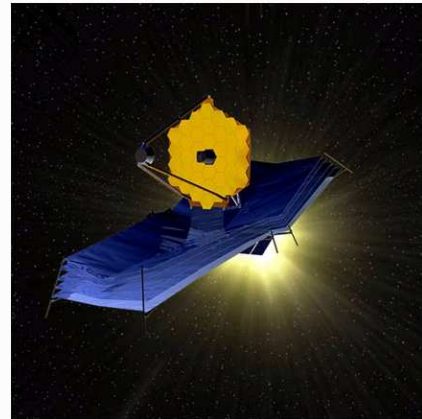
(b) James Webb Space Telescope *illustration courtesy of NASA.*

Figure 7.1:   Scalable architecture examples.

In WW1, the air war pushed aircraft development at a breakneck pace. A key to maneuverability was the ability of the aircraft wing to generate lift. The biplane, and later the development of the Sopwith triplane which was in turn had its design borrowed by the German industry to create the famous Fokker Dr.1, was

the scalable architecture solution, as design teams added fabric covered wings to create lift. However, the increased lift came at the expense of drag plus engineering, operational, and manufacturing complexity. As a result no quad-wing planes were fielded. The post war period would introduce the monocoque structure, where a metal stressed wing absorbed the in-flight loads, and revolutionized aircraft design leading to increased speeds and maneuverability.

Today, the scalable architecture approach is evident in the James Webb Space Telescope. The James Webb Space Telescope (JWST) [13] uses a primary mirror comprised of 18 individual mirror elements, to give it a surface area of 25 square meters, or nearly an order of magnitude increase over the Hubble telescope. As with the triplane of WW1, increased system complexity is evident in the control algorithms needed to govern the pointing of the 132 degree-of-freedom actuators that manipulate the JWST mirror system. Also, the mirrors can only be made so thin and lightweight, so even larger structures made using a similar approach will be more costly and complex. For a truly revolutionary increases in space telescope aperture size, another method of manufacture is required.

To increase the aperture size with a single monolithic structure that is lightweight, and one that also may be rolled compactly and unfurled once in orbit is the domain of membrane optics. Appreciating the order of magnitude of the scales of the problem confronting the engineer is extremely difficult to comprehend.

Membrane optics seeks to develop thin film mirrors on the order of 100 microns in thickness and up to 20 meters in diameter. The thickness is about the same as a human hair! If you were to build a skyscraper with a footing the size of the Sears Tower (about 68 meters) with the same aspect ratio, it would reach over 1300 kilometers into the sky, and have over 1,000,000 floors! Further complicating matters, one would like the surface of the membrane optic to conform to shape tolerances of optical (sub-micron) quality, perhaps even down to 10s of nanometers. Again, a familiar analogy is to imagine driving your car around the world on a stretch of highway so

smooth you never hit a pothole deeper than a couple of centimeters! Thus, membrane optics represent a problem of scale not easily imagined, much less one that must be understood and eventually exploited.

7.1.2 *The Bekey Concept.* One of the early proponents of the membrane space telescope was Ivan Bekey. In his work, *A 25 M. Diameter Space Telescope Weighing Less Than 150 Kg* [24], he proposes a membrane mirror construction that will form the basis of our discussion.

In the Bekey concept, a large membrane primary mirror focus light on an array station kept several hundred meters distant from the primary mirror. In his concept the word membrane is a misnomer for the primary–the mirror is actually envisioned as a very thin plate with no peripheral frame structure. Ideally, if not subject to gravitational or solar forces (in the Bekey concept, this is accomplished by orbiting at a Lagrange point and protected by a solar sail), a plate would not need external support. However, for the earth-facing space surveillance mission, it is necessary to explore the effects of membrane (pellicle) tension, realizing that it creates an attendant weight penalty in proportion to the required frame stiffness and circumference. Fine surface shape control of the mirror is proposed to be achieved through remote actuation of a piezoelectric film by a scanning electron beam, which in theory can project a voltage film as fine as the beam width. Electron gun actuation of piezoelectric actuators is a fledgling technology under exploration [57, 58, 82, 95].

It may be difficult to comprehend the relative sizes in the construction. Figure 7.2(a) depicts the primary mirror in relation to the focal plane array. In the figure, a 10-meter radius primary mirror is focused on an array 400 meters away. The $f/\#$, or ratio of focal length to mirror diameter, is 20, typical of a space telescope. As a general rule, a space telescope's performance will improve with higher f/# and increased aperture size (mirror diameter).

An equation for the paraboloid surface $w(r)$ in terms of focal length f, radius R, in terms of radial variable r is:
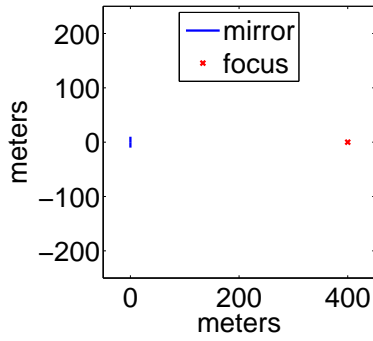
(a) System (to scale).
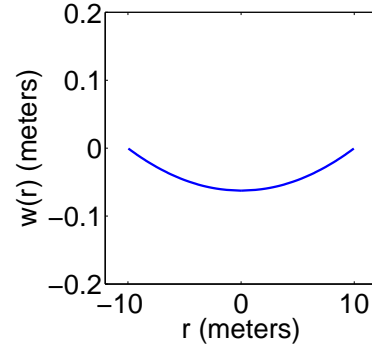
(b) Parabolic reflector.

Figure 7.2:   Space telescope with membrane primary mirror.

$$w(r) = \frac{1}{4f}(r^2 - R^2). \tag{7.1}$$

Applying Equation 7.1 with a mirror radius of 10 meters, and a focal length of 400 meters, the maximum deflection at the center of the paraboloid would be 0.0625 meters. The relative deflection is depicted in Figure 7.2(b).

7.1.3   Previous Work.   In recent years, various researchers have created sub-scale models for membrane optics. Flint et al [44, 46, 47] have created a doubly curved membrane shell that may be rolled flat and then released to form a parabolic shape. Mirrors have been constructed up to meter-class diameters, and the shell has been tested for near optical quality. At present, there are no active corrective elements in the mirror itself to correct for surface distortions, although boundary control is under investigation.

Sumali et al [134] demonstrated a pinned, flat, 80 mm square PolyVinylidine Di-Fluoride bimorph with a single actuating electrode. The bimorph was approximately 100 microns thick, and is precisely the type of construction that is envisioned in this study. Deflections on the order of several hundred microns were achieved, and were consistent with linear analysis.

Murphy, Macy and Gaspar [93] have reported on the development of solar sails for NASA. Their work is unique in that they have tested large membrane structures in as close to a space environment as possible. The difficulties encountered in the testing highlight the need for very accurate scaled models from which conclusions may be drawn, as full-scale testing in a 1-g environment can be extremely difficult, or impossible.

Chodimella, Moore, Otto [30] presented the initial design consideration studies for a large-scale electrostatic mirror. An electrostatic mirror uses a series of electrodes attached to a backing structure to pull the membrane into a desired shape. The mirror is far easier to construct than an in-plane actuated mirror, and has the additional advantage of manufacture with current technologies. The main disadvantages are weight due to the stiff backing structure. Optical level performance of this class of structure has not yet been demonstrated on a large-scale.

7.1.4 AFIT Deformable Mirror Testbed. Ultimately, the goal of the research presented herein is to allow us to draw conclusions from scale models. An example of one of the small-scale models is the AFIT deformable mirror testbed. Recall the dimensions of the the AFIT deformable mirror testbed as 0.127 meter (2.5 in) radius with the thickness of the piezoelectric material as 52 microns. Experimental quasi-static control of the mirror was reported in Chapter IV.

7.2 Governing Models and Equation

In this section, the governing differential equation for a thin, in-plane actuated structure such as a membrane primary mirror, is presented. The following discussion is based purely on the structural response of the mirror to the deterministic forcing, that is, no disturbances such as heating, solar pressure, nor body forces such as induced by gravity, are included. Furthermore, piezoelectric forces are modelled as equivalent thermal strains.

The governing differential equation for the out-of-plane displacement terms, $w(r)$, of an axisymmetric, isotropic plate-membrane with pellicle tension N_O undergoing in-plane piezoelectric forcing of radius R as developed in Chapter III:

$$D\nabla^4 w(r) - N_O \nabla^2 w(r) + N_P \nabla^2 w(r) \ldots$$
$$- N_1 \left(\frac{\partial w(r)}{\partial r}\right)^2 \frac{\partial^2}{\partial r^2} w(r) \ldots$$
$$- N_2 \left(\frac{\partial w(r)}{\partial r}\right)^2 \frac{1}{r} \frac{\partial}{\partial r^2} w(r) = -\nabla^2 M_P. \tag{7.2}$$

The other terms are defined as follows:

$$D = \frac{E(h_p + h_s)^3}{12(1 - \nu^2)}, \tag{7.3}$$

$$N_O = (h_p + h_s) P_O, \tag{7.4}$$

$$N_P = \frac{E d_{31} V(r)}{1 - \nu}, \tag{7.5}$$

$$M_P = -\frac{1}{2} h_s \frac{E d_{31} V(r)}{1 - \nu}, \tag{7.6}$$

$$N_1 = \frac{1}{2} \frac{E(h_p + h_s)}{1 - \nu^2}, \tag{7.7}$$

$$N_2 = \nu N_1. \tag{7.8}$$

In the above equations, E is the Young's modulus, h_p is the thickness of the piezoelectric layer, h_s is the thickness of the substrate (inert) layer, and P_0 is the pressure force on the circumference that provides the pellicle tension. The piezoelectric coupling matrix coefficient is d_{31} and $V(r)$ represents the voltage applied to the piezoelectric layer. The in-plane strain terms effects on the surface displacement are neglected. Table 7.1 provides a summary of the terms and units. The terms are expressed in terms of fundamental units of length (L) and the derived units pressure (P) and voltage (V).

Table 7.1:   Plate-membrane variables and parameters.

variable	description	units
r	radial coordinate (independent)	L
w	out-of-plane displacement (dependent)	L
P_O	tensile pressure	P
E	Young's modulus	P
h_s	substrate thickness	L
h_p	piezo thickness	L
ν	Poisson's ratio	$-$
d_{31}	piezoelectric coefficient	LV^{-1}
$V(r)$	voltage distribution	V
R	radius	L

Also note Equation 7.2 corresponds to units of pressure, and that the axisymmetric Laplacian operator, $\nabla^2 \equiv \frac{\partial^2}{\partial r^2} + \frac{1}{r}\frac{\partial}{\partial r}$. This problem assumes unimorph actuation. For symmetric bimorph applications, the M_P term is doubled (h_s is replaced by $h_s + h_p = 2h_s$) and the N_P term vanishes due to integration through the thickness as seen in the development of the terms in Chapter III.

7.2.1   *Choice of Non-Dimensional Variables.*   To perform a similarity scaling analysis, the physical problem must be restated in terms of non-dimensional units that are independent of units chosen. One way to do this is to write the Π parameters for the problem, and then choose the scales as they apply to the problem at hand.

To simplify our analysis, choose $hp + hs = h$, and write the Π dimensionless parameters [22, pp. 39-45]. Although somewhat unconventional, it has been chosen to use derived units in the problem. Normally this would not be recommended, but it allows for easy book-keeping in this particular case.

$$\Pi = \left(\frac{h}{R}\right)^a \left(\frac{P_0}{E}\right)^b \left(\frac{d_{31}V}{h}\right)^c (\nu)^d. \tag{7.9}$$

From Equation 7.9, appropriate scales for the two length scales, l_i (i = a,b), and pressure, p_c may be chosen as

$$l_i = \left(\frac{h}{R}\right)^a \left(\frac{P_0}{E}\right)^b \left(\frac{d_{31}V}{h}\right)^c (\nu)^d (h)^1, \quad \text{i = a,b} \tag{7.10}$$

and

$$p_c = \left(\frac{h}{R}\right)^a \left(\frac{P_0}{E}\right)^b \left(\frac{d_{31}V}{h}\right)^c (\nu)^d (E)^1. \tag{7.11}$$

Next, apply the scaled variables to Equation 7.2 by defining the non-dimensional variables $\tilde{w} = wl_a$ and $\tilde{r} = rl_b$ where l_a and l_b are derived from Equation 7.10, and divide by the pressure scale p_c to yield

$$\frac{1}{p_c}\left\{ D\frac{l_a}{l_b^4}\nabla^4\tilde{w}(\tilde{r}) - N_O\frac{l_a}{l_b^2}\nabla^2\tilde{w}(\tilde{r}) + N_P\frac{l_a}{l_b^2}\nabla^2\tilde{w}(\tilde{r}) \dots \right.$$
$$- N_1\frac{l_a^3}{l_b^4}\left(\frac{\partial\tilde{w}(\tilde{r})}{\partial\tilde{r}}\right)^2\frac{\partial^2}{\partial\tilde{r}^2}\tilde{w}(\tilde{r}) \dots$$
$$\left. - N_2\frac{l_a^3}{l_b^4}\left(\frac{\partial\tilde{w}(\tilde{r})}{\partial\tilde{r}}\right)^2\frac{1}{\tilde{r}}\frac{\partial}{\partial\tilde{r}}\tilde{w}(\tilde{r}) = \frac{1}{l_b^2}\nabla^2 M_P\right\}. \tag{7.12}$$

In a similar manner, we note the scaled solution to a parabolic mirror of focal length f would therefore be written as:

$$\tilde{w}(\tilde{r}) = \frac{R^2}{4fl_a}\left(\frac{\tilde{r}^2 l_b^2}{R^2} - 1\right) \tag{7.13}$$

7.2.2   Choice of Scales.   To choose the appropriate scales for this problem, we choose based first upon our intuition. For the scale on the displacement w, we choose the thickness of the material $l_a = h$ as the scale. For the radial term, we would like the problem to be invariant with radius, so we set $l_b = R$. Thus, the radius

is normalized, and deflections are terms of multiples of the thickness of the mirror. Other scales could of course be chosen, as we will see.

To better recognize the equation, we take one moment to rewrite it in simpler terminology. Dropping the tildes, the independent variable, and letting $,r$ and $,rr$ indicate the first and second derivatives with respect to r, Equation 7.12 becomes

$$\frac{1}{p_c}\left\{D\frac{l_a}{l_b^4}\nabla^4 w + \left(N_P - N_O\right)\frac{l_a}{l_b^2}\nabla^2 w \ldots \right.$$
$$\left. - N_1\frac{l_a^3}{l_b^4}\left(w_{,r}\right)^2 w_{rr} - N_2\frac{l_a^3}{l_b^4}\left(w_{,r}\right)^2\frac{1}{r}w_{,r} = \frac{1}{l_b^2}\nabla^2 M_P\right\}. \tag{7.14}$$

Now, applying the scales $l_a = h \equiv h_p + h_s$, $l_b = R$, and choosing $p_c = \frac{h^2}{R^2}E$ to cancel as many terms as possible in the non-dimensional aspect, we are left with:

$$\frac{R^2}{Eh^2}\left\{D\frac{h}{R^4}\nabla^4 w + \left(N_P - N_O\right)\frac{h}{R^2}\nabla^2 w \ldots \right.$$
$$\left. - N_1\frac{h^3}{R^4}\left(w_{,r}\right)^2 w_{,rr} - N_2\frac{h^3}{R^4}\left(w_{,r}\right)^2\frac{1}{r}w_r = \frac{1}{R^2}\nabla^2 M_P\right\}. \tag{7.15}$$

With collection of terms, we write the dimensionless equation as

$$D^*\nabla^4 w + \left(N_P^* - N_O^*\right)\nabla^2 w \ldots$$
$$- N_1^*\left(w_{,r}\right)^2 w_{,rr} - N_2^*\left(w_{,r}\right)^2\frac{1}{r}w_{,r} = -\nabla^2 M_P^*. \tag{7.16}$$

$$D^* = \frac{1}{12(1-\nu^2)}\frac{h^2}{R^2}, \tag{7.17}$$

$$N_O^* = \frac{P_0}{E}, \tag{7.18}$$

$$N_P^* = \frac{d_{31}V(r)}{h(1-\nu)}, \tag{7.19}$$

$$M_P^* = -\frac{1}{2}\frac{h_s}{h}N_P, \tag{7.20}$$

$$N_1^* = \frac{1}{2(1-\nu)}\frac{h^2}{R^2}, \tag{7.21}$$

$$N_2^* = \nu N_1^*. \tag{7.22}$$

7.3 Different Subcases

With the appropriate length scales assigned, the problem may now be more readily examined by analysis of Equation 7.16.

7.3.1 Linear plate.

$$D^*\nabla^4 w = -\nabla^2 M_P^* \tag{7.23}$$

The linear plate model is the simplest model. In this model, no tension is assumed, such as would be the case with a free edge condition. This is the concept Bekey proposed, in that he imagined a membrane supported only at its center point. The mirror would not be quickly steerable (as Bekey acknowledges) as the inertia term ($I = .25\pi\rho hR^4$, where ρ is density, h is thickness, and R is radius) is large. Alternately, the mirror could be suspended on roller supports at the boundary (perhaps floating in magnetic suspension) to translate and rotate the mirror.

All non-linear terms are neglected if the slopes of the mirror surface are considered small. This may not be a good assumption for the large parabolic dishes, as explored in a later section. If the mirror is also to be used for high spatial fre-

quency shaping of the received image (such as correcting for Zernike aberrations) the assumption would not hold.

While considering the material properties fixed, the effect of altering the diameter or thickness of the mirror can be determined. This might be representative of testing a small-scale structure to see what achievable surface deflection could be obtained with the full-scale structure. To do this, analyze D^* as compared to M^* to find the strength of the forcing as the radius changes. Thus it may be seen:

$$\frac{M_P^*}{D^*} \propto \frac{R^2}{h^2} \tag{7.24}$$

Note here that as the radius increases, or as the thickness decreases, the response of the membrane mirror to an applied voltage will be greater, or conversely, less voltage will be required for a similar response. This is an encouraging result, as we find that although current piezoelectric material (such as PVDF), have a very small dielectric coefficient (of expansion) d_{31}. Linear theory suggests large-scale mirrors may not require great loads create the deformations required, an idea explored in the following sections.

7.3.2 Plate-membrane with Bimorph Actuation.

$$D^*\nabla^4 w - N_O^*\nabla^2 w = -\nabla^2 M_P^* \tag{7.25}$$

In this section, the effect of adding a pre-existing tension field to the mirror is discussed. This is the classical membrane tension that gives rise to drumhead dynamics associated with membrane problems.

To analyze this class of problems, the importance of the N_O^* must be compared to D^*. If D^* is the much larger term, the effect of N_O^* will be simply to attenuate the response of the aforementioned beam problem. If D^* is the much smaller term, it will provide a set of conditions smoothing the membrane response. Figure 7.3 shows the

174

effect of membrane tension, and the demarcation between which is the dominant term. As can be seen, what intuitively might seem to be low tension forces can significantly dominate the solutions. To give a rough idea, imagine suspending a 0.1 meter radius membrane mirror by five tensioned cables providing the catenary support. Each cable would then require a force of on 0.01 newtons before tension would play a central role in the solution (e.g. .08*circumference/number of points, $0.08(2\pi 0.1m)/4 \approx 0.01N$).
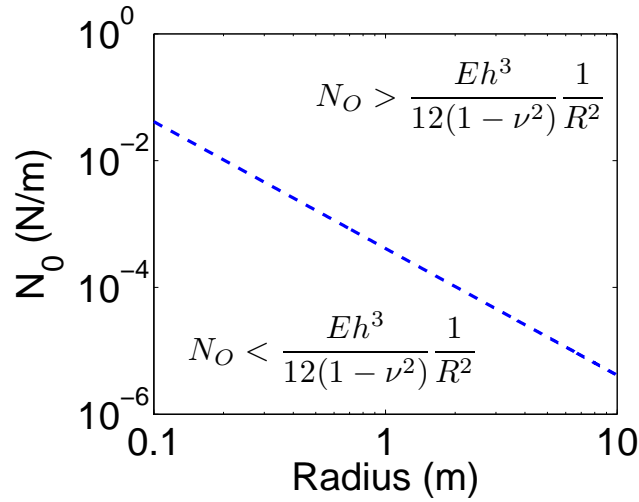
Figure 7.3:   Tensile load versus radius.

Either way, an asymptotic method may be applied. If $D^* \gg N_O^*$, then divide by D^* to yield

$$\nabla^4 w - \delta^2 \nabla^2 w = -\nabla^2 \hat{M}_P^* \tag{7.26}$$

where $\delta^2 \equiv N_O^*(D^*)^{-1}$ and $\hat{M}_P^* \equiv M_P^*(D^*)^{-1}$. Letting $w = w_0 + \delta^2 w_1 + \dots$, one can solve the following series of equations by applying the appropriate boundary conditions:

$$\nabla^4 w_0 = -\nabla^2 \hat{M}_P^* \tag{7.27}$$

$$\nabla^4 w_1 = -\nabla^2 w_0 \tag{7.28}$$

$$\vdots$$

Applying a similar solution methodology for the cases where $N_O^* \gg D^*$, and define $\varepsilon^2 \equiv D^* (N_O^*)^{-1}$ and $\hat{M}_P^* \equiv M_P^* (N_O^*)^{-1}$, thus

$$\varepsilon^2 \nabla^4 w - \nabla^2 w = -\nabla^2 \hat{M}_P^* \tag{7.29}$$

and $w = w_0 + \varepsilon^2 w_1 + \dots$.

$$\nabla^2 w_0 = -\nabla^2 \hat{M}_P^* \tag{7.30}$$

$$\nabla^2 w_1 = -\nabla^4 w_0 \tag{7.31}$$

$$\vdots$$

It is here an important discovery is made. If a voltage pattern is chosen with a spatial frequency of $f(\frac{r}{\varepsilon})$, this asymptotic method will not hold true, as all of the terms in the solution will be of the same order.

For exact solutions to the typical case where the voltage function is simply an indicator (or heaviside) function for axisymmetric rings, the reader is referred to Chapter V.

7.3.3 Plate-membrane with Unimorph Actuation.

$$D^* \nabla^4 w - (N_O^* - N_P^*) \nabla^2 w = -\nabla^2 M_P^* \tag{7.32}$$

The next system of interest is the plate-membrane with unimorph, or single-sided, actuation. This construction is a likely candidate for its simplistic nature in construction–only one side of the membrane must be activated.

In the differential equation, the N_P^* term makes an appearance, adding a level of complexity to this problem not faced with the bimorph construction. This complexity must be carefully treated. For, as $-N_P^* \rightarrow N_O^*$, the tension term vanishes in that area, and the forcing must balance with the D^* term (the plate stiffness). One also has to be aware that the voltage term that contributes to the N_P^* function may vary along the surface, so the dominance of terms in the equation may also vary.

Depending on the sign convention chosen, to initiate a parabolic shape the voltage function may be either positive or negative. For instance, in the finite element models created to date, a positive direction is defined as one from the bottom surface of the reflector, to the top, and the dielectric constants are negative. However, in actual practice, it is likely the ground electrode will be embedded along the neutral axis of the structure, resulting in a change of signs.

This is important because the rear surface may have to be expanded under voltage to draw the mirror into a parabolic shape. Analytic solutions to this form of the equation constitute an area of further research.

7.3.4 Non-linear Plate-membrane.

$$D^* \nabla^4 w + \left(N_P^* - N_O^* \right) \nabla^2 w \ldots$$
$$- N_1^* \left(w_{,r} \right)^2 w_{,rr} - N_2^* \left(w_{,r} \right)^2 \frac{1}{r} w_{,r} = -\nabla^2 M_P^*. \qquad (7.33)$$

The non-linear effects coefficients N_1^* and N_2^* scale to the same order as the plate stiffness term D^*. The non-linear term is especially significant as one recalls w is scaled against the plate thickness. That is, for deflections of several centimeters, the non-linear terms will have the greatest magnitudes, the derivative of the surface will be significant. Additionally, if the dish is deeply curved, or if the surface is actively

177

controlled to create high spatial frequency wavefront corrections (such as higher order Zernike mode shapes), these terms must be included in the analysis.

7.4 Finite Element Examples

A series of finite element examples are presented to demonstrate some of the characteristics of membrane mirrors as determined from the preceding section.

The finite element model used in these examples was previously presented in Chapter IV where the model was evaluated against the AFIT deformable mirror testbed. The model was built using MSC.Nastran. For this application, the construction of the finite element model is briefly summarized, with changes from the preceding models called out.

In this configuration, the model was constructed of 9000 QUAD4 and TRIA3 composite plate elements. In this axisymmetric configuration, all azimuthal degrees of freedom were constrained. Linear and non-linear solvers were used as called for in the discussion. The model parameters that remained constant throughout the analysis are given in Table 7.2. The material properties are for a homogeneous mirror comprised entirely of PVDF, that is, the electrodes and optical coatings are neglected in this simplified model. The piezoelectric coefficients were implemented similar to their introduction in Section 7.2 using the piezoelectric-thermal analogy (see Chapter III). The boundary condition for the edge condition was either a roller or fully clamped support. In some of the roller cases, a radial force was applied at each of the nodes along the edge to create membrane, or pellicle, tension.

Two actuation patterns (forcing functions) are used in this section. The first forcing function is a smoother application of voltage, the *drumhead forcing* function, which corresponds to a statically actuated fundamental vibration mode shape for a pure membrane. The applied voltage for this method is:

$$V(r) = 300 J_0(2.405 \frac{r}{R}) \tag{7.34}$$

variable	description	value
E	Young's modulus	$4 \times 10^9 Nm^2$
h	thickness	$104 \times 10^{-6} m$
ν	Poisson's ratio	0.3
d_{31}	piezoelectric coefficient	$-2.3 \times 10^{-11} mV^{-1}$

where J_0 represents a Bessel function of the first kind.

The second forcing function, *single electrode forcing*, is similar to the center electrode on the AFIT deformable mirror testbed. Piezoelectric forcing is applied by a voltage acting on a center electrode region with a radius of $0.2\times$ of the mirror's radius, R. Thus, the voltage acts like a heaviside function, that is

$$V(r) = \begin{cases} 300, & r \leq 0.2R, \\ 0, & r > 0.2R. \end{cases} \tag{7.35}$$

The voltage patterns are shown in Figure 7.4.
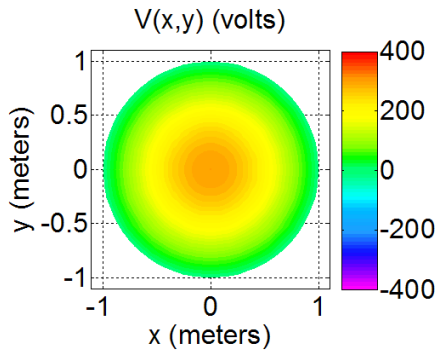
(a) Drumhead forcing actuation voltage.
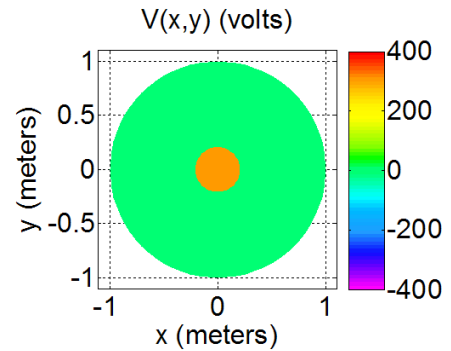
(b) Single electrode actuation voltage.

Figure 7.4:   Actuation voltage functions.

7.4.1   Linear versus Non-linear.   The main impetus for this work was the issue of extrapolating the results from a small-scale test mirror to the larger mirror sizes in the space telescope application. In particular, previously reported in Chapter IV and by researchers at Sandia [134] showed that small-scale models behaved in accordance with linear models. These small-scale models were of the same thickness/construction as proposed for the vast sheets to be used in the space telescopes.

Whether applying linear theory such as the researchers at Sandia or using linear finite element models, the trends will be the same. In Figure 7.5, the effect of varying a single parameter, the radius, is seen while holding all other dimensions and material properties constant. Figure 7.5 shows the out-of-plane displacement of the center node undergoing unimorph actuation by the single electrode voltage function for a plate with clamped boundaries (note that for the linear solver, introducing pellicle tension will have no impact on out-of-plane displacement).

From Equation 7.23, it may be observed that D^* will change inversely proportional to R^2, and thus expect linear solutions to vary accordingly. This is precisely the observed effect, as Figure 7.5 presents the results of many linear simulations for radius varying between 0.1 meters and 10 meters. Indeed, the displacement increases in proportion to the radius squared (a line depicting a constant times R^2 is provided for reference).

From this graph, one might be tempted to make the observation based on linear theory alone, that is, given its success at predicting small-scale model deflection, it may be predicted that large deflections of membranes should be possible using current constructions. As will soon be shown, this observation will prove false.

To show the fallacy of the preceding observation, another series of simulations is conducted, this time comparing linear to non-linear results for different radii. For these examples, the drumhead forcing actuation voltage from Figure 7.4(a) is used (its smoother nature has been qualitatively observed to make the numerical simulations quicker to converge, and is sufficient for the arguments herein). The mirror actuation
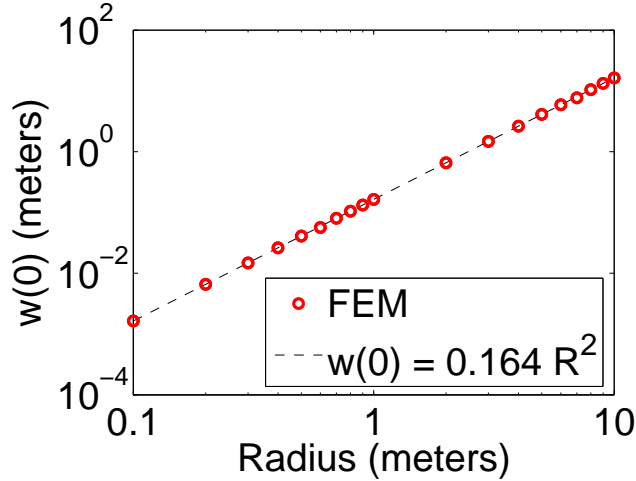
Figure 7.5:   Center displacement for linear plate.

is the bimorph configuration (eliminating any N_P^* terms), and is held in a roller boundary without any applied pellicle tension (no N_0 terms). Two cases are presented, each showing a linear and non-linear solutions. In the first case, a radius of 0.01-m (1 centimeter) to represent a small-scale test article is used, and in the second, a 10-m radius is used representing a space telescope. The results are presented in Figure 7.6.

For the 0.01-m case in Figures 7.6(a) and (b), one may observe that the linear and non-linear case present nearly indistinguishable results (in fact, the height of the center displacement is reported as 3.2647E-5 m for the linear case, and 3.19998E-5 m for the non-linear case, to indicate the graphs are different). However, changing nothing but the radius to obtain the results in Figures 7.6(c) and (d) tells a completely different story. In Figures 7.6(c), the scale of the deflection indeed increases by a factor of $(10^3)^2$, evident by the scale on the graph, while the shape of the plot is identical to the 0.01-m linear case. In contrast, the non-linear solution is severely attenuated, and the solution shape does not resemble any other of the three in the figure.

Next, one may return to the issue of scale for an explanation. The terms N_1^* and N_2^* in Equations 7.21 and 7.22 scale in the same proportion as the plate stiffness with regard to height and radius. Thus, as the plate forces become dominant (increasing ε) the non-linear term also becomes important. Recall that the out-of-plane displace-

181
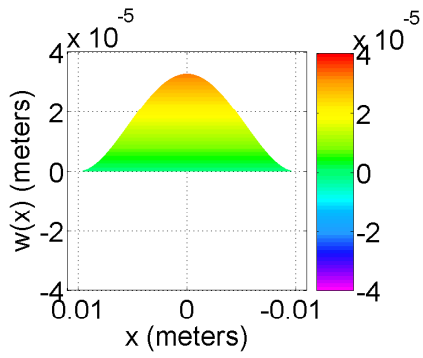
(a) 1-cm radius linear.
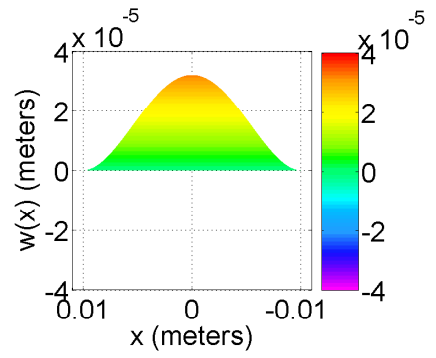
(b) 1-cm radius nonlinear.
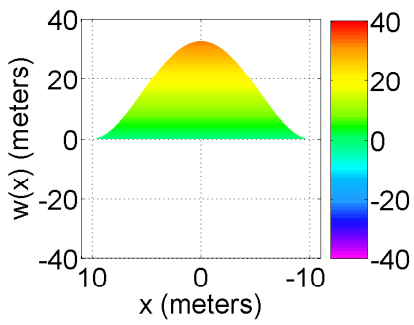
(c) 10-m radius linear.
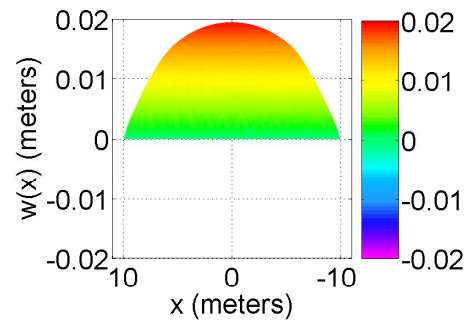
(d) 10-m radius nonlinear.

Figure 7.6:   Effect of changing radius with different solution strategies.

ment $w(r)$ was scaled by the length scale $l_a = h$. Thus displacements greater than the thickness of the substrate $h = 104$ microns (see Table 7.2 will be large displacements (and so will the corresponding slope terms) in Equation 7.16, further "activating" the non-linear terms.

It must therefore be concluded that small-scale modelling may not accurately capture the non-linear effects prevalent in large-scale space telescopes if the thickness of the small-scale and large-scale configurations is the same.

7.4.2 Plate-to-membrane Stiffness Effects. In section 7.3.2, pre-existing pellicle tension was introduced to the differential equation as N_0^*. In this section, the qualitative effect of the ε parameter is presented. Recall ε is defined as:

$$\varepsilon \equiv \frac{D^*}{N_0^*}. \tag{7.36}$$

It is important to remember the terms above are from the scaled problem. Since the original plate stiffness term is extremely small, just about any conceivable value of tension would be large, and one might incorrectly assume that the plate stiffness terms are inconsequential. However, for the small-scale model, one may realize that the plate stiffness is effectively amplified by a factor of R^{-2}. That is, small-scale mirrors in tension will see the effects of plate stiffness much sooner than a large space telescope for a similar tension value.

For the purpose of this comparison, a bimorph mirror of radius 1 meter is assumed. Again, the structure is supported by a roller support, with a pellicle tension force added at the boundary. The forcing was introduced with the single electrode forcing as shown in Figure 7.4(b).

Three cases were run where ε was changed to values of 1, 0.02, 0.004 ($50^0, 50^{-1}, 50^{-2}$), and are presented in Figure 7.7. A pure membrane linear solution (one with no plate or non-linear terms) to the problem would indicate maximum deflections of -0.8293, -3.3173E-004, -1.3269E-007 meters, for the cases respectively. However, note that

the plate stiffness and non-linear terms serve to attenuate the pure membrane linear solution to the results in Figure 7.7.

Again observe the effects of non-linear terms. In Figure 7.7(c), the deflection achieved is on the order of $1000\times$ less than the thickness h of the mirror, and correspondingly the deflection achieved is near that predicted by the pure membrane linear solution. In Figure 7.7(b), the deflection is on the same order as the mirror thickness, or alternately one may note that the deflection is attenuated by nearly half of what the linear membrane theory suggests. Further reductions in tension do much less to increase deflection, as the problem is now a large deflection problem, as shown in Figure 7.7(a).

Finally, the most notable characteristic of the ε term is its influence on the shape of the response. For small ε, as seen in Figure 7.7(c), the deflection is nearly a scaled (though attenuated) version of the input. This "bed of nails" characteristic allows for simplistic surface control algorithms. Again it is emphasized that it would require a much weaker N_0 term to overcome the plate stiffness as the radius is increased. Effectively, one can conclude: the introduction of pellicle tension which might be insignificant for small-scale structures can dominate the surface response on large space telescopes. In fact, if one does not want pellicle tension to dominate the response, care must be taken with with the chosen boundary. This may be one reason Bekey suggests a free edge condition.

Another interesting observation is made. If the impact of non-linear terms is sought to be modelled and verified, it is at the edges of discrete actuators where the slope is greatest that their impact will be the most prevalent. Therefore, to analyze the effects of non-linear terms as observed in Section 7.4.1 which will dominate responses of large-scale structures, we should study the behavior of small-scale models with distinct boundary layers.

7.4.3 The Impact of Unimorph Actuation. Although not the direct result of scaling from small to large structures, a secondary impact of lowering the pellicle
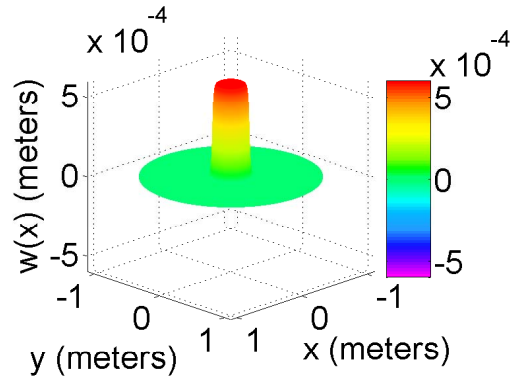
(a) $\varepsilon = 1.00$.
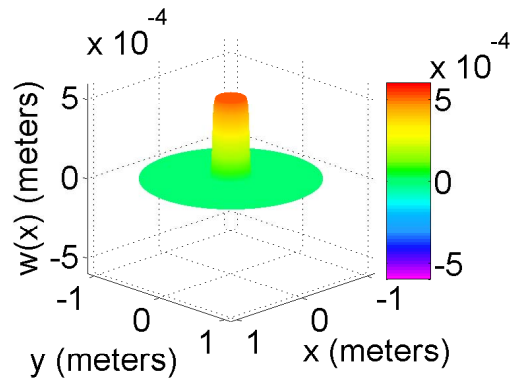
(b) $\varepsilon = 0.02$.
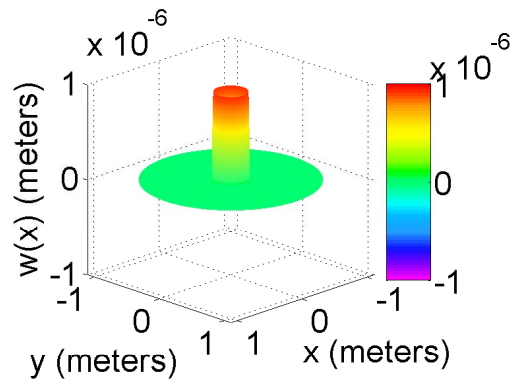
(c) $\varepsilon = 0.0004$.

Figure 7.7:   Non-linear solutions for varying ε.

tension as suggested by results of Section 7.4.2 is that the difference between unimorph and bimorph actuation becomes apparent.

Unimorph actuation is generally regarded as a simpler construct to control, especially when one considers remote actuation (electron gun) technologies which are as yet unproven. In this section the impact of unimorph construction is seen to have far-reaching implications.

The N_P^* term in Equation 7.16 is only present in the unimorph case, and has the ability to dramatically affect the response. To demonstrate its effect, two simulations were conducted. The two cases use unimorph actuation with the drumhead forcing function (Figure 7.4(a)) and the non-linear solution strategy. The mirror has a 1-m radius, and an existing pellicle tension $N_O = 39.426 Nm^{-1}$. When the voltage is applied, it has at its peak value in the center also of $N_P(0) = -39.426 Nm^{-1}$. The voltage is applied first as a positive value, and then the same field is applied, but as a negative value[1]. The results are shown in Figure 7.8.

(a) Positive voltage response.

(b) Negative voltage response.
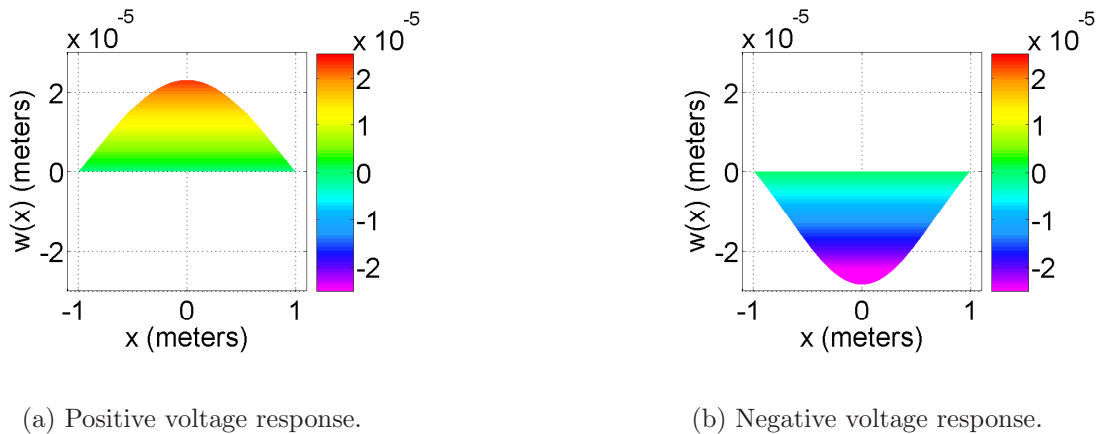
Figure 7.8:   Asymmetric response characteristic of unimorph actuation.

---

[1]This effect was not apparent in Chapter IV due to several factors. The edge tension value was in excess of $N_O = 170\ Nm^{-1}$ around the entire perimeter as reported in Section 4.3.2, the non-uniform silicone/piezoelectric construction of the mirror partially negated the effect of the N_P term, and the piezoelectric material was directional (and thus weaker in the non-primary direction than the case presented here)

Figure 7.8 shows the absolute value of the displacement is greater when the negative voltage was applied compared to the positive voltage case. First note that the scaling applied to the problem impacts both terms similarly, as seen in Equations 7.18 and 7.19, so changes in height and radius will have the same impact on each term. What is observed is $(N_P^* - N_0^*)\nabla^2 w$ in Equation 7.16 acts constructively, and effectively stiffens the response. In the second (the negative voltage) case, the two terms have the same sign, and cancel each other at the center, and otherwise weaken the membrane tension.

Further evidence of the stiffening effects are seen in Figure 7.9. To create this plot, non-linear finite element simulations were run with the single electrode forcing function (positive voltage only), and the pre-existing pellicle tension N_0 and radius were varied while the other parameters in Table 7.2 were held constant. The center displacement was plotted. Observe the following. At large values of N_0^*, the tension dominates the response and limits the magnitude of the response such as would be expected in a pure linear membrane solution. The linear response follows the expected curve $w(0) = M_p/N_0$, which for this example $M_p = 0.001$ and is represented by the dashed line.

Thus, at large N_0^*, the center deflection varies as $\frac{1}{N_0^*}$. However, at low values of N_0^*, the N_P^* becomes the dominant term in the Equation 7.16 until the radius is decreased below a reasonable range (at this point there is little interest in extending results to scale models below the 0.1 meter range). For unimorph construction it was found that the effect of piezoelectric in-plane tension in unimorph construction has the potential to dominate the structural response.

The next most obvious question is, "what happens when the sign of the voltage is changed, and instead of adding to the existing tension, the tensile field within the area of the piezoelectric material is potentially changed to compression?" This is an area of further research. Convergence issues with the finite element model prevent us from displaying results. However, it appears the model is "buckling", and this
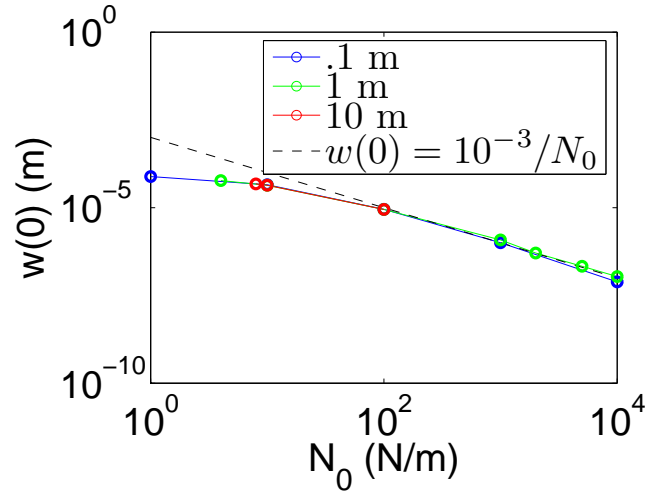
Figure 7.9:   Center displacement with varying tension.

may prove useful in achieving large deformations with a unimorph structure with low
voltage levels and within the realms of current piezoelectric materials.

7.5   Conclusions

This chapter examined the scaling issues associated with the in-plane actuated
deformable mirror for space telescope applications. To gain a better understanding of
the problem at hand, the governing differential equation for the axisymmetric system
less the in-plane strain terms was provided and transformed into a non-dimensional
form for analysis. To demonstrate some of the pertinent points, a finite element model
created in MSC.Nastran was examined.

Much of the research to date has concentrated on examining small-scale models
of membrane optics, where the through-the-thickness construction was assumed to be
of the same type as would be used in a large-scale space telescope, which would result
in tremendous weight savings. However, for the proposed applications, the radius, or
length dimensions, are scaled by orders of magnitude. From the examination of the
scaled non-dimensional equation and demonstrated through the finite element simu-
lations, it was demonstrated that although linear modelling may correctly explain the
behavior of small-scale models, only non-linear models will account for the important

terms when the full scale structure is examined. Furthermore, the achievable surface deformations for a large-scale telescope will be far less than suggested by linear theory, but may still be sufficient to create very shallow, large focal length, high f/#, parabolic membrane mirrors.

By scaling the differential equation, it was shown that the introduction of pellicle (the traditional pre-existing membrane) tension, may dominate the response of the surface deflections for a large-scale space telescope. Early proposals for space telescopes suggested not using any pre-existing pellicle tension–the results herein suggest that if it is introduced, even if it seems to be an intuitively negligible amount, it must also be carefully modelled and examined because of its significant impact on the solution.

By comparing the strength of terms in the governing differential equation, an unexplored consequence and potential benefit of unimorph versus traditional bimorph in-plane actuation strategies was found. The unimorph construction introduces a tension field in proportion to the strength of the piezoelectric forcing function that acts on the structure in the same manner as the pre-existing pellicle tension field (except it may be varied in strength as the voltage field varies). In one direction, it was shown that the piezoelectric tension serves to stiffen the structure and attenuate surface deflections. However, it remains an area of future research for the large-scale mirror to explore the region where piezoelectric tension places localized areas of the membrane in compression, and perhaps the surface may be "buckled" into large deflections with low voltage requirements within the capabilities of current piezoelectric materials and technology.

This chapter on scaling completes our investigation into membrane optics research. As seen throughout this chapter, the word membrane is something of a misnomer, as it implies that all through-the-thickness properties are negligible. This may be true in the case of an electrostatic membrane, where pressure forces are applied directly to the mirror's surface, but is certainly not the case for an in-plane actuated

189

piezoelectric unimorph of bimorph mirror as investigated herein. In the next chapter, a summary of conclusions and a series of recommendations for future work are presented.

VIII. Conclusions and Recommendations

Membrane optics has proved to be a complex, multi-dimensional field where significant advancement in the state-of-the-art is required before the goal of a large aperture space telescope may be realized. The significant findings presented in this document, and recommendations for future work, are provided below.

8.1 Research Conclusions

Experimental testing of a prototype, small-scale, in-plane piezoelectric actuated tensioned plate membrane structure, the construction of which represents the envisioned membrane optics for space telescopes, revealed that wavelength level surface control was possible. It was experimentally demonstrated that low-order Zernike modes can be controlled individually for quasi-static control inputs of 0.02 Hz. The control frequency was well below the fundamental mode of the small-scale structure, but is operationally representative of the low-order dynamic modes of a large structure. To construct a control system, MSC.Nastran can be used as a basis for *a priori* control design versus using experimentally-derived calibration curves.

Next, an exact analytical piecewise linear solution to both the beam-string and plate-membrane problem representative of an in-plane actuated structure characterized by a small (but non-vanishing) normalized plate stiffness-to-tension ratio was developed. Additionally, an approximate solution was also presented. The significant behavior observed was a local piston displacement of an actuated region, with an internal layer the width of which was governed by the plate stiffness-to-tension ratio. It was shown that for very low plate stiffness-to-tension ratios, the surface displacement, or influence function, was step-like. It was further determined that for widely discontinuous actuator spacings, such as which currently exist on the experimental prototype, linear superposition of solutions may be used due to non-intersecting boundary layers.

With both experimental and analytical results in hand, the next phase of the research addressed the perspectives of both the optical and structural engineer. For

191

membrane mirrors, a *clear aperture* region must be defined in which Zernike surfaces are formed to overcome the problem of incompatible boundary conditions that exist with a membrane mirror. A control strategy, coined the *Modal Transformation Method*, was developed which provides an algebraic formulation of the Zernike surfaces in terms of statically-actuated physical mode shapes with a known error budget. It was shown through numerical simulation that the in-plane actuated mirror when controlled by the Modal Transformation Method was capable of achieving low-order Zernike surfaces with high precision.

Finally, an investigation into the problem of scale resulted in three major findings. First, from the examination of the scaled non-dimensional equation and demonstrated through the finite element simulations, it was shown linear modelling may correctly explain the behavior of small-scale models, but only non-linear models will account for the important terms when the full scale structure is examined. Second, the introduction of pellicle (the traditional pre-existing membrane) tension may dominate the response of the surface deflections for a large-scale space telescope, and must be carefully considered in the overall telescope design trade space. Last, a consequence of unimorph versus traditional bimorph in-plane actuation strategies was established. Unimorph, or one-sided, actuation of an in-plane actuated structure introduces stiffening (or weakening) term that will impact the mirror's structural response when it is on the same order as an existing membrane pellicle tension field.

With the significant discoveries of this work thus identified, the focus is now on recommendations for future work given the content of this dissertation.

8.2   Recommendations for Additional Research

An esteemed professor once said, "additional understanding of the problem is always accompanied [by] additional questions [33]." For this investigation of membrane optics, it is the progress in its understanding that brings to light the potential for future research.

8.2.1 Research Continuation. Based on the conclusions of this document together with the understanding now developed, several issues require further investigation.

Membrane dynamics represent the next logical step in understanding the performance capabilities of the in-plane actuated deformable mirror. At the heart of the problem is acquiring a better understanding of the piezoelectric dynamic response without the assumed quasi-static conditions. Presumably, hysteretic and non-linear coupling of electromagnetic and elastic behavior will exist in the actuator, and its impact is not fully understood for the optical scale problem. Less daunting is the challenge of controlling the structural response to dynamic excitation. Additionally the effects on wrinkling and other non-linear structural behavior require further exploration.

For the researcher investigating membrane optics, continued reliance on small-scale test articles will be the norm, not the exception. From the scaling results presented, future efforts should be made to try to magnify the non-linearities that already exist, rather than accepting a linear model that generally seems to model the observed behavior. As it is unlikely without further research in high-force piezoelectric material that large deflections in small scale models will occur. Researchers should instead seek to create sharp discontinuities in the applied voltage by using discrete actuators. In the boundary layer created at the edge of actuators, the effect of the non-linear terms would be amplified against which models could be verified which in turn could be used to later simulate large-scale structures.

Another construct which could be investigated in small scale structures is the piezoelectric effect unique to unimorph actuation. With voltage applied in one direction, it was shown that with unimorph actuation the piezoelectric tension serves to stiffen the structure and attenuate surface deflections, while in the other direction the structure is weakened. It is the weakened, or compressive state, that may hold the key to achieving large deflections of an in-plane actuated mirror's surface. Through

193

further research it may be found that the unimorph construction technique, in addition to being a simpler construction than the bimorph, may also be preferred from a performance standpoint, whereas in the literature the bimorph construction is normally recognized as the preferred actuation method due to its ease of mathematical modelling.

8.2.2 System Level Investigations. Further areas of study will be required for membrane optics to be successfully realized. Some of these areas are highlighted below.

Developments are needed in the field of remote actuation of a piezoelectric surface. The proposed electron gun actuation method has not been realized, and merits renewed investigation given the potential of the in-plane actuated structure to revolutionize the deformable mirror industry. Alternate methods for remote actuation should be investigated, such as using lasers with MEMs photovoltaic converters or silicon layered meshes, to produce the grid of fine electrodes.

The deployment of a membrane structure is also a problem for the structural engineer. Folding the mirror compactly and unfurling it in a zero-g environment has never been demonstrated, but is a steadfast requirement. Shaping the mirror from flat to a curved parabolic structure should be possible based on the results herein, but the attendant effects on changing from a 2-D (flat) structure to 3-D (doubly curved, or spherical) structure have not been formally explored as they have for a pressurized lenticular solution.

Additional challenges are associated with large focal length, low-weight optical systems, which will require station-keeping on scales more stringent then even laser communication or laser weapon systems. The space environmental effects on a membrane mirror in low-earth orbit have also not been determined–especially the response to solar drag and thermal disturbances.

Appendix A. Error analysis and Least Squares Approximations

An understanding of the underlying norms in the linear space is essential when conducting error analysis and finding least squares solutions. It may be helpful to review these principles for situations encountered in this research.

The least squares approximation seeks to minimize the error between two functions. To approximate an arbitrary square integrable function f, write another function g that is a linear combination of basis functions spanning a subspace of dimension n of the domain of f:

$$g \equiv c_1 \Phi_1 + c_2 \Phi_2 + \ldots + c_n \Phi_n = \sum_{j=1}^{n} c_j \Phi_j. \tag{A.1}$$

Generically in one dimension the square of the 2-norm is minimized, where the weighted 2-norm is defined by

$$\|f - g\|_2 = \left(\int_a^b w[f - \sum_{j=1}^{n} c_j \Phi_j]^2 dx \right)^{\frac{1}{2}}. \tag{A.2}$$

The coefficients c_j may be shown to be minimized using the projection theorem,

$$c_j = \sum_{j=1}^{n} \frac{(f, \Phi_j)}{(\Phi_j, \Phi_j)} \tag{A.3}$$

If the domain is discretized by sampling at N points $(N > n)$ with equal spacing Δx, the following system may be written:

$$\boldsymbol{f} - \boldsymbol{g} = \boldsymbol{f} - \begin{bmatrix} \boldsymbol{\Phi}_1 & \boldsymbol{\Phi}_2 & \ldots & \boldsymbol{\Phi}_n \end{bmatrix} \boldsymbol{c} = \boldsymbol{f} - [A]\boldsymbol{c}. \tag{A.4}$$

where the vectors are given by the notation $\boldsymbol{v} = \{v_1, v_2, \ldots, v_N\}^T$.

The discretized, non-square, system is approximated when the square of the 2-norm of the error is minimized, where the weighted 2-norm is given by

$$\|\boldsymbol{f} - \boldsymbol{g}\|_2 = \left(\sum_{i=1}^{N} w_i [f_i - g_i]^2 \right)^{\frac{1}{2}} \tag{A.5}$$

using the pseudo-inverse, and the coefficient vector $\boldsymbol{c}$ is given by

$$\boldsymbol{c} = \frac{[A]^T [W]}{([A]^T [W][A])^{-1}} \boldsymbol{f} \tag{A.6}$$

where the weighting matrix is the diagonal matrix defined as

$$[W] \equiv \begin{bmatrix} w_1 & 0 & & \\ 0 & w_2 & & \\ & & \ddots & \\ & & & w_N \end{bmatrix} \tag{A.7}$$

However, although in both the functional and discrete case the appropriate 2-norm of the error is minimized, the residual error is not necessarily the same, that is:

$$\|f - g\|_2 \neq \|\boldsymbol{f} - \boldsymbol{g}\|_2 \tag{A.8}$$

To alleviate this condition, redefine the vector norm to the N-dimensional space with "a scaling that provides for a continuous passage from a vector to a function norm" [69]. This weighted discretized Euclidean norm depends the step size Δx and is given by

$$\|\boldsymbol{f} - \boldsymbol{g}\|_\Delta = \left(\Delta x \sum_{i=1}^{N} w_i [f_i - g_i]^2 \right)^{\frac{1}{2}}. \tag{A.9}$$

It is therefore straightforward to see that the limit of the discretized Euclidean norm approaches the functional 2-norm as the Δx approaches zero. That is,

$$\lim_{\Delta x \to 0} \|\boldsymbol{f} - \boldsymbol{g}\|_\Delta = \left(\int_a^b w[f - g]^2 dx \right)^{\frac{1}{2}} = \|f - g\|_2. \tag{A.10}$$

The results may readily be expanded to cylindrical coordinates with spacings Δr and $\Delta \theta$ in the radial and azimuthal directions, respectively. In cylindrical coordinates, the discrete Euclidean norm is

$$\|\boldsymbol{f} - \boldsymbol{g}\|_{\Delta} = \left(\Delta r \Delta \theta \sum_{i=1}^{N} r_i [f_i(r_i, \theta_i) - g_i(r_i, \theta_i)]^2\right)^{\frac{1}{2}}. \qquad (A.11)$$

Assuming a circular domain with unit radius, this limit of the vector norm as the step size decreases is

$$\lim_{\Delta r, \Delta \theta \to 0} \|\boldsymbol{f} - \boldsymbol{g}\|_{\Delta} = \left(\int_0^{2\pi} \int_0^1 [f - g]^2 r \, dr \, d\theta\right)^{\frac{1}{2}} = \|f - g\|_2. \qquad (A.12)$$

This result will give us a stable error term to use for comparisons with differing grid sizes for instance. Compare this norm to the familiar Root Mean Square error, which does not account for the weighting factor, and does not readily account differing grid spaces on orthogonal axes within the vectors themselves:

$$E_{RMS} \equiv \frac{1}{N} \left(\sum_{i=1}^{N} [f_i - g_i]^2\right)^{\frac{1}{2}}. \qquad (A.13)$$

Appendix B. Finite Element Model Input Deck

A sample of the MSC.Nastran input deck, or .bdf file, is included here for reference.

This is the case for the AFIT deformable mirror in Chapter IV with properties defined in Tables 4.2 and 4.3. In this example, the equivalent of 600 Volts is applied to the center actuator. The edge tension is set according to Equation 4.2. The grid, element, and temperature entries are not shown in their entirety.

```
ID MAJ SHEPHERD MEMBRANE NON-LINEAR STATIC ANALYSIS (CYLINDRICAL COORDINATES)
SOL 106  $NLSTATIC
TIME 100
CEND
LINE = 999
TITLE = CIRCULAR MEMBRANE
SUBTITLE = VARY TENSION
SPC = 10
DISPLACEMENT = ALL
STRESS = ALL
SUBCASE 1
NLPARM = 201
LOAD = 1000
SUBCASE 2
LOAD = 1000
NLPARM = 202
TEMPERATURE(LOAD) = 1003
TEMPERATURE(INITIAL) = 1004
BEGIN BULK
$   1  ..   2  ..   3  ..   4  ..   5  ..   6  ..   7  ..   8  ..   9  ..  10  .
$CORD2C    CID     RID      A1      A2      A3      B1      B2      B3
$          C1      C2      C3
CORD2C      1              0.      0.      0.      0.      0.      1.
            1.      0.      1.
$GRDSET            CP                              CD      PS
$GRDSET             1                               1       2
GRID,   1 , 1, 0.00000,  0.0000, 0.0,1

GRID,9001 , 1, 0.06350, 355.0000, 0.0,1
 FORCE , 1000 , 8930 , 1 , 0.9915, 1.0 , 0.0 , 0.0
 FORCE , 1000 , 8931 , 1 , 0.9643, 1.0 , 0.0 , 0.0
 FORCE , 1000 , 8932 , 1 , 0.9477, 1.0 , 0.0 , 0.0
 FORCE , 1000 , 8933 , 1 , 0.9420, 1.0 , 0.0 , 0.0
 FORCE , 1000 , 8934 , 1 , 0.9477, 1.0 , 0.0 , 0.0
 FORCE , 1000 , 8935 , 1 , 0.9643, 1.0 , 0.0 , 0.0
 FORCE , 1000 , 8936 , 1 , 0.9915, 1.0 , 0.0 , 0.0
 FORCE , 1000 , 8937 , 1 , 1.0284, 1.0 , 0.0 , 0.0
 FORCE , 1000 , 8938 , 1 , 1.0740, 1.0 , 0.0 , 0.0
 FORCE , 1000 , 8939 , 1 , 1.1267, 1.0 , 0.0 , 0.0
 FORCE , 1000 , 8940 , 1 , 1.1850, 1.0 , 0.0 , 0.0
 FORCE , 1000 , 8941 , 1 , 1.2472, 1.0 , 0.0 , 0.0
 FORCE , 1000 , 8942 , 1 , 1.3113, 1.0 , 0.0 , 0.0
 FORCE , 1000 , 8943 , 1 , 1.3754, 1.0 , 0.0 , 0.0
```

```
FORCE , 1000 , 8944 , 1 , 1.4376, 1.0 , 0.0 , 0.0
FORCE , 1000 , 8945 , 1 , 1.4960, 1.0 , 0.0 , 0.0
FORCE , 1000 , 8946 , 1 , 1.5487, 1.0 , 0.0 , 0.0
FORCE , 1000 , 8947 , 1 , 1.5942, 1.0 , 0.0 , 0.0
FORCE , 1000 , 8948 , 1 , 1.6311, 1.0 , 0.0 , 0.0
FORCE , 1000 , 8949 , 1 , 1.6583, 1.0 , 0.0 , 0.0
FORCE , 1000 , 8950 , 1 , 1.6750, 1.0 , 0.0 , 0.0
FORCE , 1000 , 8951 , 1 , 1.6806, 1.0 , 0.0 , 0.0
FORCE , 1000 , 8952 , 1 , 1.6750, 1.0 , 0.0 , 0.0
FORCE , 1000 , 8953 , 1 , 1.6583, 1.0 , 0.0 , 0.0
FORCE , 1000 , 8954 , 1 , 1.6311, 1.0 , 0.0 , 0.0
FORCE , 1000 , 8955 , 1 , 1.5942, 1.0 , 0.0 , 0.0
FORCE , 1000 , 8956 , 1 , 1.5487, 1.0 , 0.0 , 0.0
FORCE , 1000 , 8957 , 1 , 1.4960, 1.0 , 0.0 , 0.0
FORCE , 1000 , 8958 , 1 , 1.4376, 1.0 , 0.0 , 0.0
FORCE , 1000 , 8959 , 1 , 1.3754, 1.0 , 0.0 , 0.0
FORCE , 1000 , 8960 , 1 , 1.3113, 1.0 , 0.0 , 0.0
FORCE , 1000 , 8961 , 1 , 1.2472, 1.0 , 0.0 , 0.0
FORCE , 1000 , 8962 , 1 , 1.1850, 1.0 , 0.0 , 0.0
FORCE , 1000 , 8963 , 1 , 1.1267, 1.0 , 0.0 , 0.0
FORCE , 1000 , 8964 , 1 , 1.0740, 1.0 , 0.0 , 0.0
FORCE , 1000 , 8965 , 1 , 1.0284, 1.0 , 0.0 , 0.0
FORCE , 1000 , 8966 , 1 , 0.9915, 1.0 , 0.0 , 0.0
FORCE , 1000 , 8967 , 1 , 0.9643, 1.0 , 0.0 , 0.0
FORCE , 1000 , 8968 , 1 , 0.9477, 1.0 , 0.0 , 0.0
FORCE , 1000 , 8969 , 1 , 0.9420, 1.0 , 0.0 , 0.0
FORCE , 1000 , 8970 , 1 , 0.9477, 1.0 , 0.0 , 0.0
FORCE , 1000 , 8971 , 1 , 0.9643, 1.0 , 0.0 , 0.0
FORCE , 1000 , 8972 , 1 , 0.9915, 1.0 , 0.0 , 0.0
FORCE , 1000 , 8973 , 1 , 1.0284, 1.0 , 0.0 , 0.0
FORCE , 1000 , 8974 , 1 , 1.0740, 1.0 , 0.0 , 0.0
FORCE , 1000 , 8975 , 1 , 1.1267, 1.0 , 0.0 , 0.0
FORCE , 1000 , 8976 , 1 , 1.1850, 1.0 , 0.0 , 0.0
FORCE , 1000 , 8977 , 1 , 1.2472, 1.0 , 0.0 , 0.0
FORCE , 1000 , 8978 , 1 , 1.3113, 1.0 , 0.0 , 0.0
FORCE , 1000 , 8979 , 1 , 1.3754, 1.0 , 0.0 , 0.0
FORCE , 1000 , 8980 , 1 , 1.4376, 1.0 , 0.0 , 0.0
FORCE , 1000 , 8981 , 1 , 1.4960, 1.0 , 0.0 , 0.0
FORCE , 1000 , 8982 , 1 , 1.5487, 1.0 , 0.0 , 0.0
FORCE , 1000 , 8983 , 1 , 1.5942, 1.0 , 0.0 , 0.0
FORCE , 1000 , 8984 , 1 , 1.6311, 1.0 , 0.0 , 0.0
FORCE , 1000 , 8985 , 1 , 1.6583, 1.0 , 0.0 , 0.0
FORCE , 1000 , 8986 , 1 , 1.6750, 1.0 , 0.0 , 0.0
FORCE , 1000 , 8987 , 1 , 1.6806, 1.0 , 0.0 , 0.0
FORCE , 1000 , 8988 , 1 , 1.6750, 1.0 , 0.0 , 0.0
FORCE , 1000 , 8989 , 1 , 1.6583, 1.0 , 0.0 , 0.0
FORCE , 1000 , 8990 , 1 , 1.6311, 1.0 , 0.0 , 0.0
FORCE , 1000 , 8991 , 1 , 1.5942, 1.0 , 0.0 , 0.0
FORCE , 1000 , 8992 , 1 , 1.5487, 1.0 , 0.0 , 0.0
FORCE , 1000 , 8993 , 1 , 1.4960, 1.0 , 0.0 , 0.0
FORCE , 1000 , 8994 , 1 , 1.4376, 1.0 , 0.0 , 0.0
FORCE , 1000 , 8995 , 1 , 1.3754, 1.0 , 0.0 , 0.0
FORCE , 1000 , 8996 , 1 , 1.3113, 1.0 , 0.0 , 0.0
FORCE , 1000 , 8997 , 1 , 1.2472, 1.0 , 0.0 , 0.0
FORCE , 1000 , 8998 , 1 , 1.1850, 1.0 , 0.0 , 0.0
FORCE , 1000 , 8999 , 1 , 1.1267, 1.0 , 0.0 , 0.0
FORCE , 1000 , 9000 , 1 , 1.0740, 1.0 , 0.0 , 0.0
FORCE , 1000 , 9001 , 1 , 1.0284, 1.0 , 0.0 , 0.0
$   1  ..   2  ..   3  ..   4  ..
$TEMP  ..  SID ..   G1 ..   T1 ..
```

```
TEMP      1003            1 11.54E6


TEMP      1003         1801 11.54E6
TEMP      1003         1802  0.00E6


TEMP      1003         9001  0.00E6
TEMPD     1003         0.0
TEMPD     1004         0.0
CTRIA3       1      400        1        2        3        0


CTRIA3      72      400        1       73        2        0
CQUAD4      73      400        2       74       75        3        0


CQUAD4    9000      401     8929     9001     8930     8858        0
PARAM   COUPMASS-1
PARAM   LGDISP  1
PARAM   K6ROT   1.0E6
$EIGRL  SID      V1       V2       ND
EIGRL   200                        20
$NLPARM ID       NINC     DT       KMETHOD KSTEP    MAXITER CONV
NLPARM  201      20       0.0      AUTO             9999    PWU
NLPARM  202      50       0.0      AUTO             9999    PWU
        1E-3
$   1  ..  2  ..  3  ..  4  ..  5  ..  6  ..  7  ..  8  ..  9  .. 10  .
$PCOMP  PID      Z0       NSM      SB      FT       TREF     GE      LAM
PCOMP   400      -.001552                         0.0      0.2
$       MATID    T
        100   0.000052
$       MATID    T
        101   0.000500
$       MATID    T
        101   0.000500
$       MATID    T
        101   0.000500
PCOMP   401      -.001552                         0.0      0.2
$       MATID    T
         99   0.000052
$       MATID    T
        101   0.000500
$       MATID    T
        101   0.000500
$       MATID    T
        101   0.000500
$MAT1   MID            E        G       NU       RHO      A       TREF
MAT1    99       4.00E9          0.300   1.78E3   0.0      0.0
$MAT2   MID          G11      G12      G13      G22      G23      G33      RHO
$            A1      A2       A3       TREF     GE
MAT2    100      4.40E9   1.32E9  0.00E9   4.40E9   0.00E9   1.54E9   1.78E3
        -0.3E-11-2.3E-11 0.0E-11    0.0
MAT1    101      1.013E6         0.497   1020.0   0.0      0.0
ENDDATA
```

Appendix C.   Piezoelectric Moment Calculations

The purpose of this appendix is to provide an example calculation of the moment strength, and show the equivalent representation of the moment forcing terms in the polar-cylindrical and Cartesian coordinate systems. The methods may be applied to the examples throughout the document.

C.1   Strength of Piezoelectric Moment

Begin by referencing Figure 3.3 and Equation 3.104. It is noted in this example, the actuation layer is represented by the thickness h_p and the inert substrate layer is represented by the thickness h_s. The actuating layer is below the inert layer as shown in the figure. Equation 3.104 is repeated below as:

$$M_1^P = \frac{E_p}{1 - \nu_p} \int_Z \left(\cos^2 \theta d_{31} + \sin^2 \theta d_{32} \right) \frac{V_3}{h_p} z dz \qquad (C.1)$$

Integrating for the limits shown in Figure 3.3 depend on the location of the neutral axis. For this example, assume the neutral axis is for materials of the same Young's modulus and Poisson's ratio (otherwise these procedures could be amended using the techniques in Section 3.4.4). Equation 3.104 is re-written with the limits of integration written explicitly:

$$M_1^P = \frac{E_p}{1 - \nu_p} \int_{\frac{-(h_s+h_p)}{2}}^{\frac{-(h_s-h_p)}{2}} \left(\cos^2 \theta d_{31} + \sin^2 \theta d_{32} \right) \frac{V_3}{h_p} z dz + \int_{\frac{-(h_s-h_p)}{2}}^{\frac{(h_s+h_p)}{2}} 0 z dz. \qquad (C.2)$$

The second integral term has no value and indicates the integration through the inert substrate layer. It will be subsequently dropped. To further simplify the expression, assume the isotropic piezoelectric condition where $d_{31} = d_{32}$, and note that none of the material properties are assumed to vary in the z-direction. Thus rewrite Equation C.2 as

$$M_1^P = \frac{E_p}{1 - \nu_p} d_{31} \frac{V_3}{h_p} \int_{\frac{-(h_s+h_p)}{2}}^{\frac{-(h_s-h_p)}{2}} z \, dz. \tag{C.3}$$

Now perform the integration

$$M_1^P = \frac{E_p}{1 - \nu_p} d_{31} \frac{V_3}{h_p} \frac{z^2}{2} \Big|_{\frac{-(h_s+h_p)}{2}}^{\frac{-(h_s-h_p)}{2}}. \tag{C.4}$$

Substitute for z in the above equation and simplify with the following steps.

$$M_1^P = \frac{E_p}{1 - \nu_p} d_{31} \frac{V_3}{h_p} \left(\frac{(\frac{(h_s-h_p)}{2})^2}{2} - \frac{(\frac{(h_s+h_p)}{2})^2}{2} \right), \tag{C.5}$$

$$= \frac{E_p}{1 - \nu_p} d_{31} \frac{V_3}{h_p} \left(\frac{(\frac{(h_s^2 - 2h_s h_p + h_p^2)}{4})}{2} - \frac{(\frac{h_s^2 + 2h_s h_p + h_p^2}{4})}{2} \right), \tag{C.6}$$

$$= \frac{E_p}{1 - \nu_p} d_{31} \frac{V_3}{h_p} \left(\frac{(\frac{-4h_s h_p}{4})}{2} \right), \tag{C.7}$$

$$= -\frac{1}{2} \frac{E_p}{1 - \nu_p} d_{31} V_3 h_s. \tag{C.8}$$

As an example, values could be substituted into this equation. Using the values from Table 5.3,

$$M_1^P = -\frac{1}{2} \frac{4.0 \times 10^6}{1 - 0.3} (-2.3 \times 10^{-11})(192.4)100 \times 10^{-6} H(r, \theta) \tag{C.9}$$

$$= 1.26 \times 10^{-3} H(r, \theta) \tag{C.10}$$

where $H(r, \theta)$ represents the indicator function as in Equation 5.2. The final units for M_1^P are Newtons (N), as previously indicated in Table 5.1.

C.2 Transformation to Cartesian Coordinates

It may be desired, as it is in Chapter V, to relate the moment forcing function in polar-cylindrical coordinates to the Cartesian coordinate system. This could be done from first principles, as in the text by Nayfeh and Pai [94]. In this section, another method is shown from the results of Chapter III.

That is, from Equation 3.146, it is desired to have an equivalent form of the moment forcing in the Cartesian coordinate system. Specifically, one might question if the following equation is valid:

$$-\{\frac{\partial^2}{\partial r^2} + \frac{2}{r}\frac{\partial}{\partial r}\}M_1^P - \{\frac{1}{r^2}\frac{\partial^2}{\partial \theta^2} - \frac{1}{r}\frac{\partial}{\partial r}\}M_2^P \cdots$$
$$- \{\frac{2}{r}\frac{\partial^2}{\partial r \partial \theta} + \frac{2}{r^2}\frac{\partial}{\partial \theta}\}M_6^P = -\frac{\partial^2}{\partial x^2}M_x^P - \frac{\partial^2}{\partial y^2}M_y^P \tag{C.11}$$

where

$$M_x^P = \frac{E_p}{1-\nu_p}\int_Z d_{31}\frac{V_3}{h_p}zdz \tag{C.12}$$

$$M_y^P = \frac{E_p}{1-\nu_p}\int_Z d_{32}\frac{V_3}{h_p}zdz. \tag{C.13}$$

For the isotropic case where $d_{31} = d_{32}$ this is easily verified, as $M_1^P = M_2^P$, $M_6^P = 0$, and $M_x^P = M_y^P$. Equation C.11 therefore becomes

$$-\{\frac{\partial^2}{\partial r^2} + \frac{2}{r}\frac{\partial}{\partial r}\}M_1^P - \{\frac{1}{r^2}\frac{\partial^2}{\partial \theta^2} - \frac{1}{r}\frac{\partial}{\partial r}\}M_1^P = -\frac{\partial^2}{\partial x^2}M_x^P - \frac{\partial^2}{\partial y^2}M_x^P, \tag{C.14}$$

$$-\{\frac{\partial^2}{\partial r^2} + \frac{1}{r}\frac{\partial}{\partial r} + \frac{1}{r^2}\frac{\partial^2}{\partial \theta^2}\}M_1^P = -\frac{\partial^2}{\partial x^2}M_x^P - \frac{\partial^2}{\partial y^2}M_x^P, \tag{C.15}$$

$$-\nabla^2 M_1^P = -\nabla^2 M_x^P. \tag{C.16}$$

In Equation C.16, the Laplacian operator is substituted appropriately. Recognizing that for the isotropic case $M_1^P = M_x^P$, it is therefore shown the polar cylindrical and Cartesian formulations are equivalent.

For the non-isotropic case where $d_{31} \neq d_{32}$, a straightforward explanation is more tedious. To show formally, the derivatives of Equation C.11 must be expanded using the chain rule since M_1^P, M_2^P, M_6^P are functions of r and θ (it is noted the V_3 component is a function $V_3(r, \theta, z)$ in Equation 3.104 through 3.106). For example

$$\frac{\partial}{\partial\theta} M_1^P = \frac{\partial}{\partial\theta}\left(\frac{E_p}{1-\nu_p} \int_Z \left(\cos^2\theta d_{31} + \sin^2\theta d_{32} \right) \frac{V_3}{h_p} z \, dz \right) \tag{C.17}$$

$$= \frac{E_p}{1-\nu_p} \frac{1}{h_p} \int_Z z \, dz \frac{\partial}{\partial\theta}\left(\left(\cos^2\theta d_{31} + \sin^2\theta d_{32} \right) V_3 \right) \tag{C.18}$$

$$= \frac{E_p}{1-\nu_p} \frac{1}{h_p} \int_Z z \, dz \left(\frac{\partial}{\partial\theta}\left(\cos^2\theta d_{31} + \sin^2\theta d_{32} \right) \frac{V_3}{h_p} + \ldots \right.$$
$$\left. \left(\cos^2\theta d_{31} + \sin^2\theta d_{32} \right) \frac{\partial}{\partial\theta} V_3 \right). \tag{C.19}$$

After performing all the derivative operations on the terms on the left hand side of Equation C.11, one will be left with

$$-\left\{ \frac{\partial^2}{\partial r^2} + \frac{2}{r}\frac{\partial}{\partial r} \right\} M_1^P - \left\{ \frac{1}{r^2}\frac{\partial^2}{\partial\theta^2} - \frac{1}{r}\frac{\partial}{\partial r} \right\} M_2^P \cdots$$
$$-\left\{ \frac{2}{r}\frac{\partial^2}{\partial r\partial\theta} + \frac{2}{r^2}\frac{\partial}{\partial\theta} \right\} M_6^P = \ldots$$
$$- \frac{E_p}{1-\nu_p} \frac{d_{31}}{h_p} \int_Z z \, dz \left(\cos^2\theta \frac{\partial^2}{\partial r^2} - \frac{2\sin\theta\cos\theta}{r}\frac{\partial^2}{\partial r\partial\theta} \cdots \right.$$
$$\left. + \frac{2\sin\theta\cos\theta}{r^2}\frac{\partial}{\partial\theta} + \frac{\sin^2\theta}{r}\frac{\partial}{\partial r} + \frac{\sin^2\theta}{r^2}\frac{\partial^2}{\partial\theta^2} \right) V_3 \cdots$$
$$- \frac{E_p}{1-\nu_p} \frac{d_{32}}{h_p} \int_Z z \, dz \left(\sin^2\theta \frac{\partial^2}{\partial r^2} + \frac{2\sin\theta\cos\theta}{r}\frac{\partial^2}{\partial r\partial\theta} \cdots \right.$$
$$\left. - \frac{2\sin\theta\cos\theta}{r^2}\frac{\partial}{\partial\theta} + \frac{\cos^2\theta}{r}\frac{\partial}{\partial r} + \frac{\cos^2\theta}{r^2}\frac{\partial^2}{\partial\theta^2} \right) V_3. \tag{C.20}$$

Note that the terms in the parentheses on the right hand side of Equation C.20 indicate linear operators acting on V_3. Recognizing these linear operators are exactly the linear operators for $\frac{\partial^2}{\partial x^2}$ and $\frac{\partial^2}{\partial y^2}$ [121, pp. 111-112] expressed in polar-cylindrical coordinates, Equation C.20 simplifies to

$$
\begin{aligned}
- \{\frac{\partial^2}{\partial r^2} + \frac{2}{r}\frac{\partial}{\partial r}\}M_1^P - \{\frac{1}{r^2}\frac{\partial^2}{\partial \theta^2} - \frac{1}{r}\frac{\partial}{\partial r}\}M_2^P \cdots & \\
- \{\frac{2}{r}\frac{\partial^2}{\partial r \partial \theta} + \frac{2}{r^2}\frac{\partial}{\partial \theta}\}M_6^P = & \\
- \frac{E_p}{1-\nu_p}\frac{d_{31}}{h_p}\int_Z zdz \frac{\partial^2}{\partial x^2}V_3 - \frac{E_p}{1-\nu_p}\frac{d_{32}}{h_p}\int_Z zdz \frac{\partial^2}{\partial y^2}V_3 & \qquad \text{(C.21)}
\end{aligned}
$$

As the constant values with respect to x and y may be brought inside the derivative operations, Equation C.21 may simply be re-written as Equation C.11, thus demonstrating the equivalence of the expressions in the polar-cylindrical and Cartesian coordinate systems.

Appendix D. Wavescope Information

The purpose of this appendix is to document two issues when using the Wavescope wavefront sensor to obtain data. The Wavescope uses Shack-Hartmann sensing to collect data on an aberrated wavefront, as is any introductory optics text book such as the text by Goodman [54]. Using the 42 coefficients (c_i) provided by the Wavefront sensor, the aberrated wavefront is given by the equation:

$$w(r, \theta) = \sum_{i=1}^{42} c_i Z_i. \tag{D.1}$$

The Zernike polynomials in this summation are the "Wavescope Zernikes" identified by index in Table D.1.

The first issue is that the normalization coefficient is included in the Wavescope Zernike coefficients and *must not be reapplied.*

The second issue is in how the angle is measured for applying the Wavescope Zernike data. Given the Zernike coefficients, the appropriate angle is measured clockwise from the 12 o'clock position. Figure D.1 graphically depicts this angle as the traditional Zernike angle, θ_Z. The reader may be more comfortable with the right hand coordinate system with measurement of angle here termed the mathematical angle, θ_M. Finally note, this angle may not be consistent depending on software version.

The following equation converts mathematical angle traditional Zernike angle and vice versa.

$$\theta_Z = -\theta_M + 90 \tag{D.2}$$

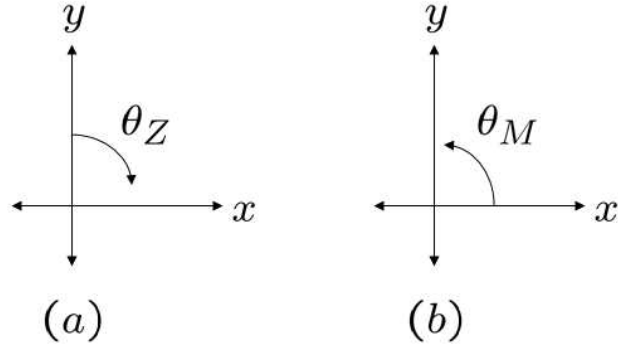$$\theta_M = -\theta_Z - 90 \tag{D.3}$$

Figure D.1: Angle for Zernike polynomial: (a) Traditional, (b) Mathematical.

Table D.1: Wavescope polynomials compared to other numbering schemes.

Wavescope Index	Noll's Index	Traditional Index	m	n	m+n	Normalization	Polynomial
0	1	1	0	0	0	0	1 $(Piston)$
1	2	3	1	1	2	2	$rcos(\theta)$ $(XTilt)$
2	3	2	1	1	2	2	$rsin(\theta)$ $(YTilt)$
3	4	5	0	2	2	$\sqrt{3}$	$2r^2 - 1$ $(Focus)$
4	6	6	2	2	4	$\sqrt{6}$	$r^2cos(2\theta)$ $(0 Astigmatism)$
5	5	4	2	2	4	$\sqrt{6}$	$r^2sin(2\theta)$ $(45 Astigmatism)$
6	8	9	1	3	4	$\sqrt{8}$	$(3r^2 - 2)rcos(\theta)$ $(XComa)$
7	7	8	1	3	4	$\sqrt{8}$	$(3r^2 - 2)rsin(\theta)$ $(YComa)$
8	11	13	0	4	4	$\sqrt{5}$	$6r^4 - 6r^2 + 1$ $(Spherical)$
9	10	10	3	3	6	$\sqrt{8}$	$r^3cos(3\theta)$
10	9	7	3	3	6	$\sqrt{8}$	$r^3sin(3\theta)$
11	12	14	2	4	6	$\sqrt{10}$	$(4r^2 - 3)r^2cos(2\theta)$
12	13	12	2	4	6	$\sqrt{10}$	$(4r^2 - 3)r^2sin(2\theta)$
13	16	19	1	5	6	$\sqrt{12}$	$(10r^4 - 12r^2 + 3)rcos(\theta)$
14	17	18	1	5	6	$\sqrt{12}$	$(10r^4 - 12r^2 + 3)rsin(\theta)$
15	22	25	0	6	6	$\sqrt{7}$	$20r^6 - 30r^4 + 12r^2 - 1$
16	14	15	4	4	8	$\sqrt{10}$	$r^4cos(4\theta)$
17	15	11	4	4	8	$\sqrt{10}$	$r^4sin(4\theta)$
18	18	20	3	5	8	$\sqrt{12}$	$(5r^2 - 4)r^3cos(3\theta)$
19	19	17	3	5	8	$\sqrt{12}$	$(5r^2 - 4)r^3sin(3\theta)$
20	24	26	2	6	8	$\sqrt{14}$	$(15r^4 - 20r^2 + 6)r^2cos(2\theta)$
21	23	24	2	6	8	$\sqrt{14}$	$(15r^4 - 20r^2 + 6)r^2sin(2\theta)$
22	30	33	1	7	8	4	$(35r^6 - 60r^4 + 30r^2 - 4)rcos(\theta)$
23	29	32	1	7	8	4	$(35r^6 - 60r^4 + 30r^2 - 4)rsin(\theta)$
24	37	41	0	8	8	3	$70r^8 - 140r^6 + 90r^4 - 20r^2 + 1$
25	20	21	5	5	10	$\sqrt{12}$	$r^5cos(5\theta)$
26	21	16	5	5	10	$\sqrt{12}$	$r^5sin(5\theta)$
27	26	27	4	6	10	$\sqrt{14}$	$(6r^2 - 5)r^4cos(4\theta)$
28	25	23	4	6	10	$\sqrt{14}$	$(6r^2 - 5)r^4sin(4\theta)$
29	32	34	3	7	10	4	$(21r^4 - 30r^2 + 10)r^3cos(3\theta)$
30	31	31	3	7	10	4	$(21r^4 - 30r^2 + 10)r^3sin(3\theta)$
31	38	42	2	8	10	$\sqrt{18}$	$(56r^6 - 105r^4 + 60r^2 - 10)r^2cos(2\theta)$
32	39	40	2	8	10	$\sqrt{18}$	$(56r^6 - 105r^4 + 60r^2 - 10)r^2sin(2\theta)$
33	46	51	1	9	10	$\sqrt{20}$	$(126r^8 - 280r^6 + 210r^4 - 60r^2 + 5)rcos(\theta)$
34	47	50	1	9	10	$\sqrt{20}$	$(126r^8 - 280r^6 + 210r^4 - 60r^2 + 5)rsin(\theta)$
35	56	61	0	10	10	$\sqrt{11}$	$252r^{10} - 630r^8 + 560r^6 - 210r^4 + 30r^2 - 1$
36	28	28	6	6	12	$\sqrt{14}$	$r^6cos(6\theta)$
37	27	22	6	6	12	$\sqrt{14}$	$r^6sin(6\theta)$
38	34	35	5	7	12	4	$(7r^2 - 6)r^5cos(5\theta)$
39	33	30	5	7	12	4	$(7r^2 - 6)r^5sin(5\theta)$
40	79	85	0	12	12	$\sqrt{13}$	$924r^{12} - 2772r^{10} + 3150r^8 - 1680r^6 + 420r^4 - 42r^2 + 1$
41	36	36	7	7	14	4	$r^7cos(7\theta)$
42	35	29	7	7	14	4	$r^7sin(7\theta)$

Bibliography

1. "IEEE Standard on Piezoelectricity". *ANSI/IEEE Std 176-1987*, 1988.

2. Abramowitz, M. and I. A. Stegun. *Handbook of Mathematical Functions, with Formulas, Graphs, and Mathematical tables.* Dover, 1965.

3. Acikmese, A., E. Mettler, W. G. Breckenridge, S. A. Macenka, and E. F. Tubbs. "L2 Earth Atmosphere Observatory: Formation Guidance, Metrology, and Control Synthesis". *AIAA/AAS Astrodynamics Specialist Conference and Exhibit*, volume AIAA-2004-5212. American Institute of Aeronautics and Astronautics, Inc., 2004.

4. Adelman, N. T. "Spherical Mirror with Piezoelectrically Controlled Curvature". *Applied Optics*, 16(12):3075–3077, 1977.

5. Adetona, O., L. G. Horta, B. K. Taleghani, J. R. Blandino, and K. J. Woods. "Vibration Studies of an Inflatable/Rigidizable Hexapod Structure with a Tensioned Membrane STRUCTURE WITH A TENSIONED MEMBRANE". *44th AIAA/ASME/ASCE/AHS/ASC Structures, Structural Dynamics, and Materials Conference*, volume AIAA-2003-1737. American Institute of Aeronautics and Astronautics, Inc., 2003.

6. Agnes, G. S. and J. W. Wagner. "Adaptive Structures Technology for Membrane Optical Surfaces". *42nd AIAA/ASME/ASCE/AHS/ASC Structures, Structural Dynamics, and Materials Conference*, volume AIAA-2001-1199. American Institute of Aeronautics and Astronautics, Inc., 2001.

7. Albertinetti, N. P., R. E. Aldrich, and J. H. Everson. "Deformable Mirrors with Bimorph Actuators". S. Holly (editor), *Adaptive Optical Components 2*, volume 179, 28–31. SPIE, 1979.

8. Anderson, E. and J. Lindler. "Smart Material Actuator with Long Stroke and High Power Output". *43th AIAA/ASME/ASCE/AHS/ASC Structures, Structural Dynamics, and Materials Conference*, volume 2002-1254. American Institute of Aeronautics and Astronautics, 2002.

9. Angel, R. "Future Very Large Space Telescopes". *AIAA Space 2000 Conference and Exposition*, volume AIAA-2000-5304. American Institute of Aeronautics and Astronautics, Inc., 2000.

10. anonymous. *Piezo Film Sensors Technical Manual.* Measurement Specialties, Inc. Sensor Products Division, 1999.

11. anonymous. *MSC.Nastran Quick Reference Guide*, volume 2. MSC.Software Corp, 2004.

12. anonymous. *GE Silicones RTV615 Clear General Purpose Potting/Encapsulating Compound.* MatWeb. http:www.matweb.com, 2005.

13. anonymous. *James Webb Space Telescope, www.jwst.nasa.gov.* 2006.

14. Apollonov, V. V., V. Aksinnin, S. A. Chetkin, V. V. Kijko, S. V. Muraviev, and G. V. Vdovin. "Magnetostrictive Actuators in Optical Design". *Proceedings SPIE*, 1543:313–324, 1991.

15. Ash, J. T., C. H. Jenkins, D. K. Marker, and J. M. Wilkes. "Shape Achievement of Optical Membrane MirrorsUsing Coating/Substrate Intrinsic Stresses". *Journal of Spacecraft and Rockets*, 41(4):551–557, 2004.

16. Babuska, V. and B. D. Freed. "Composite Piezoelectric Beam and Plate Elements for Structural Control". *38th AIAA/ASME/ASCE/AHS/ASC Structures, Structural Dynamics, and Materials Conference and Exhibit*, volume AIAA-1997-1312, 1607–1620. 1997.

17. Bailey, T. and J. E. Hubbard. "Distributed Piezoelectric-Polymer Active Vibration Control of a Cantilever Beam". *AIAA Journal of Guidance and Control*, 8(5):605–611, 1985.

18. Bao, X., Y. Bar-Cohen, Z. Chang, S. Sherrit, and M. Madescu. "Wirelessly Controllable Inflated Electroactive Polymer (EAP) Reflectors". E. Udd and D. Inaudi (editors), *Smart Structures and Materials 2005: Smart Sensor Technology and Measurement Systems*, volume 5759, 371–378. 2005.

19. Bar-Cohen, Y. "Electroactive Polymers as Artificial Muscles–Reality and Challenges". *42nd AIAA/ASME/ASCE/AHS/ASC Structures, Structural Dynamics, and Materials Conference*, volume AIAA 2001-1492. American Institute of Aeronautics and Astronautics, Inc., 2001.

20. Bar-Cohen, Y. "Biologically Inspired Intelligent Robots Using Artificial Muscles". *MEMS, NANO and Smart Systems, 2003. Proceedings. International Conference on*, 2–8, 2003.

21. Bar-Cohen, Y. "Electroactive Polymers (EAP) As Actuators for Potential Future Planetary Mechanisms". *Evolvable Hardware, 2004. Proceedings. 2004 NASA/-DoD Conference on*, 309–317, 2004.

22. Barenblatt, G. I. *Scaling, Self-Similarity, and Intermediate Asymptotics.* Cambridge University Press, 1996.

23. Bathe, K. J. *Finite Element Procedures.* Prentice-Hall, Inc., 1996.

24. Bekey, I. "A 25 M. Diameter Space Telescope Weighing Less Than 150 Kg". *AIAA Space Technology Conference and Exposition*, volume AIAA-1999-4478. American Institute of Aeronautics and Astronautics, Inc., 1999.

25. Berger, K. T., L. G. Horta, and B. K. Taleghani. "Static Testing of an Inflatable/Rigidizable Hexapod Structure". *45th AIAA/ASME/ASCE/AHS/ASC Structures, Structural Dynamics, and Materials Conference.* American Institute of Aeronautics and Astronautics, 2004.

26. Bishop, J. A. "Shape Correction of Initially Flat Inflated Membranes by a Genetic Algorithm". *39th AIAA/ASME/ASCE/AHS/ASC Structures, Structural Dynamics, and Materials Conference*, volume AIAA-98-1984. American Institute of Aeronautics and Astronautics, Inc., 1998.

27. Blandino, J. R., J. D. Johnston, and U. K. Dharamsi. "Corner Wrinkling of a Square Membrane Due to Symmetric Mechanical Loads". *Journal of Spacecraft and Rockets*, 39(5):717–724, 2002.

28. Born, M. and E. Wolf. *Principles of Optics : Electromagnetic Theory of Propagation, Interference and Diffraction of Light*. Cambridge University Press, 7th edition, 1999.

29. Bush, K., D. German, B. Klemme, A. Marrs, and M. Schoen. "Electrostatic Membrane Deformable Mirror Wavefront Control Systems: Design and Analysis". J. D. Gonglewski, M. T. Gruneisen, and M. K. Giles (editors), *Advanced Wavefront Control: Methods, Devices, and Applications II*, volume 5553, 28–38. SPIE, 2004.

30. Chodimella, S. P., J. D. Moore, and J. Otto. "Design Evaluation of a Large Aperture Deployable Antenna". *47th AIAA/ASME/ASCE/AHS/ASC Structures, Structural Dynamics and Materials Conference*, volume AIAA 2006-1603. 2006.

31. Choi, S. H., K. D. Song, W Golembiewskii, S. H. Chu, and G. C. King. "Microwave Power for Smart Material Actuators". *Smart Materials and Structures*, 1:38–48, 2004.

32. Claflin, E. S. and N. Bareket. "Configuring an Electrostatic Membrane Mirror by Least-squares Fitting with Analytically Derived Influence Functions". *Journal Optical Society of America*, 3(11):1833–1839, 1986.

33. Cobb, R. G. *Structural Damage Identification from Limited Measurement Data*. Phd, Air Force Inst of Tech, 1996.

34. Costen, R. C., J. Su, and J. S. Harrision. "Model for Bending Actuators that use Electrostrictive Graft Elastomers". Y. Bar-Cohen (editor), *Smart Structures and Materials 2001: Electroactive Polymer Actuators and Devices*, volume 4329. SPIE, 2001.

35. Cote, F., P. Masson, N. Mrad, and V. Cotoni. "Dynamic and Static Modelling of Piezoelectric Composite Structures Using a Thermal Analogy With Msc/nastran". *Composite Structures*, 65(3), 2004.

36. Dargaville, T. R., M. C. Celina, P. M. Chapyla, and R. A. Assink. "Evaluation of Piezoelectric PVDF Polymers for Use in Space Environments". *45th AIAA/ASME/ASCE/AHS/ASC Structures, Structural Dynamics, and Materials Conference*, volume 2004-1547. American Institute of Aeronautics and Astronautics, 2004.

37. Das, A., J. M. Sater, C. R. Crowe, and R. Antcliff. *An Assessment of Smart Air and Space Structures: Demonstrations and Technology Descriptive Note: Final rept. Sep 1998-Sep 2000.* Technical report, Institute for Defense Analyses Alexandria VA, 2000.

38. DeSilva, C. W. *Vibration: Fundamentals and Practice.* CRC Press, 2000.

39. Dias, C. J. and D. K. Das-Gupta. "Electroactive Polymer-ceramic Composites". *Properties and Applications of Dielectric Materials, 1994., Proceedings of the 4th International Conference on*, 1:175–178 vol.1, 1994.

40. Dorrington, A. A., T. W. Jones, P. M. Danehy, and R. S. Pappa. "Laser-Induced Fluorescence Photogrammetry for Dynamic Characterization of Transparent and Aluminized Membrane Structures". *39th AIAA/ASME/SAE/ASEE Joint Propulsion Conference*, volume AIAA 2003-4798. American Institute of Aeronautics and Astronautics, Inc., 2003.

41. Dorrington, A. A., T. W. Jones, P. M. Danehy, and R. S. Pappa. "Membrane Vibration Analysis above the Nyquist Limit with Fluroescence Videogrammetry". *39th AIAA/ASME/SAE/ASEE Joint Propulsion Conference.* 2004.

42. Duvvuru, H. K. and C. H. Jenkins. "Active Shape Control of Gossamer Apertures". H. A. MacEwen (editor), *UV/Optical/IR Space Telescopes: Innovative Technologies and Concepts*, volume 5166, 247–258. SPIE, 2004.

43. Errico, S., R. Angel, B. L. Stamper, J. H. Burge, and T. Connors. "Stretched Membrane with Electrostatic Curvature (SMEC) Mirrors: A New Technology for Large Lightweight Space Telescopes". H. A. MacEwen (editor), *Highly Innovative Space Telescope Concepts*, volume 4849, 356–364. SPIE, 2002.

44. Flint, E., G. Bales, R. Glaese, and R. Bradford. "Experimentally Characterizing the Dynamics of 0.5m Diameter DoublyCurved Shells Made From Thin Films". *44th AIAA/ASME/ASCE/AHS/ASC Structures, Structural Dynamics, and Materials Conference*, volume 2003-1831. American Institute of Aeronautics and Astronautics, 2003.

45. Flint, E. M. and K. K. Denoyer. "Approach for Efficiently Evaluating Internally Reacted Global Shape Control Actuation Strategies for Apertures". *44th AIAA/ASME/ASCE/AHS/ASC Structures, Structural Dynamics, and Materials Conference*, volume AIAA-2003-1738. American Institute of Aeronautics and Astronautics, Inc., 2003.

46. Flint, E. M., J. E. Lindler, and J. L. Hall. "Experimental Validation of Discrete Location Boundary Shape Control for Thin Film Shells". *47th AIAA/ASME/ASCE/AHS/ASC Structures, Structural Dynamics and Materials Conference*, volume AIAA-2006-1903. American Institute of Aeronautics and Astronautics, Inc., 2006.

47. Flint, E. M., J. E. Lindler, J. L. Hall, C. Rankine, and Regelbrugge. "Overview of Form Stiffened Thin Film Shell Characteristic Behavior". *47th AIAA/AS-ME/ASCE/AHS/ASC Structures, Structural Dynamics and Materials Conference*, volume AIAA-2006-1900. American Institute of Aeronautics and Astronautics, Inc., 2006.

48. Furuya, H. and Y. Inoue. "Dynamic Properties of Rotationally Skew Fold Membrane for Spinning Solar Sail". *47th AIAA/ASME/ASCE/AHS/ASC Structures, Structural Dynamics and Materials Conference*, volume AIAA-2006-1980. American Institute of Aeronautics and Astronautics, Inc., 2006.

49. Gaspar, J. L. and R. S. Pappa. *Membrane Vibration Tests Using Surface-Bonded Piezoelectric Patch Acutuation*. Technical Report NASA/TM-2003-212150, National Aeronautics and Space Administration, 2003.

50. Gaspar, J. L., M. J. Solter, and R. S. Pappa. *Membrane Vibration Studies Using a Scanning Laser Vibrometer*. Technical Report NASA/TM-2002-211427, National Aeronautics and Space Administration, 2002.

51. Gelfand, I. M. and S. V. Fomin. *Calculus of Variations*. Dover, 2000.

52. Gere, J. M. and S. P. Timoshenko. *Mechanics of Materials*. Brooks/Cole Engineering Division, 2nd ed. edition, 1984.

53. Glaese, R. M., M. E. Regelbrugge, K. F. Lore, S. W. Smith, and E. M. Flint. "Modeling the Dynamics of Large Diameter Doubly Curved Shells Made from Thin-Films". *44th AIAA/ASME/ASCE/AHS/ASC Structures, Structural Dynamics, and Materials Conference*, volume 2003-1830. American Institute of Aeronautics and Astronautics, 2003.

54. Goodman, J. W. *Introduction to Fourier Optics*. McGraw-Hill series in electrical and computer engineering. McGraw-Hill, 2nd edition, 1996.

55. Gorinevsky, D., T. T. Hyde, and C. Cabuz. "Distributed Localized Shape Control of Gossamer Space Structures". *42nd AIAA/ASME/ASCE/AHS/ASC Structures, Structural Dynamics, and Materials Conference*, volume 2001-1197. American Institute of Aeronautics and Astronautics, 2001.

56. Greschik, G. "Solar Sail Scalability and the Concept of a Truly Scalable Architecture". *47th AIAA/ASME/ASCE/AHS/ASC Structures, Structural Dynamics and Materials Conference*, volume AIAA 2006-1703. American Institute of Aeronautics and Astronautics, Inc., 2006.

57. Hadinata, P. C. and J. A. Main. "Time Response of Electron Gun Strain Control of Piezoelectric Materials". N. M. Wereley (editor), *Smart Structures and Materials 2000: Smart Structures and Integrated Systems*, volume 3985, 378–384. SPIE, 2000.

58. Hadinata, P. C. and J. A. Main. "Survey of Piezoelectric Material Strain Response to Electron Gun Excitation". L. . P. Davis (editor), *Smart Structures*

and *Materials 2001: Smart Structures and Integrated Systems*, volume 4327, 331–341. SPIE, 2001.

59. Haertling, G., E. Furman, G. Li, B. Barron, and W. Paradise. *Stress-Enhanced Ferroelectric Materials and Structures. Descriptive Note: Final rept. 1 Jun 96-14 Jun 97,.* Technical report, Clemson Univ Sc Dept of Ceramic Engineering, 1997.

60. Halevi, P. "Bimorph Piezoeletric Flexible Mirror: Graphical Solution and Comparison with Experiment". *Journal Optical Society of America*, 73(1):110–113, 1983.

61. Hall, J., E. Flint, and J. Lindler. "Experimental Validation of Discrete Location Boundary Shape Control for Thin Film Shells". *47th AIAA/ASME/ASCE/AHS/ASC Structures, Structural Dynamics and Materials Conference*, volume AIAA-2006-1903. American Institute of Aeronautics and Astronautics, Inc., 2006.

62. Heald, J. C., M. J. Potvin, and X. X. Jiang. "Experimental Investigations to Support a Multi-Layer Deployable Membrane Structure for Space Antennae". *46th AIAA/ASME/ASCE/AHS/ASC Structures, Structural Dynamics and Materials Conference*, volume 2005-2317. 2005.

63. Hecht, E. *Optics.* Addison-Wesley, 4th edition, 2002.

64. Hiddleston, H. R., D. D. Lyman, and E. L. Schafer. "Comparisons of Deformable-Mirror Models and Influence Functions". M. A. Ealey (editor), *Active and Adaptive Optical Systems*, volume 1542, 20–33. SPIE, 1991.

65. Hill, L., G. Carman, D. G. Lee, and B. Patrick. "Shape Memory Alloy Film for Deployment and Control of Membrane Apertures". H. A. MacEwen (editor), *UV/Optical/IR Space Telescopes: Innovative Technologies and Concepts*, volume 5166, 271–280. SPIE, 2004.

66. Holmes, J. T., D. J. Albert, .. R. Mancini, L. M. Murphy, and P. O. Schissel. "Development of Concentrating Collectors for Solar Thermal Systems". *Proceedings of the 24th Intersociety Energy Conversion Engineering Conference, 1989. IECEC-89.* IEEE, 1989.

67. Huang, C., R. Klein, F. Xia, H. Li, Q. M. Zhang, F. Bauer, and Z. Y. Cheng. "Poly(vinylidene Fluoride-trifluoroethylene) Based High Performance Electroactive Polymers". *Dielectrics and Electrical Insulation, IEEE Transactions on [see also Electrical Insulation, IEEE Transactions on]*, 11(2):299–311, 2004.

68. Hubbard, S. E. and J. E. Burke. "Shape Control of Piezoelectric Bimorph Mirrors". D. C. O'Shea (editor), *Analysis of Optical Structures*, volume 1532, 207–214. SPIE, 1991.

69. Iserles, A. *A First Course in the Numerical Analysis of Differential Equations.* Cambridge Texts in Applied Mathematics. Cambridge University Press, 1996.

213

70. Kaneda, Y., N. Kamamichi, M. Yamakita, K. Asaka, and Z. W. Luo. "Control of Linear Artificial Muscle Actuator Using IPMC". *SICE 2003 Annual Conference*, volume 2, 1650–1655. 2003.

71. Kutz, M. *Handbook of Materials Selection.* J. Wiley, 2002.

72. Lee, C. K. "Theory of Laminated Piezoelectric Plates for the Design of Distributed Sensors/Actuators. I. Governing Equations and Reciprocal Relationships". *J. Acoust. Soc. Am. (USA)*, vol.87, no.3:1144–1158, 1990.

73. Lee, C. K., W. W. Chiang, and T. C. O'Sullivan. "Piezoelectric Modal Sensor/Actuator Pairs for Critical Active Damping Vibration Control". *J. Acoust. Soc. Am. (USA)*, vol.90, no.1:374–384, 1991.

74. Lee, C. K. and F. C. Moon. "Laminated Piezopolymer Plates for Torsion and Bending Sensors and Actuators". *J. Acoust. Soc. Am. (USA)*, 85(6):2432–2439, 1989.

75. Lee, C. K. and T. C. O'Sullivan. "Piezoelectric Strain Rate Gages". *J. Acoust. Soc. Am. (USA)*, vol.90, no.2, pt.1:945–953, 1991.

76. Lee, J. H., T. K. Uhm, W. S. Lee, and S. K. Youn. "First Order Analysis of Thin Plate Deformable Mirrors". P. L. Wizinowich and D. Bonaccini (editors), *Adaptive Optical System Technologies II*, volume 4839, 757–764. SPIE, 2003.

77. Lee, S. H. *MSC/NASTRAN Handbook for Nonlinear Analysis : based on Version 67.* MacNeal-Schwendler Corp., 1992.

78. Lindler, J. and E. Flint. "Robustness of Thin Film Shells with Boundary Actuation". *47th AIAA/ASME/ASCE/AHS/ASC Structures, Structural Dynamics and Materials Conference*, volume AIAA-2006-1904. American Institute of Aeronautics and Astronautics, Inc., 2006.

79. Lindler, J. E. and E. M. Flint. "Boundary Actuation Shape Control Strategies for Thin Film Single Surface Shells". *45th AIAA/ASME/ASCE/AHS/ASC Structures, Structural Dynamics, and Materials Conference*, volume 2004-1825. American Institute of Aeronautics and Astronautics, Inc., 2004.

80. Lutz, B. J. *Axisymmetric Optical Membrane Modeling Based on Experimental Results.* masters, Air Force Inst of Tech, 2004.

81. Madden, J. D., N. A. Vandesteeg, P. A. Anquetil, P. G. Madden, A. Takshi, R. Z. Pytel, S. R. Lafontaine, P. A. Wieringa, and I. W. Hunter. "Artificial Muscle Technology: Physical Principles and Naval Prospects". *Oceanic Engineering, IEEE Journal of*, 29(3):706–728, 2004.

82. Main, J. A., G. C. Nelson, and J. W. Martin. "Electron Gun Control of Smart Materials". M. E. Regelbrugge (editor), *Smart Structures and Materials 1998: Smart Structures and Integrated Systems*, volume 3329, 688–693. SPIE, 1998.

83. Malin, M., W. Macy, and G. Ferguson. "Edge Actutation for Figure Control". volume 365, 114–122. SPIE, 1982.

84. Mansuripur, M. "The Ronchi Test". *Optics and Photonics News*, 8(7):42–46, 1997.

85. Marker, D. K. and C. H. Jenkins. "Surface Precesion of Optical Membranes with Curvature". *Optics Express*, 1(11):324–331, 1997.

86. Martin, H. M., S. P. Callahan, B. Cuerden, W. B. Davison, S. T. Derigne, L. R. Dettmann, G. Parodi, T. J. Trebisky, S. C. West, J. T. Williams, L. M. Ed Stepp, and B. . *Advanced Technology Optical/IR Telescopes VI JF - Advanced Technology Optical/IR Telescopes VI JA - Proc. SPIE Int. Soc. Opt. Eng. CY - Kona, HI, USA*, volume 3352, 412–423. 1998.

87. Martin, J. W. and J. A. Main. "Noncontact Electron Gun Actuation of a Piezoelectric Polymer Thin Film Bimorph Structure". *Journal of Intelligent Material Systems and Structures*, 13:329–337, 2002.

88. Meirovitch, L. *Principles and Techniques of Vibrations*. Prentice-Hall, Inc., 1997.

89. Menikoff, A. "Actuator Influence Functions of Active Mirrors". *Applied Optics*, 30(7):833–838, 1991.

90. Mindlin, R. D. *On the Equations of Motion of Piezoelectric Crystals*. Problems of Continuum Mechanics. Society for Industrial and Applied Mathematics, 1961.

91. Moore, J. D., B. Patrick, P. A. Gierow, and E. Troy. "Design, Test, and Evaluation of an Electrostatically Figured Membrane Mirror". H. A. MacEwen (editor), *UV/Optical/IR Space Telescopes: Innovative Technologies and Concepts*, volume 5166, 188–196. SPIE, 2004.

92. MSC.Software. *MSC.Nastran Quick Reference Guide*. MSC.Software Corporation, 2004.

93. Murphy, D. M., B. D. Macy, and J. L. Gaspar. "Demonstration of a 10-m Solar Sail System". volume AIAA 2004-1576. American Institute of Aeronautics and Astronautics, Inc., 2004.

94. Nayfeh, A. H. and P. F. Pai. *Linear and Nonlinear Structural Mechanics*. Wiley Series in Nonlinear Science. Wiley-Interscience, 2004.

95. Nelson, G. C., J. A. Main, and J. W. Martin. "Wavefront Conjugation Using Electron-Gun-Controlled Piezoelectric Materials". P. L. Wizinowich (editor), *Adaptive Optical Systems Technology*, volume 4007, 582–589. SPIE, 2000.

96. Nichols, J. S., D. Duneman, and J. Jasso. "Performance Evaluation of an Edge-actuated, Modal, Deformable Mirror". *Optical Engineering*, 22(3):366–370, 1983.

97. Noll, R. L. "Zernike Polynomials and Atmospheric Turbulence". *Journal Optical Society of America*, 66(3):207–211, 1976.

215

98. Otake, M., Y. Kagami, M. Inaba, and H. Inoue. "Dynamics of Gel Robots Made of Electro-active Polymer Gel". *Robotics and Automation, 2001. Proceedings 2001 ICRA. IEEE International Conference on*, 2:1457–1462 vol.2, 2001.

99. Otake, M., Y. Kagami, Y. Kuniyoshi, M. Inaba, and H. Inoue. "Inverse Kinematics of Gel Robots Made of Electro-active Polymer Gel". *Robotics and Automation, 2002. Proceedings. ICRA '02. IEEE International Conference on*, 3:3224–3229, 2002.

100. Otake, M., Y. Kagami, Y. Kuniyoshi, M. Inaba, and H. Inoue. "Inverse Dynamics of Gel Robots Made of Electro-active Polymer Gel". *Robotics and Automation, 2003. Proceedings. ICRA '03. IEEE International Conference on*, 2:2299–2304 vol.2, 2003.

101. Panofsky, W. K. and M. Phillips. *Classical Electricity and Magnetism.* Addison-Wesley Series in Physics. Addison-Wesley, 1962.

102. Pappa, R. S., J. T. Black, J. R. Blandino, T. W. Jones, P. M. Danehy, and A. A. Dorrington. *Dot-Projection Photogrammetry and Videogrammetry of Gossamer Space Structures.* Technical Report NASA/TM-2003-212146, American Institute of Aeronautics and Astronautics, 2003.

103. Paquette, J. W. and K. J. Kim. "Ionomeric Electroactive Polymer Artificial Muscle for Naval Applications". *Oceanic Engineering, IEEE Journal of*, 29(3):729–737, 2004.

104. Patrick, B., J. Moore, S. Chodimella, D. Marker, and B. deBlonk. "Final Testing and Evaluation of a Meter-Class Actively Controlled Membrane Mirror". *47th AIAA/ASME/ASCE/AHS/ASC Structures, Structural Dynamics and Materials Conference*, volume AIAA-2006-1901. American Institute of Aeronautics and Astronautics, Inc., 2006.

105. Patrick, B. G. and J. D. Moore. "Manufacturing and Evaluation of Membrane Optical Elements for Ultra-Lightweight Optics". H. P. Stahl (editor), *Optical Manufacturing and Testing IV*, volume 4451. SPIE, 2001.

106. Pearson, J. E. and S. Hansen. "Experimental Studies of a Deformable-mirror Adaptive Optical System". *Journal Optical Society of America*, 67(3):325–333, 1977.

107. Peterson. *Control Demonstration of a Thin Deformable In-Plane ActuatedMirror.* masters, Air Force Inst of Tech, 2006.

108. Philen, M. and K. W. Wang. "Analytical and Experimental Investigations of the Active Stiffener Concept for Shape Control of a Circular Plate Structure". *44th AIAA/ASME/ASCE/AHS/ASC Structures, Structural Dynamics, and Materials Conference*, volume AIAA-2003-1636. 2003.

109. Philen, M. and K. W. Wang. "Active Stiffener Actuators for High-Precision Shape Control of Circular Plate Structure". *AIAA Journal*, 42(12):2570–2578, 2004.

110. Pollard, E. L. and C. H. Jenkins. "Shape Memory Alloy Deployment of Membrane Mirrors for Spaceborne Telescopes". *47th AIAA/ASME/ASCE/AHS/ASC Structures, Structural Dynamics and Materials Conference*, volume AIAA-2005-2196. 2005.

111. Polyanin, A. D. *Handbook of Linear Partial Differential Equations for Engineers and Scientists*. Chapman and Hall/CRC, 2002.

112. Preumont, A. *Vibration Control of Active Structures*, volume 96 of *Solid Mechanics and It's Applications*. Kluwer Academic Publishers, 2nd edition, 2002.

113. Reddy, J. N. *Mechanics of Laminated Composite Plates: Theory and Analysis*. CRC Press, 1997.

114. Redmond, J. M., P. S. Barney, T. D. Henson, J. A. Main, and J. W. Martin. *Distributed Sensing and Shape Control of Piezoelectric Bimorph Mirrors*. Technical Report SAN099-1974C, DOE, 1999.

115. Rogers, J. W. and G. S. Agnes. "Active Axisymmetric Optical Membranes". *43th AIAA/ASME/ASCE/AHS/ASC Structures, Structural Dynamics, and Materials Conference*, volume AIAA-2002-1450. American Institute of Aeronautics and Astronautics, Inc., 2002.

116. Rogers, J. W. and G. S. Agnes. "Modeling a Piezothermoelastic Beam-String". *Journal of Spacecraft and Rockets*, 39(5):725–731, 2002.

117. Rogers, J. W. and G. S. Agnes. "Asymptotic Finite Elements Introducing the Method of Integral Multiple Scales". *AIAA Journal*, 41(9):1797–1807, 2003.

118. Rogers, J. W. and G. S. Agnes. "Modeling Discontinuous Axisymmetric Active Optical Membranes". *Journal of Spacecraft and Rockets*, 40(4):553–564, 2003.

119. Roggemann, M. C. and B. Welsh. *Imaging through Turbulence*. The CRC Press Laser and Optical Science and Technology Series. CRC Press, 1996.

120. Ruggiero, E. J. and Babb B. Jacobs, J. H. "A Spider Technology Overview". *45th AIAA/ASME/ASCE/AHS/ASC Structures, Structural Dynamics, and Materials Conference*, volume AIAA-2004-1822. American Institute of Aeronautics and Astronautics, Inc., 2004.

121. Saada, A. S. *Elasticity Theory and Applications*. Krieger., 1993.

122. Schowengerdt, R. A. *Remote Sensing*. Elsevier, 2nd edition, 1997.

123. Sessler, G. M. and A. Berraissoul. "Tensile and Bending Piezoelectricity of Single-film Pvdf Monomorphs and Bimorphs". *Electrical Insulation, IEEE Transactions on [see also Dielectrics and Electrical Insulation, IEEE Transactions on]*, 24(2):249–254, 1989.

124. Shahinpoor, M., Y. Bar-Cohen, T. Xue, J. O. Simpson, and J. Smith. "Ionic Polymer-Metal Composites (IPMC)As Biomimetic Sensors and Actuators". *Smart Structures and Materials 1998*, volume 3324. SPIE, 1998.

125. Shih, H. R., R. Smith, and H. S. Tzou. "Photonic Control of Cylindrical Shells with Electro-Optic Photostrictive Actuators". *AIAA Journal*, 42(2):341–347, 2004.

126. Shih, H. R. and H. S. Tzou. "Opto-Electromechanical Actuator Patches For Active Vibration Control Of Thin Plates". *42nd AIAA/ASME/ASCE/AHS/ASC Structures, Structural Dynamics, and Materials Conference*, volume AIAA-2001-1556. 2001.

127. Sobers, D. M. *Smart Structures for Control of Optical Surfaces.* masters, Air Force Inst of Tech, 2002.

128. Sobers, D. M., G. S. Agnes, and D. Mollenhauer. "Smart Structures for Control of Optical Surfaces". *44th AIAA/ASME/ASCE/AHS/ASC Structures, Structural Dynamics, and Materials Conference.* American Institute of Aeronautics and Astronautics, Inc., 2003.

129. Solter, M., L. G. Horta, and A. Panetta. "A Study of a Prototype Actuator Concept for Membrane Boundary Control". *44th AIAA/ASME/ASCE/AHS/ASC Structures, Structural Dynamics, and Materials Conference*, volume AIAA-2003-1736. American Institute of Aeronautics and Astronautics, Inc., 2003.

130. Stamper, B. L., J. . R. Angel, J. . H. Burge, T. Connors, B. Duffy, and N. J. Woolf. "Stretched Membrane with Electrostatic Curvature (SMEC) Mirrors for Extremely Large Space Telescopes". H. . P. Stahl (editor), *Optical Manufacturing and Testing IV*, volume 4451, 105–113. SPIE, 2001.

131. Steel, M. R., F. Harrison, and P. G. Harper. "The Piezoelectric Bimorph: an Experimental and Theoretical Study of Its Quasistatic Response". *J. Phys. D: Appl. Phys.*, 11(6):979–989, 1978.

132. Steele, C. R., C. D. Balch, G. J. Gorgensen, T. Wendelin, and A. Lewandowski. *Membrane Dish Analysis: A Summary of Structural and Optical Analysis Capabilities.* Technical Report NREL/TP-253-3432, National Renewable Energy Laboratory, 1991.

133. Steinhaus, E. and S. G. Lipson. "Bimorph Piezoelectric Flexible Mirror". *Journal Optical Society of America*, 69(3):478–481, 1979.

134. Sumali, H., J. E. Massad, P. L. Reu, P. L. Chaplya, and J. W. Martin. "Analytical and Experimental Studies of Orthotropic Corner-Supported Plates with Segmented In-Plane Actuators". *2005 ASME International Mechanical Engineering Congress and Exposition.* American Society Of Mechanical Engineers, 2005.

135. Tiersten, H. F. *Linear Piezoelectric Plate Vibrations; Elements of the Linear Theory of Piezoelectricity and the Vibrations of Piezoelectric Plates.* Plenum Press, 1969.

136. Tokovinin, A., S. Thomas, and G. Vdovin. "Using 50-mm Electrostatic Membrane Deformable Mirror in Astronomical Adaptive Optics". D. B. Calia, B. L. Ellerbroek, and R. Ragazzoni (editors), *Advancements in Adaptive Optics*, volume 5490, 580–585. SPIE, 2004.

137. Trad, E. M. *Dynamic Characterization of Thin Deformable PVDF Mirror.* masters, Air Force Inst of Tech, 2005.

138. Tragesser, S. G. and A. Tuncay. "Orbital Design of Earth-Oriented Tethered Satellite Formations". *AIAA/AAS Astrodynamics Specialist Conferece and Exhibit*, volume 2002-4641. American Institute of Aeronautics and Astronautics, Inc., 2002.

139. Tung, S., S. R. i. ., L.A. Roe, A. Silano, .. P. Maynard, and F. . "A MEMS-based Flexible Sensor and Actuator System for Space Inflatable Structures". *Smart Materials and Structures*, 6:1230–1239, 2001.

140. Tyson, R. K. *Principles of Adaptive Optics.* Academic Press, 1991.

141. Tzou, H. S. and R. Ye. "Piezothermoelasticity and Precision Control of Piezoelectric systems - Theory and Finite Element Analysis". *Journal of Vibration and Acoustics*, 116(4):489–495, 1994.

142. Vaughan, H. "Pressurising a Prestretched Membrane to form a Paraboloid". *J. Engng. Sci.*, 18:99–107, 1980.

143. Wagner, J. W. *Optical Meterology of Adaptive Membrane Mirrors.* masters, Air Force Inst of Tech, 2000.

144. Wagner, J. W., G. S. Agnes, and E. Magee. "Optical Metrology of Adaptive Membrane Mirrors". *Journal of Intelligent Material Systems and Structures*, 11:837–847, 2000.

145. Waldie, D. D. and L. N. Gilman. "Technology Development for Large Deployable Sunshield to Achieve Cryogenic Environment". *Space 2004 Conference and Exhibit*, volume AIAA-2004-5987. American Institute of Aeronautics and Astronautics, Inc., 2004.

146. Wang, P. K. and F. Y. Hadaegh. "Modal Noninteracting Controls for Deformable Mirrors". *Control Applications, 1993., Second IEEE Conference on*, volume 1, 121–128. 1993.

147. Wang, P. K. and F. Y. Hadaegh. "Computation of Static Shapes and Voltages for Micromachined Deformable Mirrors with Nonlinear Electrostatic Actuators". *Journal of Microelectromechanical Systems*, 5(3):205–220, 1996.

148. Weisstein, E. W. *Euler-Mascheroni Constant. From MathWorld–A Wolfram Web Resource.* 2006.

149. White, C., J. Salama, D. Barber, and A. E. Hatheway. "Shaping of Parabolic Cylindrical Membrane Reflectors for the DART Precision Test Bed". *44th AIAA/ASME/ASCE/AHS/ASC Structures, Structural Dynamics, and Materials Conference*, volume AIAA-2003-1652. American Institute of Aeronautics and Astronautics, Inc., 2003.

150. Wilkes, J. M. *Mechanics of a Near Net-Shape Stress-Coated Membrane, Vol 2. Theory Development using the Method of Asymptotic Expansions.* Technical Report AFRL-DE-TR-2002-1063, Air Force Research Lab Kirtland AFB NM Directed Energy Directorate, 2002.

151. Wilkes, J. M. *Mechanics of a Near Net-Shape Stress-Coated Membrane. Volume I of II: theory Development Using the Method of Asymptotic Expansions Descriptive Note: Final technical rept. Oct 2000-Sep 2002.* Technical Report AFRL-DE-TR-2002-1063, Air Force Research Lab Kirtland AFB NM Directed Energy Directorate, 2002.

152. Wilkes, J. M., C. H. Jenkins, D. K. Marker, R. A. Carreras, D. C. Duneman, and J. R. Rotge. "Concave Membrane Mirrors from Aspheric to Near-Parabolic". J. D. Gonglewski and M. A. Vorontsov (editors), *High-Resolution Wavefront Control: Methods, Devices, and Applications*, volume 3670. SPIE, 1999.

153. Yang, E. H., R. Dekany, and S. Padin. *Design and Fabrication of a Large Vertical Travel Silicon Inchworm Microactuator for the Advanced Segmented Silicon Space Telescope.* Technical Report 02-3144, National Aeronautics and Space Administration, 2002.

154. Zwillinger, D. *CRC Standard Mathematical Tables and Formulae, 31st Edition.* CRC Press, 2003.

Index

The index is conceptual and does not designate every occurrence of a keyword. Page numbers in bold represent concept definition or introduction.

REPORT DOCUMENTATION PAGE

Form Approved
OMB No. 0704–0188

1. REPORT DATE *(DD–MM–YYYY)*	2. REPORT TYPE		3. DATES COVERED *(From — To)*
21–03–2005	Ph D Dissertation		Sept 2003 — Sep 2006

4. TITLE AND SUBTITLE

Lightweight In-Plane Actuated Deformable Mirrors for Space Telescopes

5a. CONTRACT NUMBER

DACA99–99–C–9999

5b. GRANT NUMBER

5c. PROGRAM ELEMENT NUMBER

6. AUTHOR(S)

Michael J. Shepherd, Lt Col, USAF

5d. PROJECT NUMBER

05-165

5e. TASK NUMBER

5f. WORK UNIT NUMBER

7. PERFORMING ORGANIZATION NAME(S) AND ADDRESS(ES)

Air Force Institute of Technology
Graduate School of Engineering and Management
2950 Hobson Way
WPAFB OH 45433-7765

8. PERFORMING ORGANIZATION REPORT NUMBER

AFIT/DS/ENY/06-03

9. SPONSORING / MONITORING AGENCY NAME(S) AND ADDRESS(ES)

AFOSR
Lt Col Sharon Heise
4015 Wilson Blvd, Rm 713
Arlington VA, 22203-1954

10. SPONSOR/MONITOR'S ACRONYM(S)

11. SPONSOR/MONITOR'S REPORT NUMBER(S)

12. DISTRIBUTION / AVAILABILITY STATEMENT

Approval for public release; distribution is unlimited.

13. SUPPLEMENTARY NOTES

14. ABSTRACT

This research focused on lightweight, in-plane actuated, deformable mirrors, with the ultimate goal of developing a 20-meter light gathering aperture for space telescopes. The 0.127 meter diameter deformable mirror small scale testbed was modelled in finite elements using MSC.Nastran software and then used as a basis for a quasi-static controller. Experimental tracking of Zernike tip, tilt, and defocus modes was accomplished. The analytical solutions to plate-membrane and beam-string ordinary differential equations were developed. A simplified approach to modelling the axisymmetric cases was also presented. A novel static control strategy, the Modal Transformation Method, was developed to form Zernike surfaces within an interior, or clear aperture, region using a number of statically-actuated Bessel-based vibration modes. The scaling problem for membrane optics is addressed. Significantly, it is shown linear modelling may correctly explain the behavior of small-scale models, but only non-linear models will account for the important terms which govern the full-scale large aperture membrane telescopes.

15. SUBJECT TERMS

deformable mirror, piezoelectric, membrane optics, adaptive optics, Zernike polynomial, plate-membrane, space telescope

16. SECURITY CLASSIFICATION OF:

a. REPORT	b. ABSTRACT	c. THIS PAGE
U	U	U

17. LIMITATION OF ABSTRACT

UU

18. NUMBER OF PAGES

238

19a. NAME OF RESPONSIBLE PERSON

Dr. Richard G. Cobb

19b. TELEPHONE NUMBER *(include area code)*

(937) 255–3636, ext 4559

Standard Form 298 (Rev. 8–98)
Prescribed by ANSI Std. Z39.18